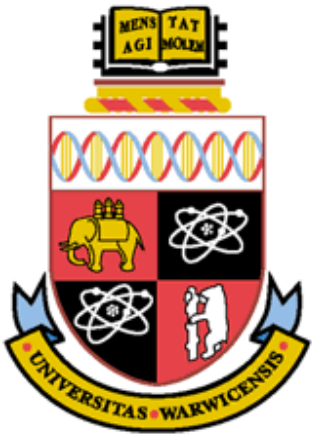

Jet Noise: Aeroacoustic Distribution Of A Subsonic Co-Axial Jet

Amit Kiran

October 2008

This report is submitted in partial fulfilment

of the requirements for the PhD Programme of the

School of Engineering

University of Warwick

2008

To Dad

Abstract

The noise generated by aircraft can be easily heard by those living under the flight path of passenger or cargo carriers. It is considered an environmental pollutant and is treated as such by the International Civil Aviation Organization (ICAO) who monitor and review noise levels. The ICAO imposes substantial fines on those carriers who do not adhere to the decibel limitations. With the new limit or 'stage' enforced in 2006, aircraft manufacturers (including jet engine manufacturers) are seeking ways to reduce the noise created by an aircraft.

A 1/150th scale model, based on the exit geometry typically found on commercial jet engines, was designed and manufactured at Warwick. The laboratory jet flow conditions operated at 0.7 Mach. The work presented in this thesis looks at the noise generated in a subsonic, co-flowing jet, with particular focus given to the distribution sound sources from 5 kHz to 80 kHz (0.375 St to 6.0 St).

An acoustic mirror mounted on a motorized 3-way traverse measured radiated sound in the co-flowing jet to produce 2D sound source maps. This is done using combinations of smooth cowl and chevrons for the core and bypass nozzles. For frequencies less than 30 kHz, a reduction of noise was observed using the bypass chevron nozzle compared with the bypass smooth cowl nozzle.

Laser Doppler Anemometry (LDA) was used to reveal the 2D flow dynamics of the jet, supporting the acoustic distribution results with velocity profiles of the flow. The change in the flow dynamics with different nozzle combinations is discussed and different regions of the flow were identified.

Keywords: jet noise, aeroacoustics, acoustic mirror, co-flow

Contents

List of Figures

List of Tables

Nomenclature

$\hat{\theta}_i$	Estimate of θ_i, page 137
θ_i	Maximum Likihood Estimate for an i_{th} value, page 136
Δz	Displacement downstream, page 91
δ_{bl}	boundary layer thickness, page 192
η_p	Relative amplitude of particulates in a flow, page 56
γ	Adiabatic index , page 15
γ_f	Factor accounting for the time lag between the passage of a vortex and the emission of a sound pulse at the downstream corner of the cavity, page 304
$\hat{b}$	Estimated shape parameter for probability density function, page 140
$\hat{c}$	Estimated shape parameter for simulated probability density function, page 140
$\hat{d}$	Estimated scale parameter for simulated probability density function, page 140

κ	Ratio of convection velocity of vortices to free stream velocity, page 304
$Ł_{cav}$	Length of a cavity, page 304
λ_f	Wavelength of the laser light, page 77
λ_{he}	frequency of vortex shedding, page 17
λ_w	Acoustic wave length, page 92
μ_p	Viscosity of a flow, page 56
ν_{re}	kinematic viscosity of the fluid, page 16
$\Phi_{ff}(f)$	Power spectral density at the far field, page 83
$\Phi_m(x, f)$	Mirror measured power spectral density, page 82
Ψ_m	Normalization factor for the mirror measured power spectral density, page 82
ρ	Density, page 22
ρ_p	Density of particulates, page 56
τ	Small measure of time, page 37
θ_f	Angle between two laser beams, page 77
θ_{res}	Angular resolution angle, page 92
$\theta_{rsm,n}$	Angle between the normal vector and microphone displacement vector, at a given point on the surface of the acoustic mirror, page 80

$\tilde{b}$	Shape parameter for a simulated probability density function, page 140
$\tilde{c}$	Shape parameter for a simulated probability density function, page 140
$\tilde{d}$	Scale parameter for a simulated probability density function, page 140
$\tilde{x}$	Calculated scalar value used in a probability density function, page 141
a	Parameter used for skewness in a probability density function, page 141
a_m	Radius of the long axis of the ellipse used for the acoustic mirror, page 71
a_z	Noise source, page 80
b	Shape parameter for the probability density function, page 135
b_m	Radius of the short axis of the ellipse used for the acoustic mirror, page 71
c	Shape parameter for the probability density function, page 135
c_0	Speed of sound in a given medium, page 83
c_∞	Speed of sound in the ambient, page 23
D	Kullback-Liebler Divergence, page 137
d	Scale parameter for the probability density function, page 135

d_f	Fringe spacing in the LDA measurement volume, page 77
D_m	Diameter of the acoustic mirror, page 71
d_p	Diameter of particulates, page 56
D_{re}	aperture diameter used to calculate the Reynolds number, page 16
f	Frequency of tones, page 304
f_D	Doppler frequency, page 77
f_f	Frequency reflecting the fluctuation in light intensity, page 78
f_{m1}	Distance of the near focus from the centre of the acoustic mirror, page 71
f_{m2}	Distance of the far focus from the centre of the acoustic mirror, page 71
f_p	Oscillation frequency of particulates in a flow, page 56
f_{st}	frequency of vortex shedding, page 17
f_s	frequency of a sound source, page 93
f_u	Probability density function, page 135
f_v	vectors of length N containing signal data, page 114
F_x	Cumulative distribution function, page 130
$f_x(x)$	probability density function , page 129
$G(r_m, r_s)$	Free field spherical far field Greens function, page 81
G_0	Gain in sound pressure level, page 72

g_v	vectors of length N containing signal data, page 114
h_m	Distance between the point source and shear layer along the direct transmission path to the mirror, page 91
i	Integer, page 136
I_m	Acoustic intensity at the near focus of the acoustic mirror, page 72
I_{ref}	Acoustic intensity at a reference microphone, page 72
k_H	wave number in the Helmholtz Number, page 43
L	Maximum Likihood Function, page 136
L_m	Sound pressure level at the near focus of the acoustic mirror, page 72
l_m	Distance of a reference microphone to a sound source, page 72
L_{ref}	Sound pressure level at a reference microphone, page 72
L_{res}	Limit of resolution, page 93
L_{st}	characteristic length, page 17
m	Arbitrary integer, page 304
m_a	Integer, page 114
m_{ff}	Far focus position of the acoustic mirror, page 81
M_m	Molar mass, page 15
M_p	Mach number of the primary jet, page 12

M_s	Mach number of the secondary jet, page 12
Ma	Mach number, page 15
N	Natural Number, page 114
n	Normal at r_s, page 81
n_a	Integer, page 114
n_b	Integer, page 136
n_{sn}	Normal to the surface of the acoustic mirror at a given point, page 80
P	Power of radiated noise, page 24
p'	Total pressure fluctuations, page 22
p'_a	Acoustic pressure, page 22
p'_h	Hydrodynamic fluctuations, page 22
$P(r_m, r_a)$	Frequency domain pressure, page 81
$p(y_k, t + \tau_f)$	Far field sound readings, page 37
$P_0(r_{am})$	Direct free field pressure from a source at r_{am}, page 81
$P_s(r_{as})$	Reflected free field pressure from a source at r_{am}, page 81
R	Molar gas constant, page 15
r	Distance from the source, page 22
r_{am}	Displacement from the noise source to the microphone at the near focus, page 80

r_{as}	Displacement from the noise source to the surface of the acoustic mirror, page 80
r_a	Position of a sound source in the far focus of the acoustic mirror, page 81
r_H	radius in the Helmholtz Number, page 43
r_{jm}	distance from a point on the jet axis to the far field microphone, page 83
r_{mic}	Distance of a microphone from a noise source, page 48
r_m	Near focus of the acoustic mirror, page 80
r_{sm}	Displacement from the surface of the acoustic mirror to the microphone, page 80
r_s	Internal surface of the acoustic mirror at a given point, page 80
rho_0	density of the ambient medium, page 83
$S(x_k, t)$	Sound source contribution at position x_k at time t, page 37
S_m	Internal surface of the acoustic mirror, page 71
T	Temperature in Kelvin, page 15
t	Time, page 37
T_{ij}	Lighthill stress tensor, page 23
T_p	Temperature of the primary jet, page 12
T_s	Temperature of the secondary jet, page 12
U_∞	Free stream velocity, page 304

u_c	Velocity of sound in the medium, page 15
U_i	Velocity, page 22
U_j	Velocity, page 22
V_j^8	Jet velocity to the eighth power, page 24
v_c	Velocity of the jet flow, page 15
v_f	Velocity of particle travelling through LDA fringes, page 78
V_p	Primary jet velocity, page 12
V_{re}	mean fluid velocity used to calculate the Reynolds number, page 16
V_s	Secondary jet velocity, page 12
$W'(x, f)$	Source strength per unit length, page 82
w_0	Half width of the diffraction pattern, page 93
x	Input value for the probability density function, page 135
x_i	Spatial value, page 22
x_j	Spatial value, page 22
x_k	Position in the jet flow, page 37
y_i	Observed empirical probably value, page 137
y_k	Far field position, page 37
z	Input value used for in a probability density function, page 141
z_m	Depth of the acoustic mirror, page 71

Acknowledgements

I would firstly like to thank Dr Paul Dunkley for his expert academic and non academic supervision. His clear vision and direction coupled with his brilliance in practical engineering has made this research project possible.

I would also like to thank Professor Peter Carpenter, Professor Robert Kerr and Professor Peter Bryanston-Cross for introducing me to research at Warwick and for their overall supervision and encouragement.

Paul Hackett can not go unmentioned for his extraordinary skills in precision engineering and for being so reliable in finding pragmatic solutions.

I would also like to thank Amar Gill and Raphael Albrecht from RBS, London who have inspired me through their work, to look beyond conventional statistical techniques for aeroacoustics.

Finally I would like to extend a warm thank you to my friends Mark Brend, Sandy Gregorio, David Hunter, Joe Nawasra and Andrew Skeen who have unequivocally supported me in all of my endeavours.

Declaration

I declare the work contained in this thesis is entirely my own work except where explicit acknowledgement has been given or collaborations declared. This work has not been submitted in whole or part for any other degree or diploma.

This thesis is available in accordance with the regulations governing the University of Warwick theses.

Amit Kiran

CHAPTER 1

Introduction

In the research community, jet noise is a fascinating area of research combining applied mathematics, statistics and engineering to advance our understanding of the sound source mechanisms. However this is not just of academic importance; jet noise is very relevant to the aeronautics industry and on a wider scale, has social, economic and subsequently political effects.

1.1 Background and motivation

The first commercial jet airliner was the 36 seat Comet 1, which was built for the British Overseas Aircraft Corporation (the national British carrier at that time) by De Havilland, a British aviation manufacturer based in Hatfield, UK. Its test flight was on 27th July 1949, followed by an inaugural indirect passenger service flight from London to Johannesburg on the 2nd May 1952 as detailed by Boyne & Lopez. (1979).

Coincidentally, in the same year Sir James Lighthill, then the Beyer Professor of Applied Mathematics at Manchester University, gave rise to the new field of Aeroacoustics with his publication in the Proceedings of the Royal Society of London entitled "On sound generated aerodynamically. I. General theory". This was the opening paper that proposed the notion through mathematical analysis,

that sound is a by product of flow dynamics. This remarkable conclusion formed the basis for future aeroacoustics research both by academics and aviation industry specialists.

Since the time of Lighhill's proposition, the aviation industry has grown phenomenally and has become a significant commercial presence, which in part is due to the considerable advances in technology, which has made it easier and cheaper to manufacture aviation products and parts. Its growth has also been fuelled by a strong demand for flight by the worlds population. Even states who have recently emerged through political change such as Uzbekistan, have set up a national carrier, to generate a state income and satisfy the demand of their population for long haul flights.

More and more people can afford to travel and are doing so. Which is why airports such as London Heathrow Airport have had to change and develop to cope with passenger and civil aviation demands.

From its humble beginnings as a small aerodrome in 1946, to its current standing as one of the world's busiest airports, Heathrow has become a land mark in civil aviation. It is home to 90 airlines, who fly 67 million passengers a year through its terminals to over 180 world wide destinations. Note, the entire UK population as recorded by Brown & Redgwell (2006) was 60.6 million.

With the recent completion of the fifth terminal and now a sixth terminal and third runway in conception, B.A.A. Ltd (the owners of Heathrow) are certainly anticipating an increase in air and passenger traffic; that is more aeroplanes, more flights and more noise.

1.2 Noise, the community and the law

There are millions of people, in this country alone that live in areas under the flight path of aeroplanes. Jet noise affects their physiological and psychological health as described by Skeen (2006). Some of these effects include hypertension (leading to cardiovascular problems), high stress levels (leading to memory loss), annoyance, aggression, and even panic attacks.

In addition to these particular effects there is also a general impact on quality of life of the community and the environment. In densely populated regions such as the areas surrounding Heathrow in Greater London, many people are subjected to high decibel aircraft noise every few minutes throughout the day.

L_{Aeq} (dB), the equivalent continuous sound level, is an international measure of aircraft noise which averages the noise levels during the day and night and is commonly used by the UK Government. It is calculated by averaging 16 hours of noise levels from 0700 to 2300 over a 92 day period from 16th June to 15th September as described by Monkman & McMahon (2007).

These noise levels represent the far field noise levels, away from the noise sources of the aircraft (near field and far field is discussed later in Chapter 2). The UK Government considers 57 dB and above to be annoying to a far field observer on the ground and have produced noise contour maps to indicate the affected areas.

An example of the far field footprint of noise emissions at Heathrow can be seen

in Figure 1.1. The contour noise map was generated by the Environmental Research and Consultancy Department (ERCD) using the Aircraft Noise Contour Model (ANCON) a semi-empirical model, which takes into account noise propagation on the approach and at take off, runaway modal split between the east and west runways, air traffic movement, flight paths and glide scope as described by Rhodes & Beaton (2007).

The map shows contours in steps of 3 dB from 72 dB to 57 dB as is conventional with ERCD, where 57, 63 and 69 dB represent low, medium and high observer annoyance. The contours are elongated due to higher noise levels at the ends of the runway (where aircraft approach and take off) than at the sides. The area covered by the contours can be seen in Table 1.1 as well as an estimate of the population and households affected using the 2001 Census data. An average reduction in noise levels of 3 dB, which in the case of jet noise emissions could potentially be achieved by the using chevron nozzles instead of smooth cowl nozzles, would reduce the area affected of 57 dB or more from 126.6 km^2 to 71.7 km^2. This corresponds to a 52% reduction in the population affected.

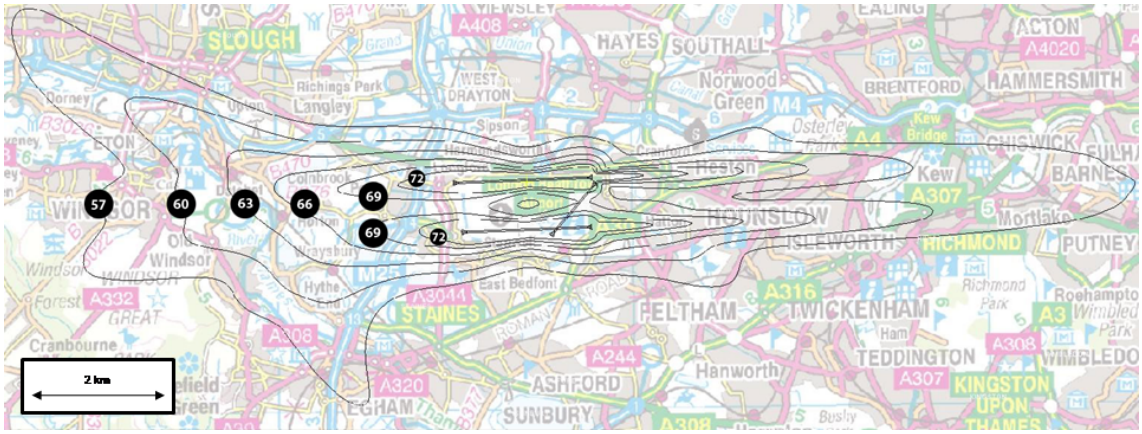

Figure 1.1: Noise contour map for Heathrow Airport, contour values in dB *(BAA plc - reproduced by permission of Ordnance Survey on behalf of HMSO)*

L_{Aeq} (dB)	Area (km^2)	Population (000's)	Households (000's)
> 57	126.6	257.8	107.6
> 60	71.7	123.3	50.1
> 63	43.8	64.2	25.6
> 66	28.8	29.7	11.6
> 69	16.3	8.6	3.3
> 72	8.4	3.0	1.2

Table 1.1: Population and household count, Rhodes & Beaton (2007)

The UK Government supports enterprize and growth and as Heathrow already contributes 1% of the UK GDP (a figure that will almost certainly grow once the developments are complete, along with employee numbers, revenue and tax contributions), approval for Heathrows development plans were granted in a white paper by the Department for Transport, DfT (2003), on the condition that certain environmental limits are met.

"The further development of Heathrow is supported, including a further new runway and additional terminal capacity to be delivered as soon as possible (within the 2015-2020 period) after the new runway at Stansted, but only if stringent environmental limits can be met".

One of the key aims stated in the white paper was to reduce the number of people significantly affected by aircraft noise, by actively taking measures such as:

- limits on the size of the area around major airports affected by significant noise levels.

- promoting research into low-noise aircraft.
- strengthening existing rules, applying international regulations and changing the law where we need to.
- making more use of noise-related landing charges, and using the money to reduce the effects of noise.
- stronger measures by airport operators to insulate properties against noise.

A subsequent white paper, DfT (2006), built on these measures by imposing a *"no more noise than in 2002"* condition, for Heathrow to continue with its expansion plans. The government set up a body to manage this called the Project for the Sustainable Development of Heathrow (PSDH).

Other existing government policies on noise include specific flight paths for aircraft when ascending or descending at Heathrow (when under 4,000 ft). These routes are called Noise Preferential Routes (NPR) and are in place to minimize flights and noise over densely populated areas.

Acceptable noise standards for aircraft are also set by the International Civil Aviation Organization and are published as a technical annex to the Convention on International Civil Aviation (Chicago, 1944). Annex 16 - Environmental Protection, volume 1, chapter 4 is the latest regulatory standard for subsonic jet noise and came into effect in 2006.

1.3 Aircraft noise

The noise from aircraft predominately occurs from airframe noise and engine noise. Noise from aircraft systems such as cabin pressurization system, air conditioning systems and auxiliary power unit are also apparent but less so than airframe and engine noise.

Airframe noise arises from the airflow around the body of the aircraft and its control surfaces such as elevator, rudder and ailerons. This includes 'bluff body noise' caused by vortex shedding from either side of the bluff body such as a landing gear and 'edge noise' caused by the airflow passing over an edge such as a slat. These noise sources are most significant during the approach (as shown in Figure 1.2) and are difficult to reduce without considerably affecting the general performance of the aircraft. Clarke (2000) suggested using noise abatement procedures such as using slower, steadier decent as this reduces the use of wing control surfaces and thereby lowers airframe noise.

At take off, engine noise is more dominant than airframe noise (also shown in Figure 1.2). The noise sources here can be subdivided into internally generated noise from the fan, turbine blades and other aeromechanical movements and externally generated noise from the mixing of exhaust gases (jet noise).

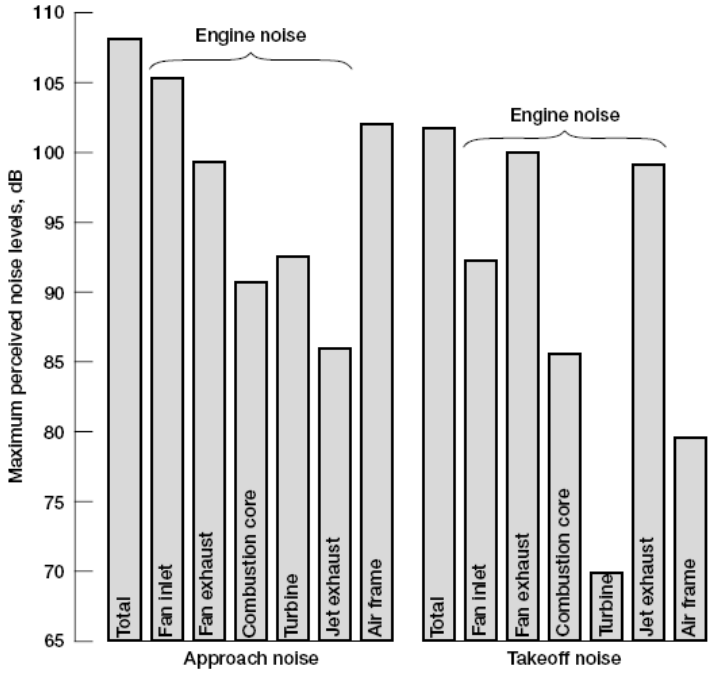

Figure 1.2: Breakdown of noise components typically produced by engines circa 1992 NASA (1999)

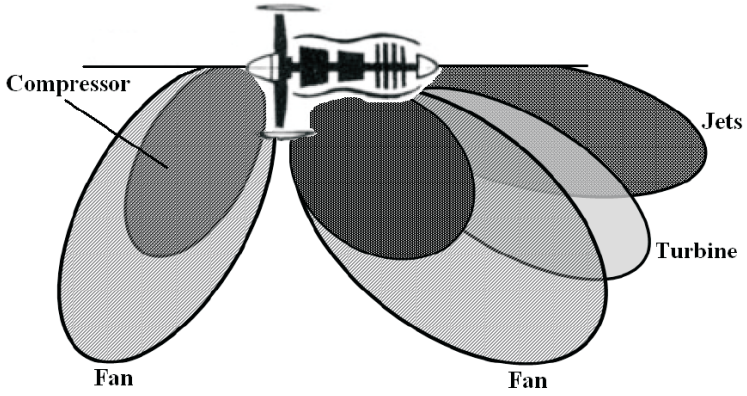

Figure 1.3: Radiated noise from a typical modern turbofan NASA (1999)

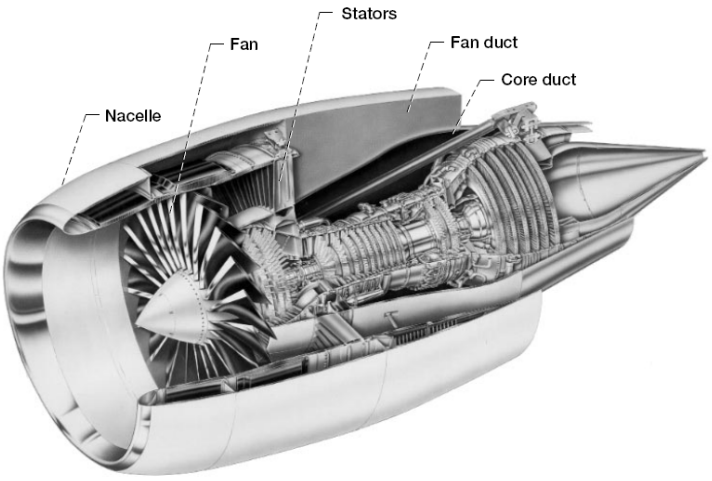

Figure 1.4: A typical modern turbofan NASA (1999)

The characteristic noise radiation from a typical turbofan engine is shown in Figure 1.3.In a typical turbofan engine as shown in Figure 1.4, air is sucked into the front of the nacelle duct by rotating fan blades and is then pushed through resulting causing noise and a swirl in the air flow. The air then enters either the fan duct or core duct.

The fan duct contains stators to straighten the flow but in doing so they interact with the wakes of air expelled from the rotating fan blades. This interaction or 'slapping' is dependent on the rate of blades passing by and generates a tone called blade passage frequency (BPF). The non-uniformities in the flow can cause high frequency tones of the BPF to occur. These tones are often heard as a piercing noise. The fan/stator interaction also generates broadband noise caused by the unsteadiness in the flow which can be heard as a low rumbling sound.

In the core duct, the air is further compressed by a series of small rotors with stators between them and in doing so generate noise. Once the air is compressed, it is mixed with fuel and is ready for combustion which is another source of noise.

The high pressure combusted air is then sent downstream to the turbine which drives the fan and compressor rotors causing additional noise. The compressed air finally exits from the core nozzle generating thrust. Upon exit the core flow meets with the bypass flow (from the fan duct). Their interaction with each other and the ambient air generates broadband jet noise. There are a number of noise sources and mechanisms in the exhaust flow which will be discussed in more detail in Chapter 2.

Internally generated noise can be reduced to some extent by using noise-deadening materials for the engine body and inlets. Reduction in externally generated noise can be achieved by changing the nozzle geometry such that turbulent mixing in the exhaust plume is reduced. The reduction of jet noise is a challenging problem in the aviation industry with results that directly impact the public. It is an environmental concern to the government as well as being of academic interest to mathematicians and engineers.

1.4 CoJeN project

One particular project that combined the interests of academics and industry was the Coaxial Jet Noise (CoJeN) project. This was a 5.7m Euro EU funded project comprising of 24 industry and academic partners across Europe, one of which was the University of Warwick. It was the 6th framework research programme in 'Aeronautics and Space' and was managed and coordinated by QinetiQ. The principle aim of CoJeN was,

'To develop and validate prediction tools which can be used by the aerospace in-

dustry to assess and optimize jet noise reduction techniques.'

This was achieved through three technical objectives,

- To identify and improve optimal CFD techniques for the prediction of jet flow development from co-axial nozzles of arbitrary geometry.
- To develop aeroacoustic codes which can predict the acoustic fields from the CFD results.
- To acquire aerodynamic and acoustic data with which to validate these codes.

Warwick contributed to the third technical objective through its large scale optical operation at the Noise Test Facility (NTF) at QinetiQ in Farnborough, the results of which were used to validate CFD techniques from the first objective.

1/10th scale coplanar and short cowl jet nozzles were used at the NTF. The short cowl nozzles were modelled on the Rolls-Royce Trent engine, with a core diameter of 135.86 mm and bypass diameter of 273.42 mm giving an area ratio of 3:1 as described by Almeida (2008). The test operating conditions can be seen in Figure 1.5, where V is the jet velocity, M is the Mach number and T is the total temperature for the primary and secondary flows denoted by subscripts of p and s respectively.

Operating Point:		1.1	1.2	1.3
Core	V_p (m/s)	340.3	404.5	480.7
	M_p	0.621	0.738	0.877
	T_p (K)	827.9	849.5	879.9
Bypass	V_s (m/s)	306.8		
	M_s	0.902		
	T_s (K)	335.0		
V_S / V_P		0.902	0.759	0.638

Figure 1.5: CoJeN operating conditions (Skeen (2006))

Skeen (2006) performed 2D PIV exhaust mapping and volumetric PIV on the flow, making it the largest PIV survey done for a 1/10th scale jet. The results lead to time resolved PIV and time space correlations of a hot jet.

1.5 Co-axial jet noise project

This thesis was funded by the EPSRC to study jet noise. The scale model inspired by the EU funded CoJeN programme was used as the basis of its experiments.

Although in principle, both the CoJeN and the scaled laboratory co-axial project are working on jet noise research, there are some differences in their aims and approaches. Warwick's involvement in CoJeN focused entirely on the flow dynamics using PIV where as the focus of the co-axial project is the acoustic distribution of the jet, with supporting results of flow dynamics using LDA. Also the co-axial project uses an unheated jet whilst CoJeN used a hot core jet. This is due to a restriction in the budget as the costs of safely running a hot jet or simulating one using a lower density flow such as a helium/air mix, are substantially more. However, there are still similarities between the CoJeN arrangement and the co-

axial project. The flow velocities in both projects generate a subsonic jet and the nozzle geometries are based on the Rolls-Royce Trent engine, with the short cowl co-axial nozzles at Warwick being 1/15th scale of the CoJeN nozzles.

Following on from this introductory chapter, jet noise source mechanisms are introduced in Chapter 2 and theoretical explanations proposed for the sources are reviewed. Computational and experimental observations are also discussed, leading to comments about the appropriateness of using scaled jet models for jet noise research.

The experimental design and equipment for the co-axial jet noise project are outlined in Chapter 3 with the suitability of the acoustic and optical techniques chosen described in Chapter 4.

Once the experiment was assembled, preliminary testing of the equipment and the jet rig was conducted and can be seen in Chapter 5. The testing extends to Chapter 6 where the acoustic asymmetry of the jet is accounted for using cross correlation techniques and the flow asymmetry is revealed using circle fitting and contour methods. Chapter 7 furthers the work on acoustic asymmetry with the derivation of a new statistical approach to support existing traditional engineering methods.

With satisfactory preliminary tests, Chapter 8 moves on to the principle investigation of the co-axial jet noise project using an acoustic mirror to produce 2D sound source maps and a LDA system to provide 2D velocity profiles of the flow dynamics. The results are also discussed in Chapter 8 before concluding the project in Chapter 9.

CHAPTER 2

Review of jet noise

Over the past fifty years the field of aeroacoustics has grown and developed, providing a more in depth understanding of noise sources, their generation and occurrences. Advancements in experimental measurement technology such as microphones and data acquisition systems and in analysis techniques such as beamforming, has broadened our understanding in this field. Gains have also been made with numerical simulations, which have also improved our understanding of the physics of aeroacoustic sound. In this chapter, an overview of experimental and numerical progress is detailed.

The chapter starts with an introduction to jet noise, quoting common formulae and highlighting the physics involved. The section on source mechanisms builds on the physics described and is succeeded by an account of our understanding of jet noise to date. The theory and analytics stem to computational and experimental work which are also reviewed. In the case of experimental work, the effects of using scaled nozzles is discussed and the chapter concludes with final remarks.

2.1 Introduction to jet noise

2.1.1 The speed of sound and dimensionless quantities

The speed of sound is a dependant variable. Under the ideal gas law (non-interacting point particles) it is defined as Equation 2.1,

$$c = \sqrt{\frac{\gamma RT}{M_m}} \tag{2.1}$$

where T is the temperature in Kelvin, γ is the adiabatic index which varies with temperature and is usually accepted as 1.4 at International Standard Atmosphere (ISA), R is the molar gas constant approximately 8.3145 $Jmol^{-1}K^{-1}$ and M_m is the molar mass in kilograms per mole which for dry air is about 0.0289645 $kgmol^{-1}$.

At typical cruising altitudes of 33,000 feet, the ambient temperature is $\sim -50\,^{\circ}\mathrm{C}$ making $c \approx 300ms^{-1}$. This is lower than the speed of sound in a normal laboratory with a standard room temperature of $20\,^{\circ}\mathrm{C}$ giving $c \approx 340ms^{-1}$.

Because of this difference in speed, flight conditions are better matched using a dimensionless quantity called the Mach number. The Mach number Ma is a ratio of speed of the jet flow or body v_c to the speed of sound of the ambient flow or medium u_c, as shown by Equation 2.2.

$$Ma = \frac{v_c}{u_c} \tag{2.2}$$

A typical fleet such as that of Air-France (2009) for example has a range of carriers that cruise from ∼0.7 Ma (Fokker 100 with Rolls-Royce Tay 620 engines) to ∼0.85 Ma (Boeing 777-300ER with General Electric GE90-115B engines). The

majority of their fleet cruise at 0.8-0.85 Ma. Under normal laboratory conditions, a jet flow speed of 240 ms^{-1} produces 0.7 Ma which within the range of in flight conditions.

Other dimensionless quantities that are significant to jet noise include the Reynolds number, Strouhal number and Helmholz number. In accordance with Timmerman *et al.* (2009), Skeen (2006) and CoJeN, non dimensional numbers were calculated using the core jet velocity and the bypass nozzle diameter.

The Reynolds number (Re) of the flow is a measure of inertial forces to viscous forces and helps characterize the different flow regimes, such as laminar (low Re) or turbulent (high Re). It is defined by Equation 2.3,

$$Re = \frac{V_{re} D_{re}}{\nu_{re}} \tag{2.3}$$

where V_{re} is the mean fluid velocity, which in the case of the laboratory co-axial core jet flow at Warwick is 240 ms^{-1}, D_{re} is the aperture diameter which is 18 mm for the bypass nozzle and ν_{re} is the kinematic viscosity of the fluid which for air at standard atmospheric pressure at room temperature is about 1.45×10^{-5} $m^2 s^{-1}$. This gives a high Reynolds number of ∼300,000.

The Strouhal number (St) describes the oscillating flow mechanisms and is defined by Equation 2.4,

$$St = \frac{f_{st} L_{st}}{V_{re}} \tag{2.4}$$

where f_{st} is the frequency of vortex shedding and L_{st} is the characteristic length. This important dimensionless number is essential when comparing sound spectra

from different scaled nozzles (including full scale). Frequency alone cannot be used to compare jet noise from different sized nozzles as the frequency spectra is dependent on the scale of the jet model. As the jet model scales down, the frequency spectra scales up.

The Helmholz number (He) helps understand the radiated noise in terms of broadband levels. It is defined by Equation 2.5,

$$He = \frac{D_{re}}{\lambda_{he}} \tag{2.5}$$

where λ_{he} is the acoustic wavelength.

2.1.2 Jet noise regions

The co-axial jet noise project used 1/150th scale core and bypass nozzles in short cowl design with smooth and chevron nozzle lips. The short cowl design is modelled on the typical exit geometry of full scale commercial carriers, an example of which can be seen in Figure 2.1.

Figure 2.1: Rolls-Royce Trent 800 engine on a Boeing 777 *(photograph is reproduced with the permission of Rolls-Royce plc, copyright Rolls-Royce plc 2006)*

In the jet flow, there are different noise producing regions as shown in Figure 2.2. The primary potential core emanates from the core nozzle of the jet and the secondary potential core comes from the bypass nozzle. Both potential cores are high velocity flows with relatively low turbulence, which contribute to the formation of shear layers. That is, since the edge of the primary potential core is travelling faster than the neighbouring flow, this causes an inner shear layer to form which encourages the roll up of small vortices as described by Schram (2003). The same process occurs with the secondary potential core and the ambient. Generally, the greater the difference between two flows (in terms of their velocity and density) the sharper the interface will be. As the end of the primary potential core slows down, it enters the transition region where turbulent mixing begins. This mixing continues downstream to the developed region where it develops into large scale turbulent mixing.

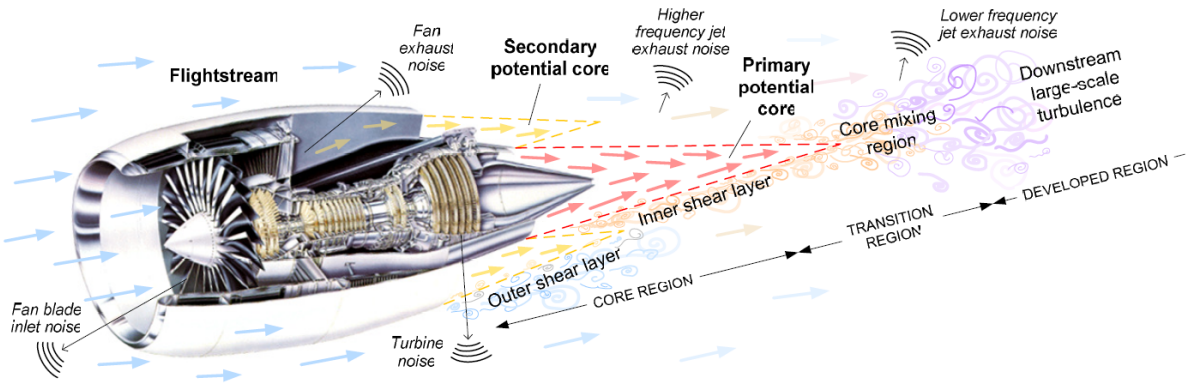

Figure 2.2: Jet noise mixing regions Skeen (2006)

The shear layer also acts as an interface for refracting sound waves. The amount of refraction depends on the frequency (or rather wavelength), jet flow velocity, and interface composition (temperature, velocity difference). The stronger the interface, the greater the refraction.

Sound is produced from all areas of the jet flow, such as potential core, transition region, fully expanded region and shear layers. The occurrence of high and low frequencies span the jet flow. However, as will be shown in this thesis, high frequencies show larger SPLdB values near the jet exhaust and shear layers, and lower frequencies are more profound downstream in the transition and fully expanded regions.

The flight stream (also shown in Figure 2.2) is a parallel air flow generated from the ambient air that passes around the plane which includes the jet engine exhaust. This interferes with the exhaust flow dynamics. Work by Grosche & Stiewitt (1983) and Michalke & Michel (1979) show that general regions in the jet (such as the turbulent mixing region) are stretched or elongated due to the flight stream.

Most laboratory jet noise experiments (as is the case with the co-axial jet noise project) are done without a flight stream. This is mainly due to the experimental difficulties in getting a separate considerably larger compressor to run a parallel air flow of a different (cold) temperature, density and pressure to that of the jet exhaust. There is also the added difficulty of safely extracting this extra mass of airflow out of the anechoic chamber. The associated costs in simulating this in-flight air stream can easily double the monetary requirements for a project.

2.1.3 Source mechanisms

As shown previously in Figure 2.2, there are a number of defined regions in a jet flow, some of which have their own turbulent characteristics, and so we would

intuitively expect there to be a number of different sound producing mechanisms in place. Theoretical, experimental and computational work have confirmed this expectation.

The mixing layer near the nozzle exit is a highly sheared region and contains important sound sources as identified experimentally by Bridges & Hussain (1995) and Tinney *et al.* (2006) for a high Reynolds number, high Mach number co-axial jet and numerically by Viswanathan *et al.* (2006a). An important factor here in the production of sound is the presence or close proximity of the nozzle to the mixing layer. As Bogey & Bailly (2004) discovered, when the nozzle is removed from simulations, the sound source is not as strong.

The potential core has been shown by Fuchs & Michel (1972), Lau *et al.* (1972), Chan (1974) and Armstrong *et al.* (1977) to have characteristic wavelike instabilities. The wavy wall mechanisms induce spatially stationary, directive sound sources as shown analytically, experimentally and numerically by Ffowcs-Williams & Kempton (1978), Laufer & Yen (1983), Mankbadi & Liu (1984), Crighton & Huerre (1990) and Colonius *et al.* (1997). In the case of excited, low Reynolds number flows, it has been strongly suggested by Stromberg *et al.* (1980), Laufer & Yen (1983) and Sandham *et al.* (2005), that the sound production mechanisms are non-linear. In unexcited flows, the sound production mechanisms were observed by Coiffet *et al.* (2006) and Jordan *et al.* (2007) to be linear.

The transition region starts just past the end of the potential core where the annular mixing layer occurs and shows wavelike instabilities/coherent structures which undergo a intense transition. This has been described as an ‘intermittent

volcano effect' by Jung *et al.* (2004) who attributed this to the collapse of the low order azimuthal coherent ring like structures. Early causality methods by Lee & Ribner (1972), Siddon & Rackl (1972), Scharton & White (1972), Seiner & Reethof (1974), Juve *et al.* (1980) and Schaffar & Hancy (1982), show the transition region to be a dominant sound production region. A linear relationship was found between the turbulent velocity fluctuations and the far field pressure. However Laufer & Yen (1983) found this to be applicable in the case of unexcited jets, as it agreed with his results on excited jets; implying different sound source mechanisms exist in this region for excited and unexcited jets.

In high Reynolds number flows, the existence of an additional source mechanism which relates to the fine scale random turbulence has also been suggested by Tam (1998). In this flow, there are no obvious length and time scales in the mixing layer in the core and the transition region downstream. This means the mean flow and the turbulence statistics of the flow must follow a similar profile. By this reasoning, the two independent turbulent mixing noise components also share a similarity in spectra. Viswanathan (2002) showed that the proposed similarity spectra by Tam (1998) fits subsonic jet noise data, which supports the existence of this additional sound source mechanism. Furthermore, Bogey & Bailly (2004) implied this mechanism is responsible for the differences in their results between high Reynolds and low Reynolds number flows. Understanding and explaining the underlying physics for this sound mechanism is an important area for future work.

2.1.4 Near field and far field measurements

Experimental jet noise measurements can fundamentally be classed as either near field or far field measurements. Near field regions lie inside the jet flow or very

close to it. Far field regions lie outside the jet flow only.

In terms of acoustic measurements, microphones placed too close to a noise source have considerable errors in their measurement. This is because near a noise source, the dominating pressure is due to hydrodynamic fluctuations (pressure fluctuations dominated by inertial effects) and not acoustic pressure (attributable by compressibility). Therefore at this region, the sound waves propagating to the far field can not be accurately measured. To overcome this, it is generally accepted as described by Mueller (2002) that the source to microphone distance should be at least one acoustic wavelength and two source dimensions. This places the microphone outside of the geometric near field and beyond hydrodynamic fluctuations.

Ribner (1964) showed the total pressure fluctuation p' comprises of the pseudo sound generated by the hydrodynamic fluctuations p'_h plus the acoustic pressure p'_a. The hydrodynamic pressure is governed by Equation 2.6 as described by Roger (2006) and has a $1/r^3$ drop off where r is the distance from the source.

$$\Delta p'_h = -\rho \frac{\partial^2 (U_i U_j)}{\partial x_i \partial x_j} \tag{2.6}$$

The acoustic pressure is governed by Equation 2.7 and has a $1/r$ drop off.

$$\Delta p'_a - \frac{1}{c^2} \frac{\partial^2 p'_a}{\partial t^2} = \frac{1}{c^2} \frac{\partial^2 p'_h}{\partial t^2} \tag{2.7}$$

Given the small size of the scaled jet in the co-axial project, even 1/4" microphones are too large to be placed in the near field and will certainly significantly obscure the natural acoustics of the jet. In addition, as the flow is seeded, this would damage typical condenser microphones which are cased and vented

for ordinary measurement conditions and therefore specialist (and more expensive equipment) would have to be purchased which lies outside of the co-axial projects microphone budget. With respect to the public community, far field measurements are of more interest as they represent (in a real case scenario) the propagated sound from a jet to an observer.

2.2 Jet noise to date

2.2.1 The beginning

The field of aeroacoustics began with the work by Lighthill (1952) on aerodynamically generated sound. There were other researchers at the time, such as Moyal (1952) who were also exploring this field, by way of the spectra of turbulence in a compressible fluid media, but Lighthill's particular attention to sound generation led him to rearrange the fluid equations of motion (conservation of mass and conservation of momentum) to form an inhomogeneous wave equation as shown in Equation 2.8,

$$\frac{\partial^2 \rho}{\partial t^2} - c_\infty^2 \nabla^2 \rho = \frac{\partial^2 T_{ij}}{\partial x_i \partial x_j} \tag{2.8}$$

where ρ is the density, c_∞ is the ambient speed of sound and T_{ij} is the Lighthill stress tensor defined by Equation 2.9,

$$T_{ij} = \rho \nu_i \nu_j + (p - \rho c_\infty^2)\delta_{ij} - \tau_{ij} \tag{2.9}$$

where ν_i is the velocity, p is the pressure, τ_{ij} is the viscous stress and δ_{ij} is the Kronecker delta.

Equation 2.8 shows how an acoustic field or rather propagating linear distur-

bance is dependent on a non-linear term. The left hand side represents the acoustic wave propagation and the right hand side represents noise generating sources. The source terms are second spatial derivatives and are referred to as quadrupoles.

Lighthill identified this to be applicable to noise produced by jets, in which a freely propagating sound field is induced by a heavily rotational region dominated by non-linearity. With this, the Acoustic Analogy Theory was established.

The noise scaling law is an important result obtained from the Acoustic Analogy Theory by solving Equation 2.8 using the Green's function of the wave equation. Lighthill found, by applying dimensional analysis, that the acoustic power radiated from a jet, scales with the eighth power of jet velocity, namely $P \sim V_j^8$.

The quadrupole sources are acoustically compact, meaning that cancellations in sound wave emissions (due to time differences) from the same eddy are ignored. They are moving sources and are convected downstream by the mean flow for which Lagrangian dynamics predict the sound field. Ffowcs-Williams (1963) investigated the effect source convection has on the directivity of jet noise and found by extending Lighthill's dimensional analysis work, that for high speed jets the power of the radiated noise P follows the third power of the jet velocity. That is $P \sim V_j^3$.

As the sound field is convected downstream it is refracted away from the jet axis. This is because the wave front is dependent on the local speed of sound and the local flow velocity. As the centre flow of the jet is faster than other regions, a wave front emanating from the mixing layer for example, will tilt and bend out-

wards. This leads to the next development in this field regarding flow-acoustic interaction, where sound is refracted away from the jet axis.

With the refraction of quadrupole sources, Lighthill determined a cone of relative silence which exits the nozzle at small angles to the jet axis. This is a relatively quiet region in which the sound pressure levels drop by more than 20 dB as shown by Atvars *et al.* (1965). However, when reviewing this analytically by collecting together all the non-linear terms (from the flow equations) on the right hand side of Lighthill's equation, the flow-acoustic interaction terms are not obviously placed. Ribner (1962) started a discussion on this topic and upon inspection, Lilley (1974) separated the flow-acoustic interaction from the production mechanisms to produce a modified wave equation. He proposed the use of linearized Euler equations as the wave operator. This improved the understanding for many researchers of sound mechanisms in free jets from compact, convected noise sources.

However, a source term representing temperature fluctuations was also believed to exist by Fisher *et al.* (1973), for which Tester & Morfey (1976) found analytical solutions and did further investigations on the scattering of turbulence pressure fields by density inhomogeneities, which they claimed were temperature dependent. Their far field solutions for sound, gave way to outlining the shape of radiated sound at the sidelines, based on a master spectrum and dipole term which scaled to the sixth power of velocity.

These findings were widely accepted until recently when Viswanathan (2004a) questioned the experimental data that was used to show a dipole master spectrum and a sixth power velocity term. Viswanathan showed that the 'hump'

in far field spectra is not due to the dipole master spectrum but is based on the Reynolds number. By keeping the Mach number constant, he compared the spectra of a cold jet with a high Reynolds number, to that of a hot jet with a lower Reynolds number, which showed that temperature alone does not alter the profile of the sideline noise radiation or side lobes. Because of these discrepancies, further work is needed for clarity on the effects of hot jets.

The heating of the jet does however, affect the sound field radiated at small angles to the jet axis. It also increases/decreases the sound power levels of the jet flow, for the respective heating of jets with low/high velocities, as also described by Tanna *et al.* (1975) and Tanna (1977), with the effects of heating being reversed at a critical point of Mach 0.7.

There have also been a number of significant acoustic theories proposed, such as Powell (1964), Howe (1975) and Mohring (1978) who expressed the source term, in terms of the vorticity of the flow, which is simpler to deal with mathematically than the double divergence of the stress tensor. This analogy is supported by Ewert & Schroeder (2003), Cabana *et al.* (2006) and Schram *et al.* (2005).

These analogies differ to Lighthill and Lilley, in that they use an implicit linearization about a given base flow. In Lighthill based analogies, the base flow is homogeneous and uniform, and with Lilley the base flow is parallel and sheared. In each case, the source is defined such that it holds the position of driving or exciting the base flow. But as the source definitions are different, there is some lack of agreement regarding the noise mechanisms. There is also a degree of redundancy in each in the dynamics of the noise mechanisms. In Lighthill's analogy, the flow-acoustic effects are largely ignored. With Lilley, these effects are

accounted for by the mean flow-acoustic effects of the base flow, however some information is still lost. This is where controversy lies, in which approach to use to describe the physics of sound production. Although in both cases, the solution to the base flow is found using the Green's function.

Goldstein (2003) believed the Lighthill and Lilley analogies are particular cases of a more general solution to the production of noise. He showed the linearization of any base flow can be done on a generalized basis. In a later paper Goldstein (2005a), proposed an acoustic analogy showing no redundancy in the sound source term, however this would not be practically possible in a periodic, homogeneous, unsteady flow system where it would contradict locality constraints as described by Jordan & Gervais (2008).

2.2.2 The emergence of coherent structures

Developments in the understanding of flow dynamics have changed since the early ideas of randomly distributed eddies which radiated into the mean-flow. The turbulence community identified more coherent structures in the shear layers of the flow, which made the aeroacoustic community believe that the coherent structures affect the sound production mechanisms. Early work by Bradshaw *et al.* (1964) showed the existence of organized eddies near the nozzle exit, but it was after the work of Crow & Champagne (1971), Lau *et al.* (1972), Fuchs & Michel (1972) and Brown & Roshko (1974), that coherent structures were recognized as being notably involved in sound production of the jet.

Based on Lighthill's analogy, Michalke & Fuchs (1975) used analytical techniques to recast the source terms into azimuthal Fourier modes, of which the lowest or-

der modes were considered to be the most highly efficient producers of sound. These modes are dependent on a strong azimuthal coherence in the sound field of the jet, which along with the work of Maestrello (1977) and Juve *et al.* (1979), gave rise to the idea that azimuthal vortex ring-like structures may exist. Bonnet & Fisher (1979) showed that both coherent and incoherent ring-like structures could produce an azimuthal coherent sound field with the more dominating factor being the Helmholtz number. The presence of azimuthal coherent structures in the flow was further supported by Armstrong *et al.* (1977) and Chan (1974) who showed the growth and decay of pressure disturbances adhere to linear hydrodynamic stability theory as outlined by Michalke (1964).

A similarity between the flow dynamics of coherent structures and the linear instabilities in laminar flows, lead to a discussion in using linear stability theory to predict jet noise, as first shown by Tam (1972) who focused on the linear instability of an infinitely thin shear layer in a parallel mean flow. This was subsequently followed by Liu (1974) who used a spreading mean flow to sustain the large scale instability when mixed with fine grained background turbulence, which induced dissipation. The flow components comprised of time averaged, phase averaged and random components which reflected the mean flow, large scale instability and fine scaled random turbulence respectively.

Ffowcs-Williams & Kempton (1978) furthered this work by studying the effects with a wavy wall instability and vortex mergers. In both of these scenarios, a rapid amplification, saturation and decay of the fluctuations was observed, indicating their importance in the sound production. The importance of coherent structures in jet noise was also supported by Moore (1977) and Dahan *et al.* (1978) who showed in experiments with jets, that half of the sound radiated to

the far field is due to coherent structures.

At the end of the 1970's, the existence of coherent structures and their influence in jet noise was established; although this contested the validity of earlier ideas of randomly distributed convected quadrupoles as described by Fuchs (1978b).

2.2.3 Acoustic radiation inside and outside of the jet

The work of Saric & Nayfeh (1975) and Crighton & Gaster (1976) who used a multiple scale expansion method to explain the slow divergence of the mean flow, was also contested. Tam & Morris (1980) showed the instability wave solution (based on a multiple scale expansion) was not applicable in the mixing layer or outside the jet. Hence, no acoustic radiation could be accounted for by this solution. Tam & Burton (1984) then used a method of matched asymptotic expansions to produce an instability wave solution that was valid both inside and outside of the jet. The inner solution comprised of the multiple scales instability wave solution which was valid inside of the jet and immediately outside of the jet. It captured the mixing layer region of the jet. The outer solution was derived from the acoustic wave equation and was valid from just outside of the jet through to the far field. The change over from instability wave solution to acoustic wave solution occurs just outside of the edge of the jet and is accounted for in the outer solution.

In a supersonic flow, sound generated at the edge of the jet, takes the form of Mach wave which is a highly directional radiated sound front. For supersonic hot jets, Mach waves are a distinct noise generator. Although Mohensi *et al.* (2002) showed that linear stability theory does not adequately account for all Mach wave mechanisms, especially with the more subtle radiations.

In subsonic cold jets, the presence of Mach waves is significantly reduced, giving way to fine scale turbulence as the more dominant noise source. Mankbadi & Liu (1984) worked on subsonic jets and used the work of Michalke & Fuchs (1975), which in turn was based on Lighthill's theory, to derive source terms from a combination of local inviscid linear theory (giving the shape function) and non-linear theory (giving axial amplitude function). This gave predictions of the radiated acoustic field from spatially stationary coherent source mechanisms. These predictions were supported by experimental results, in which the axisymmetric and helical source modes were observed to resemble longitudinal and lateral quadrupoles. The largest radiated noise was detected at small angles to the jet axis, with a Strouhal number of about 0.3 suggesting the presence of dominate shear noise mechanisms.

Although energy transfers between the mean flow, large scale instability and the fine scale turbulence were reasonably quantified by this model, there were still some differences in between the predictions and the empirical results.

Tam *et al.* (1996) investigated at supersonic jet conditions, the large scale coherent component and the small scale turbulent component co-existing and outlined two related spectra for these mechanisms, which agreed with a large number of supersonic jet experiments. This was also shown to agree with the subsonic case by Viswanathan (2002). However, for subsonic jets, the mechanisms are still unclear, causing difficulties in modelling large scale coherent/small scale turbulent source duality mechanisms.

Goldstein & Leib (2005b) interpreted the source duality mechanism as a low fre-

quency response, occurring most often at small angles to the jet axis, and a high frequency response, dominating at the larger angles to the jet axis. From an experimental perspective, more work is needed developing a way to separately identify the coherent component and the random turbulence component from a moving frame, two point space-time velocity correlation tensors. At present, the correlation tensor is largely expected to be dominated by the large scale coherent flow dynamics.

There is no real consensus as to the actual underlying mechanisms involved. Early research suggested vortex pairing and/or wavy wall like instabilities which is supported by Coiffet *et al.* (2006) who found these mechanisms upstream of the potential core. However Kopiev & Chernyshev (1997) have shown analytically the presence of another mechanism, an octupole sound production mechanism generated by eigen-oscillations of a single vortex structure.

There are also a number of experimental and numerical results suggesting the end of the potential core houses the most dominate sound producing mechanisms. Juve *et al.* (1980) investigated this region of the jet and found a high level of intermittency in the sound production at the end of the potential core due to fluid entrainment from the upstream. Hileman *et al.* (2005) also found intermittent noise producing events in this region experimentally and Bogey *et al.* (2003) and Viswanathan *et al.* (2006a) concluded the same with their numerical simulations.

In summary, there are a number of different propositions for sound production mechanisms such as a small scale random flow of eddies which are convected, compact, quadrupole sources; or coherent flow dynamics induced by vortex pairing,

vortex eigen-oscillations and wavy wall like mechanisms; or even an intermittent flow dynamic at the end of the potential core. The subsequent sections in this chapter further discuss these mechanisms and their analysis.

2.3 Computational work

High precision computing started to become more widely accessible in the 1990's. Prior to this, results from numerical simulations were heavily restricted by the computational power required and the cost of equipment. Simulations at best would be dependent on a coarse grid with few data points and would therefore be unable to resolve the small scales of the flow. And even these course simulations would take months of processor running time to produce results. Because of this, early simulations were limited to low Reynolds number flows, 2D flows, focusing on coherent vortex dynamics.

However, with the development of CPU power, clusters and their affordability, more detailed numerical simulations such as direct numerical simulation (DNS) were able to provide more accurate depiction of the flow dynamics. It allowed the small scale flow dynamics to be resolved which consequently permitted the exploration of complex sound source mechanisms which would not be possible using current experimental arrangements.

This lead to a number of advancements in aeroacoustic research. For example Mitchell *et al.* (1995) looked at compact and non compact co-rotating vortex pairs and their sound generation, and found the field to have a quadrupole profile while the far field was cylindrical. Colonius *et al.* (1997) found vortex pairing events to dominate in a 2D mixing layer. The sources were spatially stationary, non

compact with a highly directional sound field. This is consistent with experimental evidence of large scale, spatially stationary, non compact, sound production mechanisms and supports the hypothesis that the direction of sound from a jet is not dependent on convection but is dependent on the actual directive profile of the sound source itself as concluded by Laufer & Yen (1983). Freund (2001) extended the work on 2D simulations by performing 3D simulations using a 0.9 Ma jet with Re = 3.6×10^3. He found, by analyzing the Lighthill source term and its radiating profile, the peak turbulence levels and the peak Lighthill source levels are not indicative of the regions of source activity. Furthermore, he showed the radiating sound source structure followed a wavy wall profile.

This concurs with low Reynolds number experimental results by Stromberg *et al.* (1980) who suggested a possible source mechanism from wavelike instabilities and high Reynolds number experimental results by Coiffet *et al.* (2006) who found a linear wavy wall sound source mechanism.

Laufer & Yen (1983) also showed experimentally that the sound fields being produced by the linear instability waves of the 2D mixing layer. This was supported computationally by Sandham *et al.* (2005) who confirmed similar DNS results. Where as Wei & Freund (2006) used a number of optimized procedures to control the mixing layer and its flow dynamics and observed reductions of 5 dB to 11 dB. More recently, Eschricht *et al.* (2007) showed how this control only very slightly modifies the space time flow structure.

DNS with high Reynolds number jets are harder to perform and with the inclusion of nozzle geometry, become impossible with current technology. A way around this is to use Large Eddy Simulations (LES), which uses a coarser space

time grid. The large scale turbulence structures are calculated, and anything of subgrid scale is modelled or ignored. This is an important numerical method as large scale structures are important in sound production, and with LES, high Reynolds number flows (which are representative of the real physical conditions of a jet engine exhaust) can be achieved. This is of great practical interest to industry. Especially as by modelling more realistic flow conditions, there is a greater agreement with computational and experimental results. For example, Bogey & Bailly (2005) found through numerical simulations important intermittent sound production at the end of the potential core. This was observed by experiment by Juve *et al.* (1980), Guj *et al.* (2003), Hileman *et al.* (2005) and Panda *et al.* (2005).

Andersson *et al.* (2005) and Jordan & Gervais (2005a) had agreement with their respective numerical and experimental results of two point space time correlations. Viswanathan *et al.* (2006a) found sound sources in both the nozzle exit and at the end of the potential core, which was supported by the experimental findings of Tinney *et al.* (2006).

Groschel & Schroeder (2005) identified a dominant source mechanism in a high Mach number, high Reynolds number flow which was also seen by Cabana *et al.* (2006) in his computationally derived results.

There are a number of good computational and experimental agreements, and with improvements in computing technology more agreements on realistic modelling of industrial jet flow conditions are expected.

2.4 Experimental work

2.4.1 Approach to experiments and far field acoustics

Although advances in computing technology over the past ten years have allowed considerable progress to be made in solving flow equations using numerical methods, they are still restricted by the range of Reynolds numbers they can use and the precision in resolving heat conducting viscous compressible flows. With regards to jets, the upstream boundary layers are very thin and the shear layers need a very large number of mesh points to be accurately modelled, which is again restrictive for numerical simulations, especially in terms of the run times needed to acquire fully converged statistics. Experimental results are in demand for their suitability in solving flow equations, improving our understanding of sound production mechanisms and supporting and validating CFD results.

Early acoustic analogies of sound radiation comprise of randomly distributed, compact, convected quadrupole sources that are subject to the fourth order of the velocity correlation tensor. Although Reynolds decomposition of the velocity field reveals second, third and fourth order terms, the third term is considered negligible, since its integral is zero. The assumption here is that the turbulence is reasonably homogeneous and isotropic. The second and fourth order terms represent the shear and self noise mechanism terms as described by Lighthill (1954) and Ribner (1969).

The fourth order term can be expressed in terms of the second order velocity correlation tensor on the assumption that turbulence statistics follow a quasi-normal joint probability distribution. This was supported experimentally by Siener *et al.* (1999) and numerically by Freund (2003), which gave validity to the

two point velocity correlation that was used in earlier experiments by Davies *et al.* (1963) and Chu (1966) in determining source mechanisms from turbulence measurements. However due to limit in experimental resources, such measurements usually only noted the axial component of the correlation tensor. The remaining eight component terms were modelled based on the assumption of isotropic, homogeneous turbulence. The jet in reality is not this, but for the purposes of simplification and modelling, these assumptions are used.

This approach has been used in a number of experiments in measuring two point tensor, which includes the use of PIV and LDA, such as the work by Bridges (2002) and Chatellier & Fitzpatrick (2005).

Improvements are being made in providing a more realistic model, such as Jordan & Gervais (2005a) who have used the findings of Devenport *et al.* (2001) to account for the inhomogeneity of the jet structure, for which a direction dependent length scale was proposed to deal with the anisotropy of turbulence. This work continued by way of jet noise predictions based on two point LDA measurements. The profile of the temporal element of the two point velocity correlation is usually deemed to be of Gaussian form, however Khavaran & Bridges (2005) showed the exponential distribution is a more appropriate form.

Another approach to help add clarity in finding sound production mechanisms is to experimentally take synchronous recordings of flow and acoustic measurements. The flow readings include both rotational and irrotational regions and the acoustic readings in the far field record the sound source signatures. The flow dynamics can be related to the acoustic sound field by way of correlation and/or signal processing techniques. A causal relationship as described by Jordan &

Gervais (2008) can be found depending on what information and acoustic analogy is used, for the flow dynamics. However, the full spatial-temporal dynamics of the jet can not be accounted for by just one causal method. Different tools and techniques are applicable for different flow regions.

In its earlier form, the causality method was first noted in 1970's through two variants in the source description. The first description was based on Lighthill's analogy of linear and quadratic sources (shear and self noise), for which Siddon & Rackl (1972) used cross correlations of in flow pressure fluctuations with the far field measurements. The second, by Lee & Ribner (1972), correlated Reynolds stress fluctuations with the far field pressure.

The significance of the causality method lies in its ability to quantify sound energy radiated from the flow (i.e. the far field pressure autocorrelation) and relate this to the source-far field correlation, which in turn can be used to determine the source-source correlation. This last correlation refers to the integrand in the far field solution of Lighthill's wave equation. In this case, the two point source far field correlation is $\langle S(x_k, t)p(y_f, t+\tau_f)\rangle$, which measures the local sound contribution $S(x_k, t)$ at a point x_k in the jet at time t, and the far field readings at $t + \tau_f$ later at y_k. The integral of source-field correlations over the jet volume, provides the total sound radiated by the jet. Hence the causality method is a precision source localization technique that identifies the mechanisms emanating the sound to the far field.

One of the first experiments using the causality method was conducted by Lee & Ribner (1972), who performed a hot wire and hot film experiment to correlate the fluctuating velocity with far field pressure for a subsonic Mach 0.3 jet, us-

ing a far field microphone placed 40° to the jet axis. Scharton & White (1972) correlated the pressure measurements in a rotational region of a jet and the far field measurements at 30° to the jet axis. From this and the work of Seiner & Reethof (1974), high frequencies were found to radiate from upstream (nozzle exit) positions in the jet, where as downstream, lower frequencies dominated. It was also shown that sound measurements from the linear (shear noise) mechanism were 13 dB greater than the quadratic (self noise) mechanism, and that the transition region at the end of the potential core held a dominant position in sound production.

Schaffar (1979) measured the axial component of a 0.97 Mach jet, using LDA and correlated the linear source component and far field pressure. His results agreed with Seiner, in that nearly all of the measured noise at 20° and 30° to the jet axis is attributable to linear mechanisms that are present in the transition region, about 5 to 10 diameters downstream.

Hot wire experiments by Juve *et al.* (1980) with microphones placed 30° to the jet axis, also showed dominant sound sources in the transition region at the end of the potential core. These were identified as non compact and highly intermittent with 50% of sound generation occurring in 10-20% of the time. This observed intermittency was an important result, as it suggested statistical source models such as that of compact turbulent eddies in an isotropic, homogeneous flow (recall the third order term was considered negligible) is not sufficient in prescribing the complete dynamics of the source mechanism.

Schaffar & Hancy (1982) furthered work on the directivity of source mechanisms by placing far field microphones 30°, 45° and 60° to the jet axis and by taking

velocity components using a LDA system. At 4 to 11 diameters downstream, both linear and quadratic components were found. 70% of the sound emissions from the linear components occurred at angles less than 45 °; for quadratic components, this was 15%. At angles greater than 60 °, the emissions by the linear term were negligible, and the quadratic terms only contributed a few percent.

Similar experiments have been conducted by Panda *et al.* (2005) where simultaneous measurements of both unsteady density ρ and velocity u, v were taken using a technique based on molecular Rayleigh scattering. Flow measurements of both subsonic and supersonic jets on the jet axis and the far field acoustics at 30 ° and 90 ° to the jet axis, were taken at the same time. The correlation levels of the subsonic jet were found to be lower than the supersonic jet, particularly with regards to v, which implied the axisymmetric instability waves were significant sound producers in supersonic jets. The highest correlation in the subsonic case, was found slightly downstream from the end of the potential core. Measurements in the mixing layer region were also taken, but the correlations were considered negligible as the sound from random turbulence in the flow overshadowed the mixing layer. We do know however, from theory and other experiments, that the mixing layer does contain sound production mechanisms.

Experimentalists such as Moore (1977), Arbey & Ffowcs-Williams (1984) and Fleury *et al.* (2005) looked at the coherent motion in flows by applying an acoustic excitation that holds jets with low Mach numbers in a regular flow pattern. From this coherent vortex structures, with almost periodic roll up and pairing phases were produced by forcing the most unstable frequency in the flow.

Flow measurements in both excited and unexcited jets were also taken with si-

multaneous acoustic measurements by Laufer & Yen (1983), who related the flow and sound measurements by observation without applying any particular underlying acoustic analogy. They found that within one diameter downstream from the nozzle, the near field pressure holds a linear relationship with the turbulent velocity and a quadratic relationship with the far field pressure. A more controversial finding was the acoustic sources were not being convected despite being generated by 'moving disturbances' in the jet. This implied that the non linear saturation of unstable wave amplitudes could account for the sound source. This along with the observations contradicts original sound source models, that is if the source is not convected, there will be no amplification and no Doppler shift.

The contradiction in the linear relationship of near field flow dynamics and far field acoustics, and the causality approach which suggests the linear source term is the largest sound producing mechanism, gives rise to the idea that non-linear instability waves or vortex pairing, may not lead to the dominant sound production mechanism in flows with a high Reynolds number. The unsupported explanation by Jordan & Gervais (2008) is that the coherent dynamics in the flow may not be coherent enough to generate distinctive quadratic interactions.

The results from synchronous flow-acoustic measurements have provided valuable insights in noise production mechanisms, with dominant sound producing regions being in the transition region, which contains both linear and quadratic mechanisms. Non compact, spatially stationary, intermittent sound mechanisms have also been observed and identified. Guj *et al.* (2003) looked at the unsteady intermittent structures in the transition region of the jet and the radiated far field sound, by using synchronous flow-acoustic measurements. Intermittent sources were located between seven and nine diameters downstream, and were in the

form of a cusp, which was also observed by Juve *et al.* (1980) and Hileman *et al.* (2005). Hileman used a PIV system to record high speed flow visualizations, and used the far field acoustic measurements to separate the flow images into noisy and quiet categories. Proper Orthogonal Decomposition (POD) was used as a signal processing tool on both categories, to affiliate characteristic features in the flow with high noise production.

Synchronous flow-acoustic measurements have broadened our understanding of sound production regions and noise source mechanisms. Although these experiments look at the acoustics in the far field, work has also been done on near field pressure measurements.

2.4.2 Near field experiments

Near field microphones placed in the irrotational region just outside the jet can provide significant information. However there are some difficulties in the interpretation of the measurements. The small turbulence scales in this region are too weak to drive the pressure field and hence, sound emitted by large coherent structures filter out the weaker signals, as found by Tinney *et al.* (2006). This leads to an uncertainty in how much of the signals from the actual region have been measured. A further complication is that both hydrodynamic and acoustic measurements are recorded by the microphone, which have different governing equations.

One of the first researchers to explore near field properties was Franz (1959) and Ollerhead (1967) who looked at the near field solution to Lighthill's wave equation and found a very energetic reactive pressure field near the acoustic source,

which due to its non-progressive nature, doesn't radiate sound to the far field. The jet exit is abundant with such irrotational pressure fluctuations which have a rapid spatial decay. Howes (1960) used an alternative approach in accounting for these pressure fluctuations by treating them as incompressible. He outlined the characteristics of the near field pressure by using the Poisson equation and also derived the rms. Howes also used two point measurements, as did other researchers such as Mayes *et al.* (1959), Keast & Maidanik (1966), to obtain two point pressure correlations. However Howes was one of the first to find amplification, saturation and decay of near field pressure fluctuations.

Mollo-Christensen (1963) derived space time correlations based on his results from his two point pressure correlations and found the presence of a harmonic travelling wave and an exponential axial decay. He also observed an important near field characteristic; the near pressure field acted like a filter which extracted coherent flow dynamics from a background of random turbulence. This observed filter is not completely understood at present, which causes difficulties in explaining sound source mechanisms. A more detailed account of the difficulties in interpreting near field pressure measurements has been written by Keast & Maidanik (1966).

Arndt *et al.* (1997) improved our understanding of near field pressure fluctuations by predicting its spectral character, which was derived analytically using the unsteady Bernoulli equation and the quadrupole solutions to the wave equation. These predictions were for subsonic jet conditions and showed good agreement with experimental results of the hydrodynamic and acoustic regions. Arndt concluded that a Helmholtz number of $k_H r_H = 2$, where k_H is the wave number and r_H is the nozzle radius, marks the transition pathway from a dominance in

hydrodynamics to acoustic. In subsequent experiments, Harper-Bourne (2004) and Coiffet *et al.* (2006) found respective values of $k_H r_H = 1$ and $k_H r_H = 1.3$.

Coiffet also found an approximate relationship between the hydrodynamic and acoustic components using an axially aligned linear near field microphone array. He showed the flow dynamics responsible for the hydrodynamic component, generate sound by a linear process and that the near field is comprised of convective hydrodynamics and propagative acoustic mechanisms.

A number of microphones in large azimuthal arrays have been used to investigate near field structures by researchers such as Harper-Bourne (2004) and (Tinney *et al.*, 2006a; 2007). Guerin & Michel (2006) and Jordan *et al.* (2005b) found the first three Fourier azimuthal modes dominating the near field pressure. By placing microphones in the axial direction, further results revealed axial coherence is also present for axisymmetric and helical modes.

Suzuki & Colonius (2006) also focused on the azimuthal plane but with multiple azimuthal arrays and used the beamforming technique to acquire information on the instability wave amplitudes; while Tinney *et al.* (2006) used a filtering operation to differentiate the hydrodynamic and acoustic components. These types of measurements and analysis are aiding the understanding of coherent flow dynamics, however they do present a number of difficulties such as quantifying the information lost in the radial distance between the microphone and the sound source region. Although Suzuki & Colonius (2006) touched on resolving this issue, further reduction of this uncertainty can be achieved by comparing synchronous measurements of the near pressure field and the turbulence.

It is difficult to obtain sufficient information about the mechanisms which drive the non linear rotational flow dynamics and induce the near irrotational pressure field. This is because there is a short distance between the rotational centre of the flow and the irrotational near and mid fields and in this short distance the characteristics of the flow change from predominately elliptic to hyperbolic behaviour. However, a connection between the physics in the near field and the underlying turbulence can be found by pairing near field pressure measurements with velocity measurements in the shear layer. Laufer & Yen (1983) showed that the near field pressure amplitudes and velocity fluctuations have a linear relationship for the first diameter downstream of the jet. Picard & Delville (2000); Picard (2001) further showed pressure-velocity correlations through his work on an unexcited jet at 0.15 Ma and $\mathrm{Re} = 1.5 \times 10^5$. This was done using a 16 microphone array and 12 X-wire probes. Ricaud (2003) showed similar results for a jet at 0.3 Ma and $\mathrm{Re} = 3 \times 10^5$ using an 18 microphone array which was synchronous with LDA measurements. Tinney *et al.* (2006) also tallied these measurements for a jet at 0.6 Ma and $\mathrm{Re} = 6 \times 10^5$ using an azimuthal pressure transducer array with LDA measurements and found correlations between the near field pressure and the linear and quadratic mixing layer velocity terms.

2.4.3 Empirical data reduction

Advancements in measurement technology has allowed researchers to use a larger number of microphones in their arrays and more detailed spatial-temporal turbulence measurements using LDA and PIV. With developments in computational power and data storage, large acoustical and optical data sets can be saved directly to a hard drive, however the task of post processing the optical data sets is still onerous. With these huge data sets, it is often the case that specific data

extraction is needed to reduce the data set in order for post processing to be carried out. The techniques used to compress the data set must be such that they optimize data storage while still retaining significant information about the underlying physics of the flow. Two such techniques that perform this task and help interpret the thousands of cross correlations, are Proper Orthogonal Decomposition (POD) also known as Principle Component Analysis (PCA) and Linear Stochastic Estimation (LSE).

The PCA technique calculates the sum of eigenmodes from two point statistics of a flow such as pressure or velocity. The eigenmodes represent the fluctuations in energy and in most cases, the majority of these fluctuations are represented by small number of eigenmodes. The dynamics of the flow can be prescribed by these small number of eigenmodes with the remainder of the eigenmodes holding information that is not as significant. Hence the flow can be represented by this low order, allowing a reduction in the data set and time taken for post processing.

The eigenmodes have both spatial and temporal components. The spatial component provides information on a given feature of the flow and the temporal component reflects the amplitude of the spatial component fluctuations relative to each other.

The LSE technique looks at two fields such as pressure and velocity and relates them through multi point correlations. This gives important information regarding the underlying physics of the flow, for example the reconstruction of the underlying velocity dynamics were done from the near field pressure measurements by Picard & Delville (2000), Ricaud (2003) and Coiffet *et al.* (2006).

Extended techniques combining both LSE and PCA have been used by Bonnet *et al.* (1994) by correlating the PCA coefficients from multi point measurements in one field of interest, with single point field measurements in another field of interest.

Although these techniques reduce post processing time and provide good insight to the underlying physics, there are a few occasions where problems with the techniques have to be addressed. For example Tinney *et al.* (2006; 2007) took near field pressure measurements of a jet at 0.6 Ma and Re $= 6 \times 10^5$ and correlated them with LDA measurements from the mixing layer. LSE was then used to reconstruct the velocity field using the near field pressure data, from which the source term can be computed using Lighthill's analogy. However, Samanta *et al.* (2006) showed that having an incomplete representation of the source term, makes it more susceptible to errors. Schram (2003) proposed an improved definition of the source term based on the vortex sound theory. They used the momentum and kinetic energy conservation laws to formulate a conservative form of vortex sound theory which is less subject to experimental error. This proposal was validated by using PIV measurements of a jet to create a sound source term which would then predict far field radiation. The predictions agreed well with the actual far field measurements.

This technique along with LSE and PCA are important in low dimensional analysis. Although there is a redundancy in most of the source term definitions, Goldstein (2003; 2005a) as mentioned earlier in this chapter, presents a way to significantly reduce or possibly even remove the redundancy. For experimental source analysis, both these techniques should be considered.

2.5 Scaling effects

Full scale jet noise tests are extremely expensive to conduct. The cost of materials, construction, increased man power, large suitable test facilities and high running costs prohibit many jet noise research groups from large scale testing. Experimental investigations on jet noise are almost always conducted using scaled models of the nozzle. The validity of using scaled models has been confirmed by researchers, including Viswanathan (2008) who compared test results from different sized nozzles, for both single and dual jet streams, for a frequency range of 200 - 80,000 Hz with full scale results. In conclusion the scaled model results were applicable to full size jet engines. However, there are a number of considerations that need to be accounted for.

In full scale flight tests and engine static tests, the frequencies of interest are less than 10 kHz. However when using scaled models, sound interests lie at higher frequencies as there is a linear relationship between the scaling down of the model scaling up of the jet noise frequencies. This means that spectral measurements at high frequencies are needed in comparing data with full scale results.

The effect of atmospheric absorbtion is also a point for consideration when comparing scaled model data with full scale data. Shields & Bass (1977) showed under normal atmospheric conditions of 25 °C and 70% relative humidity, that as the frequency under review increases, so too does the coefficient of atmospheric absorbtion. Full scale data sets are often hard to acquire and may not be directly comparable with laboratory results as their set up may be different. Therefore, most scaled model laboratory jet noise experiments, for simplicity, cost and consistency with other comparable laboratory results, use standard day conditions.

Also, full scale tests outdoors are subject to some variation in weather conditions, the wind, temperature, air density, relative humidity and the ambient noise levels. Where as in an anechoic chamber, these conditions are fairly controlled allowing repeatable tests and results to be performed.

The scaling of jet noise spectra from a scaled model is another point to consider when comparing with full scale data. In full scale tests, far field microphones are placed further away from the noise source (usually at 150 ft or 45.7 m as described by Viswanathan (2008)), than those in a limited laboratory space such as an anechoic chamber. As a 6 dB reduction occurs when the distance between the noise source and microphone is doubled, the acoustic intensity recorded by the laboratory microphones, with all things being equal, will be greater than the full scale far field microphones. This is overcome by non-dimensionalising the microphone distance to the noise source using $\frac{r_{mic}}{D_{jet}}$ and by making comparisons using normalized spectra. From the experiments and discussion presented by Viswanathan (2006b) a microphone distance of at least 35 D_{jet} provides an acceptable acoustic and geometric far field.

If the flow velocity and viscosity remaining unaltered when using scaled models, then there is a notable reduction in the Reynolds number, as the nozzle diameter is reduced. Until recently, the Reynolds number was assumed to have little if any effect on the noise spectra. However work by Viswanathan (2004a) showed that by keeping the Mach number and temperature constant and by varying the Reynolds number (by changing the nozzle diameter) there is an affect on the noise spectra. Larger nozzles produced higher SPLdB values and had a different location of the characteristic hump in the noise spectra.

The boundary layer at the nozzle exit, with a thickness defined by Viswanathan (2008) to be the distance at which the local velocity reaches 99% of the core, also varies according to the nozzle geometry. In particular, the boundary layer in full scale operations is almost always turbulent, however in scale models, it could be laminar. Although studies of the turbulent or laminar boundary layers and their thickness has been done, the effects they have on noise is not well understood. However work by Viswanathan & Clark (2004b) shows the thickness of the boundary layer at the nozzle exit does not influence the radiated noise from the flow.

Another area which was thought to be influential on the jet noise spectra is the area between the shear layer and the ambient, known as the shear perimeter. Scaled models have shorter perimeters than their corresponding full scale jets. Viswanathan (2008) investigated the proposition that increasing the shear perimeter would increase mixing and reduce radiated noise. The shear perimeter was increased by a factor of two and no effect on the jet noise spectra was observed. With his additional work, Viswanathan (2006c) concluded the difference in perimeter length between the scaled model and full scale jet, have no impact on the jet noise spectra.

2.6 Final remarks

The understanding of aeroacoustics since its first conception by Lighthill (1952) has significantly developed, in terms of the sound source mechanisms, the underlying physics, the flow dynamics and the characteristic properties of sound

sources in different flow regions. However, with these theoretical, analytical, experimental and numerical developments, there is still some controversy and lack of consensus as to the definition of a source mechanism in an unbounded shear flow. This is particularly hard for experimentalists to account for as the acoustic fluctuation levels in the small sound source production region of the shear layer are overshadowed by hydrodynamic fluctuations, making it very difficult to take acoustic measurements. Numerical methods are subject to the same difficulty but to a lesser extent.

The coupling of flow dynamics with far field acoustic measurements provides information on the sound source distribution. The early causality methods used by Lee & Ribner (1972), Siddon & Rackl (1972), Scharton & White (1972), Seiner & Reethof (1974) and Juve *et al.* (1980) were initially used to obtain this information. With advances in measurement technology and signal processing techniques, improvements in the coupling of flow and acoustic measurements have been done by Guj *et al.* (2003) and Hileman *et al.* (2005). Numerical simulations have also developed our understanding of the sound source distribution.

Overall there have been a number of theoretical developments such as the work by Goldstein (2003), Goldstein (2005a) and Mankbadi & Liu (1981); a number of experimental discoveries such as Hileman *et al.* (2005), Jordan *et al.* (2005b), Reba *et al.* (2006), Tinney *et al.* (2006) and Chatellier & Fitzpatrick (2005); and a number of numerical advancements such as Freund (2001), Bogey *et al.* (2003), Wei & Freund (2006) and Cabana *et al.* (2006). The way forward in seeking and identifying spacial temporal signatures of sound source mechanisms, would be to have a closer working relationship between theoretical, experimental and numerical approaches.

CHAPTER 3

Experimental design and equipment

There are a number of different airframe components such as landing gear, high lift slats and flaps that contribute to the noise produced by an aircraft. During take off, the most significant noise sources are fan noise and jet engine exhaust noise.

This chapter describes the experimental equipment used for the co-flow research project on exhaust noise. Some of these have been designed, manufactured and engineered at the University of Warwick while other products have been purchased from industry specialists.

3.1 Compressor

A large compressor, Compair Reavell 5000, was used to generate the compressed airflow needed for the jet rig. This was a two stage compressor which held the compressed air in a cylindrical canister (1.5 m diameter by 4.5 m height) as shown in Figure 3.1. The design pressure was 36 bar and design temperature was 50^{o}C.

(a) Compressor

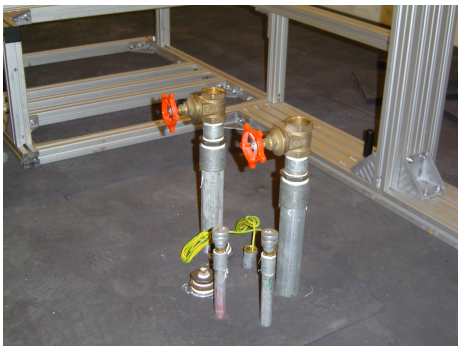

(b) Inlet pipes

Figure 3.1: Compressor and inlet pipes

Compressed airflow was released through a series of control valves into the anechoic chamber via four inlet pipes as shown in Figure 3.1. The two large inlet pipes supplied air to the core and bypass chambers in the jet rig. The two small pipes passed the airflow into the seeder, which mixed with oil particles before passing into the core and bypass chambers in the jet rig.

3.2 Anechoic chamber

The anechoic chamber was designed and constructed by the Jet Noise Group at Warwick. Its length, width, height dimensions of 4.9 m, 3.9 m, 3.3 m was large enough to house the jet rig and allow the jet flow to fully expand when running on condition.

The floor, walls and ceiling of the chamber were padded with acoustic foam, as shown in Figure 3.2, to act as a sound absorbing agent and significantly reduce the reflection of sound waves; without which microphone readings of sound sources would be contaminated and not be accurate. The foam was 22 mm thick

and was suitably chosen to be effective in its role for absorbing frequencies in the range 5 kHz to 80 kHz.

An extractor fan was mounted on one of the walls inside the chamber which was used to purge the room of seeded particles ejected from the nozzles on the jet rig. The exterior of the fan was padded with acoustic foam and was relatively distant from the jet rig and microphone placements. It produced low frequency noise (under 5 kHz) which was slightly above the ambient sound pressure levels of ∼30 dB and therefore posed no interference to aeroacoustic measurements which exceeded 100 dB.

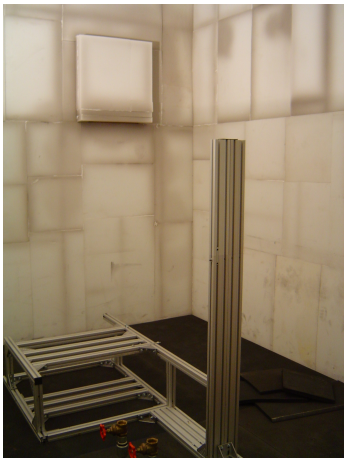

Figure 3.2: Warwick anechoic chamber

3.3 Seeder

As the compressed airflow is released into the anechoic chamber, two out of four of the chamber's inlet pipes pass the airflow to a seeding chamber. This is the MS10 MicroSeed System by Oxford Lasers Ltd as shown in Figure 3.3. It is a 4.95 litre vessel with a maximum working pressure of 10 bar, maximum working temperature of 60 °C and minimum working temperature of 5 °C.

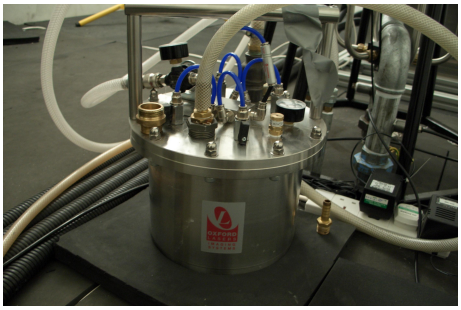

Figure 3.3: Seeder

In this chamber, the flow is seeded with suitable particulates before being passed into the main body of the jet rig.

An appropriate choice of seeding particles was made in consideration of Westerweel (1997) who stated,

- Particulates that do not interact with each other
- Particulates that do not alter the flow or properties of the fluid
- Particulates that follow the motion of the fluid exactly

Seeding materials commonly used by experimentalists was listed by Kasagi & Nishino (1991), Meinhart *et al.* (1999), Melling (1997) and Weitbrecht *et al.* (2002) and be seen in consolidated form in Figure 3.4 as provided by Skeen (2006).

	Material	ρ (kg/m^3)	Typical d_p (μm)[1]	Refractive index[2]	Melting / Boiling point	Used in…	
						Gas	Lqd
Minerals / Oxides	Zirconium oxide (ZrO_2)	5890	≥ 0.7	1.95	T_m = 2715°C	✓	✓
	Aluminium oxide (Al_2O_3)	3970	0.18-100	1.76	T_m = 2054°C	✓	✓
	Titanium dioxide (TiO_2)	3500	≥ 0.1	2.65	T_m = 1775°C	✓✓	✓
	Chalk ($CaCO_3$) dust	2830	10-50	1.59	T_m = 825°C	✓	
	Silica (SiO_2)	2650	5	1.46	T_m = 1830°C	✓	✓
	Zinc chloride ($ZnCl_2$) smoke pellet	2500	0.5		T_m = 275°C	✓	
Polymers / Plastics	Polyamide / Nylon	1060	20-200	1.53	T_m ≈ 180-265°C		✓✓
	Polystyrene	1050	0.2-1000	$1.59+3\times10^{-4}i$	T_m ≈ 190-260°C	✓	✓✓
	Eliokem Pliolite resin	1020	40-60				✓
	Thermoplastics	1020	6-200	1.54	T_m ≈ 150-400°C		✓
	Polyethylene	960	5	1.52	T_m ≈ 100-130°C		✓
Liquids	Glycerol fog	1260	0.1-3	1.47	T_b = 290°C	✓✓	
	Water droplets	1000	50	$1.34+2\times10^{-9}i$	T_b = 100°C	✓	
	Atomised water fog	1000	20	$1.34+2\times10^{-9}i$	T_b = 100°C	✓	
	Vegetable oil droplets	970	0.6-5	1.47	T_b = 299°C	✓✓	
	Oil smoke (produced at 190-240°C)	970	0.02-1.6	1.47	T_b = 299°C	✓	
	Styrene	900	0.5	1.56	T_b = 145°C	✓	
	Acetone	800	1	1.36	T_b = 56°C	✓	
	Blood cells		5				✓
Other	Glass spheres	2600	0.5	1.51	T_m ≈ 1500°C	✓	
	Burnt toast smoke	2000	0.4	$1.46+0.015i$		✓	
	Incense / Tobacco smoke	1200	0.01-0.3	1.43-1.59		✓	
	Fluorescent particles	900-1100	60-100				✓
	Pollen	1000	10-100	1.42, $k > 0$			✓
	Hollow glass balloons	100-1100	10-100		T_m ≈ 1500°C	✓	✓✓
	Hollow nylon balloon		30		T_m ≈ 180-265°C	✓	
	Hollow silica balloons	200-800	40-50	1.70	T_m = 1830°C	✓	
	Hydrogen bubbles (H_2)	0.09	40-500	1.00	-		✓

[1] Values given are ranges found in the literature, and not necessarily indicate of available sizes.

[2] At 532nm, or as close as possible, where a choice given in the literature. Unless shown, values for complex part k were not found, and can be considered negligible.

Figure 3.4: List of seeding particulates

The seeding particles should have a low mass density such that their interaction in the flow is unlikely and their potential for altering the turbulence in the flow is minimal. For example in the jet experiments by Levy & Lockwood (1981), 1 mm diameter sand particles were found to increase the jets turbulence as the particles had a relatively large inertia and passed through unaffected by some of the turbulent regions in the flow. In contrast, excessive amounts of 215 μm diameter sand was found to reduce the turbulence as they became entrained in the eddies absorbing some of the turbulence energy in the flow.

For turbulent flows, Melling (1997) proposed Equation 3.1 for calculating the relative amplitude η_p of a particle associated with an oscillation frequency f_p,

$$\eta = \left(1 + \frac{(2\pi f_p \rho_p d_p^2)^2}{324\mu_p^2}\right)^{-0.5} \tag{3.1}$$

where μ_p is the viscosity of the flow which for air is $1.8 \times 10^{-5}\ kgm^{-1}s^{-1}$, d_p is the diameter of the particulates and ρ_p is the density of particulates which in the case of vegetable oil is 970 kgm^{-3}. By rearranging Equation 3.2, the required maximum particle size (such that it passively follows the fluids oscillation) can be calculated from Equation 3.2.

$$d_p = \frac{(324\mu_p^2(\eta^{-2} - 1))^{0.25}}{(2\pi f_p \rho_p)^{0.5}} \tag{3.2}$$

In the case of vegetable oil being used as seeding in air, such that they follow the oscillations in the flow at a rate of 10 kHz with 99% amplitude accuracy, the calculated maximum diameter for the particulates is $d_p = 0.9\ \mu m$.

This of course is a theoretical value. In practice it may not be physically possible to produce particulate sizes smaller than the calculated maximum diameter. The

main considerations from a practical view point is that the particulates do not influence flow structures and that they present sufficient brightness to laser systems by having a refractive index with a high real component and low imaginary component.

By considering these points, taking material costs into account and in consideration of the particle diameters produced by the Oxford Lasers seeding chamber, corn vegetable oil of $0.8\ \mu m$ diameter, density is $970\ kgm^{-3}$ and refractive index of 1.47, was considered suitable for seeding the jet flow.

3.4 Jet rig

The experimental jet rig was designed by the Jet Noise Group. It comprises of an inner and outer stainless steel chamber of which the outer chamber was coated with anti-corrosive paint. A rod with a bullet tip ran through the length of the core chamber.

Figure 3.5: Pictures of the jet noise rig at Warwick

As seen in Figure 3.1, the compressed airflow needed for the jet rig, enters the

anechoic chamber via two large and two small inlet pipes. The two small inlet pipes pass the airflow through a seeding chamber before joining back with the large inlet pipes.

Each large pipe then passes the merged airflow to its respective junction box which further encourages mixing and homogeneity of the flow. One junction box passes the airflow through five small pipes to the core chamber of the jet rig, while the other junction box uses its five small outlet pipes to pass the airflow to the bypass chamber of the jet rig.

The use of the multiple outlet pipes provides a more even distribution of the airflow as it enters the base of the jet rig as shown in Figure 3.6.

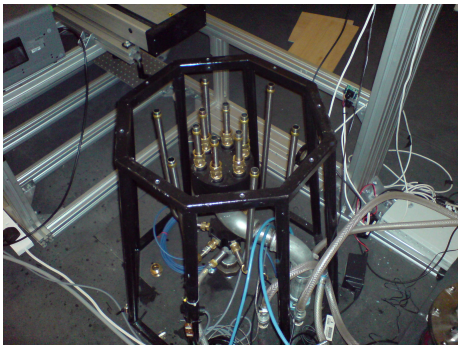

Figure 3.6: Inlet pipes for the rig

The airflow then passes through the plenum chamber in the lower body of the jet rig, up through the restriction section and onwards towards a further calming chamber which contains an aluminium honeycomb mesh which is used to calm the flow as can be seen in Figure 3.7.

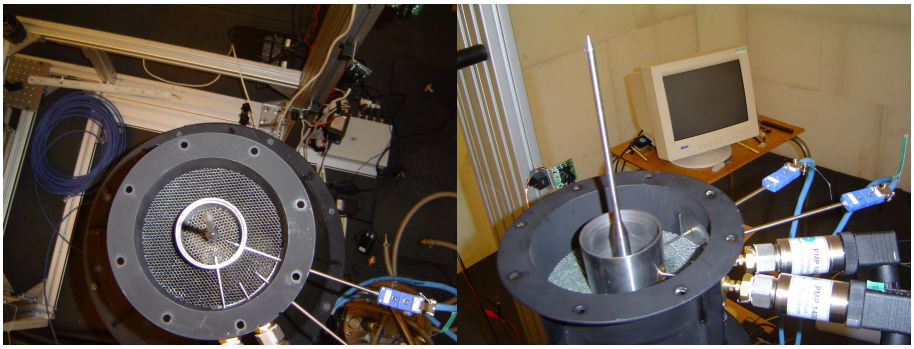

Figure 3.7: Honeycomb mesh and probes

Temperature probes and pressure transducers, also shown in Figure 3.7, were placed in both the core and bypass chambers to monitor the flow. The temperature probes were Omega type T thermocouples with a range of $-200\,^{\circ}\mathrm{C}$ to $350\,^{\circ}\mathrm{C}$, which were attached to a 24 bit National Instrument 9211 DAQ system. The pressure probes were Druck PMP1400 which attached to a National Instrument 6024E system which could measure up to 4 gauge bar above ambient room pressure. The gauge bar increase of the jet flow on condition was $\sim$0.5 bar. Mass flow was not measured.

3.5 Nozzle geometry and jet flow conditions

The budgetary limitations and the space available in the School of Engineering were important factors in determining the scale of the nozzle. Based on the available size of the anechoic chamber and the compressor, the Jet Noise Group approved the in house manufacturing of core and bypass short cowl nozzles (hereinafter referred to as cowl nozzles) of size $D_{cr} = 9$ mm and $D_{bp} = 18$ mm. The dimensions are approximately 1/15th scale of the CoJeN cowl nozzles shown in Figure 3.8, which themselves were 1/10th scale of Rolls Royce Trent nozzles.

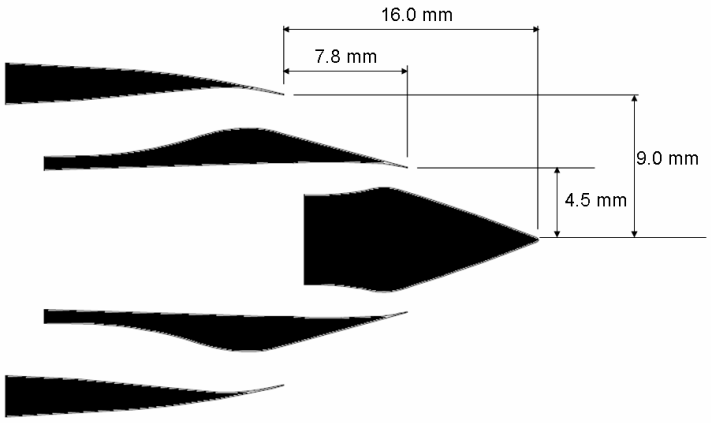

Figure 3.8: Schematics of the cowl nozzles

Chevron core and bypass nozzles were also manufactured by making copies of the cowl nozzles and then cutting out the desired number of chevrons.
Bridges & Brown (2004b) tested nine chevron nozzles of varying chevron count, penetration, length, and chevron symmetry and concluded,

- *chevron count is a strong player with good low frequency reductions being achieved with high chevron count without strong high frequency penalty.*
- *chevron penetration increases noise at high frequency and lowers it at low frequency, especially for low chevron counts.*
- *chevron length is not a major impact on either flow or sound.*
- *chevron asymmetry slightly reduces the impact of the chevron.*

With this in mind, the chevron nozzle geometry was discussed with the project technician Paul Hackett who advised on what is practically possible to machine. Twelve chevrons for the core nozzle and twenty four chevrons for the bypass were

manufactured. The angle of penetration remained at 0 degrees.

The cowl and chevron nozzles were made from brass as it was a readily available material with high robustness properties and had an acceptable cost of manufacturing. Other suitable contenders were stainless steel or an aluminium alloy which has a greater tensile strength, however for the purposes of a laboratory jet nozzle, the tensile strength of brass was perfectly acceptable. The other materials were more expensive and offered little advantage over brass. The machined cowl and chevron nozzles can be seen in Figure 3.9 with the following abbreviations for the nozzles: CrCo = Core Cowl, CrCh = Core Chevron, BpCo = Bypass Cowl, BpCh = Bypass Chevron.

Figure 3.9: (left to right) BpCo, CrCh, CrCo, BpCh

Once machined, the actual chevron length and asymmetry were examined. Photographs were taken of the core chevron nozzle against a ruler. The nozzle was rotated so that each tab was photographed. The images were then loaded into Matlab 2007a to determine the geometry of each chevron tab. The average geometry with a standard error of the mean and 95% confidence intervals were cal-

culated using Stata SE v.10. This process was repeated for the bypass chevron. The results can be seen in Table 3.1 with a typical chevron schematic shown in Figure 3.10.

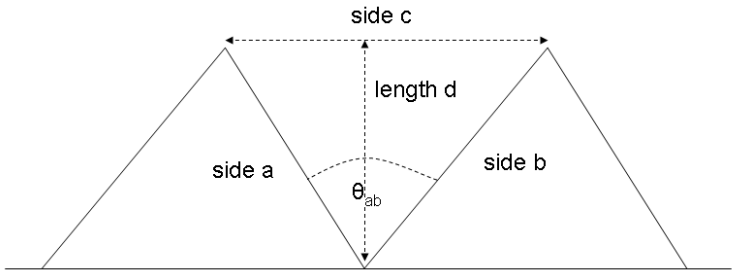

Figure 3.10: Schematic of two chevrons

Chevron geometry	Mean (mm)	Standard Error of the Mean (mm)	CI lower bound (mm)	CI upper bound (mm)
CrCh side a	1.61	0.04	1.52	1.71
CrCh side b	1.69	0.04	1.59	1.80
CrCh side c	2.55	0.03	2.47	2.62
BpCh side a	1.60	0.02	1.56	1.64
BpCh side b	1.69	0.02	1.65	1.74
BpCh side c	2.51	0.03	2.44	2.57
lip thickness	0.07	0.01	0.06	0.09

Table 3.1: Chevron geometry

The results show a slight asymmetry in the average chevron tab (i.e. *side b* is slightly longer than *side a* for both the core and bypass chevrons) which was caused during machining. Using trigonometry and Heron's formula for calculating the area of a triangle, this gives core and bypass values of 1.05 mm and 1.07

mm for 'length d' and 79.26 ° and 81.31 ° for θ_{ab}.

When the co-flowing jets were run on condition, cold subsonic flows with a temperature of 20 °C exited both nozzles. The core flow had an exit velocity of 240 ms^{-1}, which equates to 0.7 Ma. The bypass flow had an exit velocity of 215 ms^{-1} or 0.63 Ma. The effective bypass area to core area was a ratio of 3:1.

3.6 Microphones

B&K microphones are renowned for being precision instruments with great overall frequency response and excellent clarity. A free field B&K 4939 1/4" condenser microphone was used in this project with a frequency response of 4 Hz to 100 kHz, sensitivity (defined as the voltage generated in response to a certain pressure input) of 4 mV/Pa and a dynamic range of 28 dB to 164 dB. The microphone was calibrated using B&K 4231 Sound Level Calibrator 1 kHz, 94 dB.

Condenser microphones compared with ribbon or dynamic microphones are ideal for all applications where sound quality is paramount such as professional music recording and acoustic instrument and measurements. They work on the principle of capacitance. The microphone has a capacitor with two plates. The front plate is a light thin metal diaphragm. The thicker back plate is gold plated. As sound waves enter the microphone, the sound pressure moves the front plate. As the distance between the front plate and back plate varies according to the sound pressure, so too does the capacitance, resulting in the generation of a signal proportional to the sound. As there is no coil in place (as there are in dynamic and ribbon microphones) the diaphragm can be lightweight and of any shape to allow

for a better frequency response.

The sensitivity of condenser microphones does however vary with frequency and the angle of the incidence of the acoustic wave. There is a reduced bias error in the measurements of microphones at normal incidence. Corrections to the measurement data can be applied but in the case of frequencies less than 10 kHz, the corrections are negligible (∼0.1 dB). Even up to 80 kHz, the applicable corrections are very small. It is worth noting that different microphones have different sensitivity levels and subsequently their corrections especially at high frequencies, may be more significant.

The 1/4" microphone, as can be seen in Figure 3.11, is omnidirectional and attached to a B&K 2670 preamplifier which converts the microphone's high output impedance to a low impedance, making it a suitable input for the B&K PULSE data acquisition system. PULSE also supplies a fixed charge to the externally polarized microphone.

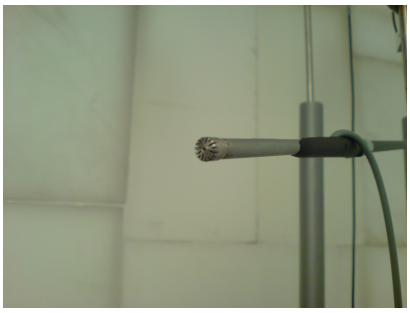

Figure 3.11: B&K 4939 microphone

3.7 Data acquisition system

The B&K PULSE 3560-D system is a 24 bit resolution data acquisition system. It is a multiframe system housing two B&K 3110 modules with two channels each as shown in Figure 3.12. Its capability can be expanded to house three additional modules. The modules have a frequency range of 0 to 102.4 kHz (the sampling frequency is 204.8 kHz) and a full dynamic output range of 7 mV to 7 V. The typical amplitude precision at 1 kHz with 1 V input is ±0.005 dB and the typical attenuator linearity at 1 kHz is also ±0.005 dB.

The PULSE system has in built anti-aliasing filters which remove frequency components above the Nyquist frequency (half the sampling frequency). This avoids errors in the frequency domain. Frequency responses are filtered with a 3rd order Butterworth filter and the frequency accuracy is within 0.0025%.

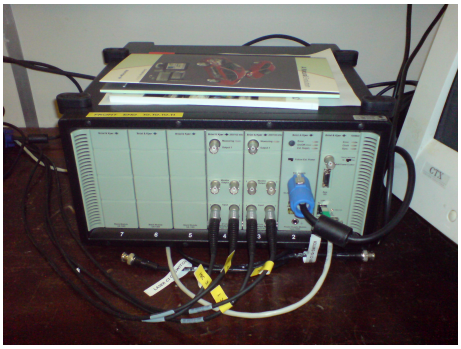

Figure 3.12: B&K PULSE 3560-D system

At high frequencies, the decibel levels recorded by the microphones were automatically corrected for by PULSE using the Transducer Electronic Data Sheets (TEDS).

The recorded data was written directly to the pc hard drive allowing more storage

than memory cards as required with alternative systems such as Nexus systems.

Statistical analysis of the data was done using Matlab 2007b, The MathWorks, Natick, MA, USA and Stata SE v10.0, StataCorp, College Station, TX, USA.

3.8 Traverse

A light weight motorized traverse from Dantec Dynamics UK, shown in Figure 3.13, was used to align optical and acoustic equipment with the jet rig. During experiments, the traverse was used to move measurement equipment. It was controlled using BSA flow software.

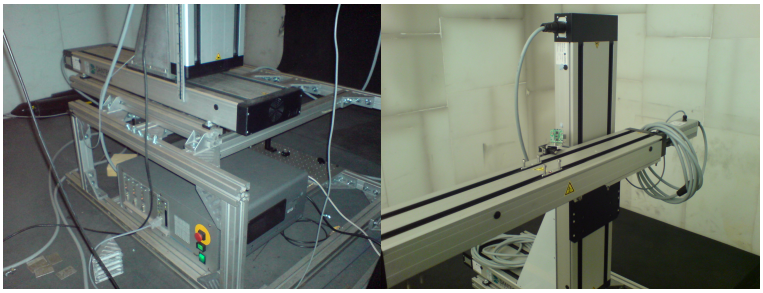

Figure 3.13: Motorized traverse

CHAPTER 4

Experimental technique

There are different ways in which the jet noise from the exhaust can be experimentally investigated. This of course depends on considerations such as looking at a specific region or a more global area of interest in the flow, the experimental design constraints, the time scales involved in developing a working system and the budgetary limitations.

This chapter reviews experimental techniques available and the acoustic and optical techniques chosen for this project.

4.1 Acoustic measurement techniques available

4.1.1 Sound intensity mapping

Sound intensity mapping gives direction and magnitude to sound measurements. To generate this vector an intensity probe (two closely spaced, facing microphones) is used to measure the average pressure change and calculate particle velocity.

The advantages are that it is easy to use, portable and provides a reasonable resolution. However its limitations are that its time consuming to take the measurements, the equipment is very expensive and only works effectively on stationary

noise sources. For these reasons it is not suitable for the co-axial project.

4.1.2 Beamforming

This is a powerful technique in which microphones in a far field array can be used to locate sound sources by setting delays in each measurement channel reflecting the distance from each microphone to the noise source. With this arrangement all the signals see the same wavefront at the same time, which in effect makes the array focus on a particular region. By changing the signal delays, the array can focus on different areas without having to physically move the microphones. The accuracy of the measurements depends on the array design, measurement distance and the frequency range of interest.

The advantage of this arrangement is that it is a fast way to acquire data. Once set up, only one measurement is needed. It also has a long range and can resolve large objects at a distance making it suitable for full scale testing. However it is unsuitable for use in the co-axial project. This is because it requires multichannel measurement. The co-axial project funded four B&K 1/4" microphones which is not a large enough number to sufficiently acquire accurate noise source locations. Typical beamforming experiments use in excess of 36 microphones. Secondly, the performance of the array is heavily dependant on its size and geometry. With four microphones, the array options are rather limited as illustrated in Appendix A.7. Another limitation is the microphone spacing requirement which is frequency dependant. The distance between microphones must be less than half a wavelength of the sound wave under review. The B&K 1/4" microphones have a diameter of 6 mm, which means when two microphones are adjacent, there is a distance of 6 mm between their centers. 6 mm represents half a wavelength for a frequency of 28.3 kHz. That is, the highest frequency that can be reviewed

using this technique with these microphones is just over 28 kHz. The frequency range of interest for this project lies in excess of this, making this technique unsuitable for this project.

4.1.3 Spatial transformation of sound fields

STSF uses the cross spectra of individual measurement points and a series of reference microphones to generate a sound field map in a measurement plane. Near field Acoustic Holography (NAH) algorithms then transform this data into a model of the sound field from which quantities such as sound pressure levels, particle velocity and intensity vectors can be derived. The algorithms project information in planes closer to or further away from the test object. This is an easy and quick way to gain good documentation of the sound field with good resolution. However, it only works for stationary sound sources.

For non stationary noise sources, Time Domain Holography (TDH) can be used to calculate the sound field parameters in a measurement plane by using a microphone array. Similar to beamforming, a large number of channels are requires and the microphone spacing is frequency dependent which restricts the range of interest.

There is another technique called Statistically Optimal Near field Acoustic Holography (SONAH) which is a calculation method introduced by B&K that allows high resolution source mapping to be obtained over a broad frequency range. A microphone array is still needed in the set up, making this technique along with NAF and TDH, unsuitable for the co-axial project.

4.1.4 Acoustic mirror

The acoustic mirror is able to separate and locate dominant noise sources even with the presence of high background noise. The mirror, which is usually elliptic in design, has two focal points such that all distances from the far focus to the near focus via the surface of the mirror are equal. Therefore all sound wave radiating from the far focus that reflects off the mirror surface onto the near focus point have travelled the same distance. This causes the sound waves at this point to superimpose which provides an amplification of that sound compared with the surrounding noise sources. This method has a reasonably good resolution with a high signal to noise ratio but it is very time consuming as each individual measurement point has to be scanned. This is problematic for full scale testing which are very expensive to run. There is also the added issue of having a mirror large enough for the test facility. The mirror diameter is dependent on the wavelengths under review and the diameter of the jet nozzle.

For small scale laboratory jet flows such as the co-axial jet noise project, where the actual running of the jet rig is an acceptable expense, time consuming scans from a budgetary point of view would not be problematic. As the nozzle geometries are small, an appropriately sized mirror would be affordable to manufacture and could be housed in the School of Engineering's anechoic chamber. For all of these reasons, it was deemed suitable for co-axial jet noise project.

4.2 Acoustic measurement technique chosen - Acoustic mirror

4.2.1 Introduction to the acoustic mirror

Acoustic mirrors are instruments governed by principles of reflection. A mirror schematic can be seen in Figure 4.1. An ellipsoid of revolution is used to create the mirror of diameter D_m and depth z_m with two focus points; a near focus at a distance f_{m1} from the centre of the mirror and far focus at a distance f_{m2}. By positioning the far focus at a point of interest in the jet, the noise generated at this point can be measured from the gain obtained at the near focus. That is, sound radiated from the far focus travels towards the surface of the mirror and is reflected such that it converges at the near focus. By positioning a microphone at the near focus, sound pressure levels at the far focus can be measured.

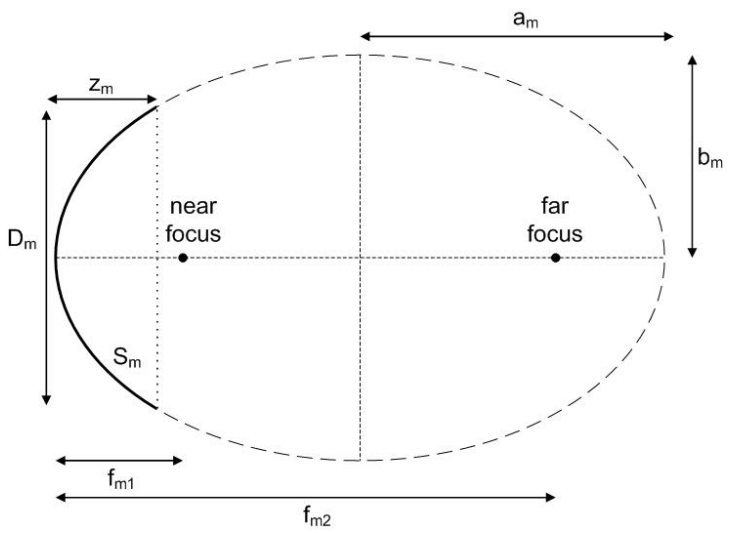

Figure 4.1: Acoustic mirror geometry

The gain G_0 in sound pressure level received by the microphone placed at the near focus m_{nf}, can be quantified by,

$$G_0 = L_m - L_{ref} = 10log\left(\frac{I_m}{I_{ref}}\right) \tag{4.1}$$

where, L_m is the sound pressure level at the near focus microphone, L_{ref} is the sound pressure level at a reference microphone placed at the same distance from the point source and I_m and I_{ref} are the respective intensities. This was approximated by Grosche *et al.* (1997) to Equation 4.2,

$$G_0 \approx 10log\left(0.5\frac{D_m^4}{\lambda_w^2 f_{m1}^2}\right) \tag{4.2}$$

This is a theoretical approximation of the gain. In practice the gain is smaller mainly due to the microphone at the near focus blocking some of the wavefronts from the far focus hitting the mirror surface.

Another advantage of using an acoustic mirror is that sound sources can be resolved in all directions normal to its axis, which allows greater flexibility over linear microphone arrays which can only resolve sound sources in one dimension. In the direction of the mirror axis however, sound sources are hard to resolve (as shown in Chapter 5).

4.2.2 Design of the acoustic mirror

The acoustic mirror was designed and manufactured in house. It is made from an aluminium block as shown in Figure 4.2, which was chosen for its affordability, machinability and light weight compared to other materials being considered such as steel. The mirror was designed to be suitable in size and weight for mounting on a motorized traverse along with potentially two LDA heads. In this arrangement, the mirror was designed such that it had the same focal point as

the LDA heads.

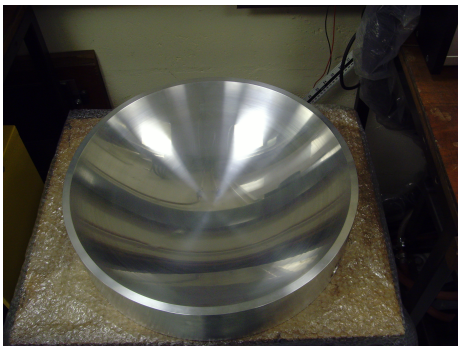

Figure 4.2: Acoustic mirror

The mirror size was calculated using the standard cartesian equation for an ellipse centered about the origin as shown in Equation 4.3,

$$\frac{x_m^2}{a_m^2} + \frac{y_m^2}{b_m^2} = 1 \tag{4.3}$$

where a_m and b_m are constants that outline the major and minor axis respectively (provided $a_m > b_m$).

Constant values of $a_m = 0.5$ m and $b_m = 0.4$ m were required to appropriately size the mirror for acoustic suitability, ease of manufacturing, cost of material and fitting on the traverse system with mounted LDA heads.

The focus positions from the origin (lying on the major axis) is calculated as $\pm\sqrt{(a_m^2 - b_m^2)} = \pm 0.3$ m. Therefore, from the centre base of the mirror, the near focus distance is $f_{m1} = 0.2$ m, far focus distance is $f_{m2} = 0.8$ m, mirror depth is $z_m = 0.1$ m and mirror diameter is $D_m = 0.456$ m with a 0.012 m ring.

The ratio of jet nozzle diameter (bypass) to acoustic mirror diameter is 25.33

and is reasonably consistent with the work of other researchers, such as Grosche & Stiewitt (1983) who used 0.06 m diameter nozzle and 1.6 m diameter elliptic mirror, giving a ratio of 26.67; Viswanathan (2007) used a 0.062 m diameter nozzle and 1.5 m diameter elliptic mirror, giving a ratio of 24.19.

Drobietz *et al.* (2008) had a ratio of 9.09 with a 0.22 m diameter nozzle and 2m diameter elliptic mirror, however this was still deemed sufficient to find a good spatial resolution of the noise sources.

4.3 Optical measurement techniques available

There are two optical velocity measurement systems predominately used in the School of Engineering. They are Particle Image Velocimetry (PIV) and Laser Doppler Anemometry (LDA) both of which are suitable for jet flow measurements.

4.3.1 Overview of PIV

PIV is a non-intrusive laser optical measurement technique which is used to look at the flow dynamics of both gaseous and liquid fluids. It has been used in a number of areas from wind tunnel velocity experiments that test the aerodynamics of objects (cars, aeroplanes etc) to environmental research involving coastal engineering and tidal modelling.

It is a whole flow field technique that illuminates a cross section of a seeded flow with a laser light sheet and uses a digital camera to capture each light pulse as separate image frames. The images are subdivided into interrogation areas

which are then cross correlated with each other to determine a signal peak. This represents a common particle displacement. From this, the displacement and velocity can be calculated using sub-pixel interpolation. Repeating this procedure for all interrogation areas generates velocity vector maps. From this, statistics regarding the turbulence and the spatial correlations can be derived.

The advantages of PIV are that it can take instantaneous measurements across the whole flow field. However, its spatial resolution is not as good as LDA and there are seeding issues that lead to 'gappy' data (areas in the flow field where the velocity information is lost or not apparent) that usually have to be addressed.

4.3.2 Overview of LDA

LDA is a non-intrusive optical measurement technique suitable for making point measurements in flows. This can be in 1D, 2D or 3D depending on the equipment available. The applications span from testing the aerodynamics of buildings/objects/vehicles to combustion research and wave dynamics.

The system works by passing a continuous wave laser through a Bragg cell which splits the beam into two beams of equal intensity with a frequency shift between them. Optical fibres pass the beams into a probe which focuses the beams upon exit to cross, forming a measurement volume. As seeded particles pass through this volume, they scatter the light. This information is collected by a receiver lens and focused on a photo-detector. The photo-detector then converts the fluctuating light intensity to an electrical signal which is processed, providing velocity components of the point measurement.

LDA has high temporal resolution and data compression making it very attractive

for specific point measurements of a jet flow and does not suffer as extensively from gappy data as PIV. Its limitation is that the measurement volume is small which means if a jet flow is scanned, it will be time consuming.

4.4 Optical measurement technique chosen - LDA

From the available equipment and resources at the School of Engineering, both optical measurement techniques could in theory be used for the jet noise project. However, in practice access to the PIV equipment was extremely limited as it was in use by a number of other projects.

The LDA system was readily available and complimented the acoustic mirror system better than the PIV set up. A grid of the same size and spacing as that used for the acoustic mirror could be used for LDA measurements. Thus making the optic and acoustic measurement area consistent.

The configuration of the LDA systems starts with a continuous wave laser that is passed through an acousto-optic modulator known as a Bragg cell. This is a glass crystal with an attached vibrating piezo crystal that generates acoustic waves, typically at 40 MHz. The acousto-optic effect causes the laser beam to diffract and split with each of the two new beam having equal intensity but with a frequency shift. The two beams are passed via optical fibres into a probe which uses a lens to focus the two beam upon exit to form a probe volume or measurement volume as shown in Figure 4.3.

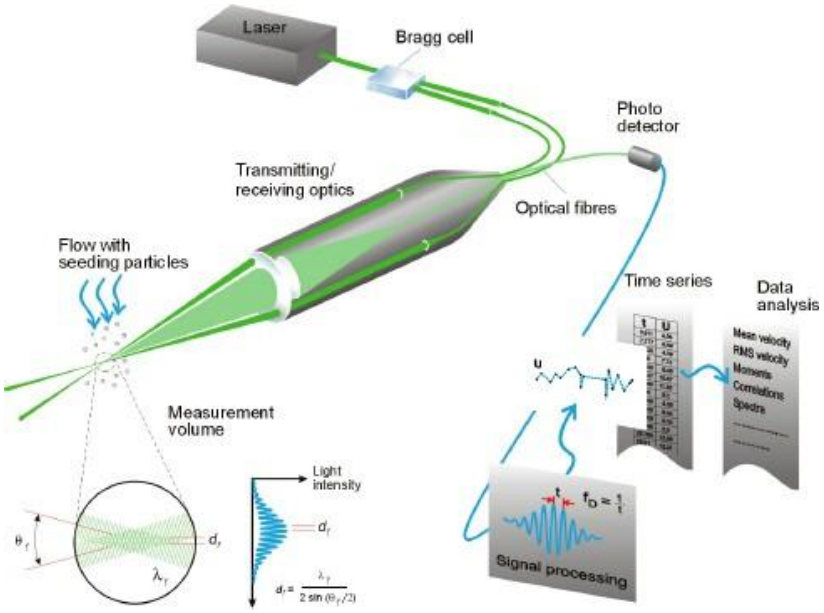

Figure 4.3: The LDA system *(www.dantecdynamics.com)*

At the probe volume, the light intensity is modulated as a result of the interference between the laser beams. This produces fringes of high and low light intensity. The fringe spacing d_f is defined by the laser light wavelength λ_f and the angle θ_f between the beams as shown by Equation 4.4.

$$d_f = \frac{\lambda_f}{2sin(\theta_f/2)} \tag{4.4}$$

As a particle traverses the fringes, the scattered light fluctuates in intensity with a frequency f_D. That is, the scattered light contains a Doppler shift with a Doppler frequency f_D. The receiver lens collects the scattered light and focuses this through an interference filter to the photo-detector. The interference filter removes noisy data such as ambient light and only lets the required wavelength pass through to the photo-detector.

The photo-detector outputs an electrical signal known as the Doppler burst, which based on the input of the fluctuating light intensity. This is a sinusoidal

function that follows a Gaussian envelope reflecting the intensity profile of the laser beams. The signal processor filters and amplifies the Doppler burst and derives f_D for each particle using a FFT algorithm.

As the fringe spacing d_f is used to find the distance travelled by a particle and the Doppler frequency f_D provides temporal information, that is time $= 1/f_D$, the velocity can be calculated using Equation 4.5.

$$v_f = d_f f_D \tag{4.5}$$

The fringe pattern moves at a constant velocity due to the frequency shift in the beams caused by the Bragg cell. Without this, the LDA system would not be able to distinguish between positive and negative flow directions.

CHAPTER 5

Measurement error and preliminary testing

The measurement error and preliminary testing of the acoustic equipment is described in this chapter with measures taken to reduce erroneous noise and subsequently improve the accuracy of the acoustic measurements. The configuration of the LDA is also described.

At the start of the preliminary tests, a discrete tone was observed when the jet rig was run on condition. This was investigated and resolved, the details of which can be found in Appendix A.8.

5.1 The acoustic mirror

5.1.1 The acoustic mirror and jet noise

Elliptic mirrors have been used since the 1970's by researchers such as Grosche (1973), Viswanathan (2007) and Drobietz *et al.* (2008) who looked at noise source location and the distribution of sound by moving the mirror and microphone assembly in one direction. This technique is essentially used for far field measurements of the sound pressure distribution. As the microphone and mirror are placed outside of the jet, near field pressure fluctuations are not applicable.

Tests with spherical mirrors have also been successfully done by Grosche (1968); Grosche *et al.* (1977), who concluded that an elliptic mirror provided greater accuracy in measuring sound source intensities.

Waldhauer (1989) also found there is a substantial improvement in the depth of focus with elliptic mirrors. However, the total sound power measured using the mirror is dependent on the directional characteristics of the sound source. A generally accepted assumption for such experimental work, is that sound sources are emitted spherically.

The theory accompanying acoustic mirrors for determining sound source distributions starts by modelling the mirror surface as rigid and impermeable, that is a fluid particle's velocity at the mirror's surface S_m (in Figure 4.1) is zero.

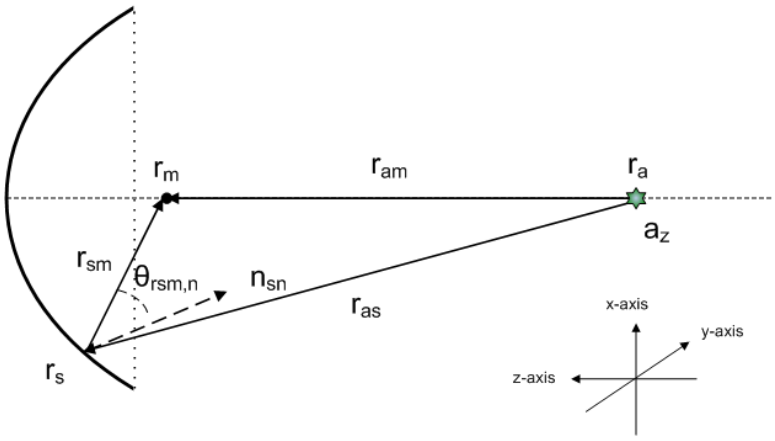

Figure 5.1: Noise source and the acoustic mirror

For a given monopole source a_z at the far focus r_a (x,y,z=0,0,0) as shown in Figure 5.1, the frequency domain pressure $P(r_m, r_a)$ measured by the mirror microphone at the near focus r_m, comprises of a direct wave and a reflected wave (via the

acoustic mirror) as shown in Equation 5.1,

$$P(r_m, r_a) = P_0(r_{am}) + \iint_S P_s(r_{as}) \frac{\partial}{\partial n} G(r_m, r_s) dS \tag{5.1}$$

where $|r_{am}| = |r_m - r_a|$ and $P_0(r_{am})$ is the direct free field pressure from the sound source wave.

The reflected wave is accounted for by applying the surface pressure $P_s(r_{as})$ where $|r_{as}| = |r_s - r_a|$, to the free field spherical far field Greens function $G(r_m, r_s)$, and integrating over the mirror surface. Note r_s is the position on the surface of the mirror with an inward pointing normal n. The Green's function shown in Equation 5.2 is calculated using the length of the mirror surface to the microphone, $r_{sm} = r_m - r_s$ and the variable wave number k, where $k = 2\pi f / c_0$.

$$G(r_m, r_s) = \frac{e^{ik|r_{sm}|}}{4\pi |r_{sm}|} \tag{5.2}$$

Using the Kirchhoff approximation for scattered wave fields and their normal derivative at the interface, the surface pressure $P_s(r_{as})$ can be replaced with $2P_0(r_{as})$. This approximation doesn't work well at low frequencies. However as used by Drobietz *et al.* (2008), a lower threshold of 1 kHz is acceptable for the approximation. This leads to Equation 5.3,

$$P(r_m, r_a) = P_0(r_{am}) - \frac{1}{2\pi} \iint_S P_0(r_{as}) \frac{ik|r_{sm}| - 1}{|r_{sm}|^2} e^{ik|r_{sm}|} cos\theta_{rn} \tag{5.3}$$

where $\theta_{rsm,n}$ is the angle between the normal and vector r_{sm} from the mirror surface as shown in Figure 5.1.

Direct sound source measurements taken by the acoustic mirror and microphone

give an implied mapping to the noise source locations. There have been a number of enhancement techniques proposed each of which claims to provide a 'truer' interpretation of the sound source map. Schlinker *et al.* (1973) compared an integral transform, a matrix inversion and a relaxation technique and deemed the relaxation technique to be the most suitable enhancement technique. This is an iterative method for which an initial condition of source strength distribution per unit length is used to calculate the mirror and microphone responses. These are then compared with the actual measured data and the differential determines the new distribution.

Laufer *et al.* (1975) used the relaxation technique to correct sound source measurements along the jet axis of a supersonic jet and confirmed the importance of this technique in providing a more accurate distribution than that of direct microphone readings. The technique was validated by comparing calculated radiated spectral densities with the spectral densities from an omni-directional microphone. However, Sen (1996) found the relaxation technique to be a coarse estimation to his own proposed direct estimation technique, which used a point spread function (PSF).

The PSF varies with space-frequency and depends on the geometry of the mirror. The source strength per unit length $W'(x, f)$ is calculated by applying a normalization factor Ψ_m to the mirror measured power spectral density Φ_m, as shown in Equation 5.4.

$$W'(x, f) = \Psi_m \Phi_m(x, f) \tag{5.4}$$

Another correction method was proposed by Viswanathan (2007) who used an

acoustic mirror with radially placed far field microphones. With this method, the PSF was not determined, but instead a normalization factor was applied to the raw measurement data such that the calculated far field spectral density agrees with the measured far field spectral density. As with the relaxation technique, the far field spectrum is calculated as shown in Equation 5.5,

$$\Phi_{ff}(f) = \rho_0 c_0 \int_0^{+\omega} \frac{W'(x,f)}{4\pi r_{jm}^2} dx \tag{5.5}$$

where $\Phi_{ff}(f)$ is the power spectral density at the far field at a given frequency f, r_{jm} is the distance from a point on the jet axis to the far field microphone, ρ_0 is the ambient density of air at normal room temperature and pressure, and c_0 is the speed of sound.

Unlike the LDA system, where the measurement volume is defined and 'fixed', the measurement volume for the acoustic mirror is more like an averaged de-blurring of a point spread function that varies with frequency. An example showing this can be seen in Figure 5.2 for 8 kHz. This averaging is subject to abberations.

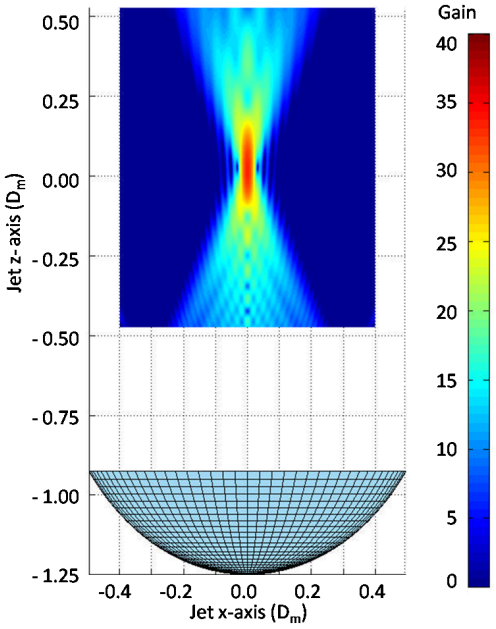

Figure 5.2: Elliptic mirror point spread function for 8 kHz, Drobietz *et al.* (2008)

5.1.2 Abberation due to source not being at the far focus (x≠0 or y≠0)

The far focus of the acoustic mirror is modelled on a theoretical basis as a point source, however in practice, the far focus point is actually more of a region or slice through which all noise sources radiating sound waves to the surface of the acoustic mirror, are integrated.

When the noise source is at the far focus, then the sound path length $r_{as} + r_{sm}$, is constant for all points on the mirror surface r_s. This results in the microphone recording a high gain in the sound pressure level. However, as the noise source moves away from the far focus (perpendicular to the mirror axis), the sound path length is no longer constant; resulting in the microphone recording a drop in signal due to interference. This reflects the diffraction pattern, which can be plotted to show the spatial resolution of the microphone with varying source positions.

The main lobe in a diffraction pattern is the resolution width; the narrower the resolution width and higher the gain factor, the more detailed the sound source map will be.

The abberation caused by the noise source being offset from the far focus position in either the x-axis or y-axis (based on the co-ordinate system shown in Figure 5.5) can be seen using a diffraction pattern. This subsection looks at an example of a diffraction pattern and the validity of the gain using the acoustic mirror.

The diffraction pattern of an offset source was initially tested by placing a 40 kHz emitting transducer on a manual traverse in the far focus facing the mirror, with tracks running perpendicular to the mirror axis as shown in Figure 5.3. As the emitter moved along the traverse track, its position was offset from the far focus.

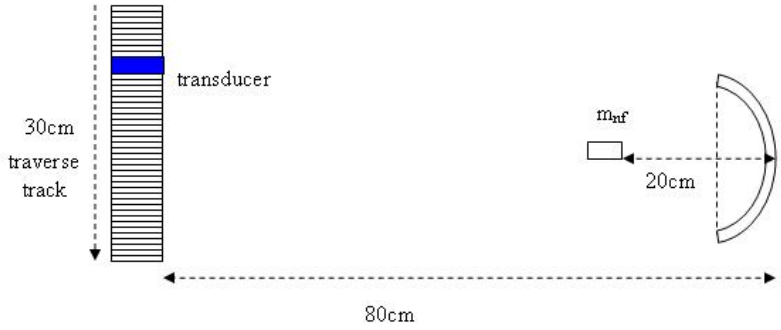

Figure 5.3: Initial arrangement for verifying the diffraction pattern

The emitter moved along the traverse track in 1.0 cm increments from -20 cm to +10 cm and the microphone in the near focus of the mirror, recorded the signal drop off. The microphone was encased with a small cylindrical block of acoustic foam to ensure only the reflected sound waves from the mirror surface

are received by the diaphragm and the interference directly from the sound source is negligible. The diffraction pattern is shown in Figure 5.4.

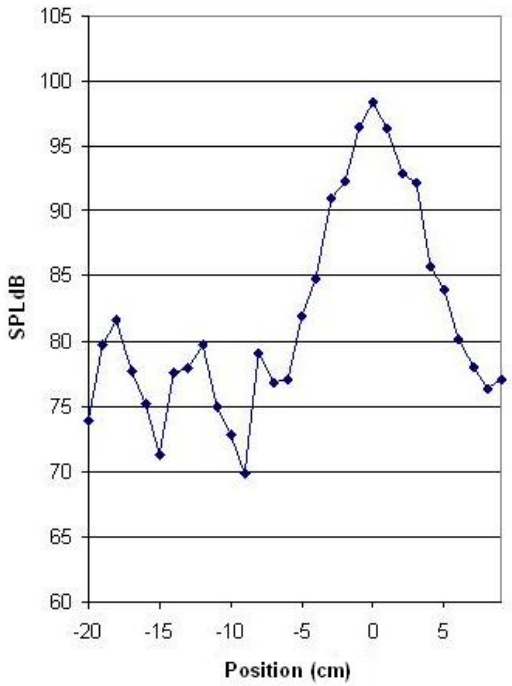

Figure 5.4: Diffraction pattern

The resolution width is relatively narrow with a large gain factor in excess of 15 dB. This validates the mirrors ability in detailing sound source maps, especially when compared with the work of Nagakura (2006) who also used an acoustic mirror and looked at similar SPLdB levels. His mirror was validated with a 10 dB gain factor.

Following this, more detailed diffraction patterns were obtained by placing the emitting transducer just above the bullet tip on the jet rig, with sound emissions this time directed upwards as shown in Figure 5.5.

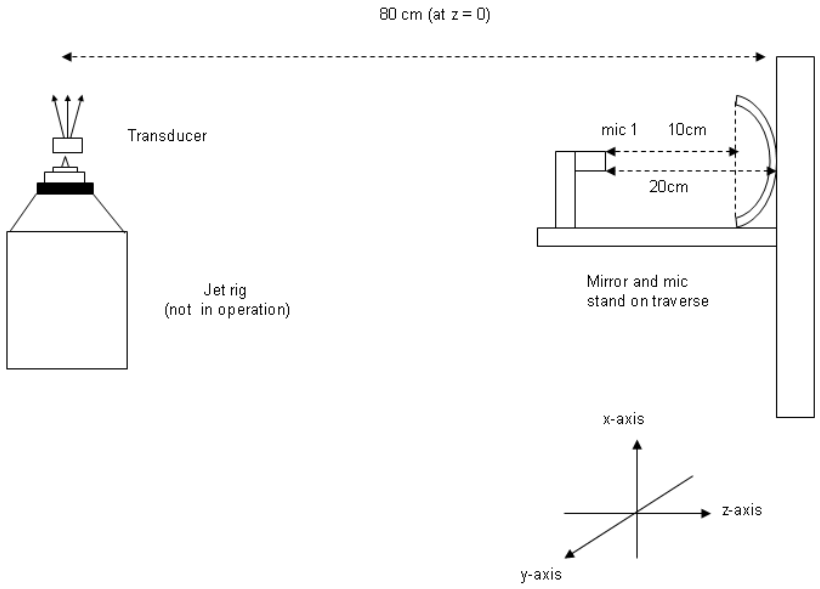

Figure 5.5: Arrangement for further diffraction pattern tests

The mirror surface was first covered with a large thick block of acoustic foam to shield the microphone from reflected sound waves and to provide reference background readings.

The centre of the mirror was aligned with the emitter in the x-axis and positioned 80 cm away in the z-axis. The x,z positions were fixed. Measurements in the y-axis from -8D_{bp} to 8D_{bp} were taken with 1.0 mm increments, with the emitter first set to 20 kHz and then 40 kHz. This can be seen in Figure 5.6.

The acoustic foam was then removed and the y-axis traverse measurements were taken again, giving a diffraction pattern as shown in Figure 5.7.

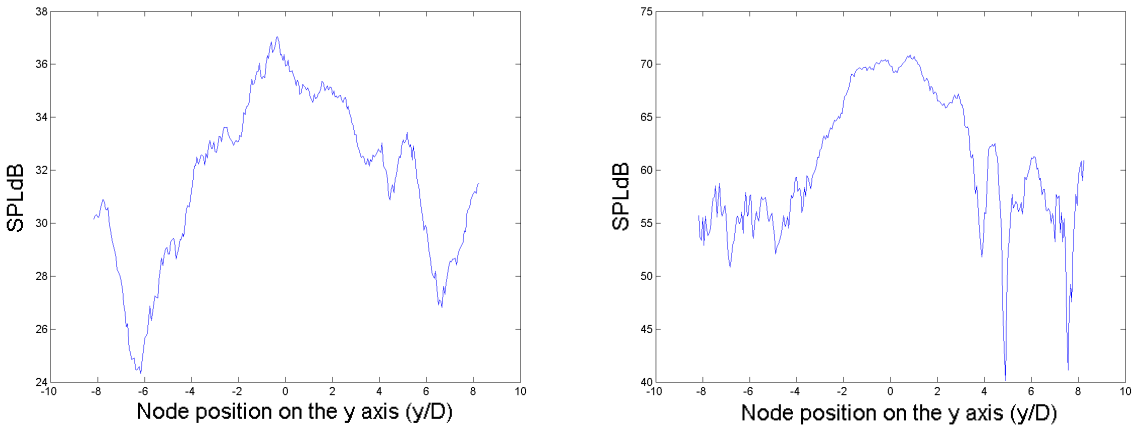

(a) 20 kHz (b) 40 kHz

Figure 5.6: Reference background readings in the y-axis

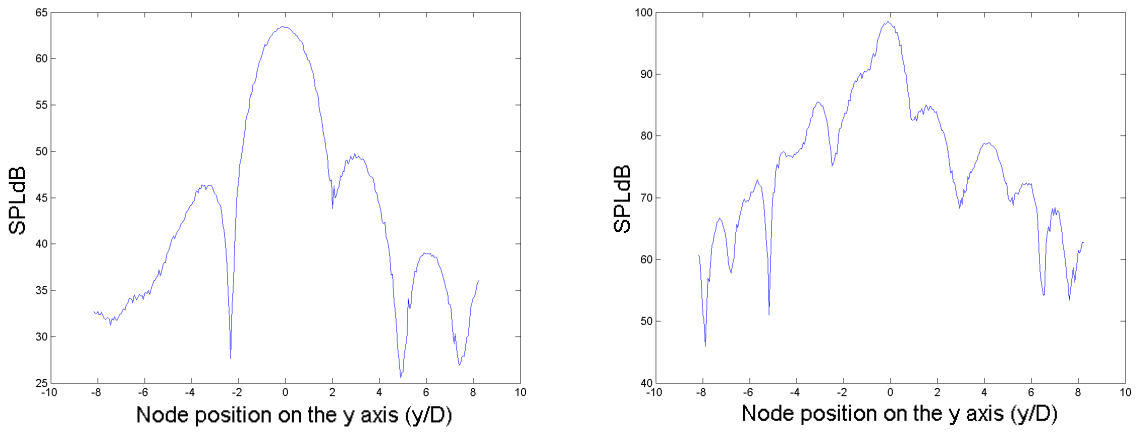

(a) 20 kHz (b) 40 kHz

Figure 5.7: Diffraction pattern in the y-axis

Figure 5.7 shows the gain factor (height of the main lobe less height of either secondary lobes) is again in excess of 15 dB, which reconfirms the mirrors suitability in detailing sound source maps for jet noise experiments. The low background measured further highlights the gain achieved by the acoustic mirror.

5.1.3 Abberation due to source not being at the far focus (z≠0)

The diffraction pattern is frequency dependent, however in the z-axis, it has little effect. This is because the depth of focus of the acoustic mirror (going through the jet) has poor resolution as observed by researchers such as Drobietz *et al.* (2008) and Sen (1996).

With the experimental arrangement in place as previously done in Figure 5.5 but this time with x=0 and y=0, measurements in the z-axis from -8D_{bp} to 8D_{bp} were taken with 1.0 mm increments. Again the emitter was first set to 20 kHz and then 40 kHz the results of which are shown in Figure 5.8.

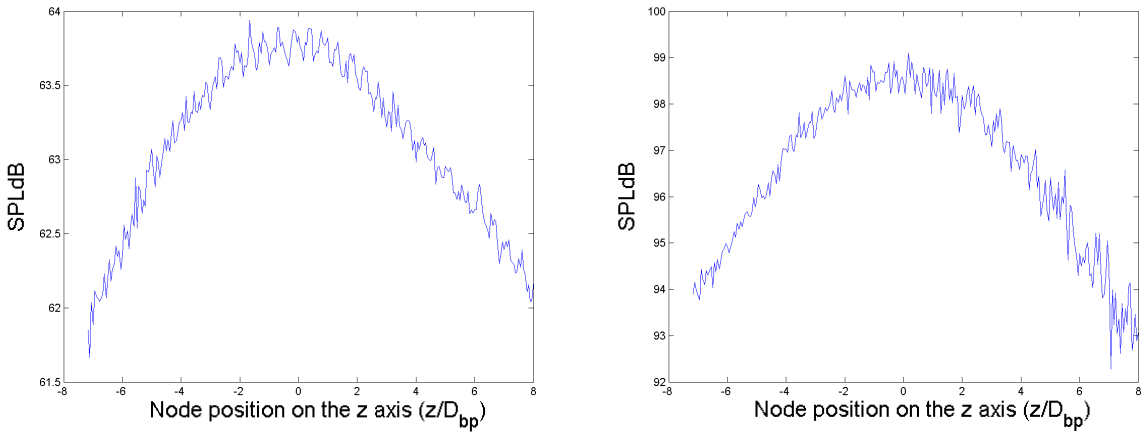

(a) 20 kHz (b) 40 kHz

Figure 5.8: Diffraction pattern in the z-axis (adjusted for abberation due to source directivity)

The resolution width spans the entire 16D_{bp} (-144 mm to +144 mm) line of measurement without the presence of a secondary lobe. This implies the mirror has very poor accuracy in the z-axis. Another point to note in Figure 5.8 is the relatively little change in SPLdB within each graph which further highlights

poor resolution of sound sources in the z-axis. Sound measurements are therefore taken by fixing the mirror in the z-axis and traversing it along the x-axis and y-axis, as done by many researchers such as Drobietz *et al.* (2008), Viswanathan (2007) and Fuchs (1978a).

5.1.4 Abberation due to microphone not being at the near focus

A common aberration when using an acoustic mirror system is the misplacement of the microphone at the near focus. Sen (1996) showed that by offsetting the microphone at the near focus by 0.5 inches in the y-axis (same axis as in Figure 5.5), the apparent source location shifted by 2.5 inches. Microphone offset in the z-axis does not cause a shift in the source location due to the insensitivity of the acoustic mirror in the z-axis (as previously discussed). This aberration is independent of frequency as the mirror is approximately an equi-phase surface with respect to the apparent source point and the microphone offset.

5.1.5 Abberation due to source directivity

If a point source has directivity with respect to its acoustic distribution, then the an abberation can be recorded by the acoustic system. The result would be an asymmetric point spread function who's peak is displaced or offset in the traverse direction (i.e. y-axis). This abberation is frequency dependent as the source directivity is often frequency dependent.

5.1.6 Abberation due to sound wave passing through shear layer

It was noted by Grosche (1973), that sound waves passing though the velocity and density gradients in the jet (more profound in the shear layers), are slightly shifted when radiated to the mirror. This suggests a slight displacement in the

location of sound sources from the measured distribution. The apparent downstream shift of sound source position is described by Grosche & Stiewitt (1983) and Nagakura (2006) who showed its effect on the maxima of the directivity patterns.

A schematic illustrating the shift is shown in Figure 5.9 where O is the source position, O' is the apparent source position detected by the mirror, V is the jet velocity, t_i is the time taken for a ray to reach the interface at I, t_0 is the time taken for a ray at the interface I to reach the mirror at P, c_0 is the speed of sound (assumed constant for the estimation of the downstream shift). The apparent downstream shift Δx_{axis} (or $OO' = Vt_i$) is approximated by,

$$\Delta x_{axis} = Ma.h_m \tag{5.6}$$

where, h_m is the distance between the point source and interface along the direct transmission path to the mirror and Ma is the Mach number. This is an accepted and documented shift which is independent of frequency as described by Sen (1996).

For the wavenormal, the total time taken $(t_i + t_0)$ is proportional to the distance $O'I + IP$. When $O'I$ is normal to the interface, then it becomes collinear with IP (i.e. refraction is close to zero) and therefore $O'P$ becomes approximately linear as described by Sen (1996).

At 90 degrees to the jet axis, Sen (1996) found roughly equal travel times for the ray path and the wavenormal path, implying the refraction through the interface is minimal. This view is also supported by supported by Drobietz *et al.* (2008)

who used a mirror at 90 degrees to the jet axis. As the mirror is positioned at 90 degrees in this project, the downstream shift recorded by the mirror will be minimal.

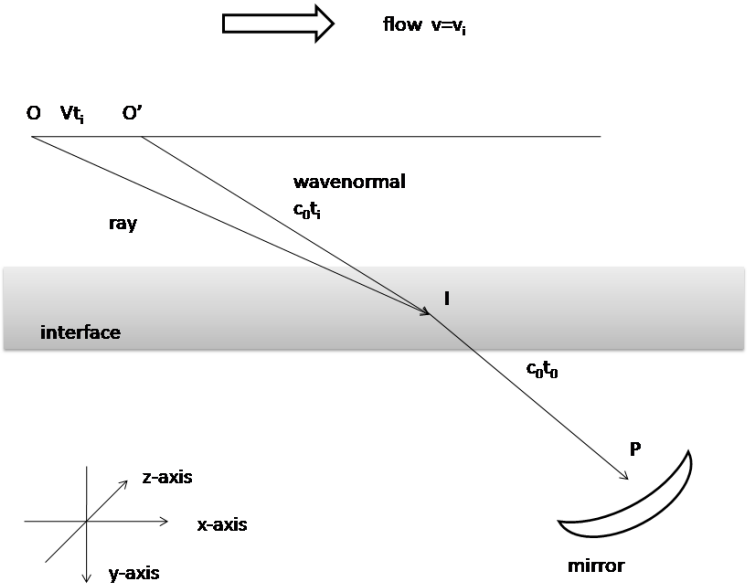

Figure 5.9: Schematic of downstream shift

5.1.7 Abberation due to multiple sources (limit of resolution)

The spatial resolution of the mirror is limited by the diffraction of sound waves at the edge of the mirror. The theory of diffraction of waves by a circular aperture defines the spatial resolution to be dependent on wavelength as shown in Equation 5.7,

$$\sin\theta_{res} = 1.2\frac{\lambda_w}{D_m} \tag{5.7}$$

where λ_w is the acoustic wavelength, D_m is the acoustic mirror diameter and θ_{res} is the angular resolution angle which describes the first minimum of intensity in a diffraction pattern. In a diffraction pattern, the distance between the centre of the diffraction pattern and the point where intensity is reduced by half is referred

to as the half width w_0. Equation 5.8 shows its approximate relationship with λ_w, as described by Grosche *et al.* (1997).

$$w_0 \approx 0.54\lambda_w \frac{f_{m2}}{D_m} \tag{5.8}$$

The limit of resolution in an acoustic mirror context is the distance between two point sources at which the microphone cannot distinguish between them. In the case of the acoustic mirror, this is dependent on its diameter D_m, the frequency of the sound source f_s, the speed of sound c and the distance from the source to the centre of the acoustic mirror f_{m2}.

The resolution capability of the mirror can be calculated using the formula for the limit of resolution, which in this case is given by Fuchs (1978a) and rearranged as Equation 5.9,

$$L_{res} = \frac{1.22cf_{m2}}{D_m f_s} \tag{5.9}$$

The change in the limit of resolution with frequency can be seen in Figure 5.10 and is consistent in form with the calculated values produced by Nagakura (2006).

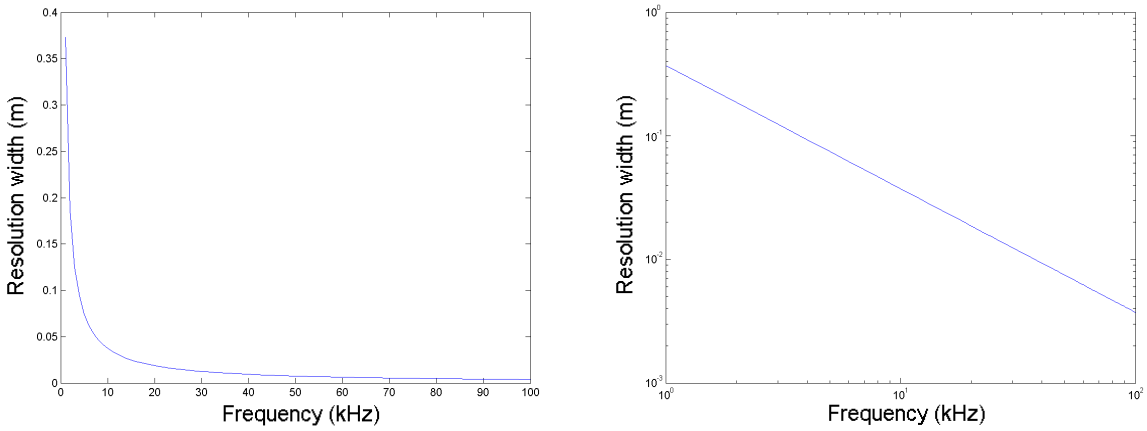

(a) Linear scale (b) Log_{10} scale

Figure 5.10: Resolution width

An experiment showing the limit of resolution in effect was conducted using three emitting transducers set at 30 kHz, each with a diameter of 10 mm (the diaphragms accounted for just over half of this size). They were placed at the bullet tip facing upwards as shown in Figure 5.11 and were in series with initially no space between them such that the total span of the series was 30 mm.

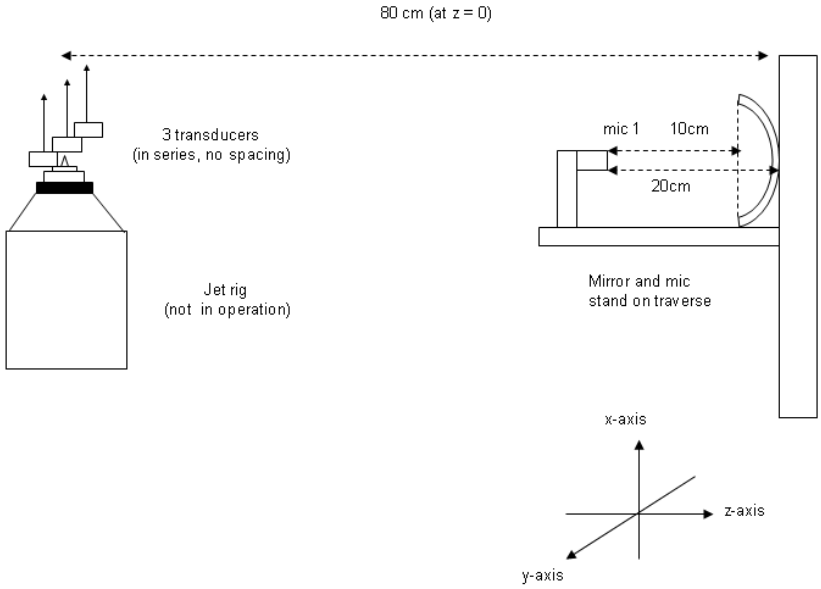

Figure 5.11: Experimental arrangement for testing the limit of resolution using 3 transducers

Using the acoustic mirror and microphone set up on the traverse with x=0 and z=0, a diffraction pattern was taken in the y-axis from -2D_{bp} to 2D_{bp} in increments of 1 mm. As can be seen in Figure 5.13 there are no distinct peaks differentiating the three sound sources.

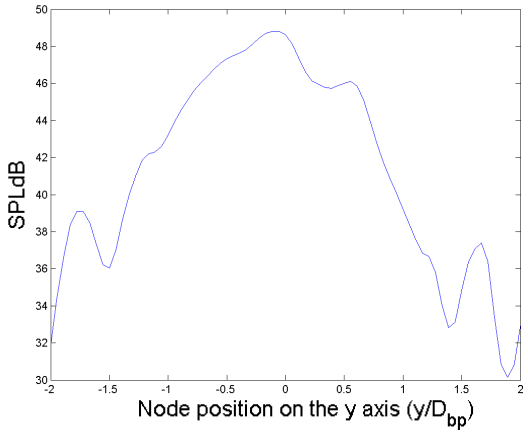

Figure 5.12: Diffraction pattern at 30 kHz of 3 transducers without spacing (adjusted for abberation due to source directivity, smoothed using moving average filter)

The transducers were then separated from centre to centre by 18 mm or 1D_{bp}, making the length of the series span 54 mm. Measurements under the same node positions as before were taken giving the diffraction pattern shown in Figure 5.13.

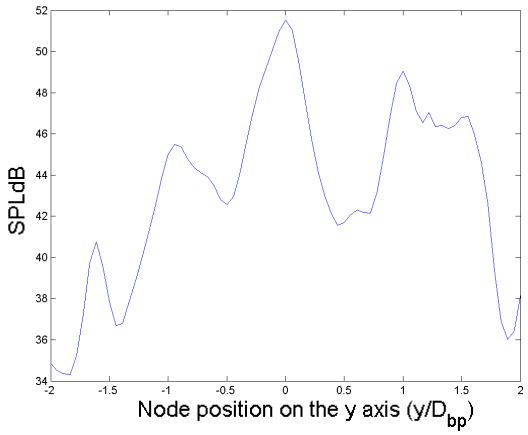

Figure 5.13: Diffraction pattern at 30 kHz of 3 transducers with spacing (adjusted for abberation due to source directivity, smoothed using moving average filter)

Three distinct peaks with a spacing of $1D_{bp}$ between them can be seen in Figure 5.13. This highlights the acoustic mirrors ability to resolve sound sources who's separation distance (which in this case is 18 mm) is greater than the calculated limit of resolution (12 mm). When the separation distance is less than the limit as is the case in Figure 5.13, then it becomes difficult to distinguish between individual sources.

With regards to the smallest wavelength that is resolvable by the acoustic mirror, Fuchs (1978a) required the diameter of the mirror to be large compared to the acoustic wavelength, such that its relationship is defined in Equation 5.10.

$$\frac{D_m}{\lambda_w} \gg 1 \tag{5.10}$$

This implies the acoustic mirror will not work for wavelengths less than 0.456 m, i.e. the frequency limitation for the approach is 745 Hz. The 2D acoustic results discussed in Chapter 8 were collected with a lower frequency limit of 5 kHz (the upper limit was 80 kHz), which is within the resolution range of the acoustic mirror.

5.2 The LDA

5.2.1 Details of the LDA

The LDA system offers high accuracy and high spatial resolution through its small measurement volume and is ideally suited for determining velocity components of a scaled laboratory jet flow.

The Dantec LDA system was used for 2D optical measurements. This comprised

of a Coherent Innova 70C Argon ion laser, Dantec fibre flow and processing box. BSA F80 processor and BSA flow software version 4 were used in processing the data.

The dual head had 45 ° rotation to acquire equal data rates for particles entering the control or measurement volume for both laser beams. The configuration of the two beams including the measurement volume (dx x dy x dz)mm for beam1 (0.1248 x 0.1244 x 1.684)mm, and for beam2 (0.1183 x 0.1180 x 1.597)mm, can be seen in Table 5.1. The size of the measurement volume could potentially be reduced using off axis detection as described by Zhang & Eisele (1995). However with the current equipment this is difficult to set up.

The seeded oil particles used in the flow (as described in Chapter 3) have a 0.8 μm diameter implying that light is scattered by the Mie scattering mechanism (Sorensen & Fischback (2000)). Under this theory, the particles have a complex intensity distribution due to the scattering of the electromagnetic radiation by the particles.

A schematic showing the position of the LDA head and axis of the traverse in relation to the jet rig can be seen in Figure 5.14. The 2D LDA results in Chapter 8 were taken using a dy x dx grid size of $4D_{bp}$ x $10D_{bp}$ (dz=0, positioned at the bullet tip) which corresponded to a traverse movement of 74 x 180 mm.

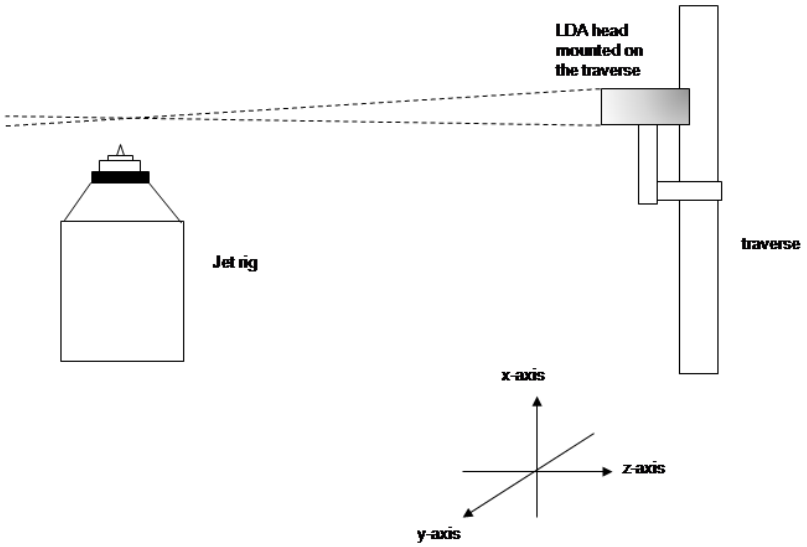

Figure 5.14: LDA and traverse in relation to the jet rig

	Beam1 (green)	**Beam2 (blue)**
Wavelength	514.50 nm	488.00 nm
Focal length	500.00 mm	500.00 mm
Beam diameter at exit	1.35 mm	1.35 mm
Expander ratio	1.95	1.95
Beam spacing	38.0 mm	38.0 mm
Frequency shift	40.0 MHz	40.0 MHz
No. of fringes	35	35
Fringe spacing	3.481 nm	3.302 nm
Beam half angle	4.238	4.238
Probe volume dx	0.1248 mm	0.1183 mm
Probe volume dy	0.1244 mm	0.1180 mm
Probe volume dz	1.684 mm	1.597 mm

Table 5.1: LDA system details

The velocity and turbulence values provided by the BSA software are averaged. The finite size of the probe or measurement volume is subject to velocity bias. If the measurement volume of the LDA probe is too large, the velocity and turbulence measurements can be overstated or understated at different regions of the jet, for example peaks in the turbulence in the shear layer will be overstated. Velocity bias can be reduced by making the finite size of the LDA probe volume smaller. However, making the probe volume smaller than the suggested dimensions by the manufacturer is practically difficult. This could be a consideration for future work, but it would require a consultation with Dantec Dynamics UK.

5.2.2 Refraction

As described by the jet flow experiments of Nogueira *et al.* (2005), there are a number of reasons that can cause a change in the refractive index of air. In a jet flow these are, temperature difference (index reduces as temperature increases), CO_2 concentrations (index increases as CO_2 increases), H_2O concentrations (index reduces as H_2O increases) and pressure variations (index increases as pressure increases).

Nogueira noted no difference in pressure between the ambient and jet air conditions. He did however note a change in H_2O and CO_2 concentrations (Δ2.6% in volume and Δ2.4% in volume respectively) which was attributed to the heating of the jet.

As the jet is unheated in this project, the temperature difference and subsequently the changes in the H_2O and CO_2 concentrations between the ambient and jet flow is negligible. The pressure in the ambient air and core and bypass

jet flows were measured, and the maximum difference found to be 0.235 atm. In consultation with Robert Jaryczewski, Engineer from Dantec Dynamics UK however, it was concluded that any refraction or deviation of the LDA beams would be very minimal.

Potential further work might include the measurement of the deviation of the LDA beams by means of a camera, focussed onto measurement volume. The measurement point's position would be measured with the jet turned on, and then off.

5.3 Repeatability of measurements

Repeatability of measurements is important in experimental work as it helps ascertain whether a set of results are a true reflection of the experiment. It also gives an indication as to the reliability of the measurer and the equipment. Repeatability shows the variation in measurements taken by the same observer using the same experimental set up, measurement procedure under the same conditions and over the same time interval.

A simple way to show repeatable results as demonstrated by Bridges & Hussain (1995) and Viswanathan (2006b) is to overlay two plots of measurements. This is a quick way to visually show their similarity, however to quantify the measurement variability, statistical methods are used.

Using the experimental set up for the principle investigation as detailed in Chapter 8, acoustic measurements were taken along the centre line of the co-flowing

jets using the core cowl and bypass cowl nozzles. The jets ran on condition with the acoustic mirror mounted on the traverse. Measurements were taken from the bullet tip at $0D_{bp}$ to $10D_{bp}$ downstream with 1 mm spacing generating 180 measurement points. Once the data was collected, the experiment was reset and the line measurements were taken again. They were respectively labelled sample A and sample B.

The range of frequencies recorded at each data point was 5 kHz to 80 kHz in steps of 256 Hz. When overlayed, there was good visual agreement at each frequency step between the two samples. An example at 10 kHz is shown in Figure 5.15. The spectra of the two samples is similar with sample B being within the range of -0.22% to 0.20% of sample A. The maximum difference between the two samples is 0.22 dB.

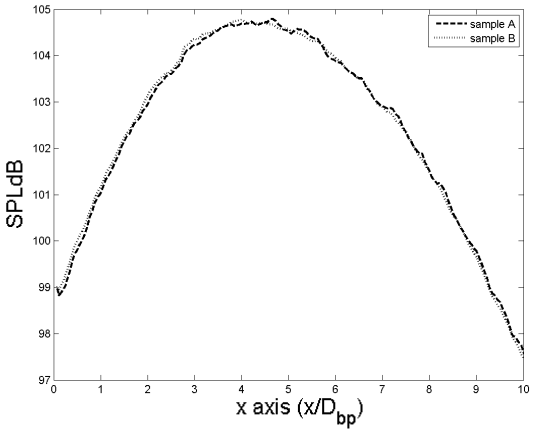

Figure 5.15: Overlay of sample A (dash) and sample B (dot)

As the data is not quite normally distributed (confirmed by plots and by using a Kolmogorov-Smirnov test for normality) a suitable non-parametric test is required. The Wilcoxon signed-rank test is a non-parametric test used for repeated measures. Under the null hypothesis that there is no difference between the paired data, it tests to see how acceptable the actual observed median dif-

ference is compared to the expected median difference of zero. This is expressed by a probability value or p-value which takes values between 0 and 1. If the p-value is less than a given critical value (usually 5%) then the observed median differences are not due to chance and the null hypothesis is rejected. In the case of Figure 5.15, the Wilcoxon signed-rank test at a 95% significance level or 5% critical level, gave a p-value of 0.54, with typical p-values across the whole data being 0.42. As this is larger than the 0.05 critical level, the null hypothesis is accepted supporting repeatability.

Repeatability of the LDA data can be checked under the same process. The experimental set up for LDA as detailed in the principle investigation in Chapter 8 was used to collect velocity measurements of the centre line of the co-flowing jets on condition. The measurements were again taken from the bullet tip at $0D_{bp}$ to $10D_{bp}$ downstream with 1 mm spacing generating 180 measurement points. Two sets of line measurements were taken.

Under the null hypothesis that the median difference between the paired data is zero, the Wilcoxon signed-rank test at the 95% significant level gave a p-value of 0.07. As this is above the critical level of 0.05, the null hypothesis is accepted; there is reasonable agreement between repeated measures.

The lower LDA p-value compared with the acoustic p-value is an expected result as the measurements taken with the LDA equipment are a lot more accurate and precise and the control volume is smaller. This makes each measurement more sensitive to small (random) changes in experimental conditions or location. The acoustic measurements are averaged over a larger spatial volume, therefore small misalignments of the traverse during repeated measures can still yield similar

acoustic results.

5.4 Absorption and reflection of the acoustic foam

Sound waves reflecting off boundaries such as walls, floors and ceilings can corrupt the acoustics measured by microphones. To minimize this effect, the anechoic chamber was constructed by padding the walls, floor and ceiling with acoustic foam sensitive to the frequencies of interest in this project. The foam increased the sound absorbed by the walls and consequently reduced the reflected sound.

Tests were performed to quantify the effects of absorbtion and reflection of sound waves using acoustic foam.

5.4.1 Absorption test

A microphone (labelled mic1) was placed on the floor, in the corner of the anechoic chamber, 2 m away from the jet nozzle. Both streams were run on condition and acoustic measurements were recorded. Acoustic foam was then placed in the same corner of the anechoic chamber such that it housed mic1. The jets were run on condition and the recordings were taken again. The results for both mic1 without surrounding foam and then with surrounding foam can be seen in Figure 5.16.

These tests were then repeated with mic1 now placed on the floor in the opposite corner of the anechoic chamber. In this corner, the aluminum radial microphone frame stood in between mic1 and the jet nozzle. The results can be seen in Figure 5.17.

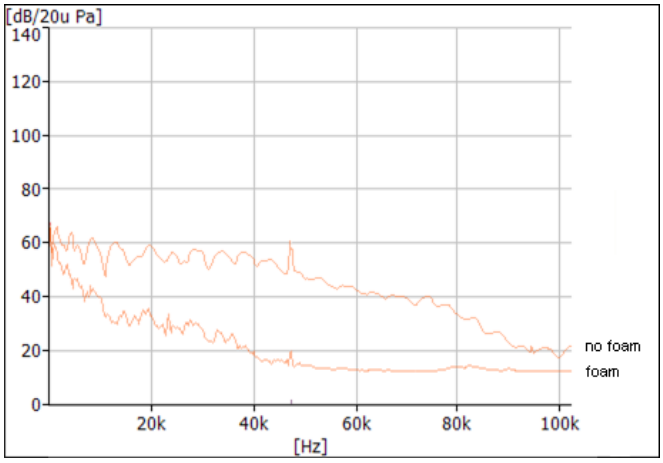

Figure 5.16: Absorption test 1

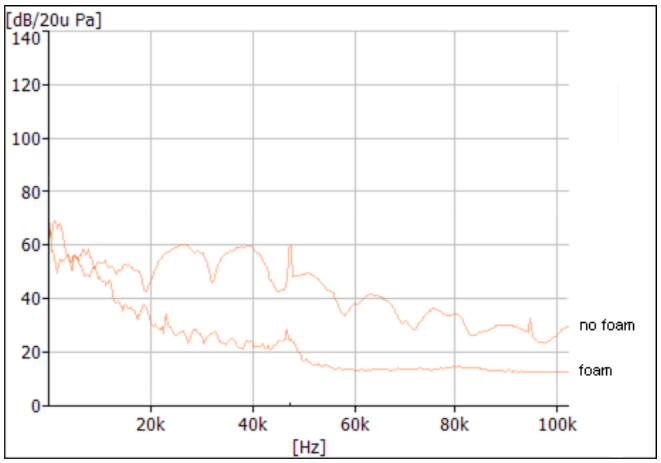

Figure 5.17: Absorption test 2

Both graphs show a significant reduction in the SPLdB levels when mic1 is housed in acoustic foam. Figure 5.16 shows a more even and significant reduction in the sound pressure levels as there is no object interference. The reduction spans the frequency range, with the largest reductions in excess of 25 dB, occurring in the central frequency range of 40 kHz to 60 kHz. Thus supporting the notion acoustic foam works very well in absorbing the sound waves.

5.4.2 Reflection test

A test was performed to observe how well the acoustic foam reduces the reflection of sound waves. Using Snells Law of equal incident and reflected rays, the experimental set up was arranged as shown in Figure 5.18.

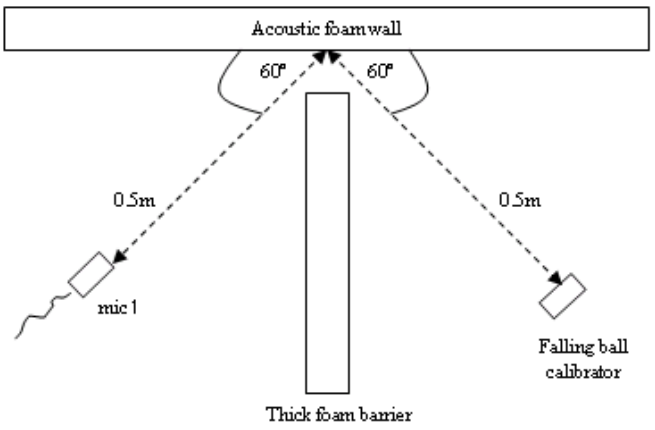

Figure 5.18: Reflection test 1

A falling ball calibrator (PSQ 101A Castle Associates) was used to generate a directional tone. A sheet of plywood surrounded by acoustic foam either side, were held together to act as a thick foam barrier and was used to directly block the acoustic field between the falling ball calibrator and mic1. This allowed mic1 to record the sound wave from the falling ball calibrator by reflection off the acoustic foam wall. The difference this barrier makes to the SPLdB can be seen in Figure 5.19.

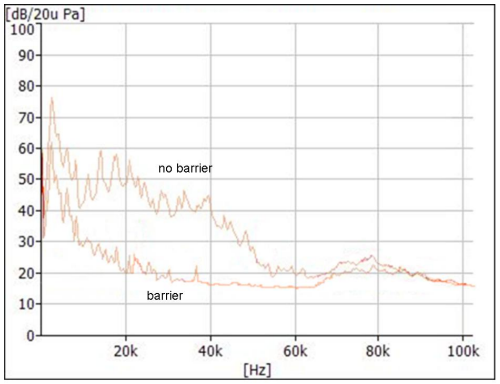

Figure 5.19: Sound recorded with the barrier and no barrier present

A steel metal plate was then placed at the point of reflection on the foam wall and the acoustic measurements were recorded again. The difference between these two results shows the importance of having acoustic foam in reducing sound reflection and can be seen in Figure 5.20.

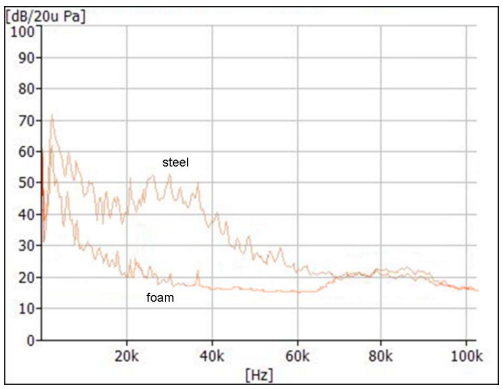

Figure 5.20: Sound reflection from the Acoustic foam wall and steel plate

Both Figure 5.19 and Figure 5.20 show a clear reduction in the SPLdB by using a barrier and by using acoustic foam instead of a more reflective surface. This reduction is as large as 20 dB in 20 kHz to 40 kHz range.

At high frequencies, there is little change but this is as expected since the falling ball calibrator doe not operate at these frequencies. The sound pressure level at

these high frequencies is of the order 20 SPLdB and is comparable to background static noise.

CHAPTER 6

Asymmetry of the jet

Far field acoustic measurements of jets are often taken by placing microphones in a desired array such as radial, inline or staged. These measurements are dependent on the acoustic pressure field which radiates out to the far field. Microphones placed in the near field are subjected to different conditions, namely hydrodynamic pressures.

With an inline or staged arrangement in the far field, the microphones at best face half of the radial axis of the jet flow. This is deemed as sufficient acoustic coverage on the assumption that the jet exhibits radial acoustic symmetry. This is an important assumption when applying acoustic theories to acoustic measurements.

Testing for acoustic symmetry is a vital point for consideration for all aeroacoustic jet flows as it helps determine the experimental bias in the flow. That is, it helps determine the variation in the noise emitted from one side of the axial jet to another. If the variation is large (i.e. the jet is asymmetric), this would affect the far field measurements as microphones facing one side of the jet would have different recordings to microphones facing another side of the jet.

In experiments it is hard to produce a jet that exhibits perfect flow and acoustic symmetry due to a number of reasons such as manufacturing, material imperfec-

tions and experimental limitations. This chapter looks at the scaled co-flowing jet on condition and examines its acoustic asymmetry and flow asymmetry.

6.1 Acoustic asymmetry

6.1.1 Experimental set up

An experiment was conducted using both the core and bypass flows with cowl nozzles. Four B&K 1/4" microphones were placed in an arrangement about the axial direction of the jet rig as shown in Figure 6.1. The distance from each microphone to the tip of the bullet was equated using a swing arm device. Once the microphones were in position, the swing arm was removed.

The co-flow was run on condition and measurements were recorded by the B&K PULSE system. The SPLdB was recorded with a reference pressure of 20 μPa. Each recording comprised of a 10 second burst which was split by the PULSE system into 5 dat files of 2 second duration each. The acoustics recorded by each dat file contained 526,336 data points. The time step was dt = 3.81470 μs with the speed of sound being c$\approx$340 ms^{-1}.

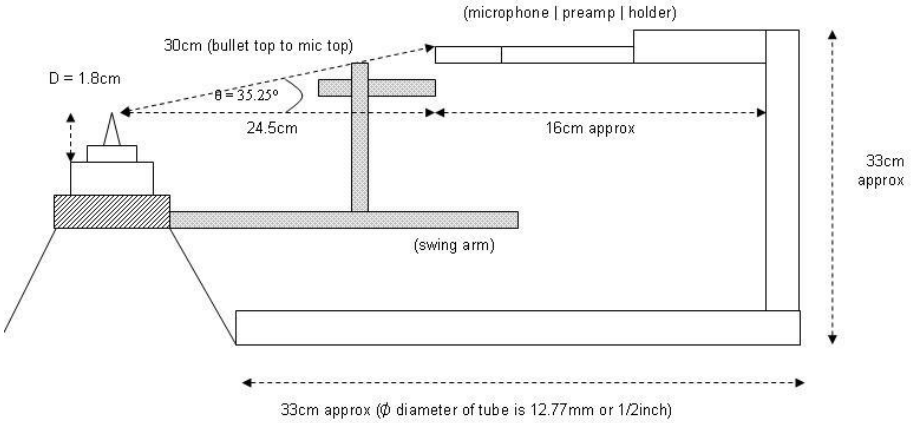

(a) Side view of the microphone set up

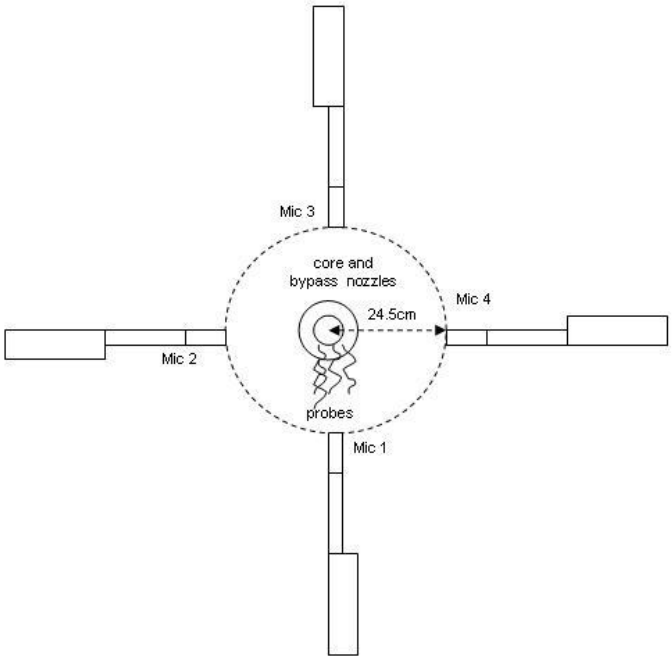

(b) Birds eye view of the microphone set up

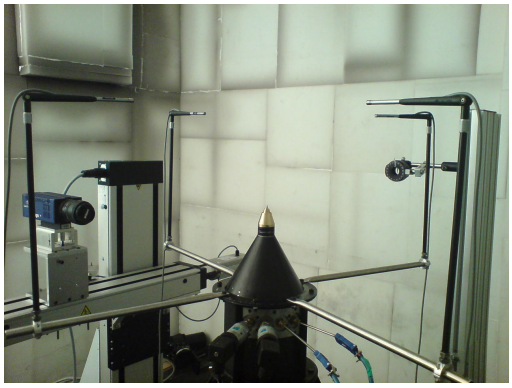

(c) Microphone set up

Figure 6.1: Microphone arrangement for the acoustic symmetry experiment

6.1.2 The raw data

The first 2 second dat file for each of the four microphones was used to see the raw time series plots, shown in Figure 6.2.

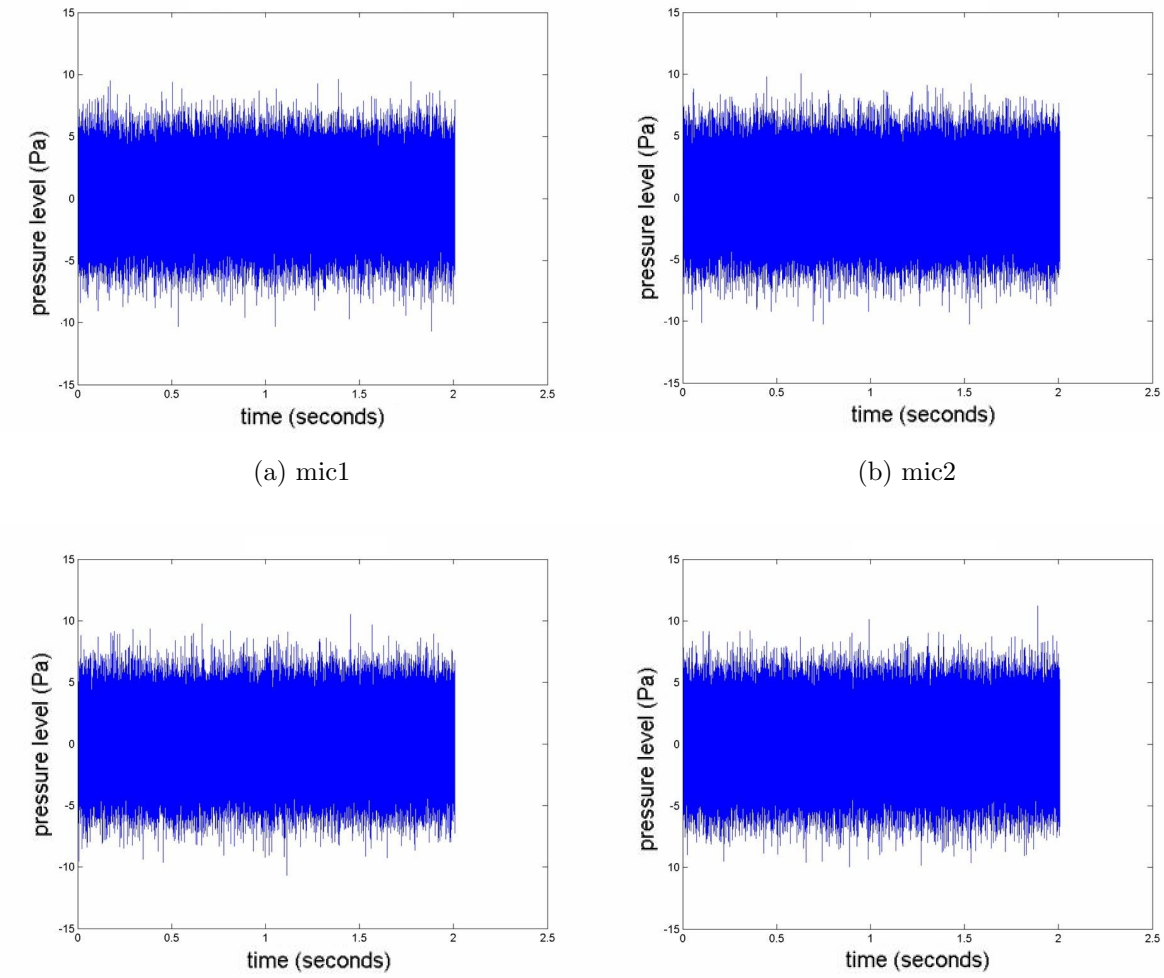

(a) mic1

(b) mic2

(c) mic3

(d) mic4

Figure 6.2: Time series plots for all four microphones

A closer inspection can be viewed in Figure 6.3 where 201 data points were taken from the middle of the data set (from data point 250,000 to 250,200). The signals from mic1 and mic2 were superimposed to give an impression of the sample.

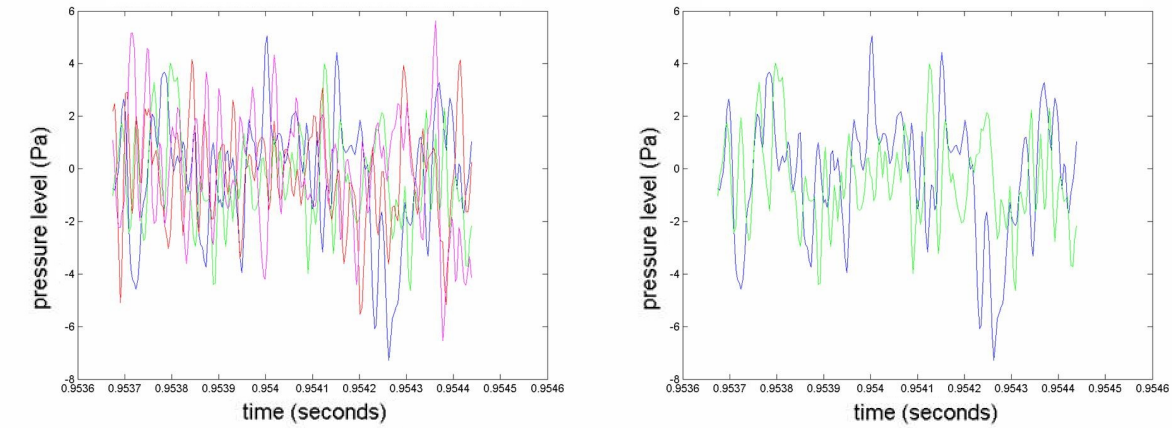

(a) mic1,mic2,mic3,mic4 (b) mic1,mic2

Figure 6.3: Time series plots for 201 data points

mic1 = blue, mic2 = green, mic3 = red, mic4 = magenta

Generally speaking (from a macro point of view), the signals from mic1 and mic2 have a similar shape, indicating there may be some level of correlation between them. However the raw time series data does contain the pressure readings of all of the frequencies recorded by the microphones and therefore contains noise. The time lag between different microphone data sets can be found by firstly filtering the signal to remove noise and unwanted frequencies, partitioning the data into smaller samples and then applying the cross correlation technique.

6.1.3 Filtration

A band width filter of 48.0 kHz - 48.5 kHz (arbitrarily chosen from the mid-range of frequencies) was used to narrow the frequency range for cross correlation of the samples. The FFT and filtered data sets are shown in Figure 6.4 and Figure 6.5.

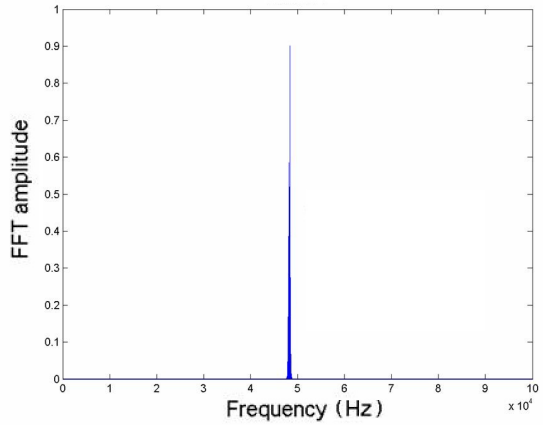

Figure 6.4: FFT of filtered data

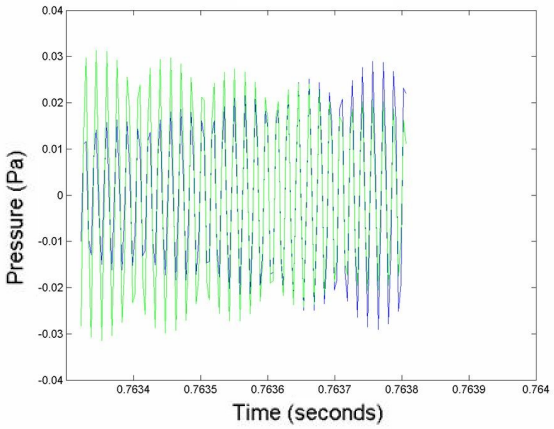

Figure 6.5: Time series plot of the filtered data

6.1.4 Suitable sample size

Working in terms of 2^n (where $n \in \mathbb{N}$) to mange the calculations more effectively, the first $2^{17} = 131,072$ data points from each dat track was used to draw time lag statistics. It was smaller and hence less computationally expensive than the full track while still being sufficiently large enough to compile statistics.

At 48.250 kHz, the period for one wavelength is 2.07253 μs. This accounts for 5.4 dt. Therefore as 6 data points contains a full wavelength, a sample size of $2^4 = 16$

was chosen. The cross correlation technique was first performed on the sample from data point 1 to 16 which was denoted as frame 1. A data point shift of 4, provided the next frame. That is, data point 5 to 21 was frame 2. The discrete shift or slide was chosen such that it was small enough to capture differences in the time lags between frames and not be computationally exhausting. This slide continued for the 131,072 data points, producing 32,765 frames.

6.1.5 The correlation of signals

Cross correlation is a technique used to see the similarity or how well related two data sets are and is defined by Equation 6.1.

$$Corr(f_v, g_v)_{m_a} = \sum_{n_a=0}^{N-m_a-1} f_{v,n_a+m_a} g^*_{v,n_a} \tag{6.1}$$

where m_a, n_a, $N \in \mathbb{Z}$, $N > 1$ and f_v, g_v are vectors of length N containing the signal data. The function is used to find the relative time lag between signals.

With the chosen sample size and frame shift, the largest cross correlated time lags in each frame for each combination of microphone pairs was calculated, the results of which are plotted in Figure 6.6. For each microphone pair, the most occurring time lag values appear to be -1, 0 and 1 dt.

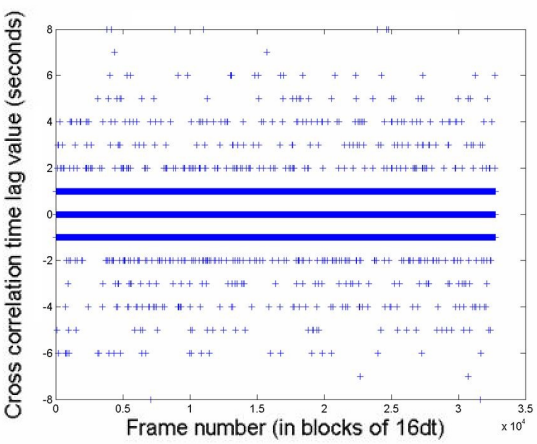

(a) mic1,mic2

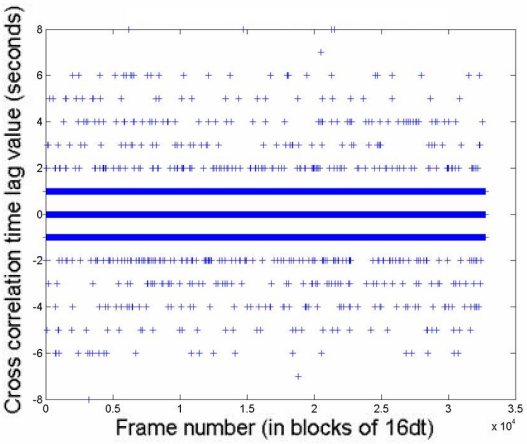

(b) mic1,mic3

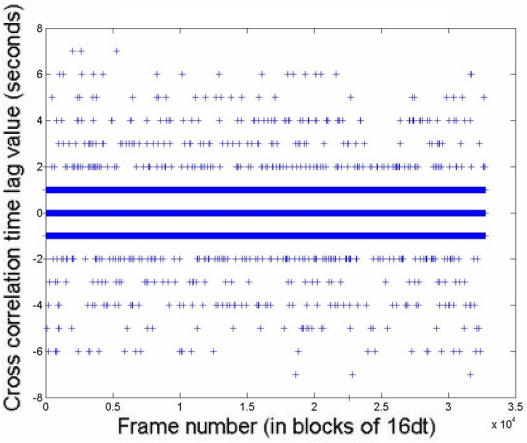

(c) mic1,mic4

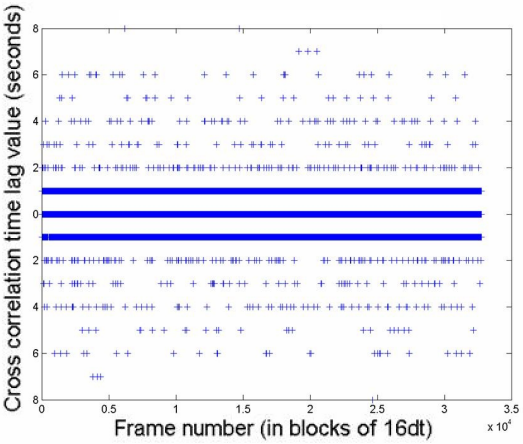

(d) mic2,mic3

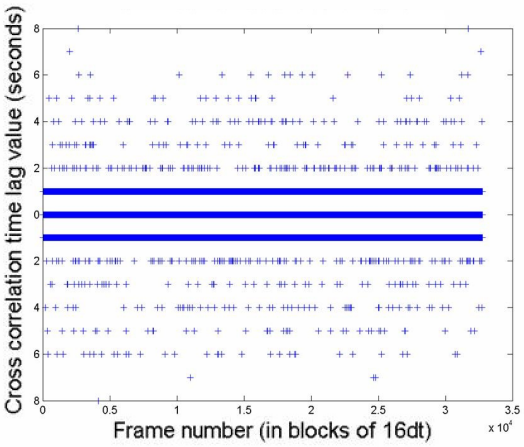

(e) mic2,mic4

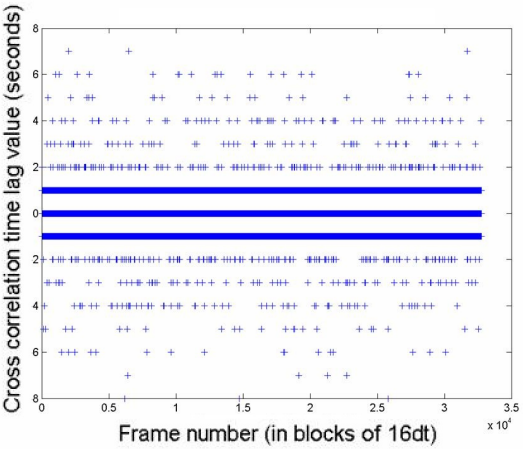

(f) mic3,mic4

Figure 6.6: Cross correlation of microphones using a sliding window

A count of time lag values from all of the cross correlated data for all microphone pairs confirms the observation and can be seen in Figure 6.8 with tabulated results in Figure 6.7.

Correlated mics	No. of time lags with values ≥ 1	= 1	= 0	= -1	≤ -1	Total	% of time lags = -1, 0, 1
mic1 mic2	301	5,842	20,154	6,154	314	32,765	98.123
mic1 mic3	293	6,308	19,880	5,965	319	32,765	98.132
mic1 mic4	302	6,152	19,861	6,146	304	32,765	98.150
mic2 mic3	289	6,382	19,907	5,874	313	32,765	98.163
mic2 mic4	289	6,283	19,976	5,905	312	32,765	98.166
mic3 mic4	302	6,029	19,898	6,219	317	32,765	98.111

Figure 6.7: Statistics of the cross correlated mic data

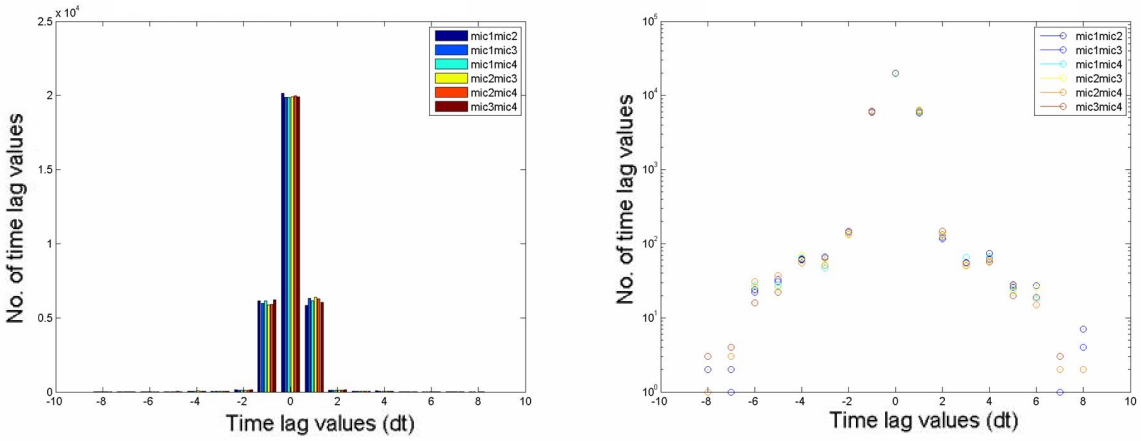

(a) Linear scale

(b) Log_{10} scale

Figure 6.8: Count of time lag values for all mics

The most frequently occurring time lag value is 0, with the majority contained in the set $\{-1, 0, 1\}$, which strongly indicates a low level of acoustic asymmetry.

6.1.6 Sound pressure levels of the data sets

Low levels of acoustic asymmetry is also supported by observing the sound pressure level across the frequency range of the microphones as shown in Figure 6.9.

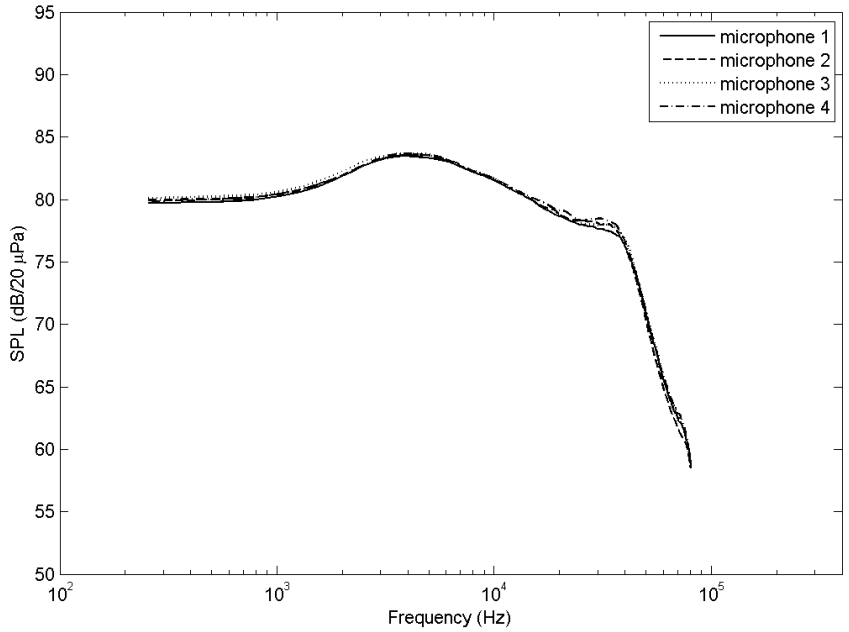

Figure 6.9: SPLdB vs Frequency for all mics

All four microphones present a good clean curvature in the graph without the presence of spikes (such as discrete tones). The sound pressure levels measured across the frequencies by each microphone are consistent with each other. Further indicating the presence of acoustic symmetry.

6.2 Flow asymmetry

The work in this section was done in collaboration with Dr Paul Dunkley, School of Engineering, University of Warwick.

6.2.1 Experimental set up

The jet rig was run on condition with the oil seeded flow exiting both the core and bypass nozzles. The Dantec 2-dimensional LDA system was used to take flow

field measurements with the LDA head mounted on the traverse and rotated 45 ° to allow higher data rates while running in coincidence. Running in coincidence was required to provide Reynold's stress values.

A polar grid was implemented with the radius varying from $0D_{bp}$-$1D_{bp}$ ($0D_{bp}$-$1.5D_{bp}$ at $10D_{bp}$ downstream) at 1 mm interval with the radial angle set at 15 °, giving 456 data points (672 data points at $10D_{bp}$). 10,000 samples were taken at each point. Cross sectional (y,z) measurements were taken at $1D_{bp}$,$2D_{bp}$,$3D_{bp}$,$4D_{bp}$,$5D_{bp}$ and $10D_{bp}$ downstream (x-axis). Vertical plane measurements were also taken from y=-$0.8D_{bp}$ to y=$0.8D_{bp}$ and x=$1D_{bp}$ to x=$5D_{bp}$. An average data rate of 8.5 kHz was achieved at $5D_{bp}$ downstream with a peak of 19 kHz. An example of the measurements taken can be seen in Figure 6.10.

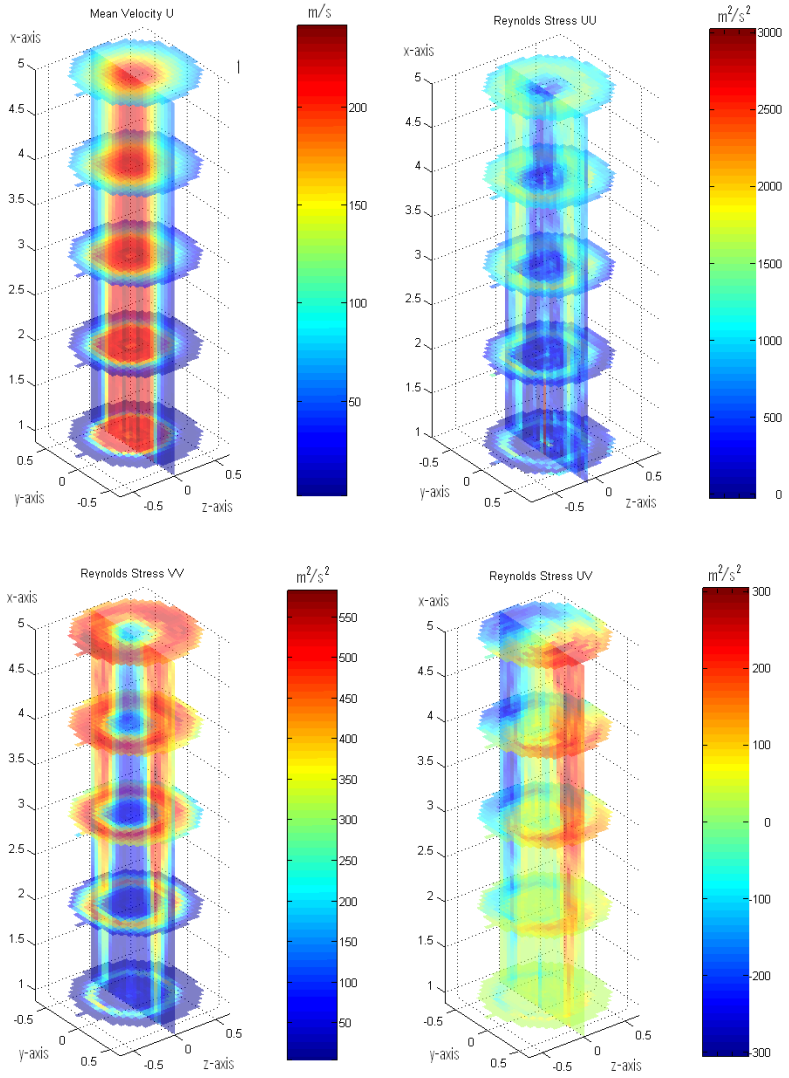

Figure 6.10: 3D flow plots

6.2.2 Circle fitting

The raw LDA data was imported into Matlab and matrices of radius vs angle were produced. For each set of angle profiles a polynomial fit was generated (typically 6th order). Arbitrary values of velocity were chosen and the corresponding radii from the polynomial fits were calculated. The radius and angle values for the velocities were converted back into cartesian coordinates and inputted into the circle fitting program. The circle fitting code was adapted from the NPL

Eurometros code which uses a Gauss-Newton non-linear least-squares approach. The y,z positions of, for example, axial velocity equal to 200 ms^{-1} are inputted into the code. A converged circle fit is produced with the center position, radius and variance information as outputs.

Figure 6.11 shows the result of the centering process for the mean axial velocity $5D_{bp}$ downstream. The fitted circles are overlaid onto the polynomial data. The blue 'x' represent the centres of the fitted circles.

Table 6.1 shows the deviation in mm from the central axis at (y,z)=(0,0). The results show that the centre of the circles for each of the velocity values is less than 0.11 mm from the central axis. The size of the LDA volume limits measuring the centre more accurately. The results therefore show that for the velocity values chosen, the fitted circles are slightly non-concentric around the central axis.

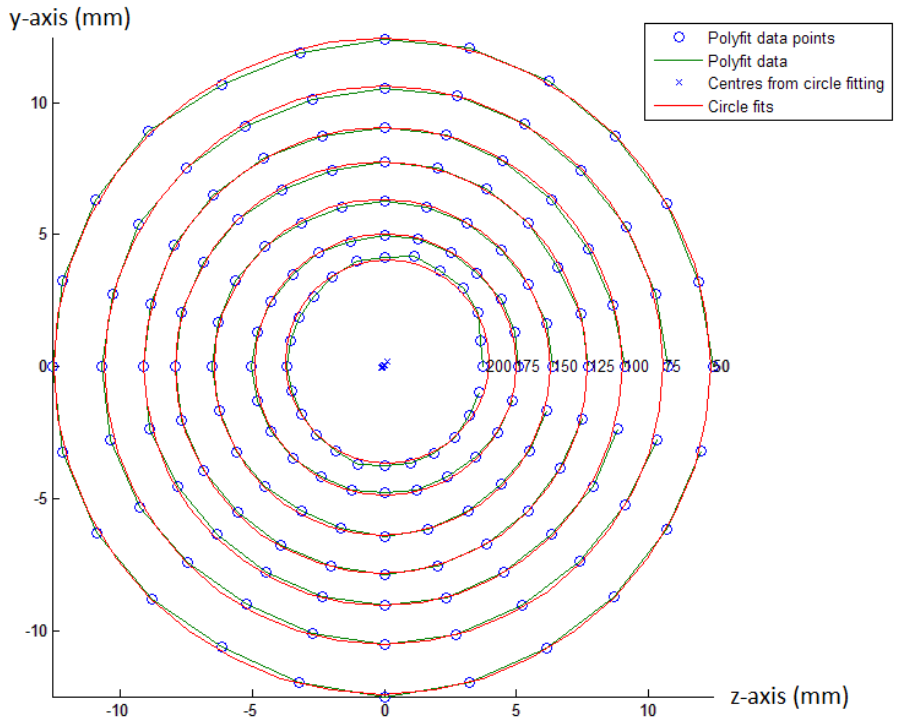

Figure 6.11: Circle fitting mean axial velocity 5 diameters downstream

velocity (ms^{-1})	centre (y,z) (mm)
50	(-0.09, 0.02)
75	(-0.02, 0.03)
100	(-0.05, 0.01)
125	(-0.11, -0.03)
150	(-0.07, -0.03)
175	(0.03, 0.07)
200	(0.10, 0.2)

Table 6.1: Variation in mean axial velocity from the centre (0,0)

The same technique has been completed for RMS squared (Reynolds stress UU) as shown in Table 6.2 and Figure 6.12. Two values for y and z appear for each

Reynolds stress value. The first value corresponds to the circle fit with the a larger radius.

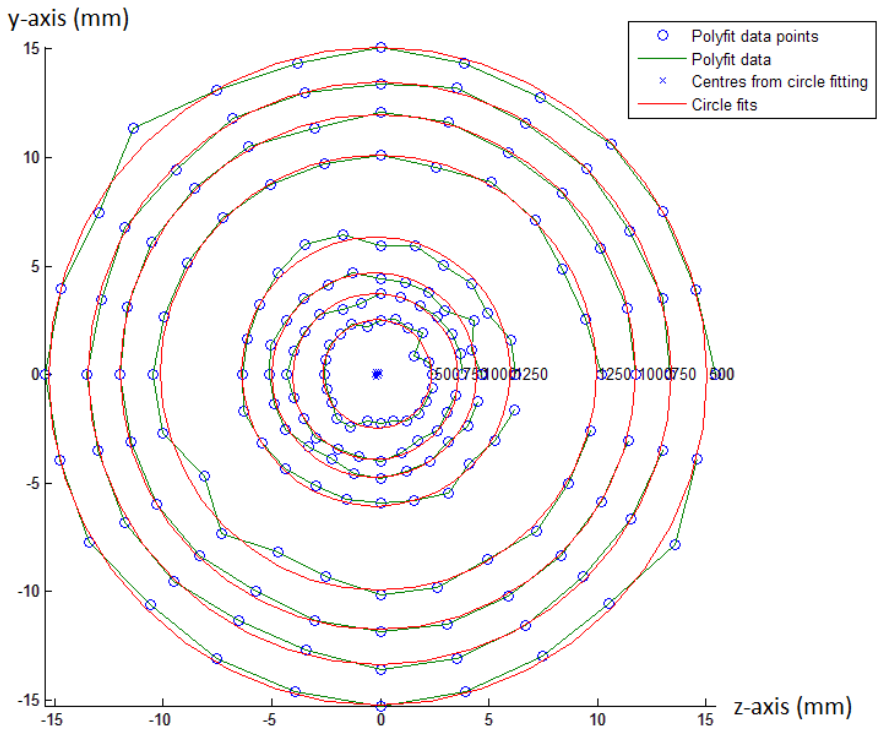

Figure 6.12: Circle fitting RMS squared 5 diameters downstream

Reynolds stress (m^2s^{-2})	centre (y) (mm)	centre (z) (mm)
500	-0.10, -0.12	0.005, 0.03
750	-0.04, -0.22	0.01, -0.08
1,000	-0.11, 0.20	0.12, -0.006
1,250	-0.08, 0.20	0.10, 0.13

Table 6.2: Variation in RMS from the centre (0,0)

6.2.3 Contour area

The LDA data in this case is interpolated using nearest neighbour to generate contours of the parameters: mean velocity, RMS and Reynolds stress. The con-

tour properties are then analyzed within Matlab supplying area, centre (based on centre of mass), eccentricity and major and minor axis. In contrast to the circle fitting method where it is assumed that the jet is circular, the area contour method does not. The values of major and minor axis and eccentricity provide details of the shape of the jet and its orientation. The definition of eccentricity ε is given by Equation 6.2, where $\varepsilon = 0$ is a circle, $0 < \varepsilon < 1$ is an ellipse and $\varepsilon = 1$ is a parabola.

$$\varepsilon = \frac{centre\ of\ major\ axis\ to\ foci}{semi\ major\ axis} \tag{6.2}$$

Figure 6.13 shows the results of the contour plots at 5 diameters downstream for axial and horizontal velocity and axial and horizontal rms. The contour area properties have been completed on the axial velocities. Table 6.3 shows the statistical results for $3D_{bp}$, $4D_{bp}$, $5D_{bp}$ and $10D_{bp}$ from the axial velocity data.

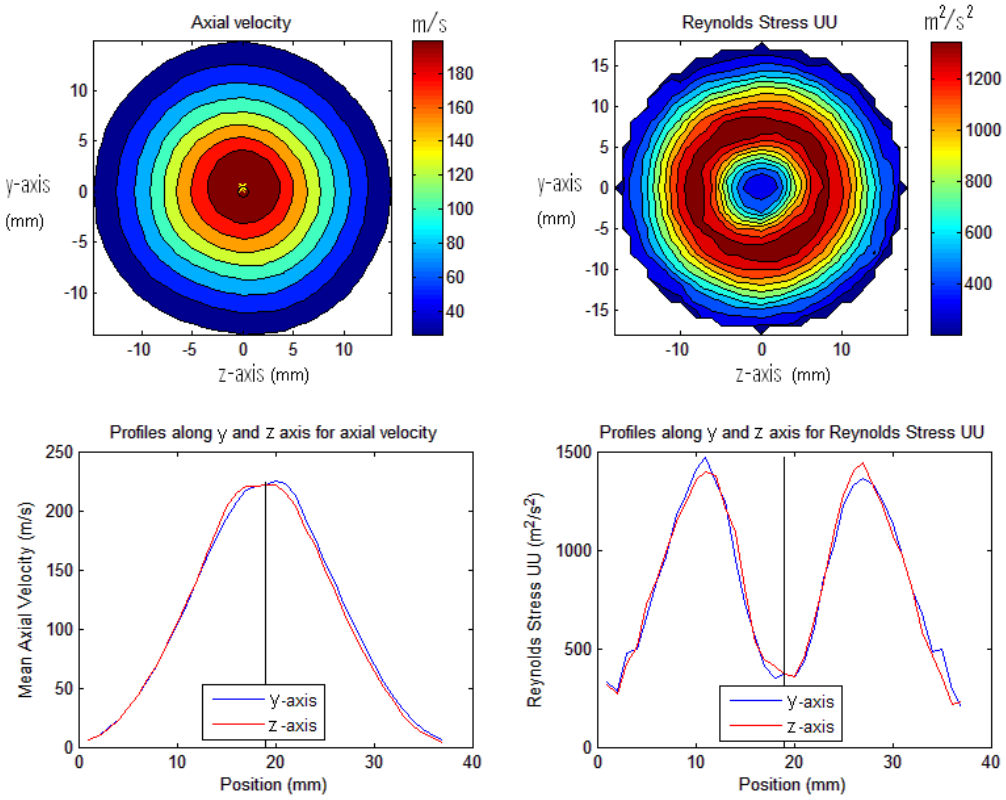

Figure 6.13: (Top) Contour plots, (Bottom) Profile plots

Diameter downstream	mean centre position (mm)	mean standard deviation (mm)	mean eccentricity
$3D_{bp}$	(0.10, -0.15)	(0.17, 0.13)	0.17
$4D_{bp}$	(-0.01, -0.20)	(0.08, 0.09)	0.23
$5D_{bp}$	(-0.07, -0.25)	(0.07, 0.09)	0.24
$10D_{bp}$	(-0.62, -0.40)	(0.13, 0.14)	0.20

Table 6.3: Statistics for $3D_{bp}$-$10D_{bp}$ contour method from axial mean values

6.3 Concluding comments

The purpose of this chapter was to look at the acoustic asymmetry and flow asymmetry of the jet. The acoustic asymmetry of the jet was identified by filtering the broadband signal to a small known bandwidth and then cross correlating the samples contained in that range. This effectively filtered out noise allowing greater accuracy in determining the time lags between microphone signals.

A low level of acoustic asymmetry was found with at least 98% of the time lag values taking the values -1 dt, 0 dt or 1 dt. The low level of acoustic asymmetry was further supported by plotting the SPLdB against the frequency range for all four microphones. The line plots were reasonably smooth and overlapped considerably, again supporting minimal acoustic asymmetry.

Low levels of flow asymmetry was also found using circle fitting and contour mapping. This was supported by the low mean deviations and mean eccentricity values (from 0.17 to 0.24) indicating slight non-concentricity.

CHAPTER 7

Statistical approach for determining acoustic asymmetry

The work in this chapter supports existing experimental testing on acoustic asymmetry by offering an additional technique for validation. An alternative statistical approach presented, which looks at the statistical distribution of the acoustic measurements.

This chapter starts by looking at the distributional characteristics of the acoustics from the co-axial jet and then fitting known distributions to the empirical data. The probability distribution function of the acoustic data is found using a generalized 3 parameter equation. The model is then developed into a 4 parameter equation to better capture asymmetry and skewness of the data set. The statistical distribution of a jet flow can be used in quantifying the acoustic intensity of a noise source and in more practical testing, can be used to investigate the acoustic symmetry of a jet by comparing the differences in distributions from a radial array of microphones placed equidistance from the central jet axis.

The importance of this work lies in its statistical approach to exploring properties of a jet flow by encouraging interdisciplinary techniques.

7.1 Introduction

The acoustic data measured from the jet rig is an empirical time series data set recording the acoustic pressure fluctuations in the jet flow. Statistical modelling of acoustic signals, or more specifically speech signals has been investigated by a number of researchers including Shin & Chang (2005), and Stacy (1962; 1973). They attributed the characteristics of their acoustic data to the Gamma Distribution, a known continuous distribution, and used appropriate estimators, such as Maximum Likelihood Estimate, in solving the distributional function. This is a popular estimator used by other researchers in the same field such as Wingo (1987) and Gazor & Zhang (2003).

As the statistical distribution of the acoustic pressure fluctuations in the jet flow is unknown, the data set must be investigated to find its probability density function (pdf). This is a significant fundamental property which is required for performing statistical tests and to understand the statistical characterization of the flow.

7.2 The data

The experimental set up used to collect acoustic data sets was the same arrangement as the tests for the acoustic asymmetry of the jet. The microphone array was placed about the axial direction in a square arrangement as shown in Figure 7.1 and Figure 7.2 and both co-flow jets were run on condition. Five successive tracks (dat files) of 2 second duration each were recorded by the PULSE system, each containing 526,336 data points, with a time step dt = 3.81470 μs between points.

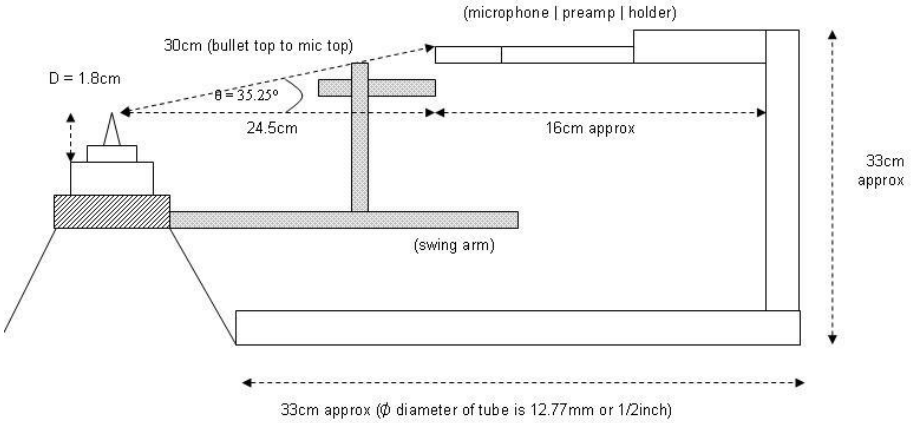

Figure 7.1: Side view of experimental set up

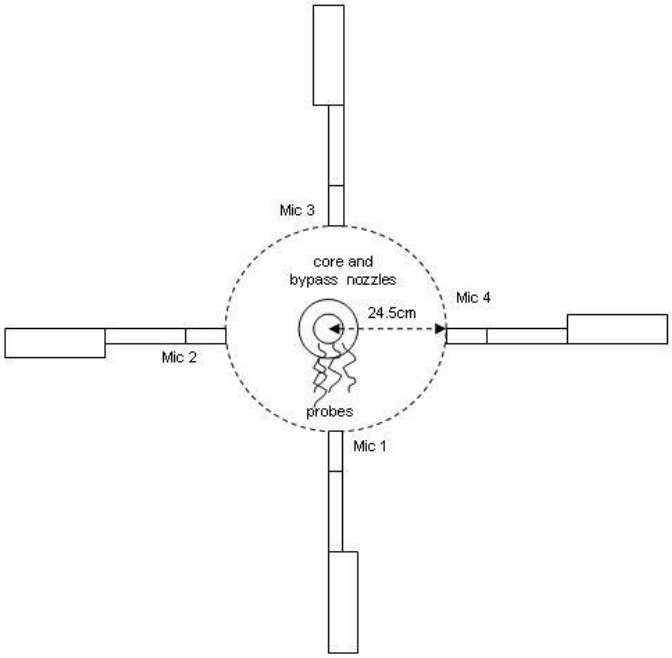

Figure 7.2: Top view of experimental set up

The data recorded by mic1 is reviewed first. Plots of the raw time series data from track1 (2 second duration) is shown in Figure 7.3.

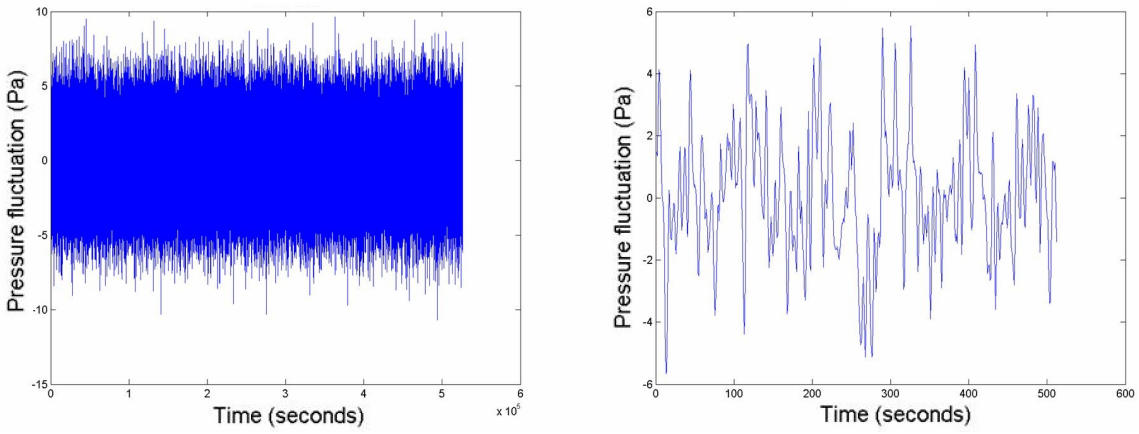

(a) full data set, 526,336 data points

(b) first 512 data points

Figure 7.3: Time series plots of raw acoustic data from mic1

7.3 Distributions and probability plots

The probability associated with an interval of values is represented by the area under the curve of a pdf, where the conditions for a function $f_x(x)$ to serve as a pdf are shown in Equation 7.1.

$$\begin{aligned} -\infty \leq x \leq \infty \\ f_x(x) \geq 0 \\ \int_{-\infty}^{\infty} f_x(x)dx = 1 \end{aligned} \tag{7.1}$$

The cumulative distribution function (cdf) is a continuous, monotonically increasing function defined by Equation 7.2.

$$\begin{aligned} F_x(x) &= P(x \leq x) \\ F_x(x) &= \int_{-\infty}^{x} f_x(t)dt \end{aligned} \tag{7.2}$$

The probability plots of the acoustic data were plotted against a number of known distributions to see the mutual deviation of one distribution versus the other with the aim of finding a general fit. This was done by looking at the Probability-Probability plots (P-P plots).

P-P plots compares the cumulative distribution function of two random variables. In this case, one random variable is from the empirical acoustic data and the other is from a selected parametric distribution. P-P plots are used to compare data sets to see if they come from the same distribution.

They comprise of a scatter plot of the empirical data against a line plot of the parametric distribution, with the probability values on the y-axis and and the raw data values on x-axis of the plot. If the scatter plot exhibits linearity, it comes from the same family of distribution as the line plot data set. The main advantages of using P-P plots are that the sample sizes do not have to be the same size and the general shape of the P-P plots are resistant to changes in scale or location of the data sets used.

For certain distributions such as the Weibull, Rayleigh, and Lognormal, P-P plots can only be generated if the data is greater than zero. As the pressure values in the acoustic data set appears to fluctuate about zero, an adjustment needs to be made for the negative values. There are two options available to make the data

greater than zero,

a) Split the data into two sets; positive and negative, as done by Malevergne *et al.* (2006). Then multiply the negative returns by -1 creating two 'positive' data sets.
b) Take the absolute values of full data set, making all of them positive.

Both of these provide very similar information about the distribution of the data set. If we follow the work of Malevergne *et al.* (2006), who opted for option a), then the corresponding P-P plots can be seen in Figure 7.4 to Figure 7.8 (note, the linear dashed line represents the chosen distribution and the blue crosses represents the acoustic data).

Normal distribution: $pdf = \frac{1}{\sigma\sqrt{2\pi}} exp(-\frac{(x-\mu)^2}{2\sigma^2}), \qquad x, \mu \in \mathbb{R}, \sigma^2 > 0$

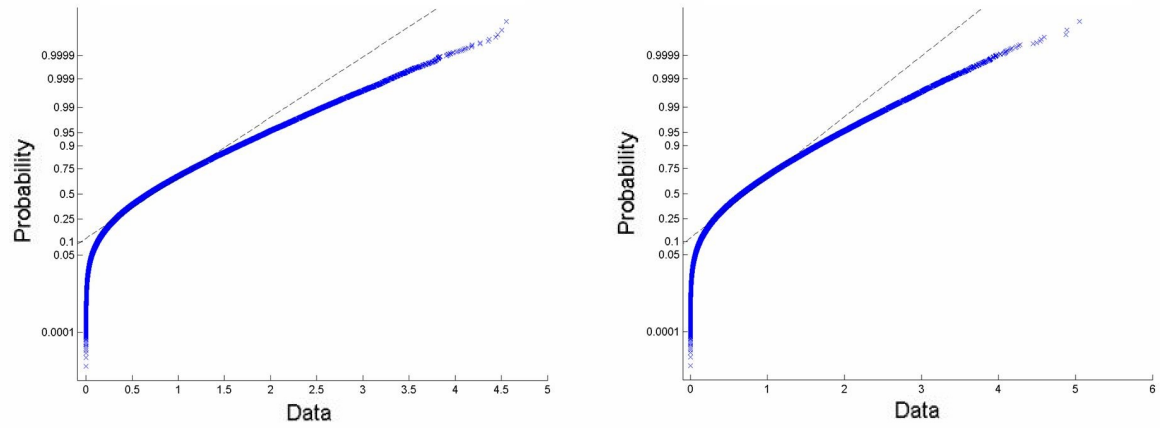

(a) absolute values of mic1 positive subset (b) absolute values of mic1 negative subset

Figure 7.4: P-P plots using the Normal distribution

Lognormal distribution: $pdf = \frac{1}{x\sigma\sqrt{2\pi}} exp(-\frac{(ln(x)-\mu)^2}{2\sigma^2})$

$x \in [0; \infty), -\infty \leq \mu \leq \infty, \sigma > 0$

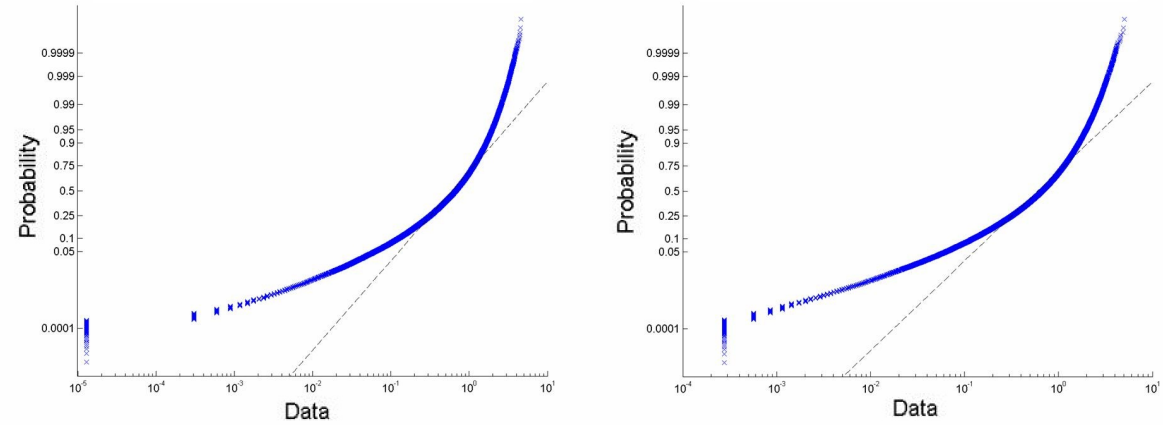

(a) absolute values of mic1 positive subset (b) absolute values of mic1 negative subset

Figure 7.5: P-P plots using the Lognormal distribution

Rayleigh distribution: $pdf = \frac{x}{\sigma} exp(-\frac{x^2}{2\sigma^2}), \qquad x \in [0; \infty), \sigma > 0$

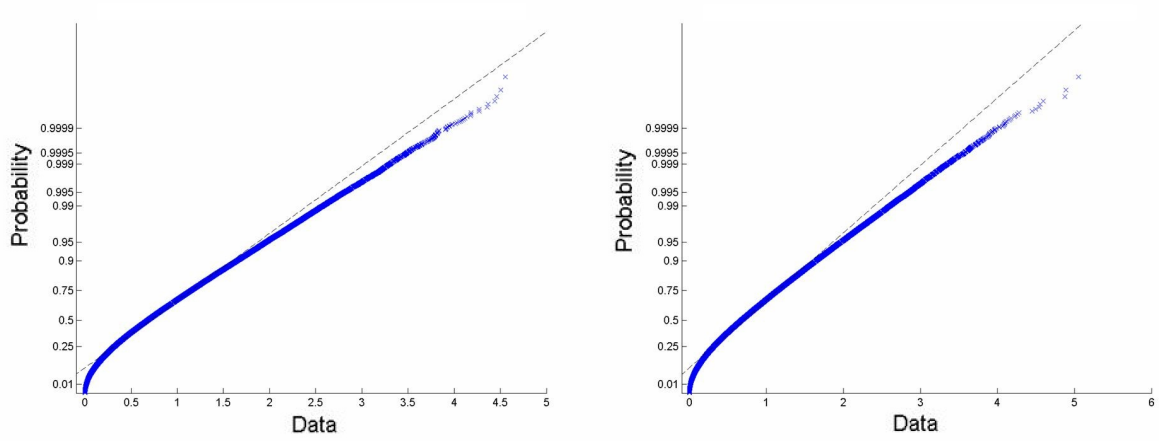

(a) absolute values of mic1 positive subset (b) absolute values of mic1 negative subset

Figure 7.6: P-P plots using the Rayleigh distribution

Exponential distribution: $pdf = \lambda exp(-\lambda x), \qquad x \in [0; \infty), \lambda > 0$

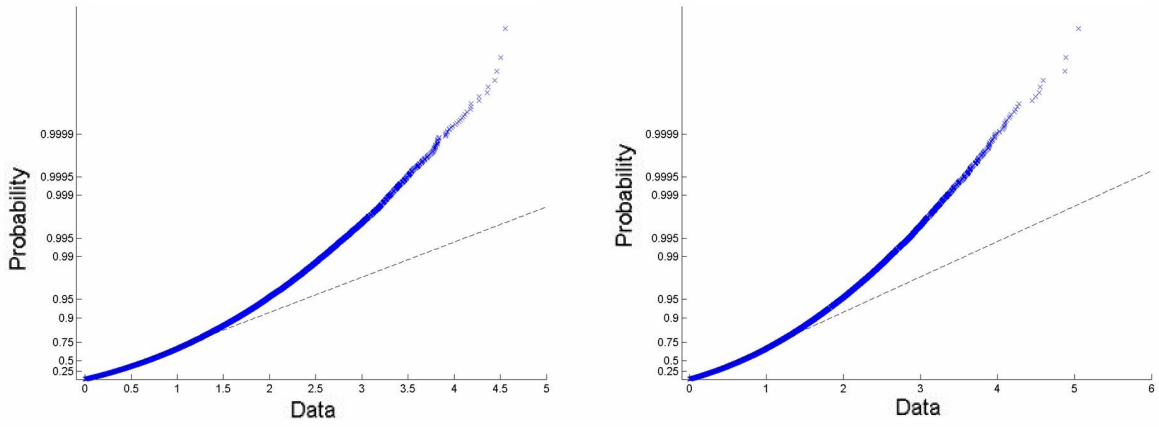

(a) absolute values of mic1 positive subset (b) absolute values of mic1 negative subset

Figure 7.7: P-P plots using the Exponential distribution

Weibull distribution: $pdf = (\frac{k}{\lambda})(\frac{x}{\lambda})^{k-1}exp(-(\frac{x}{\lambda})^k), \qquad x \in [0;\infty), \lambda > 0, k > 0$

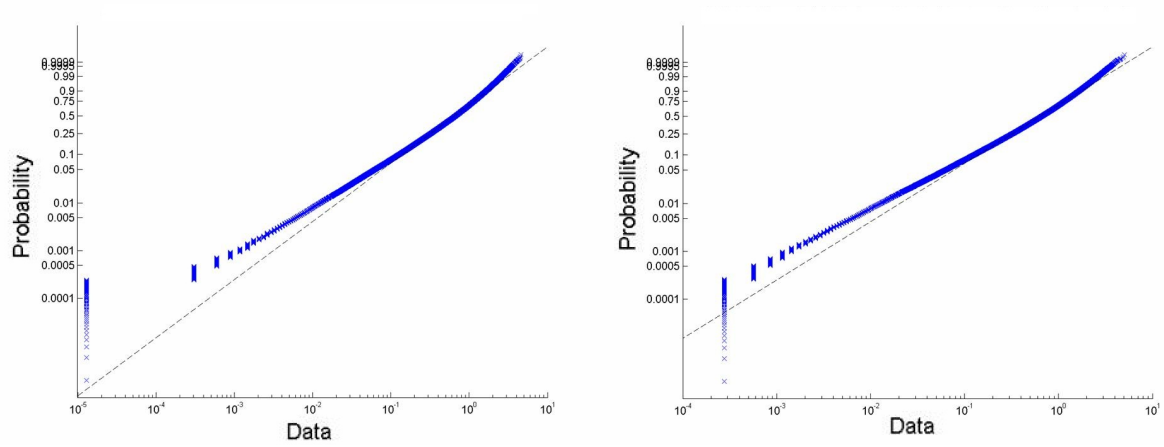

(a) absolute values of mic1 positive subset (b) absolute values of mic1 negative subset

Figure 7.8: P-P plots using the Weibull distribution

Figure 7.4 to Figure 7.8 shows there is very little difference within each distribution between its positive (left) and negative (right) data sets. Therefore, to minimize computational processing, the absolute values of the entire data set are used for future calculations (option *b*)).

The plots show the acoustic data set does not exclusively follow any particular known distribution. However, with its linearity in some graphs, such as the Rayleigh and Weibull distributions, it does suggest that the mic1 data follows a family of continuous distributions, implying a generalized formula for distributions would provide a good fit. The pdf of the acoustic data (using different sample sizes) can be seen later in this chapter in the 'a series' plots in Figure 7.12 to Figure 7.15.

7.4 General 3 parameter family of distribution

The Rayleigh distribution is a particular case of the Weibull distribution, which itself is a particular case of a 2 parameter family of distributions. Malevergne *et al.* (2006) used a generalized 3 parameter density function, as shown in Equation 7.3 where b, c are shape parameters, d is a scale parameter and u is a suitably chosen known lower threshold.

$$f_u(x|b,c,d) = \begin{cases} A(b,c,d,u)x^{-(b+1)}exp[-(\frac{x}{d})^c] & \text{if } x \geq u > 0 \\ 0 & \text{if } x < 0 \end{cases} \tag{7.3}$$

$$\text{where } -\infty < b < \infty, \quad 0 < c < \infty, \quad 0 < d < \infty$$

The normalizing constant $A(b,c,d,u)$ is defined by Equation 7.4,

$$A(b,c,d,u) = \frac{d^b c}{\Gamma(-\frac{b}{c}, (\frac{u}{d})^c)} \tag{7.4}$$

where the gamma function (an extension of the factorial function) and the incomplete gamma function are defined in general by Equation 7.5.

$$\begin{aligned} \Gamma(\alpha) &= \int_0^\infty t^{\alpha-1}e^{-t}dt \\ \Gamma(\alpha,\beta) &= \int_\beta^\infty t^{\alpha-1}e^{-t}dt \end{aligned} \tag{7.5}$$

The lower threshold u only affects the incomplete gamma function in the normalizing constant A. As there is no variation in the lower threshold for this investigation, the gamma function can be completed by setting $u = 0$, resulting in the density function as shown in Equation 7.6.

$$f_u(x|b,c,d) = \frac{d^b c}{\Gamma(-\frac{b}{c})} x^{-(b+1)} exp[-(\frac{x}{d})^c] \tag{7.6}$$

This is the 3 parameter equation in generalized form for a continuous family of distributions.

7.5 Solving for the parameters

There are different approaches that can be taken to make inferences about parameters. Arguably the best known and popular estimate is the Maximum Likelihood Estimate (MLE), which finds the optimum parametric fit of a model to an empirical data set. The likelihood function is defined by Equation 7.7,

$$L(\theta_i) = \Pi_{i=1}^{n_b} f(x_i; \theta_i) \tag{7.7}$$

where θ_i represents the parameters $\theta_1, \theta_2, \theta_3, ..., \theta_m$ whose value are being estimated and x_i is a sample from a population of size n_b, with a probability function $f(x; \theta_i)$.

The MLE of each parameter is found by partially differentiating $log(L(\theta_i))$ with respect to each parameter to be estimated, setting all derivatives to zero, and solving these equations simultaneously. That is, solving Equation 7.8.

$$\frac{\partial log(L(\theta_i))}{\partial \theta_i} = 0 \tag{7.8}$$

The MLE of the parameters from the 3 parameter density function requires the differential of the gamma function, which can only be found by using numerical optimization techniques. For this work, the MLE solver in Matlab was used. Two other popular alternative optimization approaches are the Least Squares

(LS) method and the Kullback Liebler (KL) Divergence.

The LS method is a part of regression analysis and derives the parametric estimates by minimizing the sum of residuals using the formula below.

$$S = \sum (y_i - f(x_i|\hat{\theta}_i))^2 \tag{7.9}$$

where, in the pdf case, y_i is the observed empirical probably value at x_i and $f(x_i|\hat{\theta}_i)$ is the expected probability value (calculated using estimated parameters) at xi.

The KL Divergence measures the divergence D of one probability distribution with respect to another and is defined by Equation 7.10. In the case of the acoustic data set, this is the divergence of the observed empirical pdf from the generalized parametric pdf.

$$D = \sum f(x_i|\hat{\theta}_i) log(\frac{f(x_i|\hat{\theta}_i)}{y_i}) \tag{7.10}$$

All three optimization approaches are validated on a known case such as the Weibull distribution and compared with each other.

The Weibull distribution is a particular case of Equation 7.6, the generalized 3 parametric equation, with $b = -c$, $c > 0$ and $d > 0$ (note in this case $\Gamma(1) = 1$). This produces Equation 7.11.

$$f_u(x|c,d) = \frac{c}{d^c} x^{c-1} exp[-(\frac{x}{d})^c] \tag{7.11}$$

To test the estimators for a known case, the scale and shape parameters were

arbitrarily chosen to be $d = 117$ and $c = 74$ (with $b = -74$ in the 3 parameter case). This constituted to an actual known pdf, as shown in Figure 7.9 as a green dash line.

However, this can not be used for comparing parametric estimates as each approach would lead to almost the exact values being calculated (namely $d = 117$ and $c = 74$); thus providing virtually no information on the their differences.

A simulated empirical distribution is needed to provide some slight differences from the actual known pdf, so that parametric estimates for each optimization approach can be compared.

A sample of 5,000 points from the actual known pdf, were used to compute the probability density estimate of the sample. This simulated an empirical distribution with known approximate parameters. The MLE, LS and KL estimates were calculated to fit the simulated empirical distribution. The results can be seen in Figure 7.9, Figure 7.10 and Figure 7.11.

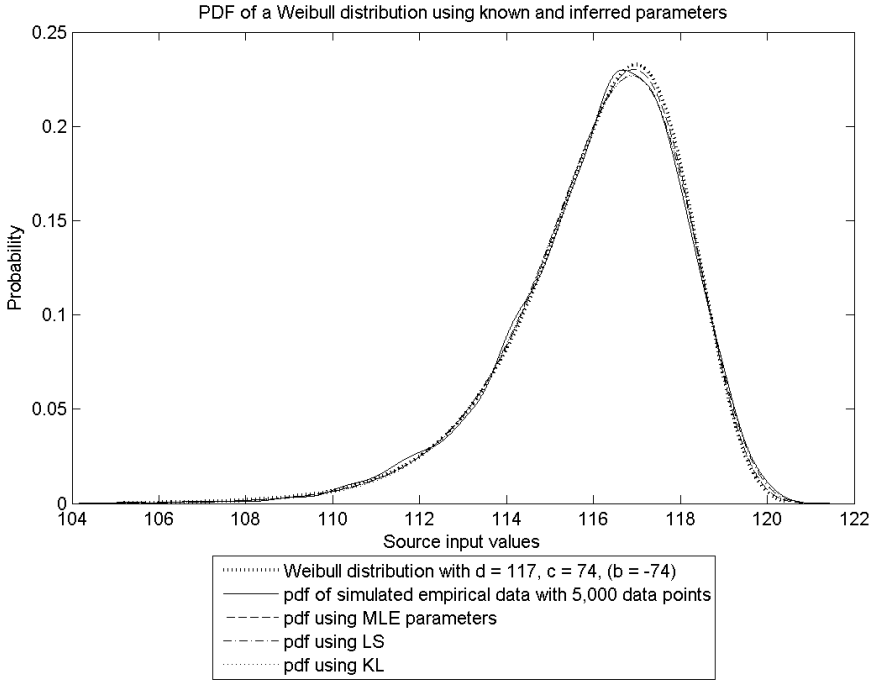

Figure 7.9: pdf of a Weibull distribution

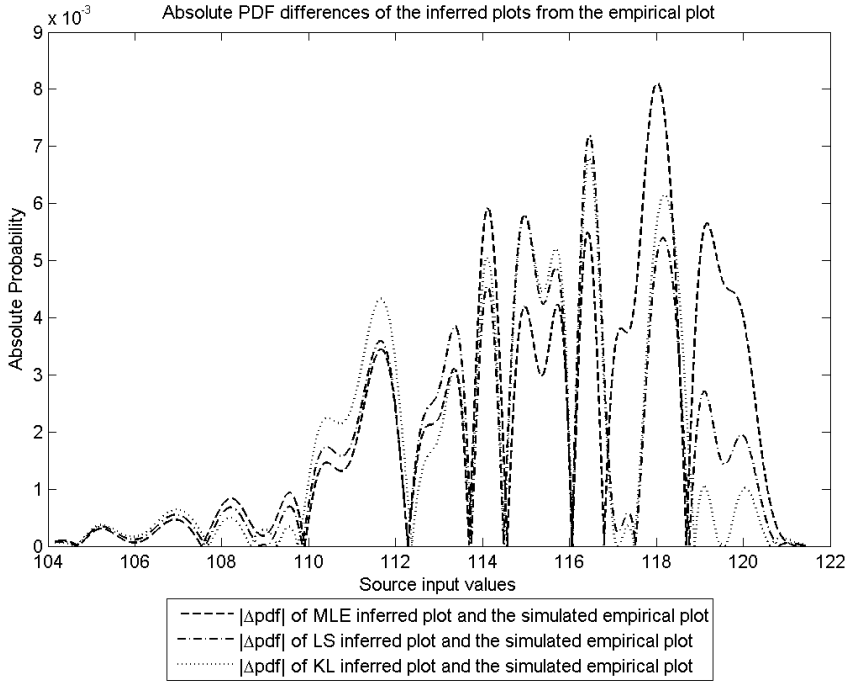

Figure 7.10: Absolute pdf differences based on the Weibull distribution

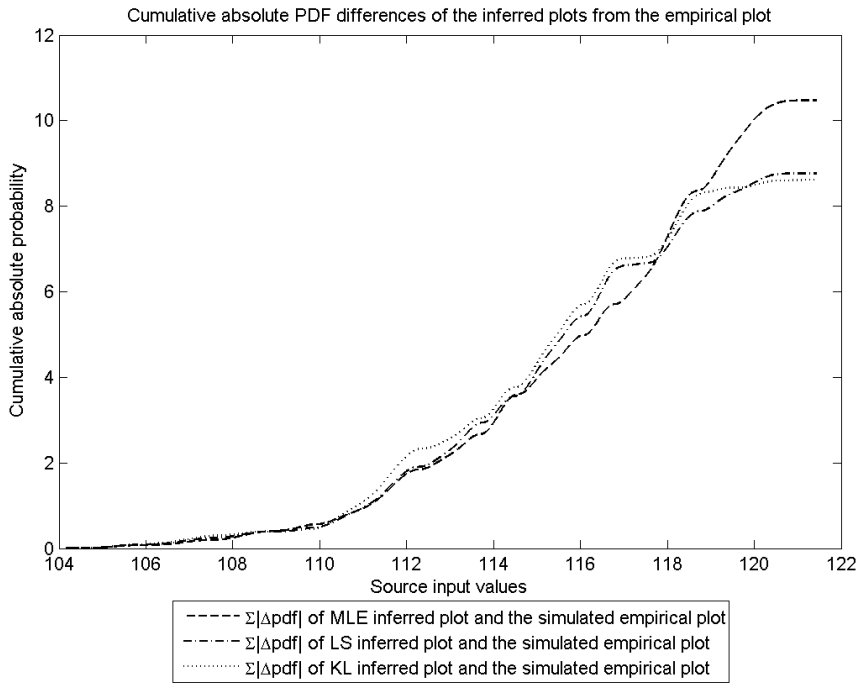

Figure 7.11: Cumulative absolute pdf differences based on the Weibull distribution

Parameters of the simulated empirical pdf: $\tilde{d} \approx 117, \tilde{c} \approx 74, \tilde{b} \approx -74$

	$\hat{d}$	$\hat{c}$	$\hat{b}$	$\frac{(\lvert\hat{c}\rvert+\lvert\hat{b}\rvert)}{2}$
MLE	116.73	67.94	-77.34	72.64
LS	116.44	62.26	-80.51	71.38
KL	116.28	59.92	-83.15	71.54

Table 7.1: Estimated parametric values

As can be seen from Figure 7.9 and Table 7.1, the optimization approaches all yield very similar results, verifying their general consistency for parametric estimates. As b and c are dependant shape parameters, their absolute average (which is of interest in the Weibull case and not general case) is shown for reference in Table 7.1. From Figure 7.10 and Figure 7.11 , the MLE provides a marginally

better parametric estimation (for the majority of the distribution) than the LS or KL approach.

7.6 Generalized 4 parameter equation

The generalized 3 parameter equation works well in fitting empirical data sets, using MLE, LS or KL estimates. However, so far the fitting distributions are by construction unable to capture any skewness of the empirical distribution.

Malevergne found this to be problem when fitting data sets to his 3 parameter generalized density function Malevergne & Sornette (2005). One set of parameters would fit the tail end of the data and another set would fit the main body, but none would provide a reasonable fit for the entire set. The main reason for this was the functions inability to capture asymmetry.

To introduce skewness a further 'twist' was applied to the 3 parameter generalized density function by multiplying it with $(1+ax_i)$ where a is the 4th parameter and is a real number with an absolute value of less than 0.1; x_i is the i^{th} value of the acoustic pressure fluctuation in the acoustic data set.

As the absolute values of the data set are used (recall option b)), the input data is shifted to centralize the distribution and aid the capture of symmetry.

The input data now reads as $z = |x| + \tilde{x}$, where $\tilde{x}$ is a constant calculated directly as shown in Equation 7.12.

$$\tilde{x} = d(-(b+1))^c : \qquad f'(\tilde{x}) = 0 \tag{7.12}$$

Applying these new inputs and constraints to the generalized 3 parameter equation, produces a novel 4 parameter density function as shown in Equation 7.13.

$$f(z|a,b,c,d) = \frac{d^b c}{\Gamma(-\frac{b}{c})} z^{-(b+1)} exp[-(\frac{z}{d})^c](1+ax) \tag{7.13}$$

This function was applied to samples from the acoustic data set and its parametric estimates were derived using the LS approach. It was then compared with the known existing 3 parametric model (non-accountability of skewness), by setting $a = 0$ and repeating the process. The pdf of these plots and the empirical distribution are shown in Figure 7.12 to Figure 7.15, with the inferred parameters in Table 7.2 and Table 7.3.

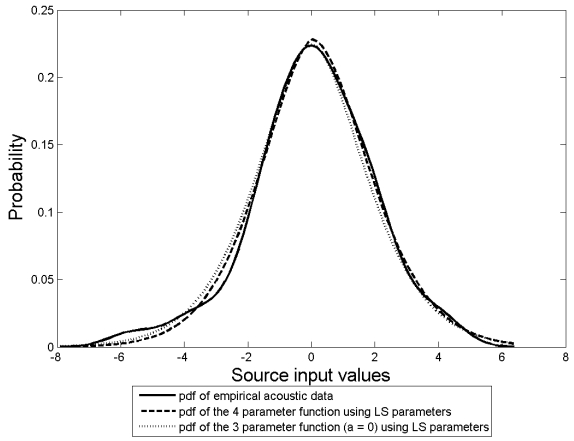

(a) pdf

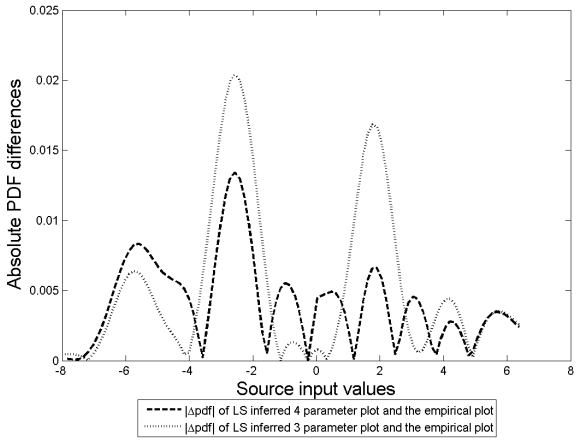

(b) $|\Delta pdf|$

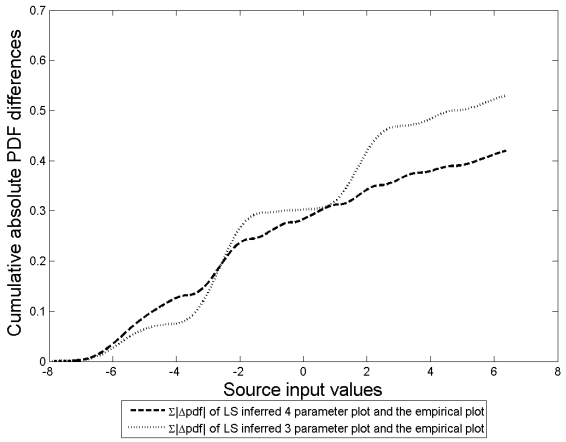

(c) $\sum |\Delta pdf|$

Figure 7.12: Distribution plots with sample size = 100 data points

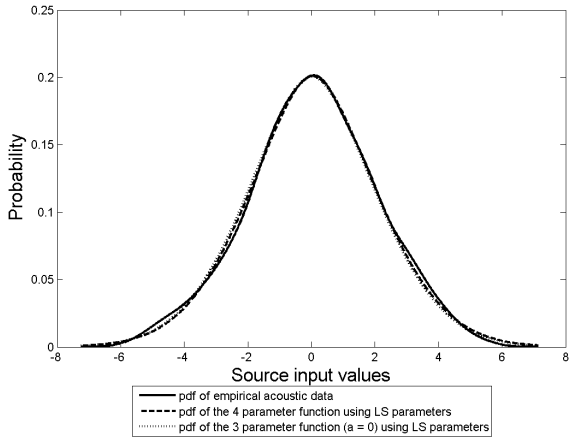

(a) pdf

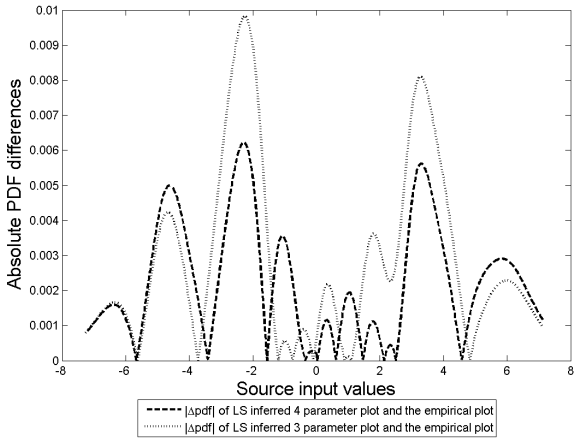

(b) $|\Delta pdf|$

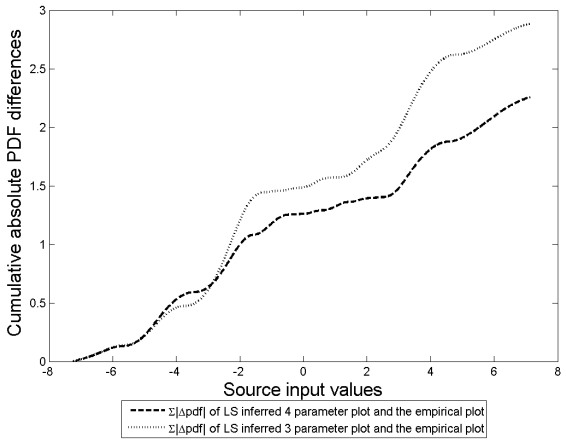

(c) $\sum |\Delta pdf|$

Figure 7.13: Distribution plots with sample size = 1,000 data points

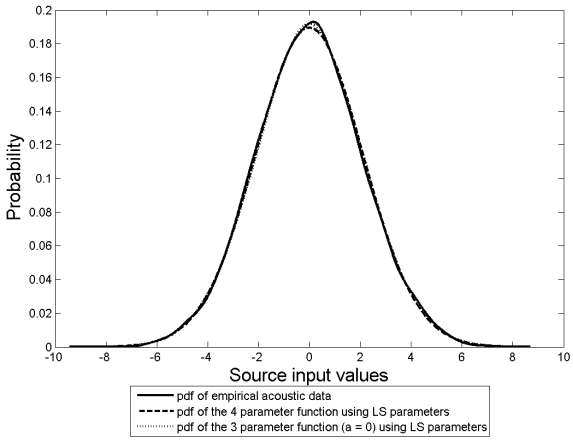

(a) pdf

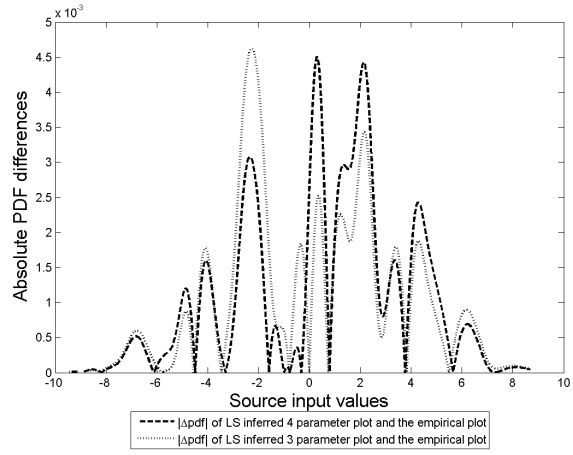

(b) $|\Delta pdf|$

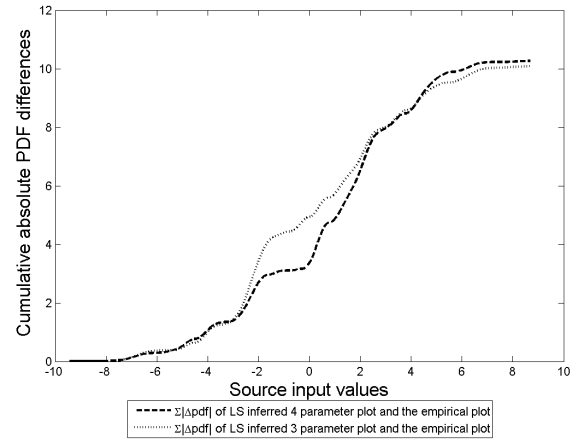

(c) $\sum |\Delta pdf|$

Figure 7.14: Distribution plots with sample size = 10,000 data points

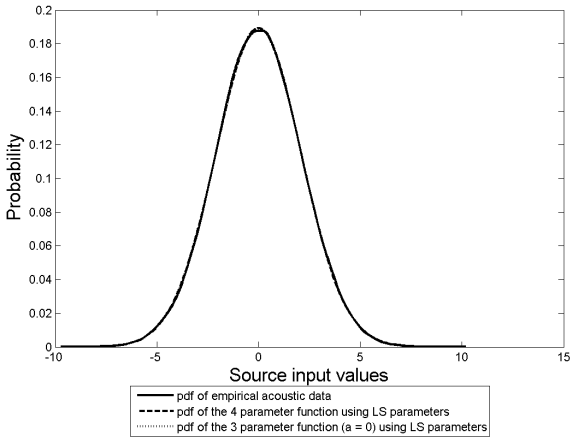

(a) pdf

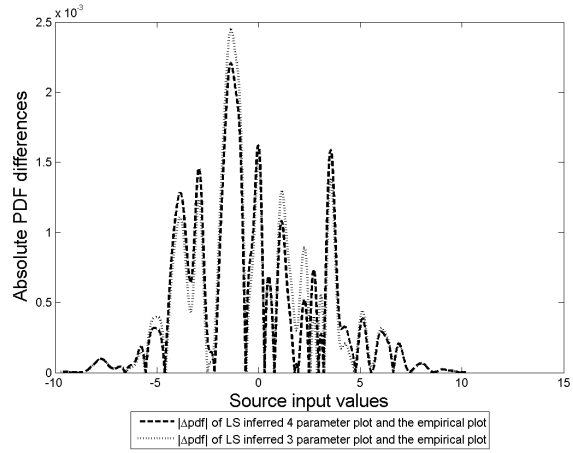

(b) $|\Delta pdf|$

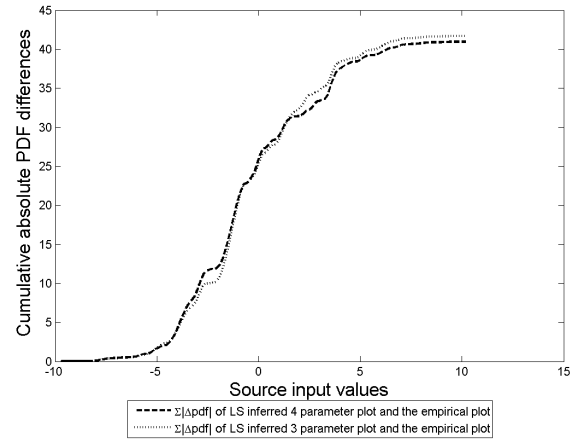

(c) $\sum |\Delta pdf|$

Figure 7.15: Distribution plots with sample size = 100,000 data points

No. of data points	$\hat{d}$	$\hat{c}$	$\hat{b}$	$\hat{a}$
100	1.1525	1.1930	-5.3240	0.0374
1,000	3.1786	1.8781	-1.1618	0.0138
10,000	3.9966	2.5040	-1.5773	-0.0057
100,000	5.4554	2.4995	-5.5807	-0.0012

Table 7.2: Inferred parameters for the 4 parameter equation

No. of data points	$\hat{d}$	$\hat{c}$	$\hat{b}$	$\hat{a}$
100	1.3756	1.1937	-2.8655	0.0000
1,000	3.1363	1.8903	-1.1238	0.0000
10,000	3.4285	2.1070	-1.0945	0.0000
100,000	6.1162	2.5513	-10.6889	0.0000

Table 7.3: Inferred parameters for the 3 parameter equation (a = 0)

Using 10,000 data points, the inferred parameters for the 4 parameter equation (as shown in Table 7.3) are $\hat{a}$=-0.0057, $\hat{b}$=-1.5773, $\hat{c}$=2.5040 and $\hat{d}$=3.9966. A 95% confidence band for each parameter is generated by bootstrapping using 1,000 runs and sampling with replacement for the full size of the data set. This process is repeated using the data from mic2, mic3 and mic4, giving a set of four confidence bands for each parameter. There was a good overlap between the confidence bands, suggesting the inferred parameters from each data set are statistically similar. This implies a low levels of acoustic asymmetry.

7.7 Final remarks

The 4 parameter general density function has proved to be successful in fitting the acoustic data set. It was developed from the 3 parameter general density function as described Malevergne *et al.* (2006), with the key differences being,

- its ability to capture asymmetry.
- its general good fit for an entire data set (not just positive and negative subsets).
- its effectiveness in finding an optimum set of parameters that fit both the main body of the empirical distribution and its tail.

As can be seen from Figure 7.12 to Figure 7.15, the 4 parameter case offers a better fit to the empirical data when skewness is present. Skewness can occur as a natural characteristic of a distribution or by having insufficient data points when estimating the pdf of an empirical data set.

With a refined distributional fit of the acoustic data, comparisons of the distributions from microphones at different radial positions were made. The inferred parameter values from each data set have overlapping 95% confidence bands, implying that the data sets are statistically similar and therefore support with a refined low levels of acoustics asymmetry.

CHAPTER 8

Experimental results and discussion

One of the key areas in investigating jet noise is to look at the sound radiation and source strength distribution of the jet. The experimental arrangement of an acoustic mirror and microphone is regarded as one of the most efficient methods in collecting the distribution of sound and has been used in both industry and academia. This is because information can be collected in the far focus of the mirror, with minimal interference from other parts of the jet, allowing a more localized result to be obtained. This chapter reports on the significant and important results obtained at Warwick.

8.1 Acoustic investigation

8.1.1 Acoustic experimental arrangement

The acoustic mirror was mounted on the motorized traverse with its far focus initially positioned at the bullet tip. This was on the geometric centreline of the jet. An overview of the experimental arrangement can be seen in Figure 8.1.

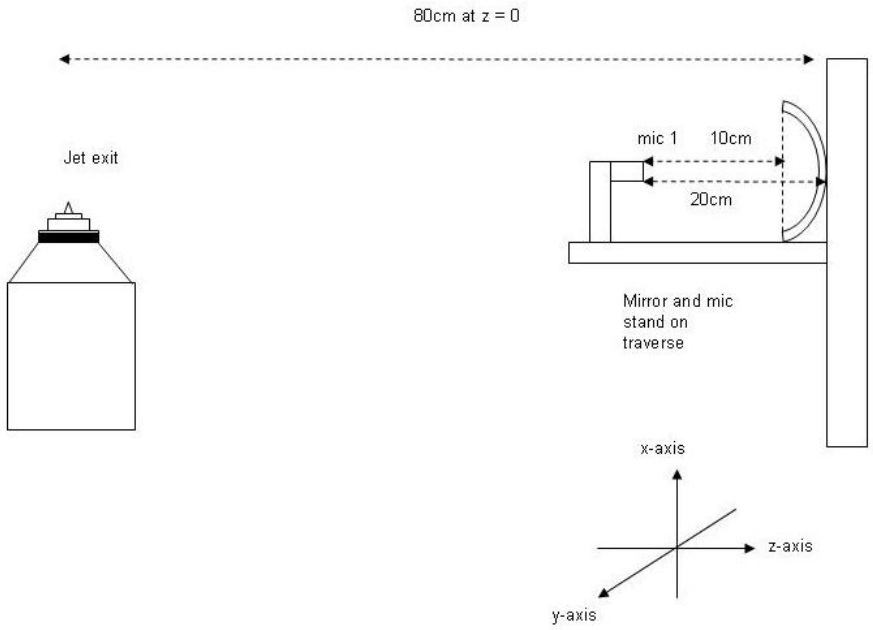

Figure 8.1: Experimental arrangement using the acoustic mirror

The mounting angle of the mirror is fixed on the traverse at 90 ° to the jet, to minimize the expected shear layer refractions (as suggested by Drobietz *et al.* (2008)) and to adequately fit with the mounted LDA heads as shown in Figure 8.2.

From preliminary line tests, a measurement grid of size $10D_{bp}$ in the x-axis by $3.425D_{bp}$ (i.e. $0D_{bp}\pm1.7125D_{bp}$) in the y-axis, with 1 mm increments in both axes provided a good balance between experimental running time and significant data extraction. A macro was written in 'Mouse and Key Recorder V6.3' to automate the saving of the acquired data after each measurement and moving the traverse ready for the next measurement. This reduced the time interval between measurements and therefore allowed a larger grid size to be measured in the same experimental running time. A grid size of $10D_{bp}$ in the x-axis by $4D_{bp}$ in the y-axis could now be achieved. Keeping the y-axis start position at $-1.7125D_{bp}$

the grid now extended to $2.2875D_{bp}$. This created a 2D grid of 13,320 points in the x-y plane.

The mirror was moved to the x,y,z position of $(0,-1.7125D_{bp},0)$ with the origin (0,0,0) being at the bullet tip. This marked the starting position of the measurement grid in the traverse controlling BSA software.

Figure 8.2: Acoustic mirror, near focus microphone and traverse arrangement

The microphone at the near focus of the acoustic mirror was encased in a small cylindrical block of acoustic foam to remove the interference of direct sound waves from noise sources in the jet flow that are not in the far focus point. With this arrangement, the microphone would only measure the sound waves reflected off the mirror surface, which emanate from the far focus point.

With the jet rig running on condition, acoustic measurements were taken in series (with respect to the y-axis) for all of the grid points. The motorized traverse moved the acoustic mirror to each of the 13,320 points in the $10D_{bp}$ by $4D_{bp}$ grid and the PULSE system recorded the sound pressure levels for all frequencies at

each point. PULSE made 2 seconds recordings at each grid point as this was found to be sufficient in statistically converging the readings. The recordings used an averaged summation method to output a result in the sound pressure level.

Measurements for all four nozzle combinations with the co-flowing jets on condition were recorded. Recall nozzle abbreviations are: CrCo = Core Cowl, CrCh = Core Chevron, BpCo = Bypass Cowl, BpCh = Bypass Chevron. 2D sound source maps were created from the empirical data using Matlab. A selection of results are discussed in this chapter with the complete set of results from 5 kHz to 80 kHz (in steps of 5 kHz) shown in the Appendix.

8.1.2 Selection of acoustic results

The full set of acoustic results can be seen in the Appendix.

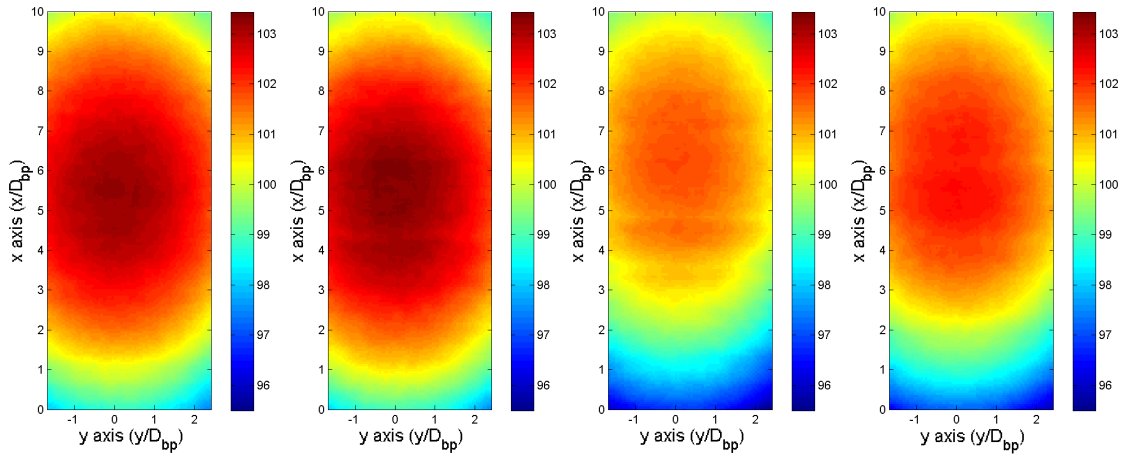

(a) CrCo, BpCo (b) CrCh, BpCo (c) CrCo, BpCh (d) CrCh, BpCh

Figure 8.3: 2D sound source maps at 5,120 Hz (colour bar in SPLdB)

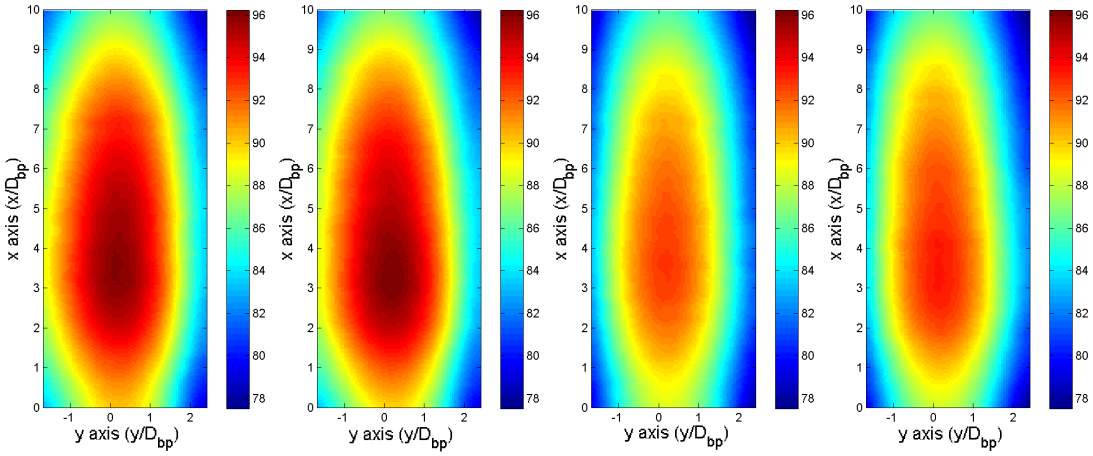

(a) CrCo, BpCo (b) CrCh, BpCo (c) CrCo, BpCh (d) CrCh, BpCh

Figure 8.4: 2D sound source maps at 20,224 Hz (colour bar in SPLdB)

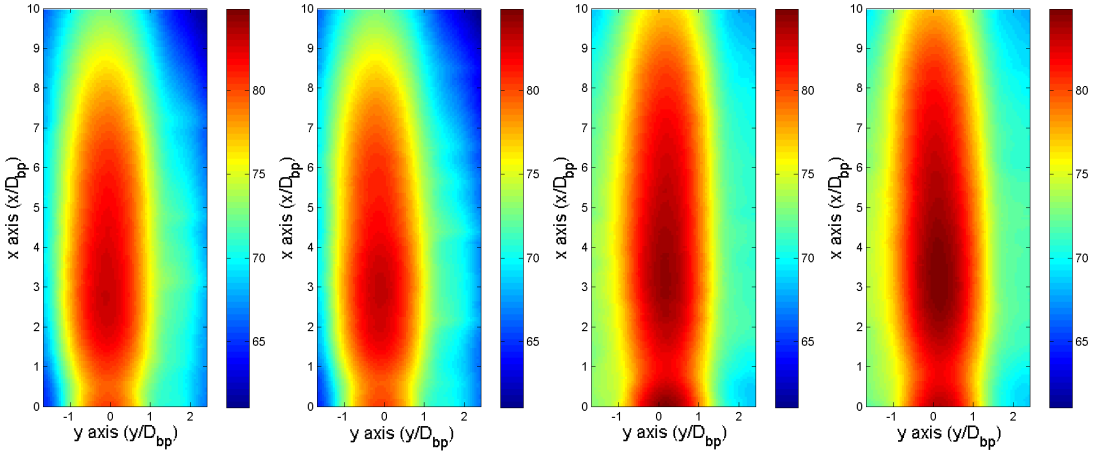

(a) CrCo, BpCo (b) CrCh, BpCo (c) CrCo, BpCh (d) CrCh, BpCh

Figure 8.5: 2D sound source maps at 35,072 Hz (colour bar in SPLdB)

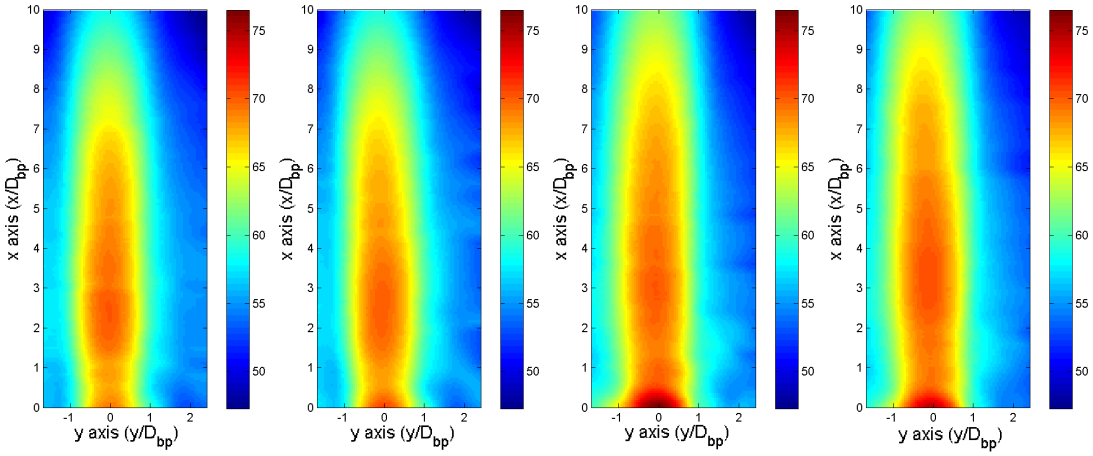

(a) CrCo, BpCo (b) CrCh, BpCo (c) CrCo, BpCh (d) CrCh, BpCh

Figure 8.6: 2D sound source maps at 65,024 Hz (colour bar in SPLdB)

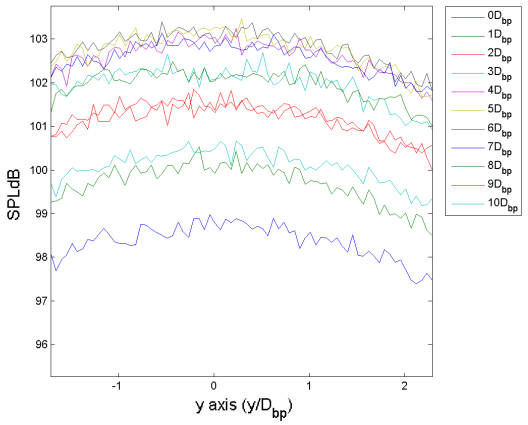

(a) CrCo, BpCo

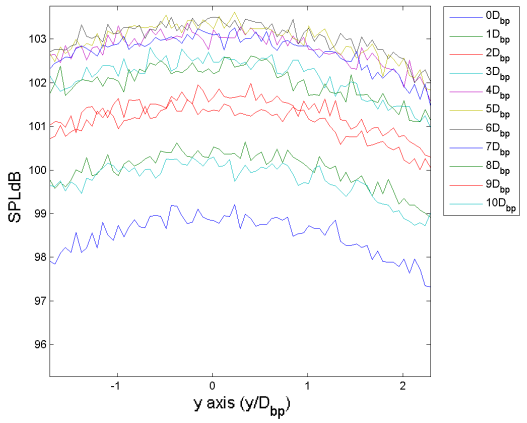

(b) CrCh, BpCo

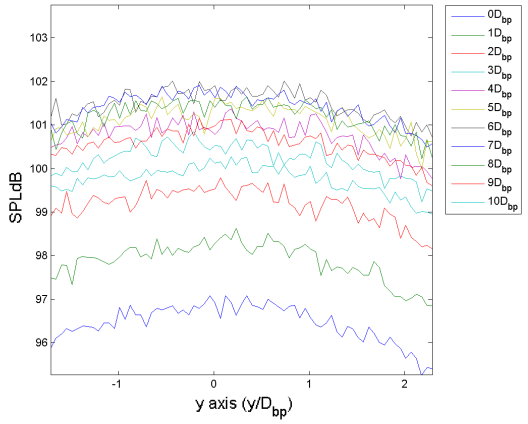

(c) CrCo, BpCh

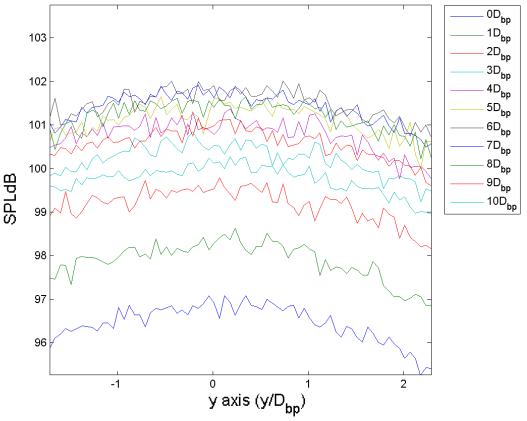

(d) CrCh, BpCh

Figure 8.7: Radial profile at 5,120 Hz

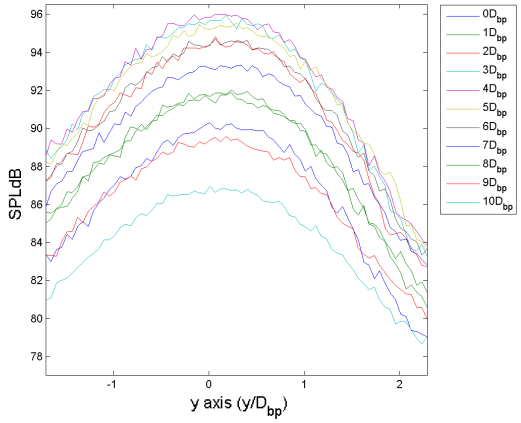

(a) CrCo, BpCo

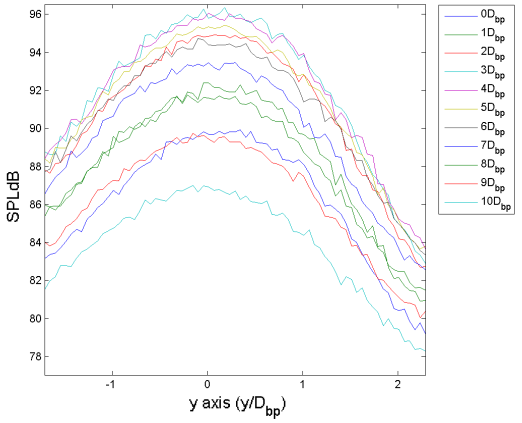

(b) CrCh, BpCo

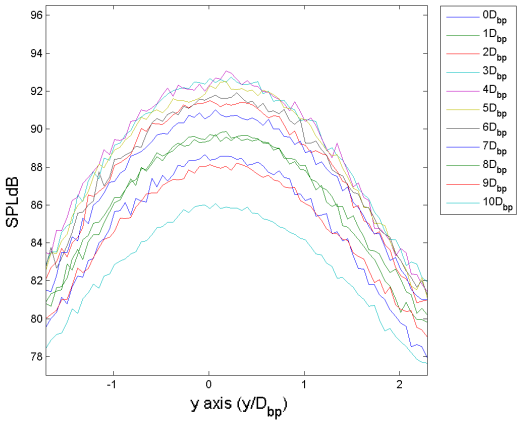

(c) CrCo, BpCh

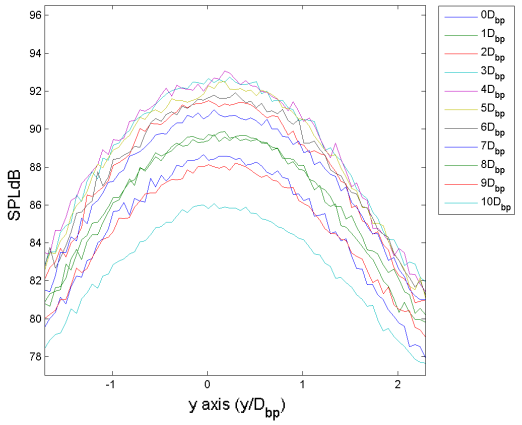

(d) CrCh, BpCh

Figure 8.8: Radial profile at 20,224 Hz

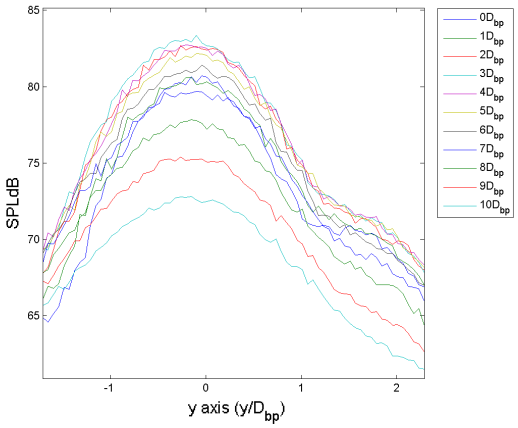

(a) CrCo, BpCo

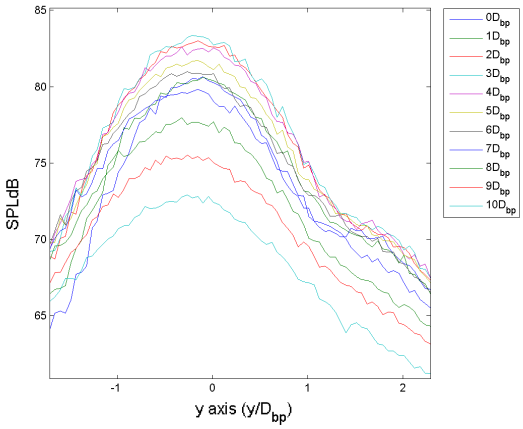

(b) CrCh, BpCo

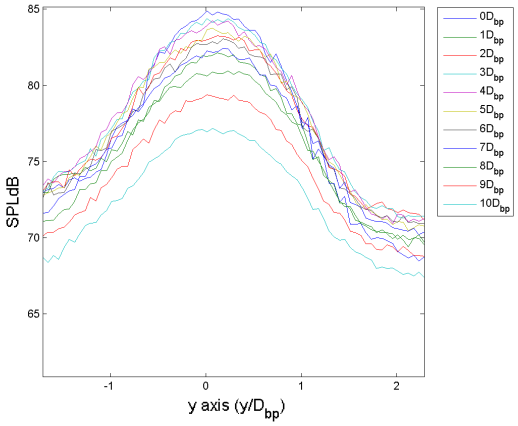

(c) CrCo, BpCh

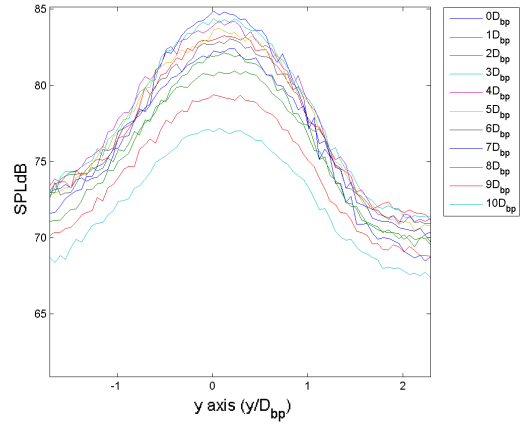

(d) CrCh, BpCh

Figure 8.9: Radial profile at 35,072 Hz

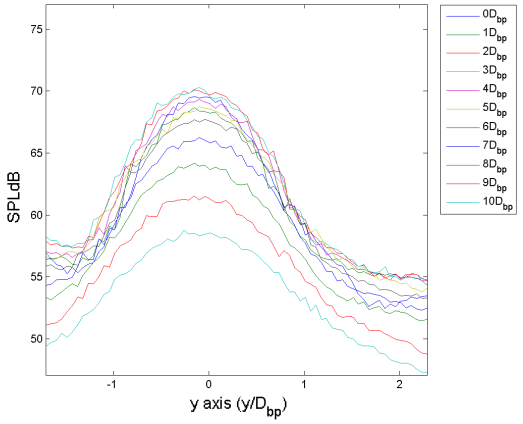

(a) CrCo, BpCo

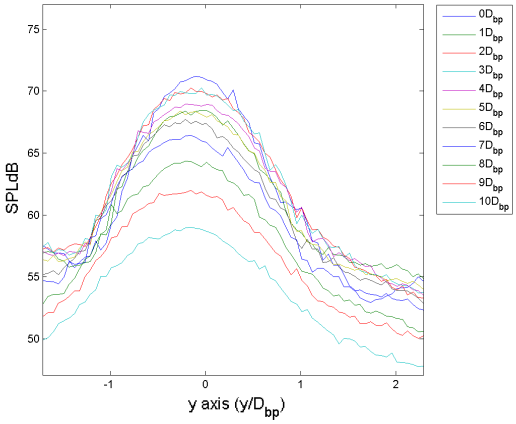

(b) CrCh, BpCo

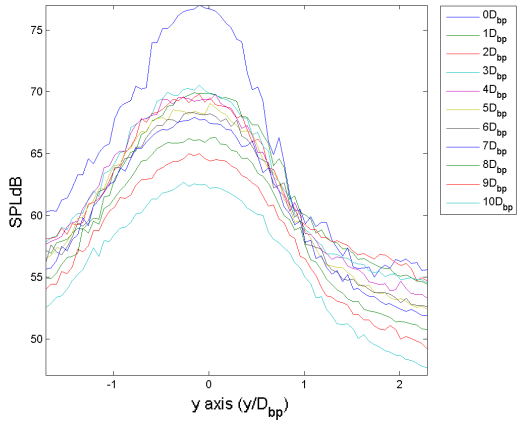

(c) CrCo, BpCh

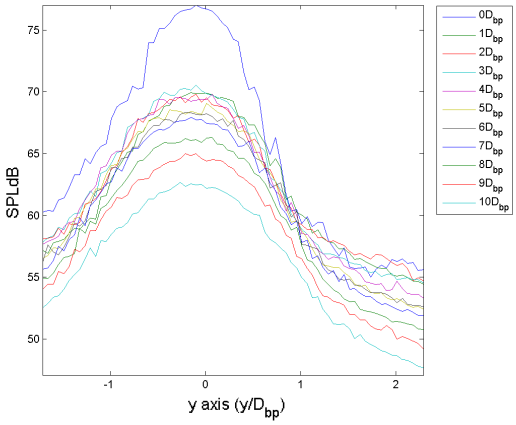

(d) CrCh, BpCh

Figure 8.10: Radial profile at 65,024 Hz

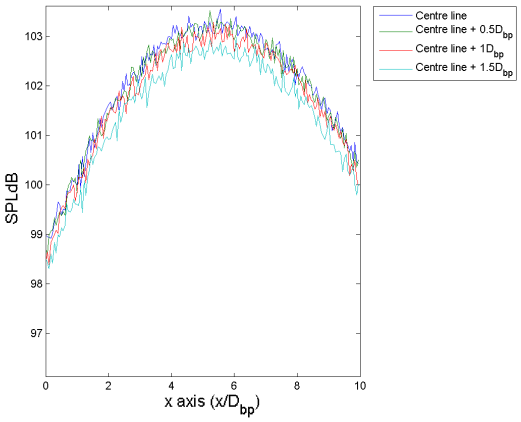

(a) CrCo, BpCo

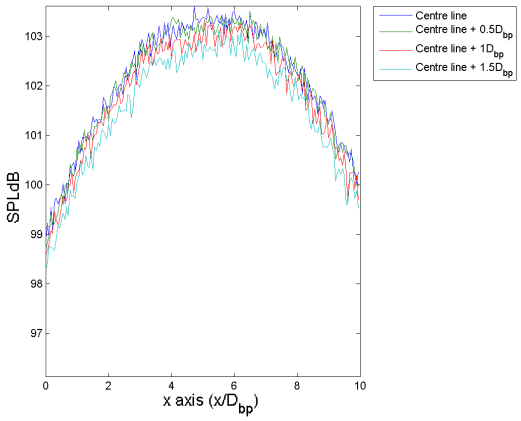

(b) CrCh, BpCo

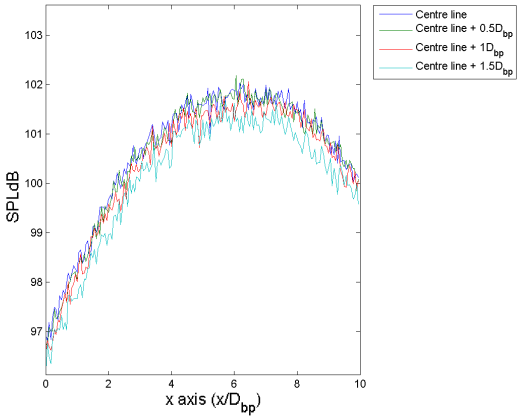

(c) CrCo, BpCh

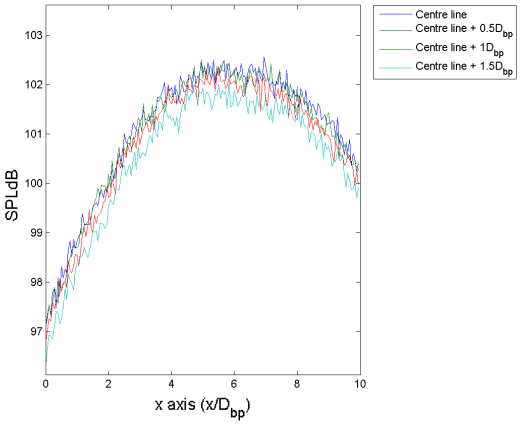

(d) CrCh, BpCh

Figure 8.11: Downstream profiles at 5,120 Hz

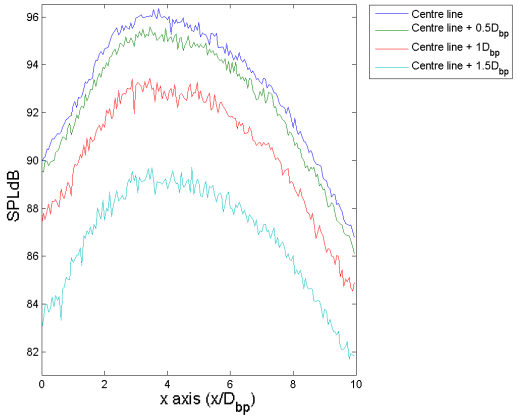

(a) CrCo, BpCo

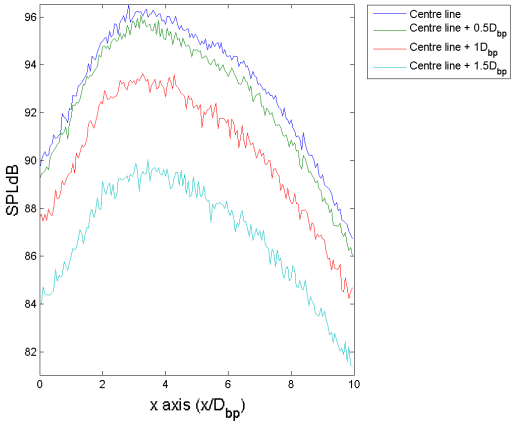

(b) CrCh, BpCo

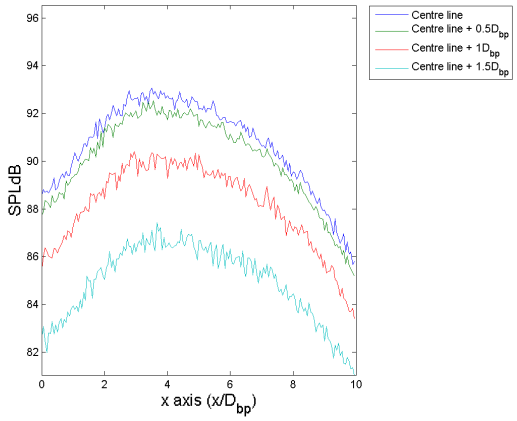

(c) CrCo, BpCh

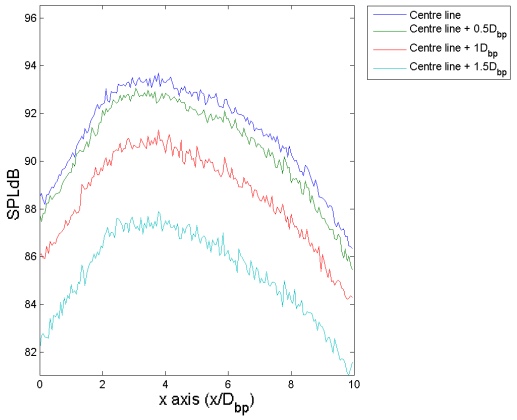

(d) CrCh, BpCh

Figure 8.12: Downstream profiles at 20,224 Hz

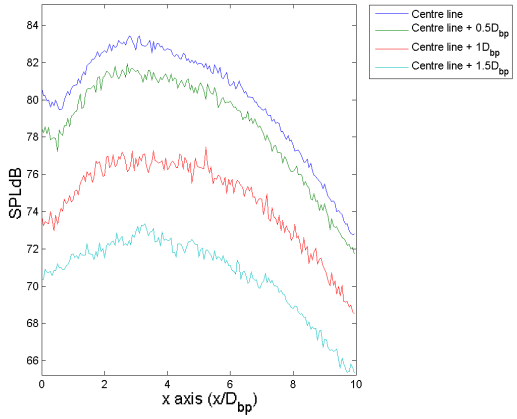

(a) CrCo, BpCo

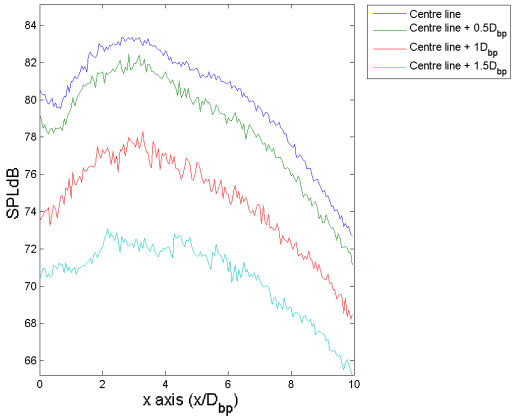

(b) CrCh, BpCo

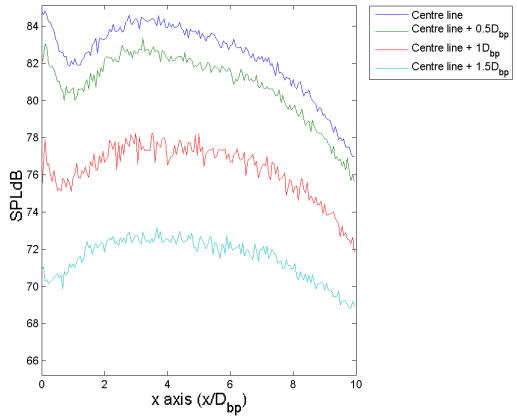

(c) CrCo, BpCh

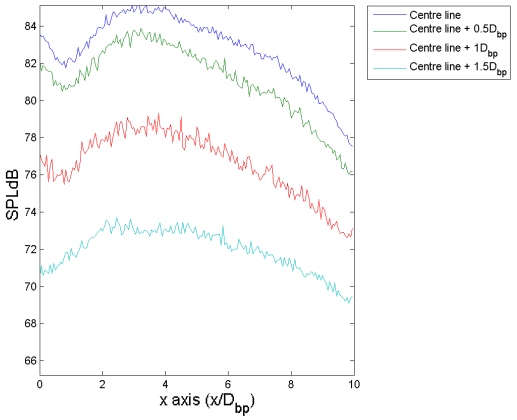

(d) CrCh, BpCh

Figure 8.13: Downstream profiles at 35,072 Hz

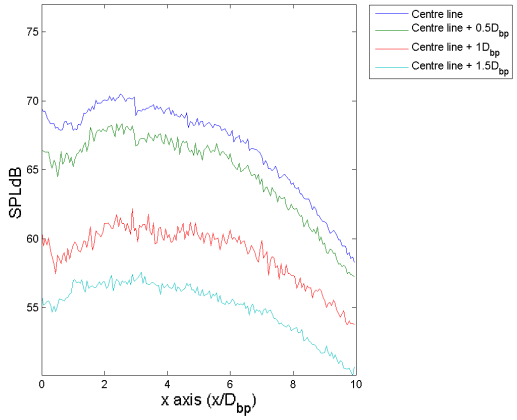

(a) CrCo, BpCo

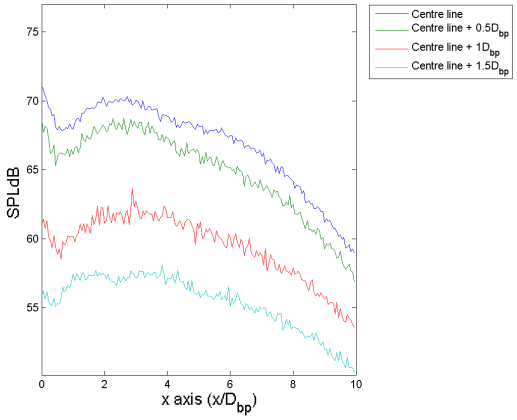

(b) CrCh, BpCo

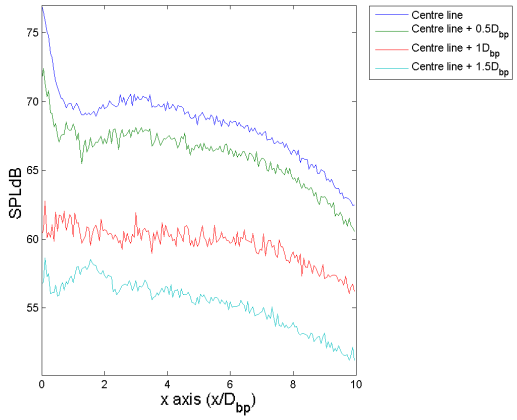

(c) CrCo, BpCh

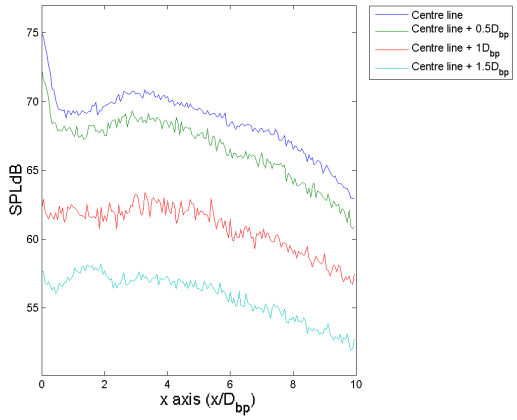

(d) CrCh, BpCh

Figure 8.14: Downstream profiles at 65,024 Hz

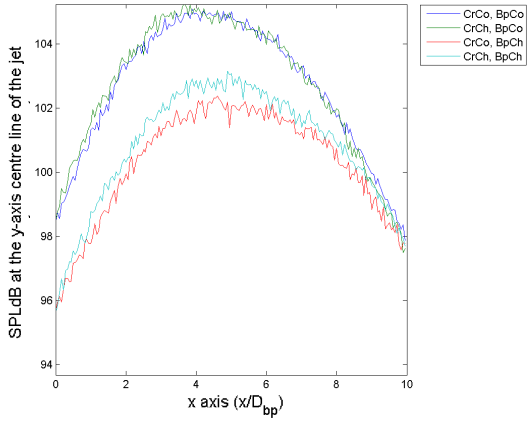

(a) Centre line

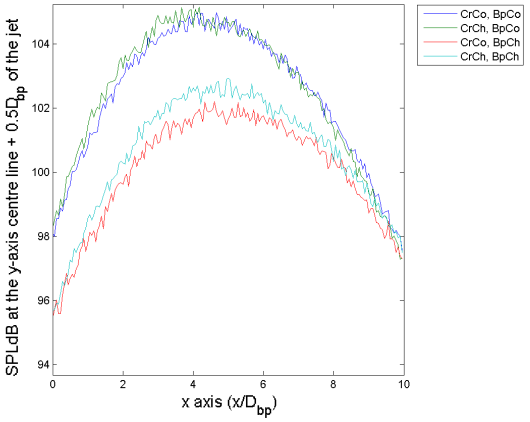

(b) Centre line + $0.5D_{bp}$

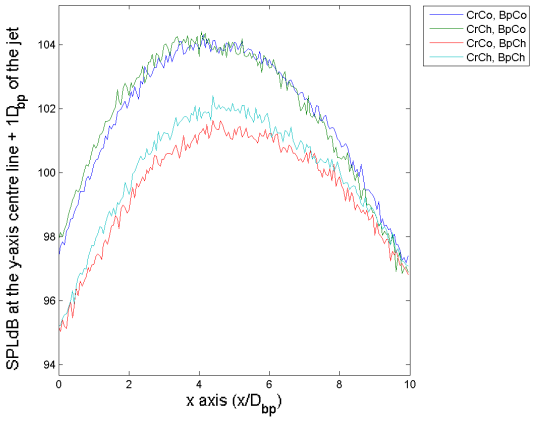

(c) Centre line + $1D_{bp}$

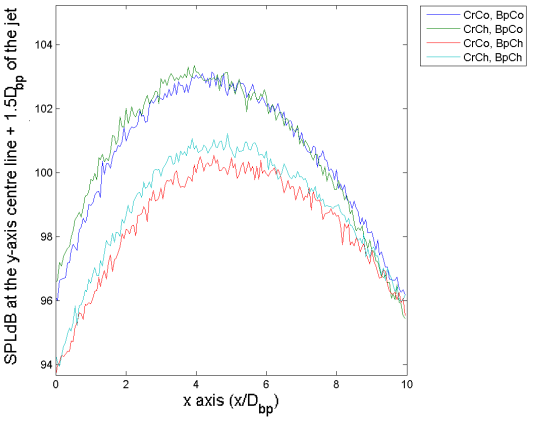

(d) Centre line + $1.5D_{bp}$

Figure 8.15: Downstream acoustic profile of all the nozzles at 10,240 Hz

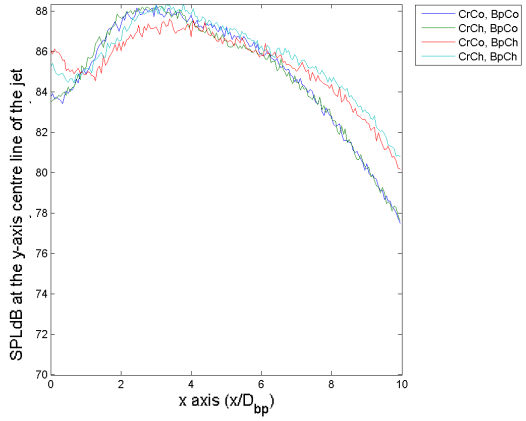

(a) Centre line

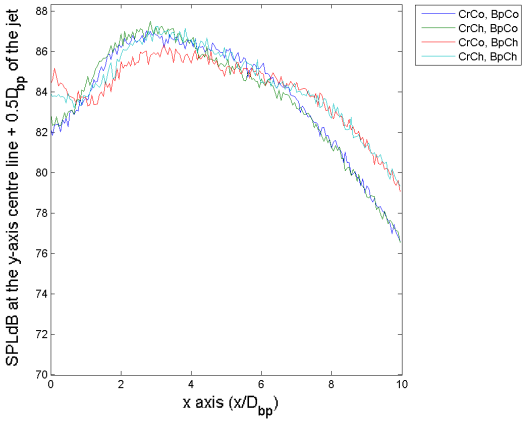

(b) Centre line + $0.5D_{bp}$

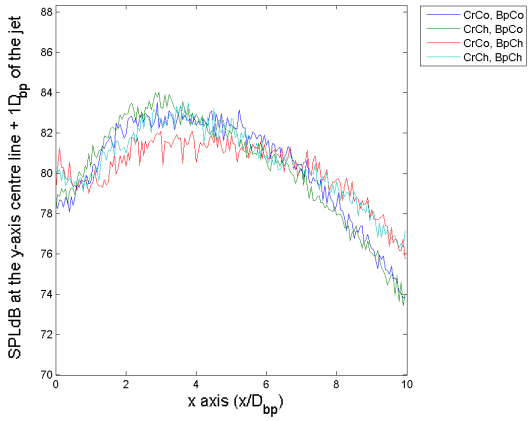

(c) Centre line + $1D_{bp}$

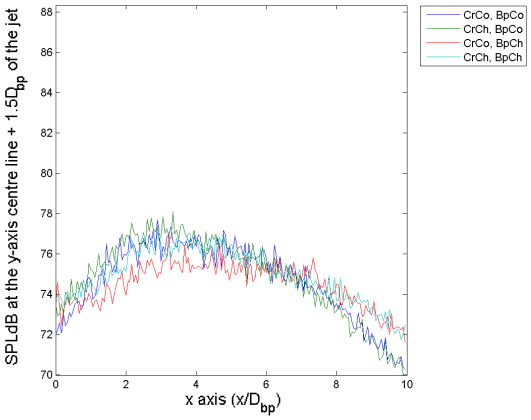

(d) Centre line + $1.5D_{bp}$

Figure 8.16: Downstream acoustic profile of all the nozzles at 30,208 Hz

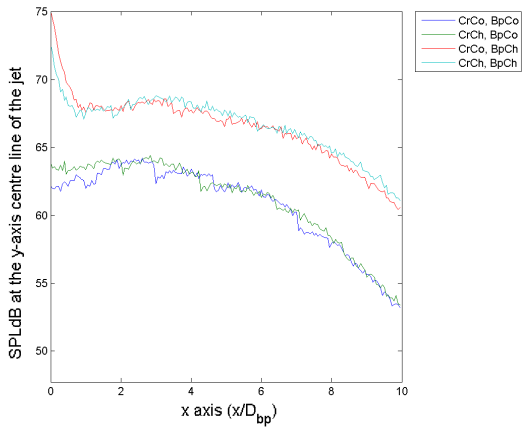

(a) Centre line

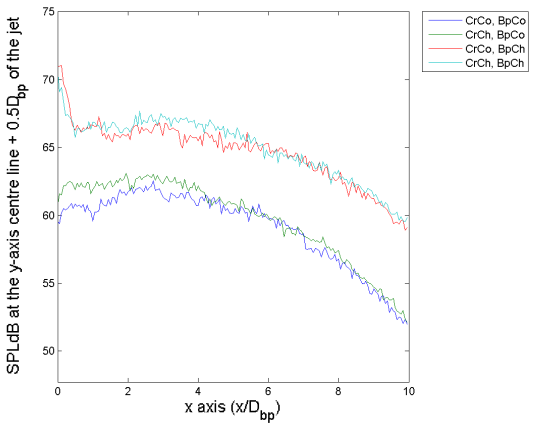

(b) Centre line + $0.5D_{bp}$

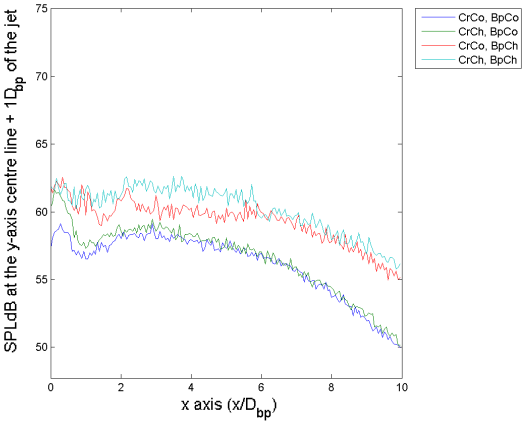

(c) Centre line + $1D_{bp}$

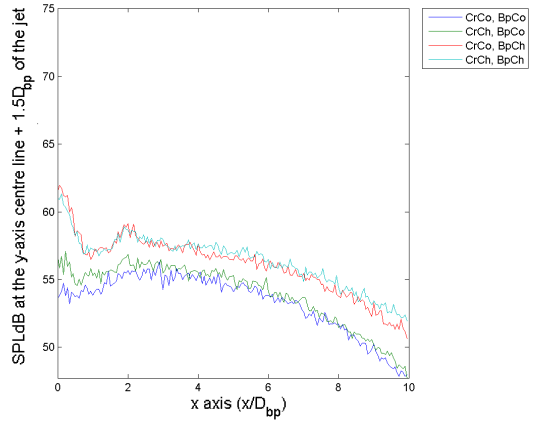

(d) Centre line + $1.5D_{bp}$

Figure 8.17: Downstream acoustic profile of all the nozzles at 70,144 Hz

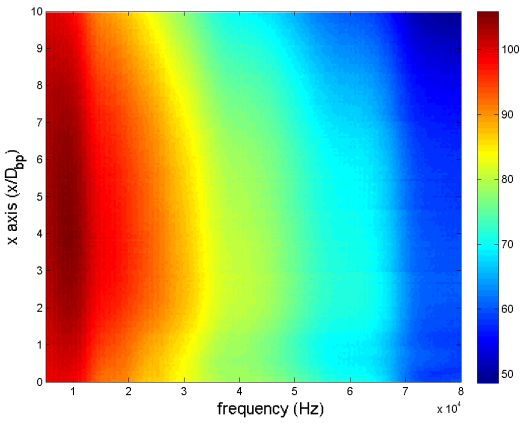

(a) CrCo, BpCo

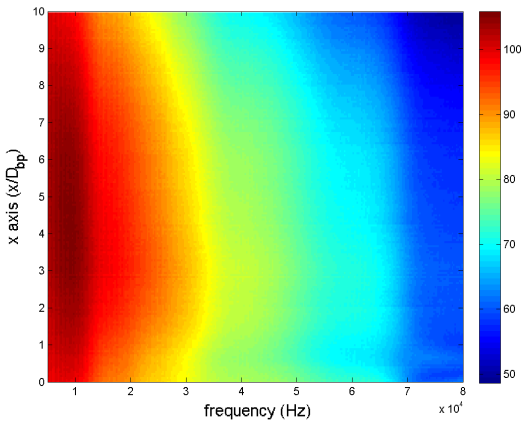

(b) CrCh, BpCo

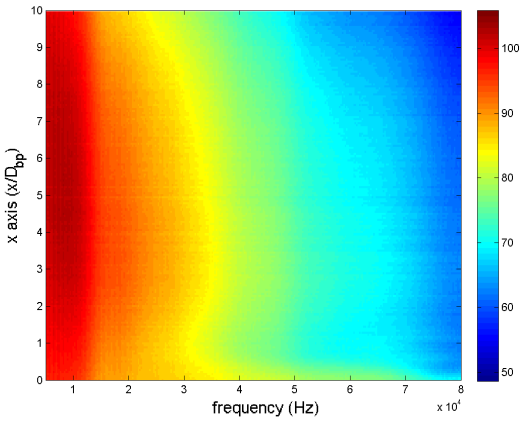

(c) CrCo, BpCh

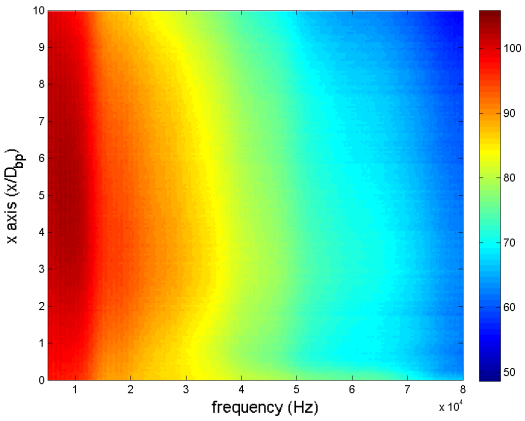

(d) CrCh, BpCh

Figure 8.18: Sound and frequency distribution at y=0 (colour bar in SPLdB)

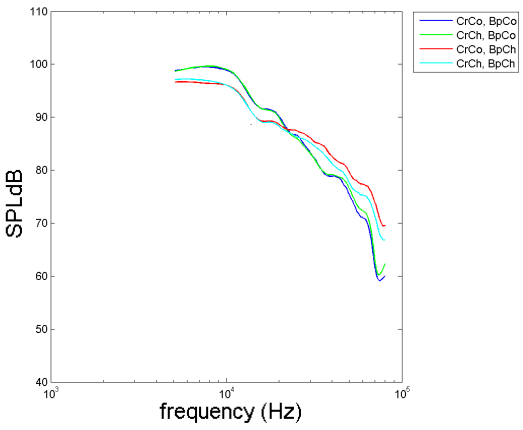

(a) x axis = $0D_{bp}$

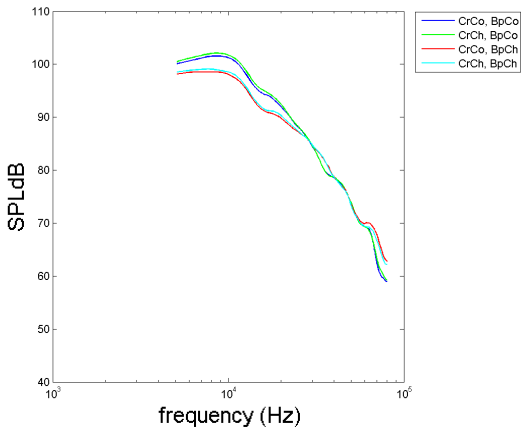

(b) x axis = $1D_{bp}$

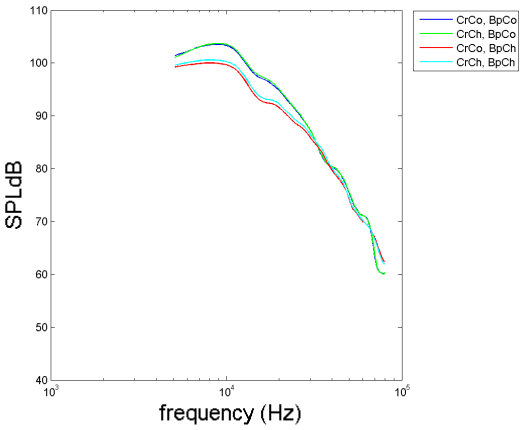

(c) x axis = $2D_{bp}$

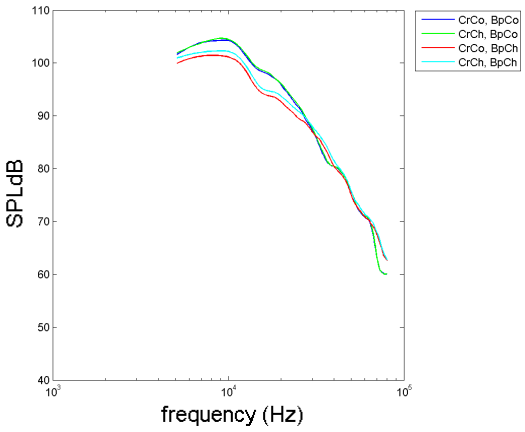

(d) x axis = $3D_{bp}$

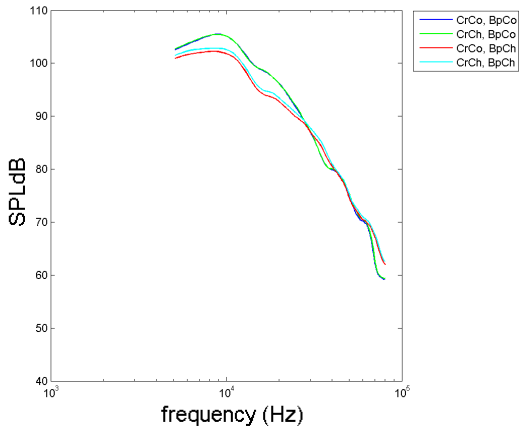

(e) x axis = $4D_{bp}$

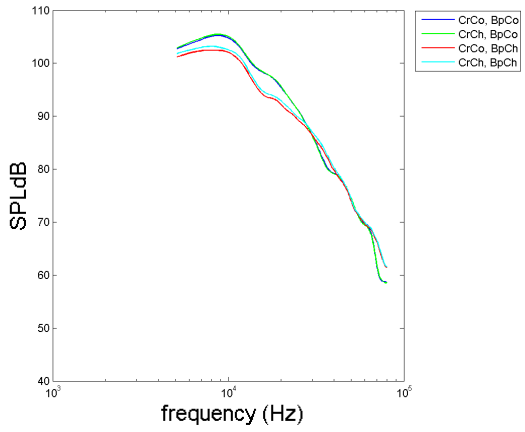

(f) x axis = $5D_{bp}$

Figure 8.19: Sound and frequency distribution at different axial positions with y=0 (colour bar in SPLdB)

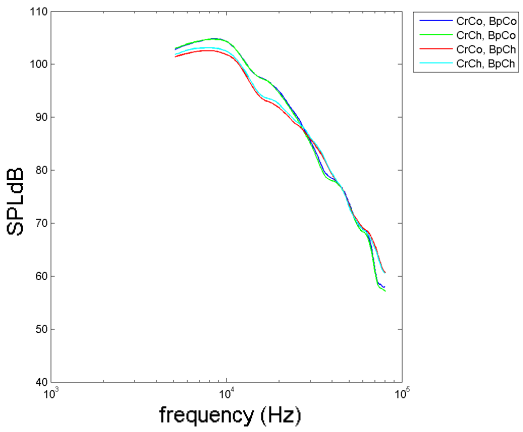

(a) x axis = $6D_{bp}$

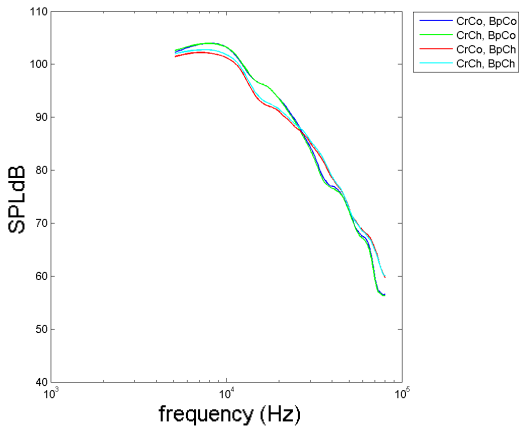

(b) x axis = $7D_{bp}$

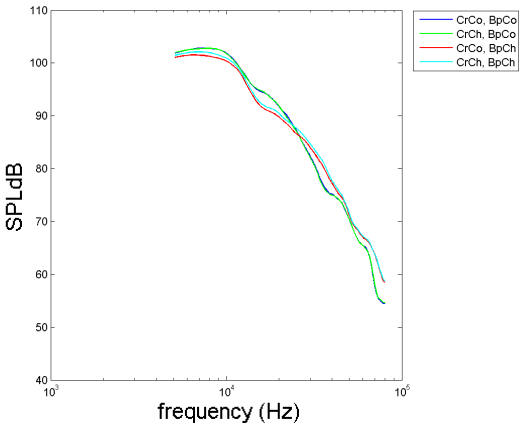

(c) x axis = $8D_{bp}$

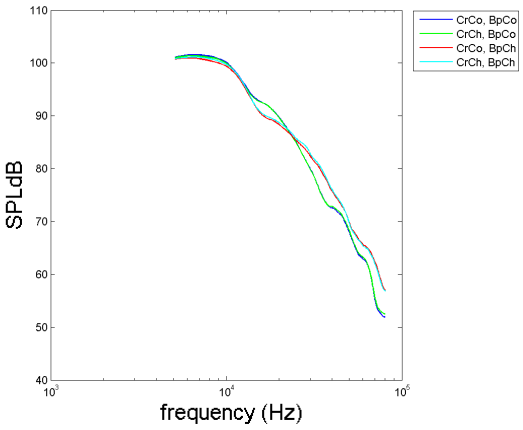

(d) x axis = $9D_{bp}$

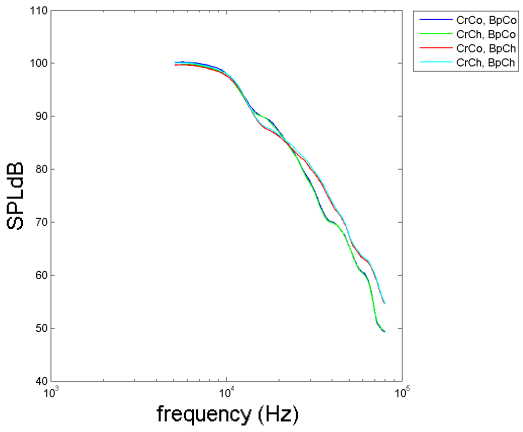

(e) x axis = $10D_{bp}$

Figure 8.20: Continued... Sound and frequency distribution at different axial positions with y=0 (colour bar in SPLdB)

8.1.3 Discussion of the acoustic results

The first observation is the effect the chevron nozzles have on the sound source maps in Figure 8.3 to Figure 8.6. There is little difference when the core chevron nozzle replaces the core cowl nozzle. More notable differences occur when the bypass chevron nozzle replaces the bypass cowl nozzle.

At 5 kHz, the dominating sound sources appear to be centred around $\sim 5D_{bp}$ downstream in the BpCo cases and $\sim 6D_{bp}$ downstream in the BpCh cases. There is also a reduction in sound intensity of about 1.25 SPLdB. From the literature review in Chapter 2, we know low frequencies dominate in the fully developed and transition region of the jet and have the larger SPLdB values compared with mid and high frequencies.

The radiation of sound at this frequency (0.37 St) appears to be approximately circular in shape. Due to the mirror's limit of resolution, it interprets the low frequency noise essentially as a point source with large radiation. As the frequency approaches 20 kHz (1.5 St), the resolution of the acoustic mirror improves and the mapping of the sound radiation takes an oval form as can be seen in Figure 8.4.

At around 35 kHz, an interesting result starts to emerge. A dominating sound source region is observed at the base of the sound source map. This region, in a physical context, lies just past the bullet tip. The sound observations as shown in Figure 8.5 represents the noise generated from the shedding of vortices from the bullet tip to form the bullet wake. The bullet wake is not observed in the low frequency sound source maps, its radiation lies in the frequencies in excess of 35 kHz. The presence of the bullet wake affects the general shape of the map,

changing it from an oval shape at low frequencies to a spear head shape at the mid-range frequencies (>2.62 St).

Another point of interest is the change in sound pressure levels with different nozzles. At frequencies less than 25 kHz, nozzle combinations involving the bypass cowl (i.e. CrCo, BpCo and CrCh, BpCo) produce greater sound pressure levels, both in terms of the maximum recorded and the region occupied in the sound source maps, than their counterpart bypass chevron nozzles. From 25 kHz to 35 kHz, the reverse starts to occur. In Figure 8.5 the central dominating region in (b)CrCo, BpCh and (d)CrCh, BpCh has higher SPLdB and occupies a larger region of the map than the nozzles using the bypass cowl. This dominance by the bypass chevron nozzles continues through to the high frequencies as shown at 65 kHz in Figure 8.6, which also shows an elongation in the central region compared with the bypass cowl nozzles.

The change in the central regions can also be seen using radial profiles at different positions downstream. These y-axis measurements going across the jet reveals the spread of the radiated sound in this axis and emphasize the general shape of the sound source maps. At 5 kHz as shown in Figure 8.7, the centre of the dominating sound region for (a)CrCo, BpCo and (b)CrCh, BpCo lies at $5D_{bp}$ to $6D_{bp}$ downstream, where as for (c)CrCo, BpCh and (d)CrCh, BpCh the centre lies at $6D_{bp}$ to $7D_{bp}$. That is, the bypass chevron nozzle has pushed the low frequency sound region $1D_{bp}$ further downstream. All four plots have a slight curve to their profile, that is the SPLdB at the ends of a line plot are only slightly lower than the centre of the line plot. This implies there is little variance in the SPLdB values at the low frequencies in the radial direction.

At 20 kHz, the centre of the dominating sound region for all nozzle combinations lies at $3D_{bp}$ to $4D_{bp}$ downstream. The profiles, as shown in Figure 8.8 have more curvature than the low frequency plots in Figure 8.7, indicating a significant drop off in the sound pressure levels at the ends of the line plots compared with the centre.

Figure 8.8 line plots of (c)CrCo, BpCh and (d)CrCh, BpCh are more closely clustered than the line plots in (a)CrCo, BpCo and (b)CrCh, BpCo implying that there is a smaller change in the sound pressure levels downstream with the bypass chevron nozzle than with the bypass cowl nozzle. The CrCo, BpCh and CrCh, BpCh line plots also have a narrower width in their profile than the CrCo, BpCo and CrCh, BpCo line plots which reflects the narrower sound source region shown in Figure 8.4. These trends continue past 35 kHz as shown in Figure 8.9 and Figure 8.10.

In addition to the radial distribution of sound, the distribution of sound downstream can be seen by taking line plots in the axial direction. Figure 8.11 shows at 5 kHz, there is little difference in the sound pressure levels between axial lines taken at different radial positions. However as the frequency increases, the line plots quickly separate as can be seen at 20 kHz in Figure 8.12.

The sound from the bullet wake starts to emerge at 35 kHz and is seen as the initial peak at $0D_{bp}$ to $1D_{bp}$ in Figure 8.13. Its presence continues through to higher frequencies as shown in Figure 8.14. This is more prominent with the nozzles involving the bypass chevron which could be due to the increased mixing in the flow induced by the chevrons.

A comparison of all four nozzle combinations can be seen more clearly by taking, for example each combinations centreline plot and overlaying it onto a graph. Examples of these type of plots can be seen in Figure 8.15. In the entire frequency range of 5 kHz to 80 kHz, the peak in SPLdB for all nozzles was found to occur at about 7.5 kHz to 10 kHz (0.56 St to 0.75 St). At this frequency band there is a ∼3 dB reduction in the peak of the line plots using the bypass chevron nozzle instead of the bypass cowl nozzle.

At frequencies less than 25 kHz the sound generated from the bypass cowl nozzle has larger SPLdB values than the bypass chevron nozzle. As the frequency approaches 30 kHz, the line plots start to converge and the SPLdB differences between them become minimal as shown in Figure 8.16. At ∼30 kHz, there appears to be cross over where the sound generated by the bypass chevron nozzle exceeds the bypass cowl nozzle. In Figure 8.16 this occurs at $\sim 5D_{bp}$ for the (a)Centre line and (b)Centre line + $0.5D_{bp}$ plots and at $\sim 6D_{bp}$ for the (c)Centre line + $1D_{bp}$ and (d)Centre line + $1.5D_{bp}$ plots. The presence of the cross over of the axial line plots, where the SPLdB from the bypass chevron nozzle is in part lower than the bypass cowl nozzle and in part higher, generally continues until ∼65 kHz. At frequencies higher than this, the line plots using the bypass chevron nozzle outright exceed the SPLdB values from the bypass cowl nozzle as shown in Figure 8.17.

The distribution of sound pressure levels and frequency taken on the centre line of the jet at y=0, can be seen in Figure 8.18. Near the nozzle exit at x=$0D_{bp}$, more noise (higher SPLdB) is radiated from the BpCh plots than the BpCo plots from about 30 kHz onwards (2.25 St). At lower frequencies the reverse is true. Figure 8.19 and Figure 8.20 provide further details of this occurrence. In these plots,

CrCo, BpCo and CrCh, BpCo have very similar spectra as do CrCo, BpCh and CrCh, BpCh. The spectral peaks at $0D_{bp}$ to $10D_{bp}$, with respect to the Strouhal number and frequency, can be seen in Table 8.1.

x/D_{bp}	CrCo, BpCo	CrCh, BpCo	CrCo, BpCh	CrCh, BpCh
0	0.56 (7,424)	0.48 (6,400)	0.42 (5,632)	0.48 (6,400)
1	0.61 (8,192)	0.61 (8,192)	0.48 (6,400)	0.56 (7,424)
2	0.61 (8,192)	0.61 (8,192)	0.56 (7,424)	0.56 (7,424)
3	0.73 (9,728)	0.67 (8,960)	0.48 (6,400)	0.73 (9,728)
4	0.61 (8,192)	0.61 (8,192)	0.61 (8,192)	0.61 (8,192)
5	0.67 (8,960)	0.67 (8,960)	0.56 (7,424)	0.61 (8,192)
6	0.61 (8,192)	0.61 (8,192)	0.61 (8,192)	0.61 (8,192)
7	0.61 (8,192)	0.61 (8,192)	0.54 (7,168)	0.61 (8,192)
8	0.48 (6,400)	0.56 (7,424)	0.48 (6,400)	0.48 (6,400)
9	0.48 (6,400)	0.42 (5,632)	0.42 (5,632)	0.48 (6,400)
10	0.42 (5,632)	0.42 (5,632)	0.48 (6,400)	0.42 (5,632)

Table 8.1: Spectral peaks at y=0, Strouhal number (frequency)

The average peak value and standard deviation (s.d.) for each of the nozzle combinations are CrCo, BpCo = 0.58(0.09), CrCh, BpCo = 0.57(0.09), CrCo, BpCh = 0.50(0.06), CrCh, BpCh = 0.56(0.01). The bypass chevron results have a lower mean Strouhal number and s.d. than the bypass cowl results. This suggests the frequencies at which the SPLdB peaks downstream is on average lower with the BpCh nozzle than with the BpCo nozzle. The peak frequencies from the BpCh nozzle are also more clustered around their mean than those from the BpCo nozzle which have greater variation.

The results from this thesis are now compared with a selection of results from other authors. A comparison is first made with the results from Drobietz *et al.* (2008), who used an acoustic mirror of diameter 0.2 m angled at 90 ° to the jet axis. The jet was a single hot jet running at a high subsonic Mach number. The temperature and flow velocity were not stated. Efforts were made to obtain this information from the authors (by email and by telephoning EADS, Germany), but they have left the company with no forwarding address.

Therefore three different temperature and flow velocity were chosen for the purposes of comparing results. Three sets of conditions or scenarios for Drobietz data are presented in Table 8.2. The first scenario 'a)' matches the temperature and flow velocity with the co-axial jet conditions at Warwick of 20 ° (293 K) and 240 ms^{-1}. Warwick however uses an unheated jet, therefore the second scenario 'b)' is arbitrarily chosen to have a temperature of 100 ° or 373 K, operating at 0.8 Ma. This gives the speed of sound in air under standard atmospheric conditions to be 387 ms^{-1}, implying the flow velocity (at 0.8 Ma) is 310 ms^{-1}. The third scenario 'c' has the same temperature and flow velocity as CoJeN, 606 ° (880 K) and 481 ms^{-1}. For each jet condition, the frequencies used by Drobietz and the corresponding Strouhal numbers can also be seen in Table 8.2.

Temperature and velocity	Strouhal number	Corresponding frequency (kHz) for Drobietz	Corresponding frequency (kHz) for the present data
a) 20°C, 240 ms^{-1}	0.92	1.0	12.2
	1.47	1.6	19.6
	2.29	2.5	30.6
	4.58	5.0	61.1
b) 100°C, 310 ms^{-1}	0.71	1.0	9.5
	1.13	1.6	15.1
	1.77	2.5	23.7
	3.55	5.0	47.3
c) 606°C, 481 ms^{-1}	0.46	1.0	6.1
	0.73	1.6	9.8
	1.14	2.5	15.2
	2.29	5.0	30.5

Table 8.2: Jet condition scenarios for Drobietz data

A comparison of the results from Drobietz and the results presented in this thesis, for the lowest and highest Strouhal numbers, for each jet condition can be seen in Figure 8.21. The actual SPLdB values are not stated by Drobietz but a grid spacing of 5 SPLdB is given. Therefore the results are shown as separate subplots. The trends between Drobietz and the present data show good overall agreement. At the lower Strouhal numbers (plots a), c), e)), Drobietz and the present results both show the baseline nozzle (i.e. without chevrons) to generally have higher SPLdB, than the chevron nozzles by about 3 dB from $1D_{jet}$ to

$8D_{jet}$ (note, for the present data D_{jet}=D_{bp}). The difference in SPLdB dramatically drops after this point but the baseline nozzles still have a higher SPLdB. At the higher Strouhal numbers (plots b), d), f)), the SPLdB for the chevron nozzles are higher to begin with at $0D_{jet}$. However this is soon over taken by the baseline nozzle at around $0D_{jet}$ for Drobietz and $1D_{bp}$ for present results, before the chevron nozzles cross back to being the higher SPLdB at around $9D_{jet}$ for Drobietz and $6D_{bp}$ for present results.

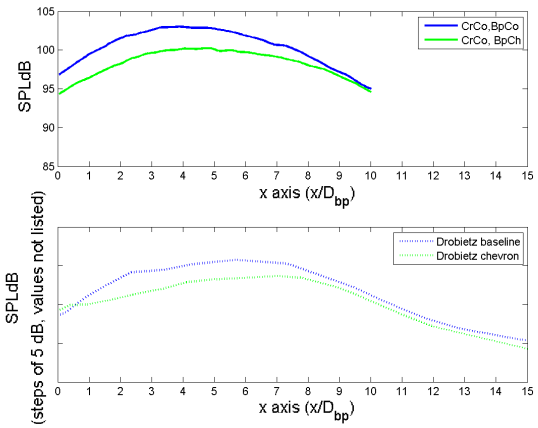

(a) jet condition=a, St=0.92

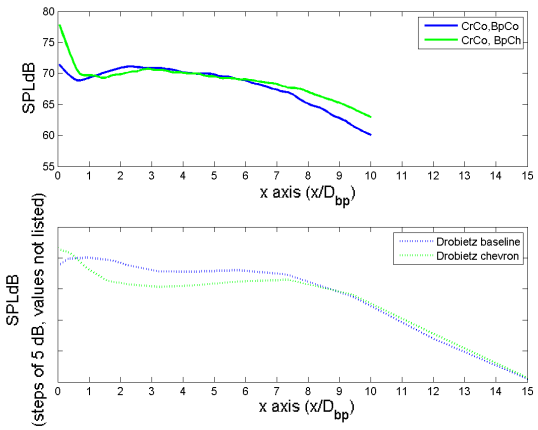

(b) jet condition=a, St=4.58

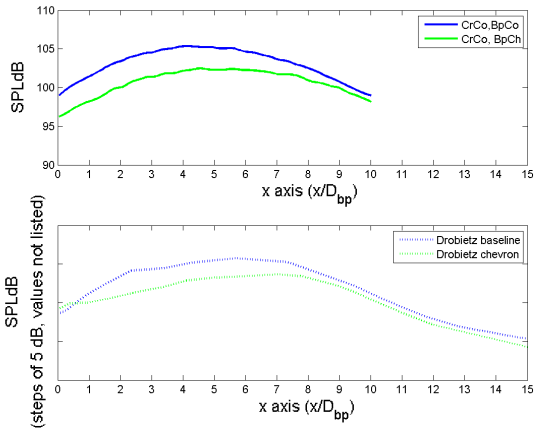

(c) jet condition=b, St=0.71

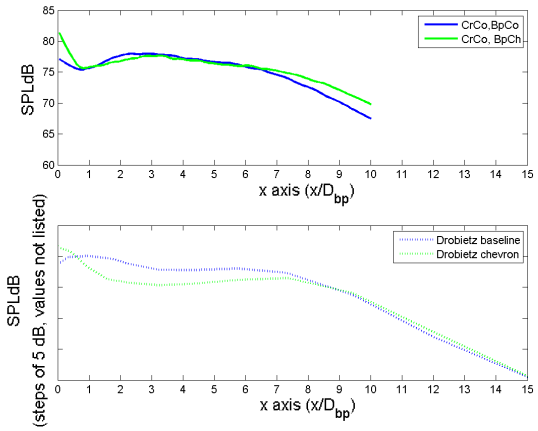

(d) jet condition=b, St=3.55

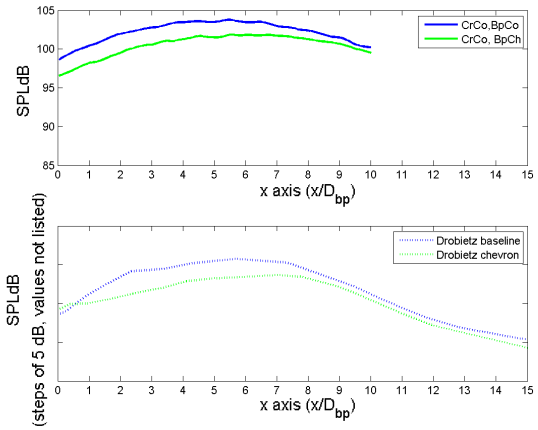

(e) jet condition=c, St=0.46

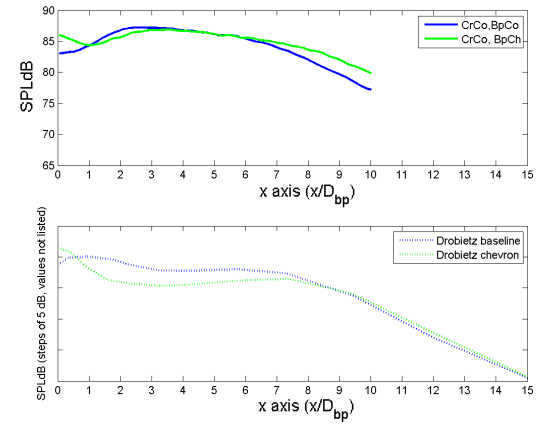

(f) jet condition=c, St=2.29

Figure 8.21: Comparison of Drobietz data with the present data

Fayard *et al.* (2008) uses the DLR (*Deutsches Zentrum für Luft−und Raumfahrt e.V., Germany*) experimental data from CoJeN and compares this with the numerical simulations (LES) from ONERA (*Office National dEtudes et Recherches Aérospatiales, France*). The test conditions using the short cowl geometry are 481 ms^{-1} and 307 ms^{-1} for the core and bypass velocity with corresponding temperatures of 880 K and 335 K. The acoustic survey was taken from a line array following the jet expansion downstream. A comparison of these results against the work in this thesis can be seen in Figure 8.22. These were not over plotted as the SPLdB values are not listed by Fayard, however a difference of 20 SPLdB between tick points was given.

The the peak in spectra from the present data shows a fairly consistent occurrence at about ∼0.58 St in all three plots. The peaks from Fayard's experimental data develop into a consistent occurrence, starting off at ∼0.20 St near the 0 D_{jet}, then moving to and staying at ∼0.32 St from 3 D_{jet} onwards. The simulated results from Fayard follow a similar trend starting at ∼0.20 St and then stabilizing to ∼0.10 St.

The change in sound pressure level downstream can be seen in Figure 8.23. While there is a similar trend in that generally the SPLdB (averaged values) increases downstream from the bullet tip, peaks in the mid stream region and then starts to decrease, there is a little difference in location of the peak SPLdB values. In present data, this occurs at 2.9 D_{jet}, the simulated data shows a peak at 3.3 D_{jet} and the experimental CoJeN data peaks at 4.7 D_{jet}. Overall, there appears to be good agreement in the shape of the spectra except under 1 D_{jet}, where Fayard data noticeably drops by about 20 SPLdB, and the present data stays roughly within a 5 SPLdB band.

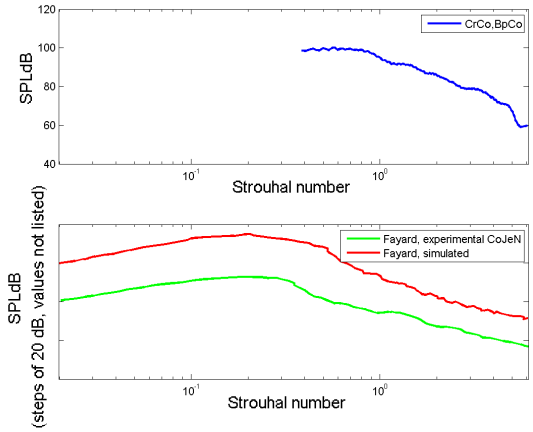

(a) $0D_{jet}$

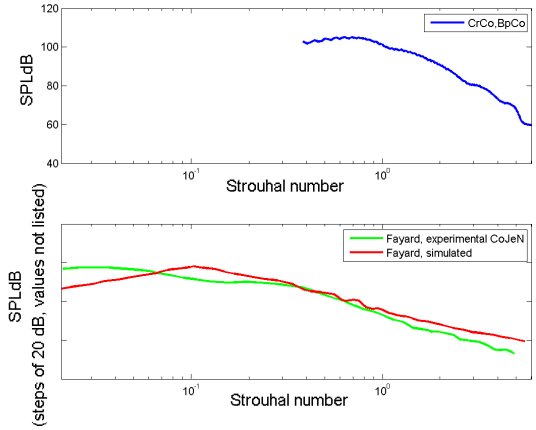

(b) $3.3D_{jet}$

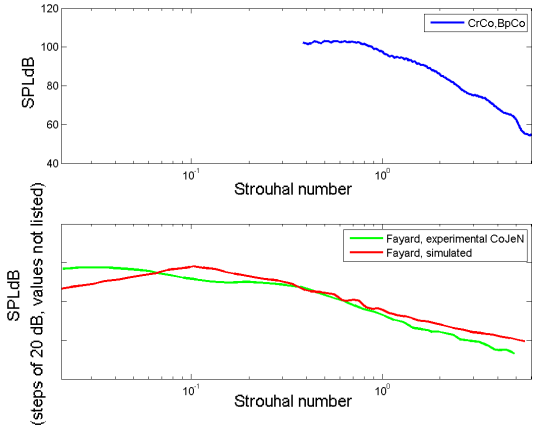

(c) $8D_{jet}$

Figure 8.22: Comparison of Fayard data with present data

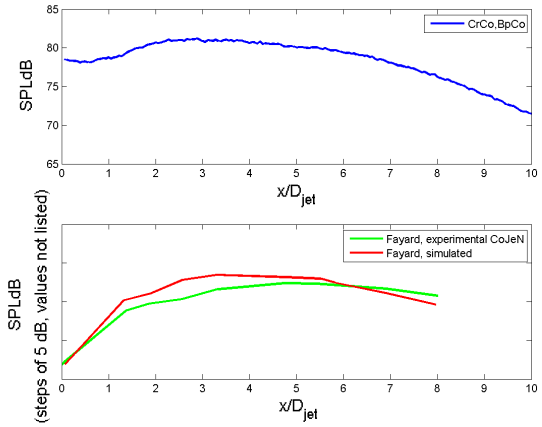

Figure 8.23: Overall SPLdB from Fayard and present results

For the same jet conditions as Fayard, Vuillot *et al.* (2008) compares the far field spectra from CoJeN for the short cowl case against the simulated acoustic results using LES. In this case, the microphone is not near the nozzle exit at 90° to the jet axis but is in the far field at 90° to the jet axis. The far field distance is $60D_{jet}$. An over plot of Vuillot's results with the results in this thesis is shown in Figure 8.24. Both the raw data and adjusted data are plotted. The adjusted values are derived by firstly removing the gain from the present data to provide the SPLdB at a known distance (0.8 m or $44.4D_{bp}$) from the centre line of the jet and then applying an adjustment of 2.6 dB to reflect the scaling of this distance to the $60D_{jet}$ (doubling the microphone distance logarithmically scales to a 6 dB drop in SPLdB).

There is good overall agreement in the spectral shape between Vuillot results and the present results. The spectral peak in the present unadjusted data occurs at ∼0.58 St. However, this peak has a low kurtosis, such that a range of 0.42-0.78 St contains values within 1 dB of the peak value. The peak value in the adjusted data occurs at 0.44 St with a peak band of 0.38-0.70 St. In Vuillot's experimental CoJeN data the peak is at 0.38 St and at about 0.35 St for the simulated data.

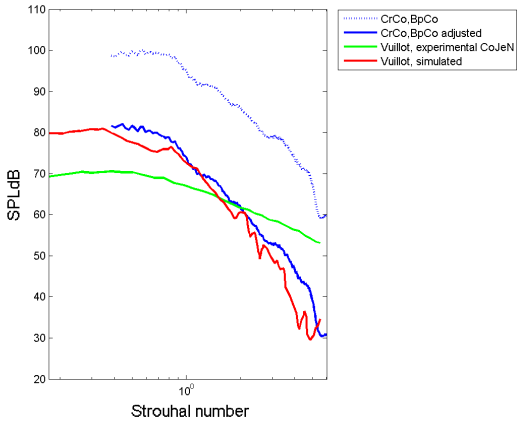

Figure 8.24: Comparison of Vuillot data and the present data

8.2 LDA investigation

8.2.1 LDA experimental arrangement

The LDA experimental arrangement as shown in Figure 8.25 was similar to the acoustic mirror experiments (Figure 8.1), except this time a LDA head was mounted on the traverse instead of the mirror. The dual head projected two green beams of wavelength 514.5 nm and two blue beams of wavelength 488.0 nm. Figure 8.26 shows the LDA head prior to being rotated by 45 °, which ensured that the average velocity measured by both beam pairs was approximately equal. This in turn equalized the error in the measurement of the two components of velocity. The beams converged above the bullet tip forming a measurement volume of dx=0.1248 mm, dy=0.1244 mm, dz=1.684 mm and dx=0.1183 mm, dy=0.1180 mm, dz=1.597 mm respectively.

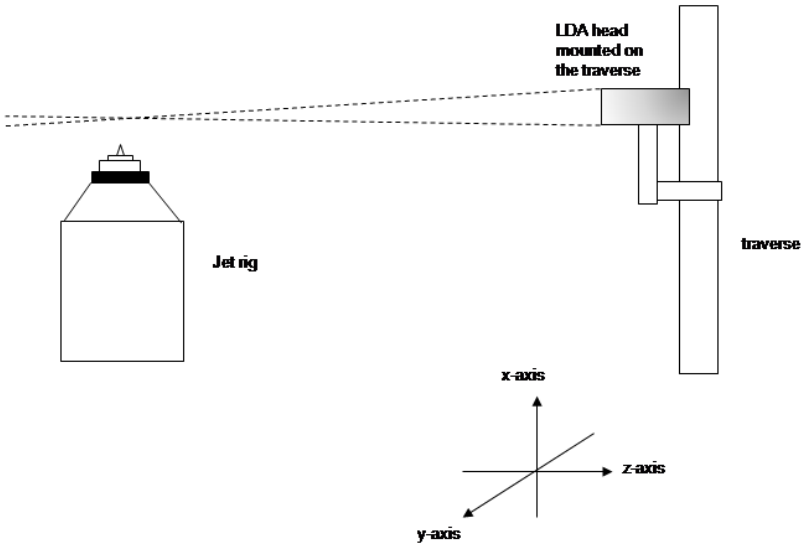

Figure 8.25: Experimental arrangement using the LDA

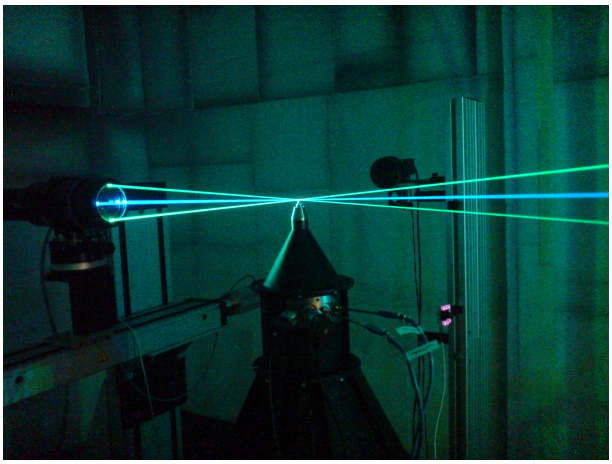

Figure 8.26: LDA system (photo taken before 45 °head rotation)

Matching the acoustic mirror experiments, a grid $4D_{bp}$ in the y-axis by $10D_{bp}$ in the x-axis with 1 mm spacing was generated (the z plane is fixed at z=0) with the initial position at the bullet tip registered with the BSA software as grid point x=0, y=0.

The co-flowing jet was run on condition with seeded oil particulates of 0.8 μm diameter. Flow measurements were taken sequentially for all 13,320 grid points,

for all four nozzle combinations, with the central jet regions having a data rate of ∼20 kHz and validation reading of ∼80% with coincidence. Velocity profiles of the flow were produced using Matlab.

8.2.2 Selection of LDA results

The full set of LDA results can be seen in the Appendix.

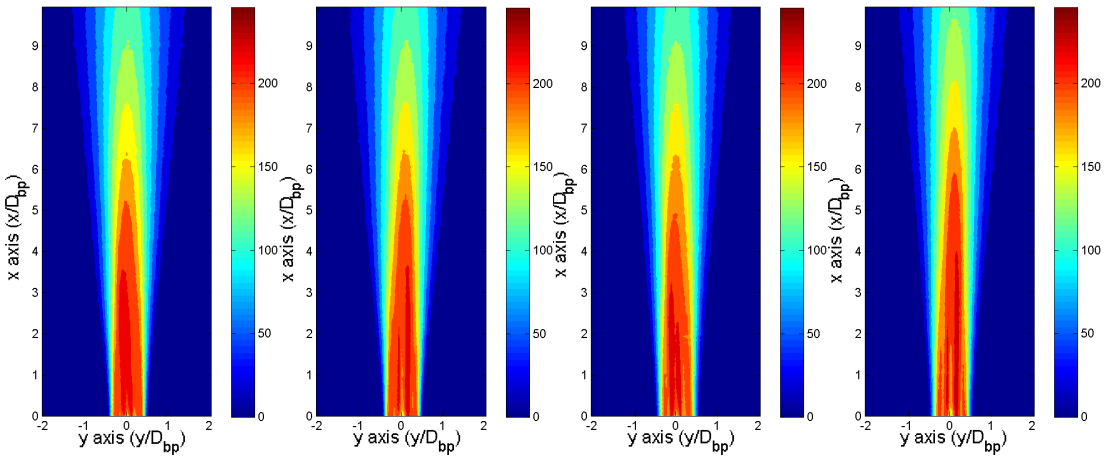

(a) CrCo, BpCo (b) CrCh, BpCo (c) CrCo, BpCh (d) CrCh, BpCh

Figure 8.27: Axial velocity (colour bar in ms^{-1})

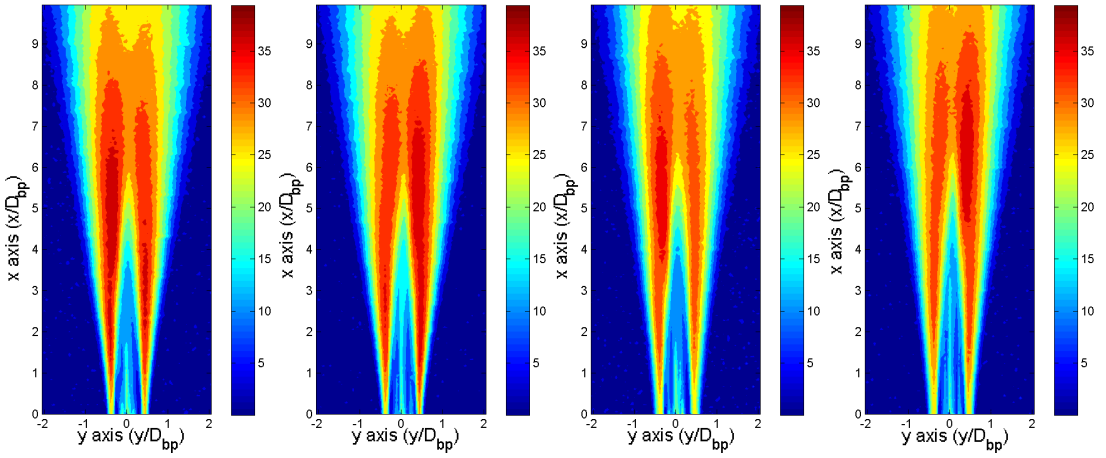

(a) CrCo, BpCo (b) CrCh, BpCo (c) CrCo, BpCh (d) CrCh, BpCh

Figure 8.28: Axial rms (colour bar in ms^{-1})

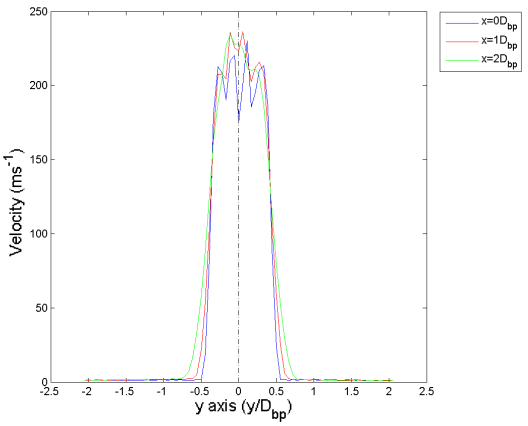

(a) CrCo, BpCo

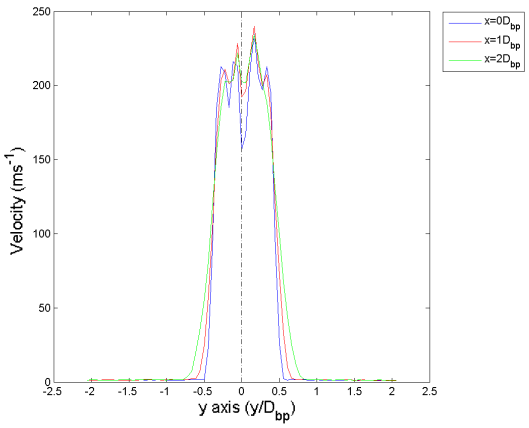

(b) CrCh, BpCo

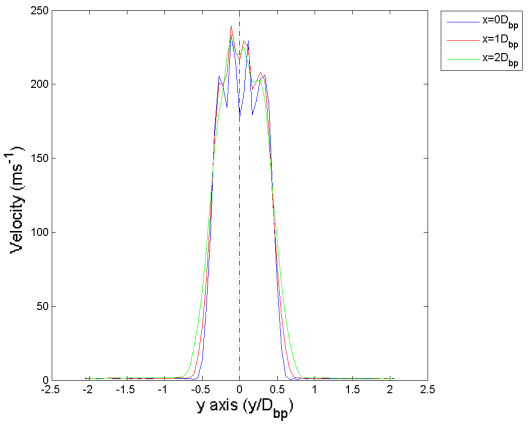

(c) CrCo, BpCh

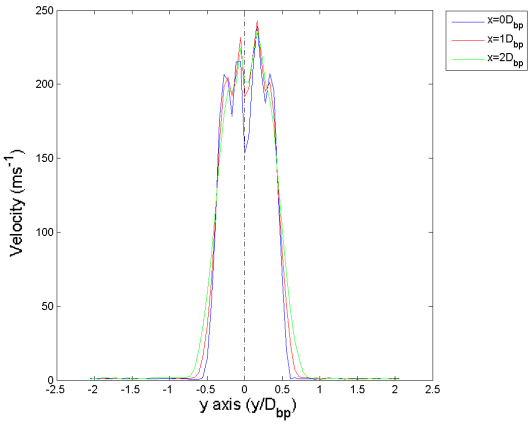

(d) CrCh, BpCh

Figure 8.29: Axial velocity profile

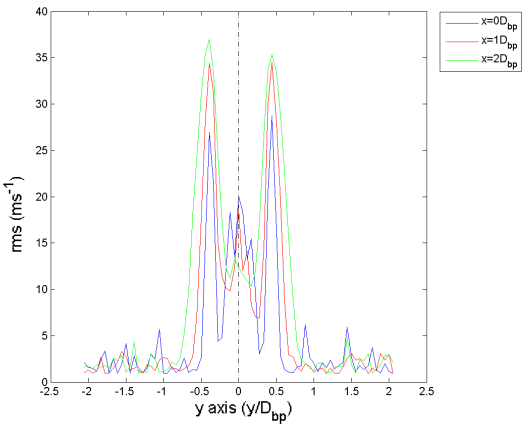

(a) CrCo, BpCo

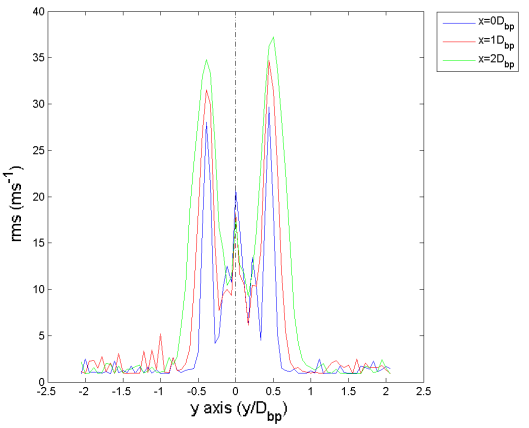

(b) CrCh, BpCo

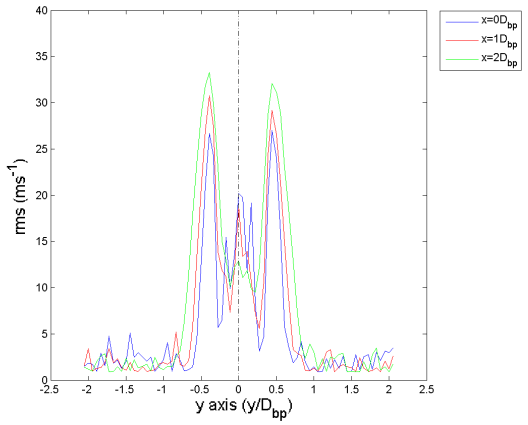

(c) CrCo, BpCh

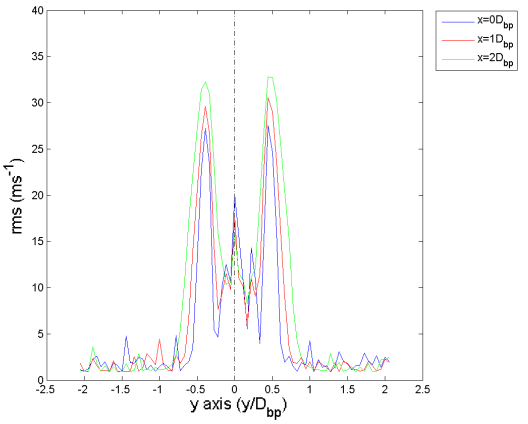

(d) CrCh, BpCh

Figure 8.30: Axial rms profile

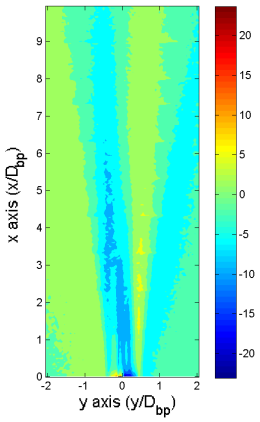

(a) CrCo, BpCo

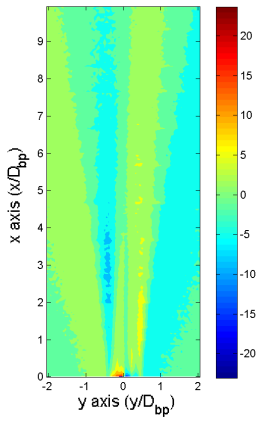

(b) CrCh, BpCo

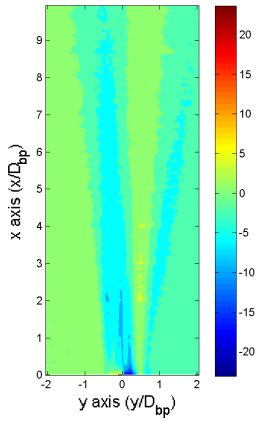

(c) CrCo, BpCh

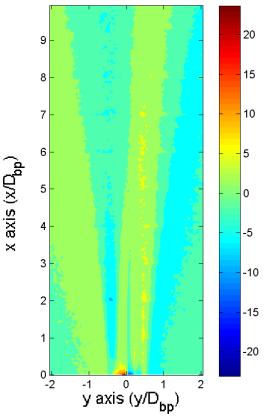

(d) CrCh, BpCh

Figure 8.31: Radial velocity (colour bar in ms^{-1})

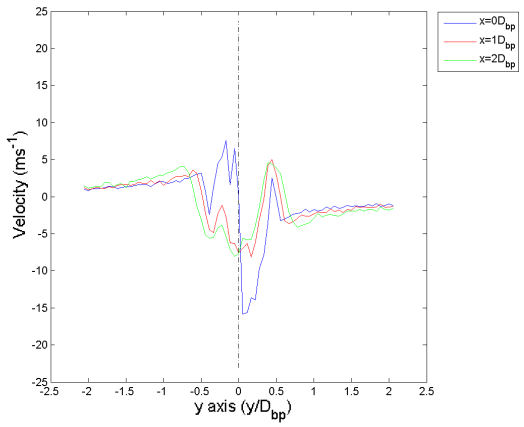

(a) CrCo, BpCo

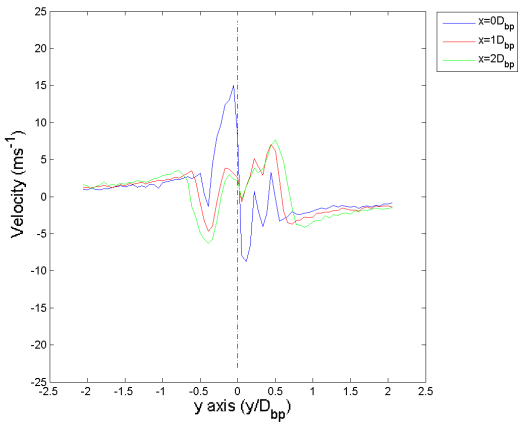

(b) CrCh, BpCo

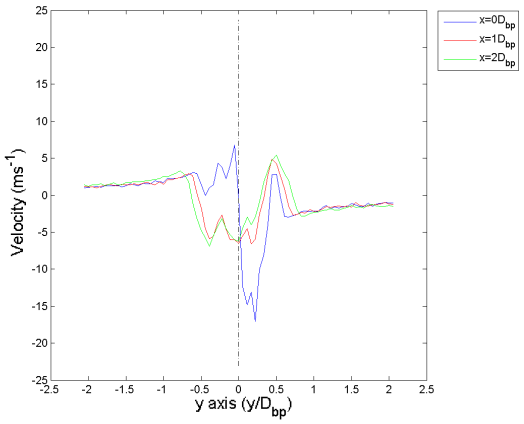

(c) CrCo, BpCh

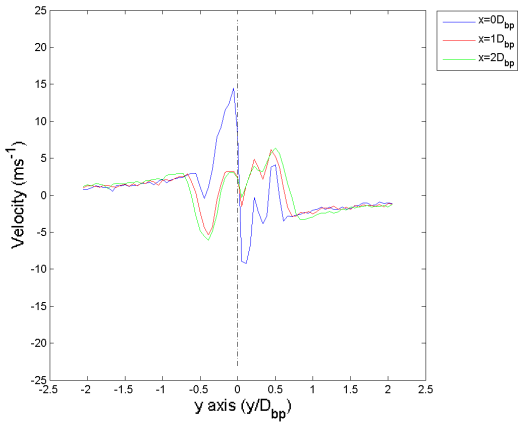

(d) CrCh, BpCh

Figure 8.32: Radial velocity profile

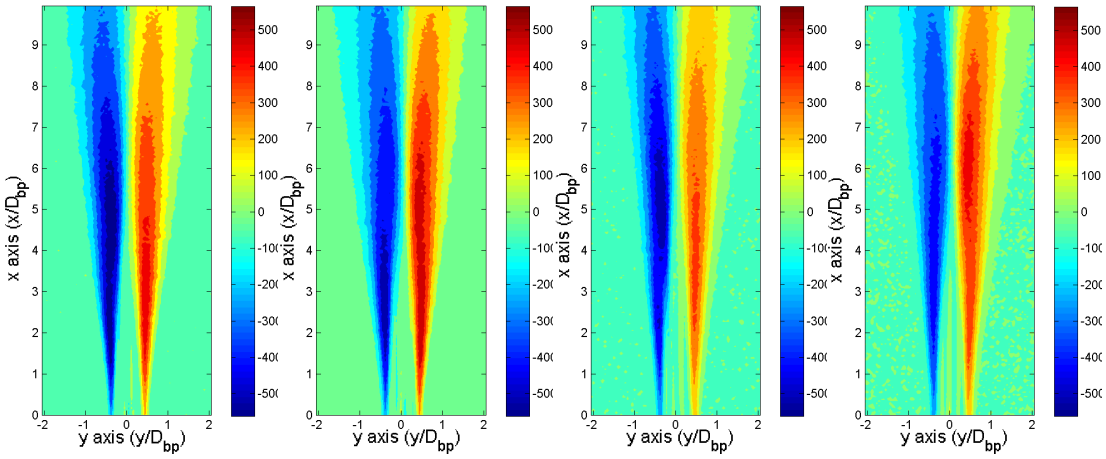

(a) CrCo, BpCo (b) CrCh, BpCo (c) CrCo, BpCh (d) CrCh, BpCh

Figure 8.33: Reynolds shear stress UV (colour bar in m^2s^{-2})

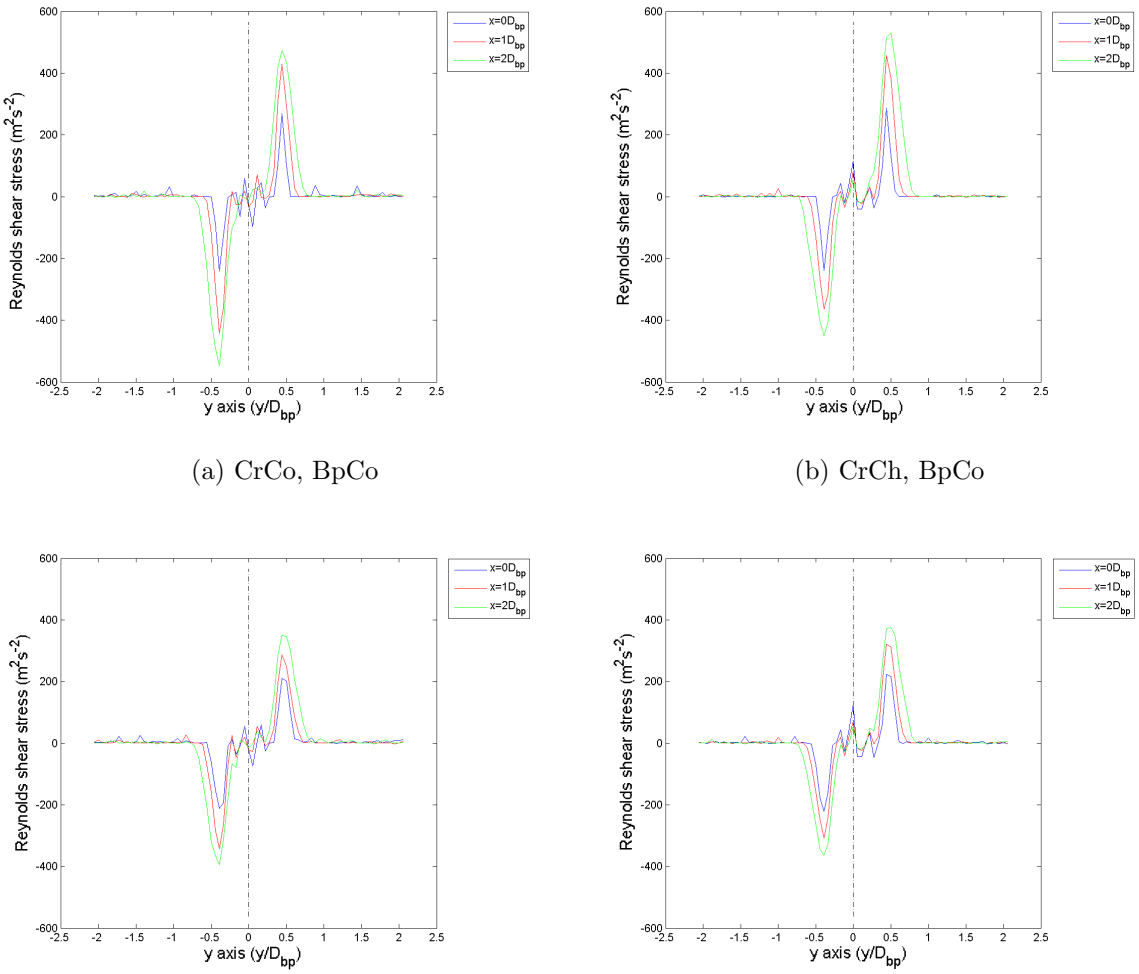

(a) CrCo, BpCo

(b) CrCh, BpCo

(c) CrCo, BpCh

(d) CrCh, BpCh

Figure 8.34: Reynolds shear stress UV profile

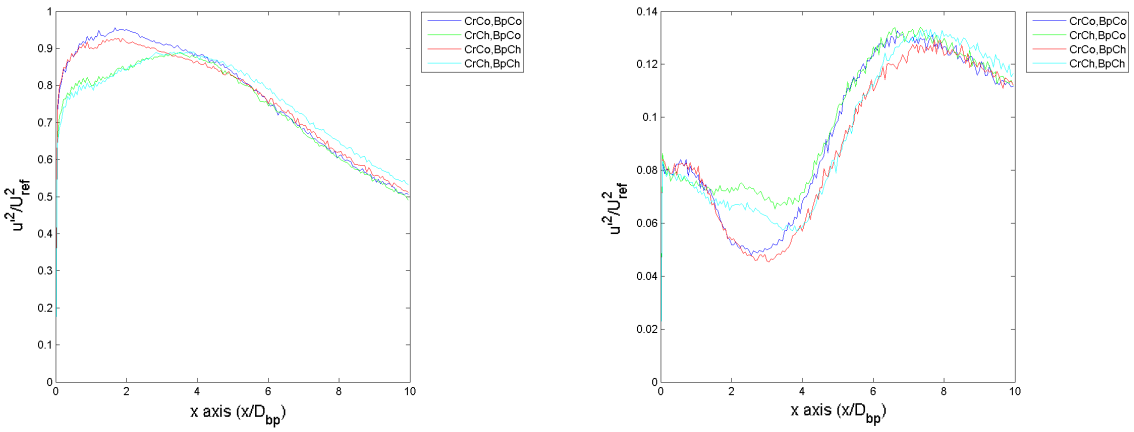

(a) mean velocity (b) turbulence intensity

Figure 8.35: Axial velocity and turbulence intensity profiles at y=0

8.2.3 Discussion of the LDA results

The 2D axial velocity and axial rms of the jet on condition is shown in Figure 8.27 and Figure 8.28 and highlights the flow output for all four nozzle combinations. Flow velocities downstream at the fully developed region at around $\sim 6D_{bp}$ appears to be noticeably higher in the CrCh, BpCh case, compared with all other cases. A check of the axial velocity profile at $0D_{bp}$ for all the nozzle combinations reveals the flow velocities are all close to 240 ms^{-1} which suggests the higher velocities observed at $\sim 6D_{bp}$ downstream with the CrCh, BpCh, is unlikely to be due to operating condition error.

The distortions or asymmetry observed in Figure 8.27 could be attributed by the state and thickness of the boundary layer at the nozzle exit. Hussain & Clark (1977) found using a single subsonic jet, the rate of spreading of the jet, the centreline decay of the mean velocity and the kinematic and geometric 'virtual origin' was influenced by the laminar or turbulent condition of the initial boundary layer. Under a laminar boundary layer the vortical structures developed in

the shear layer surrounding the jet, enhanced entrainment and mixing compared with a turbulent initial boundary layer. Hussain & Zaman (1981), Bradshaw (1966), Antonia & Zhao (2001) and others have investigated the effects of a laminar or turbulent boundary layer on the flow dynamics and concluded there is a correlation between the initial conditions and the jet development. While the state and thickness of the boundary layer at the nozzle exit affects the flow dynamics, (Viswanathan & Clark, 2004b; Viswanathan, 2008) found it did not influence the radiated noise. In his work, the state of the boundary layer had no impact on scaled model engine noise comparisons, which were laminar in scaled model tests and turbulent in full scale tests.

The nozzle lip thickness is also a source for influencing the boundary layer. Ponton & Seiner (1992) observed that changing the lip thickness affected the flow dynamics. As the lip thickness was increased from 0.015 to 0.625 nozzle diameters, the momentum thickness changed, inducing more entrainment, mixing and shear layer disturbance. These affects were supported by Kima & Lee (2007).

The conical contraction of the of jet rig also contributes to the development of the boundary layer as described by Moore (1977) who compared the boundary layer thickness from a subsonic jet using two identical nozzles that had different internal geometries. One nozzle was attached to conical contraction section and the other was attached to parallel section. The boundary layer upon exit was thinner in the conical contraction case than in the parallel section case. Similar to the axial rms plots in Figure 8.30, Moore used turbulence intensity plots to highlight the difference in the boundary layers which revealed the large area conical contraction produced a laminar flow, and the parallel section generated a turbulent flow.

The axial velocity radial profiles shown in Figure 8.29 show four peaks in each line plot. These are more distinct for measurements near the nozzle exit at $0D_{bp}$ and $1D_{bp}$. At $2D_{bp}$ the peaks start to become less apparent. The two outer peaks represent the flow velocity exiting the bypass nozzle, the two inner peaks represent the flow velocity exiting the core nozzle with the dip between them being due to the presence of the bullet and the inner shear layer.

Radial profiles of the rms can be seen in Figure 8.30. In each plot, the centre peak represents the bullet wake, the outer peaks outline the presence of the outer shear layer between flow from the ambient and bypass nozzle and the inner peaks represent the inner shear layer formed between the flow from the bypass and the core nozzle. This is weaker than the outer shear layer as velocity difference between the bypass and core is less than the bypass and ambient flow.

A point to note here is that the plots with a chevron nozzle have a wider shear layer than ones with a cowl nozzle. That is, the bypass chevron nozzle produces a wider outer shear layer than the bypass cowl nozzle and to a lesser extent, the core chevron nozzle does the same for the inner shear layer when compared with the core cowl nozzle.

A theoretical value for boundary layer thickness at the nozzle exit can be estimated using the Blasius boundary layer equation (as shown in Equation 8.1.

$$\delta_{bl} \approx (\frac{\nu_{re} D_{jet}}{V_{re}})^{0.5} \tag{8.1}$$

With the mean velocity of the core jet $V_{re} = 240\ ms^{-1}$, the kinematic viscosity

of air at standard atmospheric pressure at room temperature $\nu_{re} = 1.45 \times 10^{-5}$ $m^2 s^{-1}$ and the bypass jet diameter of $D_{jet} = 0.018$ m, the boundary layer δ_{bl} is 0.033 mm which is $0.002 D_{jet}$.

In practice however, the boundary layer is larger due to various factors such as conical contraction, quality of machining, smoothness of nozzle lip and nozzle lip thickness. Moore (1977) implied a boundary thickness of $\sim 0.07 D_{jet}$ for the conical section case. Shur *et al.* (2003) provided an approximation to the boundary layer thickness of $\sim 0.03 D_{jet}$ by numerical simulation, which is consistent with Bogey *et al.* (2009) who found $\sim 0.032 D_{jet}$ by LES and Arakeri *et al.* (2003) who proposed $\sim 0.035 D_{jet}$ by experiment. Based on these approximations the boundary layer thickness at the nozzle exit of the co-axial jet at Warwick can be expected to be $\sim 0.03 D_{bp}$ which is 0.54 mm.

Although Figure 8.30 provides a good imprint of the flow dynamics, there is scope for improvement with the spatial resolution. Under the current grid spacing of 1 mm, the inner shear layer can be completely surpassed in three points in the y-axis. This means that its displayed peak in the plots is unlikely to be the actual peak but is more likely to represent the area in which the peak lies. The same principle applies to the outer shear layer. There is also a velocity bias due to the finite size of the LDA measurement volume, which means that the velocity at the peaks in Figure 8.30 for example, is understated and the velocity at the troughs is over stated. The velocity bias in the measurements can be reduced by firstly refining the measurement grid spacing (i.e. making it smaller) near the nozzle exit, which would lead to an improved detection of the boundary layer and secondly if practical, reducing the finite size of the LDA measurement volume.

The velocity maps of the radial component as shown in Figure 8.31, indicate that the central jet flow pushes outwards while ambient flow is entrained. The difference in the flow entrainment between nozzle combinations can be seen more clearly in Figure 8.32. The core nozzle appears to be the more influencing factor in determining the shape of the profile rather than the bypass nozzle. That is, there is a more notable change in shape in changing from the core cowl nozzle to the core chevron nozzle than doing the same with the bypass nozzles.

The Reynolds shear stress representing the turbulent fluctuations for all four nozzle combinations can be seen in Figure 8.33 and Figure 8.34 which shows, as expected, the more turbulent regions are found downstream peaking at around $5D_{bp}$. The Reynolds shear stress is an important statistic for determining length scales and is especially useful in numerical simulations and turbulence models such as the $k - \epsilon$ model.

Figure 8.35 shows the mean velocity and the turbulence intensity profiles at the centre line of the jet (y=0). At 0-3D_{bp} the mean velocity is higher in the nozzle combinations with a core cowl nozzle than those with a core chevron nozzle. This loss in mean velocity could be attributed to vortex shedding off the chevron nozzle. From $3D_{bp}$ onwards the mean velocity in all nozzle combinations converges and is very similar. In the turbulence intensity profiles from 0-3.5D_{bp} the core chevron nozzle combinations have higher values overall compared with the core cowl nozzle combinations. The spectra for all nozzle combinations converges from $3.5D_{bp}$ onwards. As these results are taken at the centre line of the jet, it shows there the core chevron nozzle generates more turbulence and less overall mean velocity in its potential core than that from the core cowl nozzle.

The results from the present data are compared with a selection of CoJeN results. Firstly, a comparison of experimental CoJeN data and simulated data from Fayard *et al.* (2008) for the flow conditions described in the acoustic discussion are shown in Figure 8.36. In the mean velocity profile, all three line plots peak at about $1.8D_{bp}$ and then decline downstream. The sharpest decline is the simulation data followed by the experimental CoJeN data and then the present data.

The mean velocity profiles show the present data has a peak with the lowest kurtosis, which means that its peak has the largest spread. This spread of high mean velocity is reflective of the potential core, which implies that the present data has the longest potential core, followed by the experimental CoJeN data and the simulation data. As described in Chapter 2 the transition region at the end of the potential core has comparatively high turbulence, with the fully developed region containing the peak turbulence. Figure 8.37 shows the peak in turbulence intensity occurs at about $6.5D_{Bp}$ for the present data, $5D_{Bp}$ for the experimental CoJeN data and $3.5D_{Bp}$ for the simulation data highlighting the fully developed region.

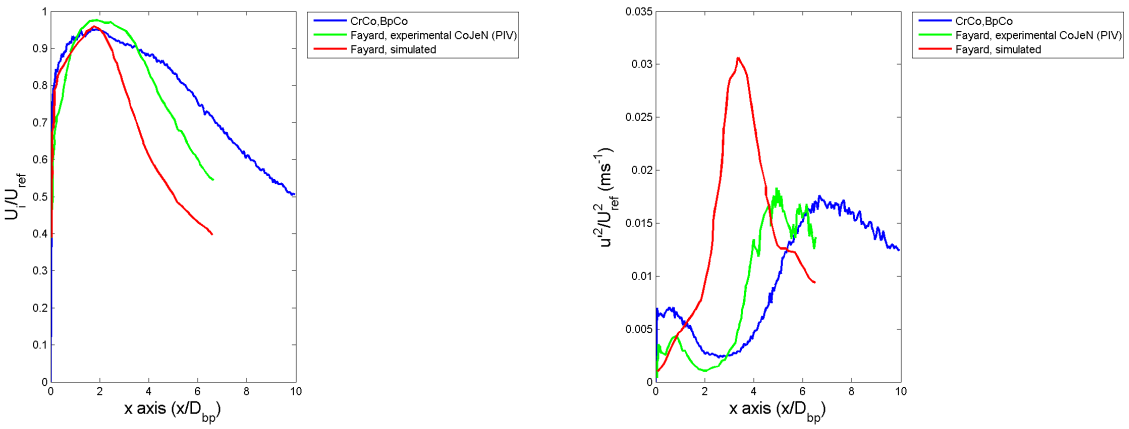

(a) velocity profile

(b) turbulent intensity profiles

Figure 8.36: Flow comparisons of Fayard and the present data along the centreline of the jet

A comparison of the velocity profile and turbulent intensity profile at $0.46D_{jet}$ and $3.2D_{jet}$ downstream (position chosen to match Fayard data) can be seen in Figure 8.37. There is good overall agreement of results in these plots. In the velocity profile at $0.46D_{jet}$, the present data shows four peaks, two of which are at $\pm 0.5D_{jet}$. This represents the bypass flow velocity which when expressed over the reference core velocity gives a value of 0.90 ($215\ ms^{-1}/240\ ms^{-1}$). The CoJeN flow conditions as shown by Fayard have a value of 0.64 ($307\ ms^{-1}/481\ ms^{-1}$) which is why the Fayard data shows two small bumps at this value while the present data shows two peaks at 0.90. At $3.2D_{jet}$ downstream, the mean velocity for the three experimental results all show a peak in excess of 0.90, where as the simulated data peaks at about 0.76. This again supports the notion that the simulated data has a shorter potential core than the experimental data. In the turbulence intensity profile at $0.46D_{jet}$, there is good agreement with the location and intensity of the peaks at $\pm 0.5D_{jet}$ which are representative of the outer shear layer. The inner shear layer occurring at about $\pm 0.25D_{jet}$ is not apparent in the present data. This is most likely due to the 1 mm grid spacing used

for measurements which was unable to fully capture the relatively small inner shear layer. Further downstream at $3.2D_{jet}$, differences between the turbulence intensity profiles are emerging. Fayard attributes the differences to experimental causes including the flow asymmetry of the jet.

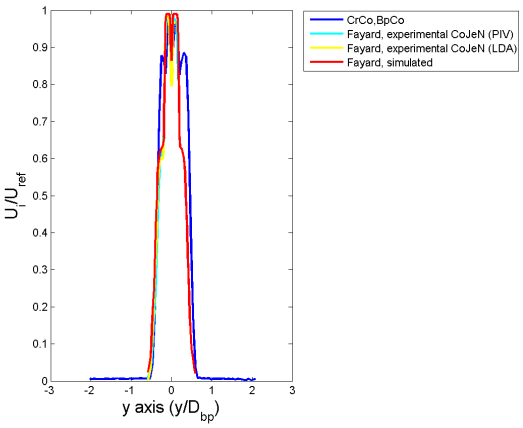

(a) velocity profile at 0.46 D_{jet}

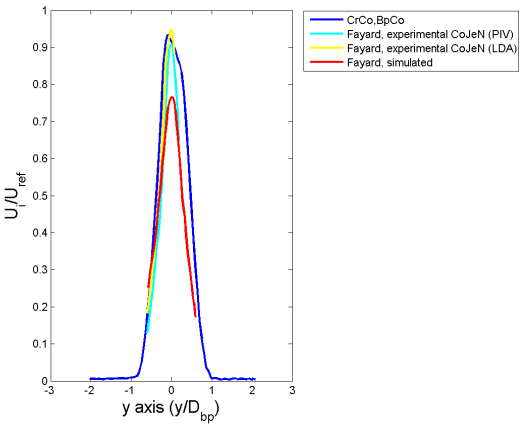

(b) velocity profile at 3.2 D_{jet}

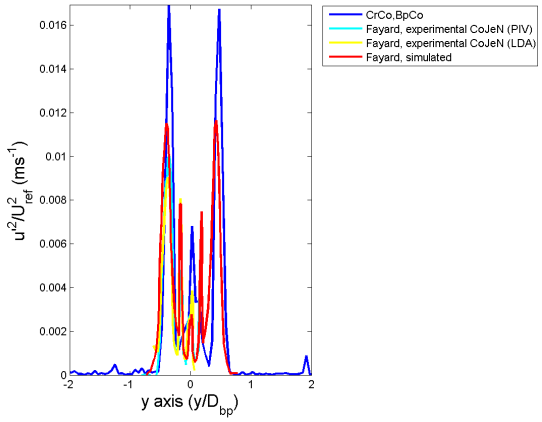

(c) turbulence intensity profile at 0.46 D_{jet}

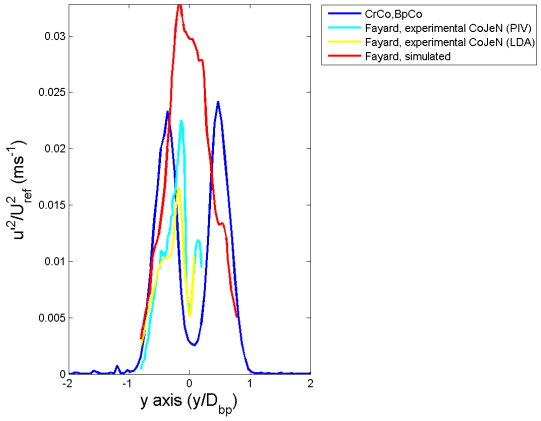

(d) turbulence intensity profile at 3.2 D_{jet}

Figure 8.37: Velocity and turbulence intensity profile comparisons of Fayard and the present data

CHAPTER 9

Conclusion and future work

9.1 Conclusion

A scaled laboratory co-axial jet rig was manufactured and engineered at the University of Warwick and housed on site in an anechoic chamber. The co-flowing nozzles were machined to 1/150th scale of a typical full size engine exhaust giving a core nozzle diameter of 9 mm and a bypass nozzle diameter of 18 mm. The co-flow was unheated and on condition ran at 0.7 Ma for core and 0.63 Ma for the bypass. The short cowl nozzles with a smooth nozzle lip and a chevron lip were manufactured for both the core and bypass. Acoustic and flow properties were independently measured for each of the four combinations of smooth/chevron nozzles for the core and bypass.

A number of considerations were made in using a scaled laboratory jet nozzle instead of full scale engine. For example, as the nozzle size scales down, the jet noise frequencies scale up and therefore suitable microphone and data acquisition system (able to measure high frequencies) was used. Also, the Reynolds number reduces with the nozzle diameter (if flow velocity and viscosity are unchanged) which changes the location of the characteristic hump in the noise spectra.

The acoustic measurements were taken using an acoustic mirror (also designed

and manufactured in house) which was mounted on a motorized traverse. A 1/4" B&K microphone was placed in the near focus of the mirror with the far focus inside the jet flow. The mirror was traversed to create a $4D_{bp}$ by $10D_{bp}$ grid (with 1 mm spacing) measuring noise emissions from the far focus.

Using the smooth core and bypass nozzle as the reference case, the most notable difference in acoustic spectra occurred when a chevron bypass nozzle was used instead of the smooth bypass nozzle.

2D sound source maps of the reference case showed at frequencies less than 10 kHz (0.75 St), the dominant noise source lay $5D_{bp}$ downstream on the centreline of the jet. This is consistent with Juve *et al.* (1980) who found by experiment the end of the potential core to house the most dominant sound production mechanism and Bogey *et al.* (2003) who found the same by numerical simulation. This low frequency peak is attributed by the large scale intermittent structures in this region of the flow. When the bypass chevron nozzle was used instead of the bypass smooth cowl nozzle the noise source lay $1D_{bp}$ further downstream. There was also a reduction in both the SPLdB and the spatial region occupied by the dominant noise source in the sound source maps. The maximum reduction of 3 dB occurred at 7.5 kHz to 10 kHz (0.56 St to 0.75 St).

At 35 kHz (2.63 St), elevated noise levels from past the bullet tip start to emerge and remain present until 80 kHz (6.00 St, the limiting range of the study). The cause of this noise source is thought to be due to vortex shedding from the bullet tip.

Generally, at frequencies less than 30 kHz (2.25 St), the SPLdB spectra of the

centre line of the jet from $0D_{bp}$ to $10D_{bp}$, is lower using the bypass chevron nozzle than with the bypass cowl nozzle. This is consistent with the work of Bridges & Brown (2004b) and Bridges *et al.* (2003) who also observed a reduction in low frequency noise using chevron nozzles instead of standard baseline nozzles. Between 30 kHz and 65 kHz (4.88 St) a transition or overlap of spectra occurs. From $0D_{bp}$ to $5D_{bp}$ the bypass cowl nozzle produces higher SPLdB and at $5D_{bp}$ to $10D_{bp}$ the bypass chevron produces higher SPLdB. For frequencies above 65 kHz, the bypass chevron nozzle produces higher SPLdB from $0D_{bp}$ to $10D_{bp}$.

The present data was compared with the work of other authors. The acoustic spectra along the centreline of the jet for a number of different Strouhal numbers was compared with the experimental data from Drobietz *et al.* (2008) who also used an acoustic mirror but on a larger scale. The spectra's showed good agreement. Similarly, the experimental data from Fayard *et al.* (2008) who used a line array of microphones along the jet expansion, also showed good overall spectral agreement but to a lesser extent than Drobietz. Comparisons with data from numerical simulations by Vuillot *et al.* (2008) also showed good overall agreement between the LES data and present data (adjusted for the near focus distance and the gain from the acoustic mirror).

2D LDA measurements were also taken, complimenting the acoustic measurements and providing visualization of the flow dynamics. In the acoustic results, the most apparent differences from the reference case occurred when the bypass smooth cowl nozzle was replaced with the bypass chevron nozzle. In the LDA results, changing the core smooth cowl nozzle to the core chevron nozzle produces the most differences from the reference case results.

A comparison of the mean velocity downstream on the centre line of the jet for all nozzle combinations shows nozzle combinations using the core cowl nozzle have a similar spectra, as do those using the core chevron nozzle.

At 0-3.5D_{bp}, the mean velocity is higher with the core cowl nozzle (peak at 2D_{bp}), than the core chevron nozzle (peak at 3.5D_{bp}), which could be largely due to the development of vortical structures by chevrons that disrupt the mean flow. From 3.5-10D_{bp} the velocity profile of all nozzle combinations converge and decline. In the case of turbulent intensities, there is an initial small peak at 0-1D_{bp} for all nozzle combinations, most likely attributed by the vortex shedding from the bullet tip. The turbulence intensities reduce until 4D_{bp} (the reduction is greater with the smooth core nozzle) where it starts to increase linearly until 6.5-7D_{bp} when the profile peaks. This peak represents the fully developed region. The end of the potential core was identified at ∼5D_{bp} for all nozzle combinations using an arbitrary cut point of 85% of the reference core velocity (240 ms^{-1}).

There is a small presence of flow asymmetry, which could be attributed by the state and thickness of the boundary layer at the nozzle exit as found by Hussain & Zaman (1981) and Bradshaw (1966) and Antonia & Zhao (2001). There are a number of factors such as the conical contraction of the jet rig and smoothness of the nozzle lip that contribute to the development of the boundary layer. The state of the boundary layer is suggested by Hussain & Zaman (1981), Bradshaw (1966), Antonia & Zhao (2001) and Moore (1977) to be laminar as the nozzles are scaled and the flow passes through a conical contraction. Based on the approximations of other authors and underpinned by the Blasius boundary layer equation, the boundary layer thickness (outer shear layer) at the nozzle exit is estimated to be 0.54 mm.

The shear layers contain vortical structures which enhance entrainment and mixing. It was observed that the bypass chevron nozzle produces a wider outer shear layer than the bypass cowl nozzle and to a lesser extent, the core chevron nozzle does the same for the inner shear layer when compared with the core cowl nozzle. Therefore suggesting the chevron nozzles induce more entrainment and mixing than the smooth lip nozzles. With regards to the acoustic effects, (Viswanathan & Clark, 2004b; Viswanathan, 2008) found the development of the boundary layer did not in influence the radiated noise.

The distribution of sound expressed using 2D sound source maps has contributed to the field of aeroacoustics by highlighting the spatial proximity of changes in SPLdB using different nozzle combinations. Previous efforts such as Grosche *et al.* (1997) and Drobietz *et al.* (2008) have used the acoustic mirror to take 1D line measurements of sound downstream of the jet. The additional information provided by 2D mapping, helps our understanding of jet noise.

9.2 Future work

The present study can be investigated further by firstly reducing the LDA grid spacing near the nozzle exit. A refined grid would provide considerable more information regarding the boundary layer or outer shear layer. At present, the boundary layer thickness is estimated to be 0.54 mm. The current grid spacing of 1 mm is too large to gather accurate statistics about this region. A refined grid with spacing of 0.1 mm or less would provide a much improved estimate of the boundary layer thickness. With the mean velocity and turbulent intensity

measurements, the state of the boundary layer could be confirmed (currently suggested by to be laminar) and the presence of coherent structures (as found by Crow & Champagne (1971), Brown & Roshko (1974)) could be identified. A reduction in the LDA measurement volume would improve the accuracy of the measurements and reduce velocity bias. However, this is difficult to achieve and may have to require the assistance of Dantec Dynamics.

Large scale structures are known to dominate in the transition and fully developed region. Coherent structures in the transition region and are described as having an intermittent volcano effect by Jung *et al.* (2004), which could be captured better using PIV instead of LDA. The spatial range of the study (0-10D_{bp}) contains the transition region and part of the fully developed region. By extending the axial range of measurements from 0-10D_{bp}) to 0-20D_{bp}), the statistics of large scale structures could be collected and analyzed. With the extended axial range, the development and behaviour of streamwise coherent structures could be investigated.

The LDA arrangement in the present study uses one LDA head to gather statistics of the flow dynamics in 2D. By adding a second LDA head, a 3D system could be constructed providing an extra dimension of detail. With off axis detection, the data acquisition rate will reduce but should still be high enough to obtain velocity rates and statistics for all three components. This would provide more detailed information on the flow dynamics of the jet.

The LDA could also be used with the acoustic mirror to take simultaneous acoustic-optical measurements of the jet flow, providing the far focus point of the mirror coincides with the probe volume of the LDA system, which in theory

under the current experimental facilities is possible. With mathematical adjustments, the simultaneous measurements would relate noise to the flow dynamics and structures potentially providing more information to their relationship.

With some adjustments, the jet rig should be capable of generating and sustaining a flow in excess of 1.0 Ma, making it a supersonic flow. However it should be noted that supersonic flows require extra considerations such as dealing with the shock cells created in the jet and mach waves that emerge from the jet edge and dominate over the noise generated by small scale turbulence.

The flow properties could also be changed to simulate a hot jet by supplying the rig with a lower density gas, such as helium, in a suitable mix. Careful safety considerations must be made in the storing, use and extraction of the gas. There is also the potential of using fluid actuators to induce excitation or generate a swirl in the jet flow.

Finally, the addition of a flight stream would provide a more true reflection of in flight conditions. This could be achieved by installing a fan and the base of the jet rig, and upgrading the anechoic chambers extractor fan to deal with the extra gaseous mass. Based on the work of Grosche & Stiewitt (1983) and Michalke & Michel (1979), it is expected that the regions of the jet flow will be elongated by the flight stream.

All of this work could be done with the existing nozzle geometry, or by manufacturing additional nozzles for example, using tabs instead of chevrons. There is significant scope in furthering jet noise research at Warwick.

Bibliography

Ahuja, K. & Mendoza, J. (1995). Effects of cavity dimensions, boundary layer, and temperature on cavity noise with emphasis on benchmark data to validate computational aeroacoustic codes, *Technical report*, NASA Contractor Report, NAS1-19061, Task 13.

Air-France (2009). A modern and rationalized fleet, viewed on 15th December 2009.
URL: *http://corporate.airfrance.com/en/fleet/a-modern-and-rationalized-fleet/*

Almeida, O. (2008). Semi-empirical methods for coaxial jet noise prediction, *Technical report*, University of Southampton, Institute of sound and vibration research, No. 326.

Andersson, N., Eriksson, L. & Davidson, L. (2005). Investigation of an isothermal mach 0.75 jet and its radiated sound using large eddy simulation and kirchoff surface integration, *International Journal of Heat Fluid Flow* **vol. 26(3)**: pp. 393–410.

Antonia, R. & Zhao, Q. (2001). Effect of initial conditions on a circular jet, *Experiments in Fluids* **vol. 31**: pp. 319–323.

Arakeri, V., Krothapalli, A., Siddavaram, V., Alkislar, M. & Lourenco, L. (2003). On the use of microjets to suppress turbulence in a mach 0.9 axisymmetric jet, *Journal of Fluid Mechanics* **vol. 490**: pp. 7598.

Arbey, H. & Ffowcs-Williams, J. (1984). Active cancellation of pure tones in an excited jet, *Journal of Fluid Mechanics* **vol. 149**: pp. 445–454.

Armstrong, R., Michalke, A. & Fuchs, H. (1977). Coherent structures in jet turbulence and noise, *AIAA Journal* **vol. 15(7)**: pp. 1011–1017.

Arndt, R., Long, D. & Glauser, M. (1997). The proper orthogonal decomposition of pressure fluctuations surrounding a turbulent jet, *Journal of Fluid Mechanics* **vol. 340**: pp. 1–33.

Atvars, J., Schubert, L. & Ribner, H. (1965). Refraction of sound from a point source placed in an air jet, *Journal of the Acoustical Society of America* **vol. 37(1)**: pp. 168–170.

Bogey, C. & Bailly, C. (2004). Investigation of subsonic jet noise using les: Mach and reynolds number effects, *10th AIAA/CEAS Aeroacoustics Conference, 8-10th May, Manchester, UK*.

Bogey, C. & Bailly, C. (2005). Investigation of sound sources in subsonic jets using causality methods on les data, *11th AIAA/CEAS Aeroacoustics Conference, 23-25th May, Monterey, USA*.

Bogey, C., Bailly, C. & Juve, D. (2003). Noise investigation of a high subsonic, moderate reynolds number jet using a compressible les, *Theoretical and Computational Fluid Dynamics* **vol. 16(4)**: pp. 273–297.

Bogey, C., Barr, S., Juv, D. & Bailly, C. (2009). Simulation of a hot coaxial jet:

Direct noise prediction and flow-acoustics correlations, *Physics of Fluids* **vol. 21**: pp. 035105–035105–14.

Bonnet, C., Cole, D., Delville, J., Glauser, M. & Ukeiley, L. (1994). Stochastic estimation and proper orthogonal decomposition: compliamentary techniques for identifying structure, *Experiments in Fluids* **vol. 17(5)**: pp. 307–314.

Bonnet, C. & Fisher, M. (1979). Correlation techniques and modal decomposition analysis for the detection of azimuthally coherent structures in jet flows, *Journal of Sound and Vibration* **vol. 66**: pp. 545–555.

Boyne, W. & Lopez., D. S. (1979). *The Jet Age: forty years of jet aviation*, Smithsonian Institution Press.

Bradshaw, P. (1966). The effect of initial conditions on the development of a free shear layer, *Journal of Fluid Mechanics* **vol. 26**: pp. 225–236.

Bradshaw, P., Ferris, D. & Johnson, R. (1964). Turbulence in the noise producing region of a circular jet, *Journal of Fluid Mechanics* **vol. 19**: pp. 591–624.

Bridges, J. (2002). Measurements of turbulent flow field in separate flow nozzles with enhanced mixing devices, *Technical report*, NASA, TM-2002-211366.

Bridges, J. & Brown, C. (2004b). Parametric testing of chevrons on single flow hot jets, *10th AIAA/CEAS Aeroacoustics Conference, 8-10th May, Manchester, UK.*

Bridges, J. & Hussain, F. (1995). Effects of nozzle body on jet noise, *Journal of Sound and Vibration* **vol. 188(3)**: pp. 407–418.

Bridges, J., Wernet, M. & Brown, C. (2003). Control of jet noise through mixing enhancement, *Technical report*, NASA/TM2003-212335.

Brown, G. & Roshko, A. (1974). On density effects and large scale structure in turbulent mixing layers, *Journal of Fluid Mechanics* **vol. 64**: pp. 775–816.

Brown, S. & Redgwell, G. (2006). Key population and vital statistics, *Technical report*, Office for National Statistics, Series VS No 33, PPI No 29.

Cabana, M., Fortune, V. & Jordan, P. (2006). Identifying the radiated core of lighthills source term, *Theoretical and Computational Fluid Dynamics* **vol. 22(2)**: pp. 87–106.

Chan, Y. (1974). Spatial waves in turbulent jets, *Physics of Fluids* **vol. 17**: pp. 1667–1670.

Chatellier, L. & Fitzpatrick, J. (2005). Spatio-temporal correlation analysis of turbulent flows using global and single-point measurements, *Experiments in Fluids* **vol. 38(5)**: pp. 563–575.

Chu, W. (1966). Turbulence measurements relevant to jet noise, *Technical report*, University of Toronto, UTIAS, Report no.19.

Clarke, J.-P. (2000). A systems analysis of noise abatement procedures enabled by advance flight guidance technology., *AIAA Journal of Aircraft* **vol. 37(2)**: pp. 266–273.

Coiffet, F., Jordan, P., Delville, J., Gervais, Y. & Ricaud, F. (2006). Coherent structures in subsonic jets: a quasi-irrotational source mechanism, *International Journal of Aeroacoustics* **vol. 5(1)**: pp. 67–89.

Colonius, T., Lele, S. & Moin, P. (1997). Sound generation in a mixing layer, *Journal of Fluid Mechanics* **vol. 330**: pp. 375–409.

Crighton, D. & Gaster, M. (1976). Stability of slowly divergent jet flow, *Journal of Fluid Mechanics* **vol. 77(2)**: pp. 397–413.

Crighton, D. & Huerre, P. (1990). Shear layer pressure fluctuations and superdirective acoustic sources, *Journal of Fluid Mechanics* **vol. 220**: pp. 355–368.

Crow, S. & Champagne, F. (1971). Orderly structure in jet turbulence, *Journal of Fluid Mechanics* **vol. 48(3)**: pp. 547–591.

Dahan, C., Elias, G., Maulard, J. & Perulli, M. (1978). Coherent structures in the mixing zone of a subsonic hot free jet, *Journal of Sound and Vibration* **vol. 59**: pp. 181–188.

Davies, P., Fisher, M. & Barrat, M. (1963). The characteristics of turbulence in the mixing region of a round jet, *Journal of Fluid Mechanics* **vol. 15**: pp. 337–367.

Devenport, W., Muthanna, C., Ma, R. & Glegg, S. (2001). Two point descriptions of wake turbulence with application to noise prediction, *AIAA Journal* **vol. 39(12)**: pp. 2302–2307.

DfT (2003). The future of air transport - white paper and the civil aviation bill.

DfT (2006). Air transport white paper progress report.

Drobietz, R., Brink, M., Borchers, I. & Bohning, P. (2008). Jet noise source distribution measurements with an acoustic mirror, *14th AIAA/CEAS Aeroacoustics Conference, 5-7 May, Vancouver, Canada.*

Eschricht, D., Wei, M., Jordan, P., Freund, J. B. & Thiele, F. (2007). Analysis of two dimentional noise controlled mixing layers, *13th AIAA/CEAS Aeroacoustics Conference, 21-23th May, Rome, Italy.*

Ewert, R. & Schroeder, W. (2003). Acoustic perturbation equations bsed on flow decomposition via source filtering, *Journal of Computational Physics* **vol. 188(2)**: pp. 365–398.

Fayard, B., Rahier, G., Vuillot, F. & Kerherve, F. (2008). Flow field analysis for double stream nozzle: application to jet noise, *14th AIAA/CEAS Aeroacoustics Conference, 5-7 May, Vancouver, Canada.*

Ffowcs-Williams, J. (1963). The noise from trubulence convected at high speed, *Philosophical Transactions of the Royal Society, Series A* **vol. 255 (1061)**: pp. 469–503.

Ffowcs-Williams, J. & Kempton, A. (1978). The noise from the large scale structure of a jet, *Journal of Fluid Mechanics* **vol. 78(4)**: pp. 673–694.

Fisher, M., Lush, P. & Harper-Bourne, M. (1973). Jet noise, *Journal of Sound and Vibration* **vol. 28(3)**: pp. 563–585.

Fleury, V., Bailly, C. & Juve, D. (2005). Shear layer acoustic radiation in an excited subsonic jet: experimental study, *Comptes Rendus Mecanique Journal* **vol. 333(10)**: pp. 746–753.

Franz, G. (1959). The near sound field of turbulence, *Technical report*, DTMB Report 982, NS715-102.

Freund, J. (2003). Noise source turbulence statistics and the noise from mach 0.9 jet, *Physics of Fluids* **vol. 15(6)**: pp. 1788–1799.

Freund, J. B. (2001). Noise sources in a low reynolds number turbulent jet at mach 0.9, *Journal of Fluid Mechanics* **vol. 438**: pp. 277–305.

Fuchs, H. (1978a). On the application of acoustic mirror, telescope and polar correlation techniques to jet noise source location, *Journal of Sound and Vibration* **vol. 58**: pp. 117–126.

Fuchs, H. (1978b). Two point correlations of jet noise and their interpretation (comments on a paper by h.s. ribner), *Journal of Sound and Vibration* **vol. 61(1)**: pp. 153159.

Fuchs, H. & Michel, U. (1972). Space correlations of the fluctuating pressure in subsonic turbulent jets, *Journal of Sound and Vibration* **vol. 23(1)**: pp. 77–99.

Gazor, S. & Zhang, W. (2003). Speech probability distribution, *IEEE Signal Processing Letters* **vol. 10(7)**: pp. 204–207.

Goldstein, M. (2003). A generised acoustic analogy, *Journal of Fluid Mechanics* **vol. 488**: pp. 315333.

Goldstein, M. (2005a). On identifying the true source of aerodynamic sound, *Journal of Fluid Mechanics* **vol. 526**: pp. 337347.

Goldstein, M. & Leib, S. (2005b). The role of instability waves in predicting jet noise, *Journal of Fluid Mechanics* **vol. 526**: pp. 3772.

Grosche, F. (1968). *Measurements of the noise of air jets from slot nozzles with and without shields*, DLR-FB.

Grosche, F. (1973). Distributions of sound source intensities in subsonic and supersonic jets, *AGARD Confeerence Proceedings 131 Brussels, Belgium* p. Paper 4.

Grosche, F., Schneider, G. & Stiewitt, H. (1997). Wind tunnel experiments on airframe noise sources of transport aircraft, *3rd AIAA/CEAS Aeroacoustics Conference, 21-23rd May, Atlanta, USA*.

Grosche, F., Stiewatt, H. & Binder, B. (1977). Acoustic wind tunnel measurements with a highly directional microphone, *AIAA Journal* **vol. 15(11)**: pp. 1590–1596.

Grosche, F. & Stiewitt, H. (1983). Flight effects on the jet noise sources investigated by model experiments in the dnw, *8th AIAA/CEAS Aeroacoustics Conference, 17 - 19th June, Colorado, USA*.

Groschel, E. & Schroeder, W. (2005). Noise generation mechanisms in turbulent jets, *Euromech Colloquium 467, 18-20 July, Marseille, France*.

Guerin, S. & Michel, U. (2006). Circumferential analysis of the near pressure field of a co-axial subsonic jet, *10th AIAA/CEAS jet noise workshop, 28-29th September, Dublin, Ireland*.

Guj, G., Carley, C. & Camussi, R. (2003). Acoustic identification of coherent structurs in a turbulent jet, *Journal of Sound and Vibration* **vol. 259(5)**: pp. 1037–1065.

Harper-Bourne, M. (2004). On modelling the hydrodynamic field of high speed jets, *10th AIAA/CEAS Aeroacoustics Conference, 8-10th May, Manchester, UK*.

Heller, H., Holmes, D. & Covert, E. (1971). Flow induced pressure oscillations in shallow cavities, *Journal of Sound and Vibration* **vol. 18(4)**: pp. 545–545.

Hileman, J., Thurow, B., Caraball, E. & Samimy, M. (2005). Large-scale structure evolution and sound emission in high-speed jets: real-time visualization with simultaneous acoustic measurements, *Journal of Fluid Mechanics* **vol. 544**: pp. 277–307.

Howe, M. (1975). Contribution to the theory of aerodynamic sound. with application to excess jet noise and the theory of the flute, *Journal of Fluid Mechanics* **vol. 71(4)**: pp. 625–673.

Howe, M. (1997). Edge, cavity and aperture tones at very low mach numbers, *Journal of Fluid Mechanics* **vol. 330(1)**: pp. 61–84.

Howes, W. (1960). Distribution of time averaged pressure fluctuations along the boundary of a round subsonic jet, *Technical report*, NASA technical note D-468.

Hussain, A. & Clark, A. (1977). Upstream influence on the near field of plane turbulent jet:, *Physics of Fluids* **vol. 20**: pp. 1416–1436.

Hussain, A. & Zaman, K. (1981). The preferred mode of the axisymmetric jet:, *Journal of Fluid Mechanics* **vol. 110**: pp. 39–71.

Jordan, P. & Gervais, Y. (2005a). Modelling self and shear noise mechanisms in inhomogeneous, anisotripic turbulence, *Journal of Sound and Vibration* **vol. 279(3-5)**: pp. 529–555.

Jordan, P. & Gervais, Y. (2008). Subsonic jet aeroacoustics: associating experiment, modelling and simulation, *Experiments in Fluids* **vol. 44(1)**: pp. 1–21.

Jordan, P., Schlegel, M., Stalnov, O., Noack, B. & Tinney, C. (2007). Identifying noisy and quiet modes in a jet, *13th AIAA/CEAS Aeroacoustics Conference, 21-23th May, Rome, Italy.*

Jordan, P., Tinney, C., Delville, J., Glauser, M. & Hall, A. (2005b). Low dimensional signitures of the sound production in subsonic jets, towards their identification and control, *35th AIAA fluid dynamics conference, 6-9th June Toronto, Canada.*

Jung, D., Gamard, S. & George, W. (2004). Downstream evolution of the most energetic modes in a turbulent axisymmetric jet at high reynolds number. part 1, the near field region, *Journal of Fluid Mechanics* **vol. 514**: pp. 173–204.

Juve, D., Sunyach, M. & Comte-Bellot, G. (1979). Filtered azimuthal correlations in the acoustic field of a subsonic jet, *AIAA Journal* **vol. 17(1)**: pp. 112–113.

Juve, D., Sunyach, M. & Comte-Bellot, G. (1980). Intermittency of the noise emission in subsonic cold jets, *Journal of Sound and Vibration* **vol. 71**: pp. 319–332.

Kasagi, N. & Nishino, K. (1991). Probing turbulence with thre dimensional particle tracking velocimetry, *Experimental Thermal and Fluid Science* **vol. 4(5)**: pp. 601–612.

Keast, D. & Maidanik, G. (1966). Studies in the near field noise properties of a small air jet:, *Technical report*, Bolt, Beranek and Newman, Report 1272.

Khavaran, A. & Bridges, J. (2005). Modelling of fine scale turbulence mixing noise, *Journal of Sound and Vibration* **vol. 279(3-5)**: pp. 1131–1154.

Kima, Y. & Lee, D. J. (2007). Acoustic properties associated with nozzle lip thickness in screeching jets, *Journal of Mechanical Science and Technology* **vol. 21**: pp. 764–771.

Kopiev, V. & Chernyshev, S. (1997). Vortex ring eigen-oscillations as a source of sound, *Journal of Fluid Mechanics* **vol. 341**: pp. 19–57.

Krishnamurty, K. (1955). Acoustic radiation from two-dimensional rectangular cut outs in aerodynamic surfaces, *Technical report*, NACA TN-3487.

Kunda, P. K. & Cohen, I. M. (2004). *Fluid Mechanics*, Elsevier Academic Press.

Lau, J., Fisher, M. & Fuchs, H. (1972). The intrinsic structure of turbulent jets, *Journal of Sound and Vibration* **vol. 22(4)**: p. 379–379.

Laufer, J., Schlinker, R. & Kaplan, R. (1975). Experiments on supersonic jet noise, *2nd AIAA Aeroacoustics Conference, 24-26th March, Hampton, USA*.

Laufer, J. & Yen, T. (1983). Noise generation by a low mach number jet, *Journal of Fluid Mechanics* **vol. 134**: pp. 1–31.

Lee, H. & Ribner, H. (1972). Direct correlation of noise and flow of a jet, *Journal of the Acoustical Society of America* **vol. 52(5A)**: pp. 1280–1290.

Levy, Y. & Lockwood, F. (1981). Velocity measurements in a particle laden turbulent free jet, *Combustion and Flame* **vol. 40**: pp. 333339.

Lighthill, M. (1952). On sound generated aerodynamically. i. general theory, *Proceedings of the Royal Society of London, Series A, Mathematical and Physical Sciences* **vol. 211**: pp. 564–587.

Lighthill, M. (1954). On sound generated aerodynamically. ii. turbulence as a sound source, *Proceedings of the Royal Society of London, Series A, Mathematical and Physical Sciences* **vol. 222**: pp. 1–32.

Lilley, G. (1974). On the noise from jets, *AGARD Conference Proceedings on Noise Mechanisms, CP-131, (compiled from noise mechanisms specialists meeting, September 1973, Brussels, Belgium)*.

Liu, J. (1974). Developing large scale wavelike eddies and the near jet noise field, *Journal of Fluid Mechanics* **vol. 62(3)**: pp. 437–464.

Maestrello, L. (1977). Statistical properties of the sound and source fields of an axisymmetric jet, *4th AIAA Aeroacoustics Conference, 3-5th October, Atlanta, USA*.

Malevergne, Y., Pisarenko, V. & Sornette, D. (2006). Empirical distributions of log-returns between the stretched exponential and power law, *Applied Financial Economics* **vol. 16**: pp. 271–289.

Malevergne, Y. & Sornette, D. (2005). *Extreme financial risks*, Springer.

Mankbadi, R. & Liu, J. (1981). A study of interactions between large-scale. coherent structures and fine grained turbulence in a round jet., *Philosophical transactions of the royal society A* **vol. 298(1443)**: pp. 541–602.

Mankbadi, R. & Liu, J. (1984). Sound generated aerodynamically revisited: large scale structures in a turbulent jet as a source of sound, *Philosophical transactions of the royal society A* **vol. 311(1516)**: pp. 183–217.

Mayes, M., Lanford, W. & Hubbard, H. (1959). Near field and far field noise surveys of solid fuel rocket engines for a range of nozzle exit pressures, *Technical report*, NASA technical note D-21.

Meinhart, C., Wereley, S. & Santiago, J. (1999). Micron resolution velocimetry techniques, *Experiments in Fluids* **vol. 27**: pp. 414–419.

Melling, A. (1997). Tracer particle and seeding for particle image velocimetry, *Mearsurement Science and Technology* **vol. 8**: pp. 1406–1416.

Michalke, A. (1964). On the inviscid instability of the hyperbolic tangent velocity profile, *Journal of Fluid Mechanics* **vol. 19**: pp. 543–556.

Michalke, A. & Fuchs, H. (1975). On turbulence and noise of an axisymmetric shear layer, *Journal of Fluid Dynamics* **vol. 70(1)**: pp. 179–205.

Michalke, A. & Michel, U. (1979). Prediction of jet noise in flight from static tests, *Journal of Sound and Vibration* **vol. 67**: pp. 341–367.

Mitchell, B., Lee, S. & Moin, P. (1995). Direct computation of the sound from a compressible co-rotating vortex pair, *Journal of Fluid Mechanics* **vol. 285**: pp. 181–202.

Mohensi, K., Colonius, T. & Freund, J. (2002). An evaluation of linear instability waves as sources of sound in a supersonic turbulent jet, *Physics of Fluids* **vol. 14(10)**: pp. 3593–3600.

Mohring, W. (1978). On vortex sound at low mach number, *Journal of Fluid Mechanics* **vol. 85(4)**: pp. 685–691.

Mollo-Christensen, E. (1963). Measurements of near field pressure of subsonic jets, *Technical report*, NATO, AGARD Report 449.

Monkman, D. J. & McMahon, J. (2007). London heathrow airport strategic noise maps, *Technical report*, Environmental Research and Consultancy Department, CAA, Report 0706.

Moore, C. (1977). The role of shear layer instability waves in jet exhaust noise, *Journal of Fluid Mechanics* **vol. 80(2)**: pp. 321–367.

Moyal, J. (1952). The spectra of turbulence in a compressible fluid; eddy turbulence and random noise, *Proceedings of the Cambridge Philosophical Society* **vol. 48**: pp. 329.

Mueller, T. (2002). *Aeroacoustic measurements*, Springer.

Nagakura, K. (2006). Localization of aerodynamic noise sources of shinkansen trains, *Journal of Sound and Vibration* **vol. 293(3-5)**: pp. 547–556.

NASA (1999). Making future commercial aircraft quieter., *Technical report*, Report FS-1999-07-003-GRC.

Nogueira, J., Lecuona, A. & Nauri, S. (2005). Notes on the the effects of refractive index variations on the lda measurements for cojen, sixth framework programme, priority 4 - aeronautics and space, *Technical report*, Universidad Carlos 3 de Madrid, (report no. not stated).

Ollerhead, J. (1967). On the prediction of the near field noise of supersonic jets, *Technical report*, NASA report CR-857.

Panda, J., Seasholtz, R. & Elam, K. (2005). Investigation of noise sources in high speed jets via correlation measurements, *Journal of Fluid Mechanics* **vol. 537**: pp. 349385.

Picard, C. (2001). *Etude experimental de l'identification des sources acoustique dans les jets par l'analyse de la fluctuation de pression en champ proche*, PhD thesis, Universite de Poitiers.

Picard, C. & Delville, J. (2000). Pressure velocity coupling in a subsonic round jet, *International Journal of Heat and Fluid Flow* **vol. 21(3)**: pp. 359–364.

Plumblee, H., Gibson, J. & Lassiter, L. (1962). A theoretical and experimental investigation of the acoustic response of cavities in an aerodynamic flow, *Technical report*, US Air Force, WADD-TR-61-75.

Ponton, M. K. & Seiner, J. M. (1992). The effects of nozzle exit lip thickness on plume resonance, *Journal of Sound and Vibration* **vol. 154(3)**: pp. 531–549.

Powell, A. (1964). Theory of vortex sound, *Journal of the Acoustical Society of America* **vol. 36(1)**: pp. 177–195.

Raman, G., E.Envia & Bencic, T. (2002). Jet cavity interaction tones, *AIAA Journal* **vol. 40(8)**: pp. 1503–1511.

Reba, N., Narayanan, S., Colonius, T. & Suzuki, T. (2006). Modelling jet noise from organised structures using near field hydrodynamic pressure, *11th AIAA/CEAS Aeroacoustics Conference, 23-25th May, Monterey, USA*.

Rhodes, D. & Beaton, D. (2007). Revised future aircraft noise exposure estimates for heathrow airport, *Technical report*, Environmental Research and Consultancy Department, CAA, Report 0705.

Ribner, H. (1962). Aerodynamic sound from fluid dilatations, *Technical report*, UTIA report No.86, AFOSR TN 3430.

Ribner, H. (1964). The generation of sound by turbulent jets, *Advances in Applied Mechanics* **vol. 8**: pp. 103–182.

Ribner, H. (1969). Quadrupole corrections governing the pattern of jet noise, *Journal of Fluid Mechanics* **vol. 38(1)**: pp. 1–24.

Ricaud, F. (2003). *Etude de l'identification des sources acoustique a partir du couplage de la pression en champ proche et de l'organisation instantee de la zone de melange de jet*, PhD thesis, Universite de Poitiers.

Roger, M. (2006). Fundamentals of aeroacoustics, in experimental aeroacoustics, *Von Karman Institute for Fluid Dynamics, VKI Lecture Series, 13-17th November 2006, Brussels, Belgium*.

Rossiter, J. (1966). Wind tunnel experiments of the flow over rectangular cavities at subsonic and transonic speeds, *Royal Aircraft Establishment* p. Paper 3438.

Samanta, J., Freund, J. B., Wei, M. & Lee, S. (2006). The robustness of acoustic analogies for predicting mixing layer noise, *AIAA Journal* **vol. 44(11)**: pp. 2780–2786.

Sandham, N., Morfey, C. & Hu, Z. (2005). Nonlinear mechanics of sound generation in a pertubed parallel jet flow, *Journal of Fluid Mechanics* **vol. 565**: pp. 1–23.

Saric, W. & Nayfeh, A. (1975). Nonparallel stability of boundary layer flows, *Physics of Fluids* **vol. 18(8)**: pp. 945.

Schaffar, M. (1979). Direct measurements of the correlations between axial in jet velocity fluctuations and far field noise near the axis of a cold jet, *Journal of Sound and Vibration* **vol. 64**: pp. 73–83.

Schaffar, M. & Hancy, J. (1982). Investigation of the jet noise emitting zones of a cold jet via causality correlations, *Journal of Sound and Vibration* **vol. 81**: pp. 377–391.

Scharton, T. & White, P. (1972). Simple pressure source model of jet noise, *Journal of the Acoustical Society of America* **vol. 51(1)**: pp. 95–95.

Schlinker, R., Petersen, R. & Kaplan, R. (1973). Enhancement of directional microphone, *AIAA Paper no. 73-1040, 15th October 1973.*

Schram, C. (2003). *Aeroacoustics of Subsonic Jets : Prediction of the Sound Produced by Vortex Pairing based on Particle Image Velocimetry*, PhD thesis, Technische Universiteit Eindhoven.

Schram, C., Taubitz, S., Anthoine, J. & Hirschberg, A. (2005). Theoretical/empirical prediction and measurement of the sound produced by vortex pairing in a low mach number jet, *Journal of Sound and Vibration* **vol. 281(1-2)**: pp. 171–187.

Seiner, J. & Reethof, G. (1974). On the distribution of source coherency in subsonic jets, *AIAA Journal* pp. Paper 4–74.

Sen, R. (1996). Interpretation of acoustic source maps made wiht an elliptic mirror directional microphone system, *2nd AIAA Aeroacoustics Conference, 24-26th March, Hampton, USA*.

Shields, F. & Bass, H. (1977). Atmospheric absorption of high frequency noise and application to fractional octave band, *Technical report*, NASA CR 2760.

Shin, J. & Chang, J. (2005). Statistical modeling of speech signals based on generalized gamma distribution, *IEEE Signal Processing Letters* **vol. 12(3)**: pp. 258–261.

Shur, M., Spalart, P., Strelets, M. & Travin, A. (2003). Towards the prediction of noise from jet engines, *International Journal of Heat and Fluid Flow* **vol. 24**: pp. 551–561.

Siddon, T. & Rackl, R. (1972). Cross correlation analysis of flow noises with fluid dilatations as source fluctuation, *Journal of the Acoustical Society of America* **vol. 51(1A)**: pp. 96.

Siener, J., Ukeiley, L. & Ponton, M. (1999). Jet noise measuremets using piv, *AIAA Journal* pp. Paper 99–1869.

Skeen, A. (2006). *The development of high speed PIV techniques and their application to jet noise measurements*, PhD thesis, School of Engineering, University of Warwick.

Sorensen, C. & Fischback, D. (2000). Patterns in mie scattering, *Optics Communication* **vol. 173**: pp. 145–153.

Stacy, E. (1962). A generalization of the gamma distribution, *Annals of Mathematical Statistics* **vol. 33**: pp. 1187–1192.

Stacy, E. W. (1973). Quasimaximum likelihood estimators for two-parameter gamma distributions, *IBM Journal of Research and Development* **vol. 17**: pp. 115124.

Stromberg, J., McLaughlin, D. & Troutt, T. (1980). Flow field and acoustic properties of a mach number 0.9 jet at a low reynolds number, *Journal of Sound and Vibration* **vol. 72**: pp. 159–176.

Suzuki, T. & Colonius, T. (2006). Instability waves in a subsonic round jet detected using a near field phased microphone array, *Journal of Fluid Mechanics* **vol. 565**: pp. 197226.

Tam, C. (1972). On the noise of a nearly ideally expanded supersonic jet, *Journal of Fluid Mechanics* **vol. 51(1)**: pp. 69–95.

Tam, C. (1998). Jet noise: Since 1952, *Theoretical and Computational Fluid Dynamics* **vol. 10(1-4)**: pp. 393–405.

Tam, C. & Burton, D. (1984). Sound generated by instability waves of supersonic flows, *Journal of Fluid Dynamics* **vol. 138**: pp. 273–295.

Tam, C., Golebiowski, M. & Siener, J. (1996). On the two components of turbulent mixing noise from supersonic jets, *AIAA Journal* pp. Paper 96–1716.

Tam, C. & Morris, P. (1980). The radiation of sound by the instability waves of a compressible plane turbulent shear layer, *Journal of Fluid Mechanics* **vol. 98(2)**: pp. 349–381.

Tanna, H. (1977). An experimental study of jet noise. part1: turbulent mixing noise; part2: shock associated noise, *Journal of Sound and Vibration* **vol. 50**: pp 405–44.

Tanna, H., Dean, P. & Fisher, M. (1975). The influence of temperature on shock free supersonic jet noise, *Journal of Sound and Vibration* **vol. 39(4)**: pp. 429–460.

Tester, B. & Morfey, C. (1976). Developments in jet noise modelling, theoretical predictions and comparisons with measured data, *Journal of Sound and Vibration* **vol. 46(1)**: pp. 79–103.

Timmerman, B., Skeen, A., Bryanston-Cross, P. & Graves, M. (2009). Large-scale time-resolved digital particle image velocimetry (tr-dpiv) for measurement of high subsonic hot coaxial jet exhaust of a gas turbine engine, *Measurement Science and Technology* **vol. 20**: pp. 074002–074016.

Tinney, C., Coiffet, F., Delville, J., Hall, A., Jordan, P. & Glauser, M. (2006a). Spectral linear stochastic estimation, *Experiments in Fluids* **vol. 41(5)**: pp. 763–775.

Tinney, C., Jordan, P., Delville, J., Hall, A. & Glauser, M. (2007). A time-resolved estimate of the turbulence and source mechanisms in a subsonic jet flow, *Journal of Turbulence* **vol. 8(7)**: pp. 1–20.

Tinney, C., Jordan, P., Guitton, A. & Delville, J. & Coiffet, F. (2006). A study in the near pressure field of co-axial subsonic jets., *12th AIAA/CEAS Aeroacoustics Conference, 8-10th May, Cambridge, USA*.

Umeda, Y. & Ishii, R. (1999). Reduction of noise radiated from a supersonic jet interaction between the screech and cavity tones, *Riron Oyo Rikigaku Koenkai Koen Ronbunshu* pp. Paper FEDSM 98–5240, pp. 419–420.

Viswanathan, K. (2002). Analysis of the two similarity components of turbulent mixing noise, *AIAA Journal* **vol. 40(9)**: pp. 1735–1744.

Viswanathan, K. (2004a). Aeroacoustics of hot jets, *Journal of Fluid Mechanics* **vol. 516**: pp. 3982.

Viswanathan, K. (2006b). Instrumentation considerations for accurate jet noise measurements, *AIAA Journal* **vol. 44(6)**: pp. 1137–1149.

Viswanathan, K. (2006c). Scaling laws and a method for identifying components of jet noise, *AIAA Journal* **vol. 44(10)**: pp. 2274–2285.

Viswanathan, K. (2007). Investigation of the sources of jet noise, *13th AIAA/CEAS Aeroacoustics Conference, 21-23th May, Rome, Italy.*

Viswanathan, K. (2008). Does a model scale nozzle emit the same jet noise as a jet engine, *AIAA Journal* **vol. 46(2)**: pp. 336–355.

Viswanathan, K. & Clark, L. (2004b). Effect of nozzle internal contour on jet areoacoustics, *International Journal of Aeroacoustics* **vol. 3(2)**: pp. 103–135.

Viswanathan, K., Shur, M., Spalart, P. & Strelets, M. (2006a). Computation of the flow and noise of round and beveled nozzles, *12th AIAA/CEAS Aeroacoustics Conference, 8-10th May, Cambridge, USA.*

Vuillot, F., Lupoglazoff, N. & Rahier, G. (2008). Double stream nozzles flow and noise computations and comparisons to experiments, *46th AIAA Aerospace Sciences Meeting and Exhibit, 7-10th January, Reno, Nevada, USA.*

Waldhauer, A. P. (1989). Comparison of elliptical and spherical mirrors for the grasshopper monochromators at ssrl, *Review of Scientific Instruments* **vol. 60**: pp. 2109–2112.

Wei, M. & Freund, J. (2006). A noise controlled free shear flow, *Journal of Fluid Mechanics* **vol. 546**: pp. 123152.

Weitbrecht, V., Kuhn, G. & Jirka, G. (2002). Large scale piv measurements at the surface of shallow water flows, *Flow Measurements and Instrumentation* **vol. 13(5-6)**: pp. 237–245.

Westerweel, J. (1997). Fundamentals of digital particle image velocimetry, *Measurement Science and Technology* **vol. 8**: pp. 1379–1392.

Wingo, D. (1987). Computing maximum-likelihood parameter estimates of the generalized gamma distribution by numerical root isolation, *IEEE Transactions on Reliability* **vol. R-36**: pp. 586590.

Zhang, Z. & Eisele, K. (1995). Off-axis alignment of an measurements lda-probe and the effect of astigmatism on measurements, *Experiments in Fluids* **vol. 19**: pp. 89–95.

APPENDIX A

Appendix

A.1 2D sound source maps

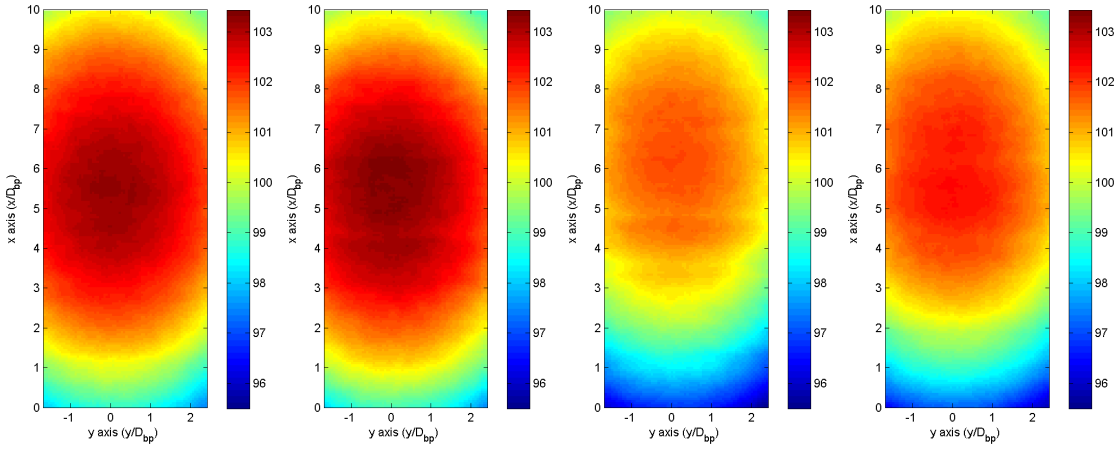

(a) CrCo, BpCo (b) CrCh, BpCo (c) CrCo, BpCh (d) CrCh, BpCh

Figure A.1: 2D sound source maps at 5,120 Hz (colour bar in SPLdB)

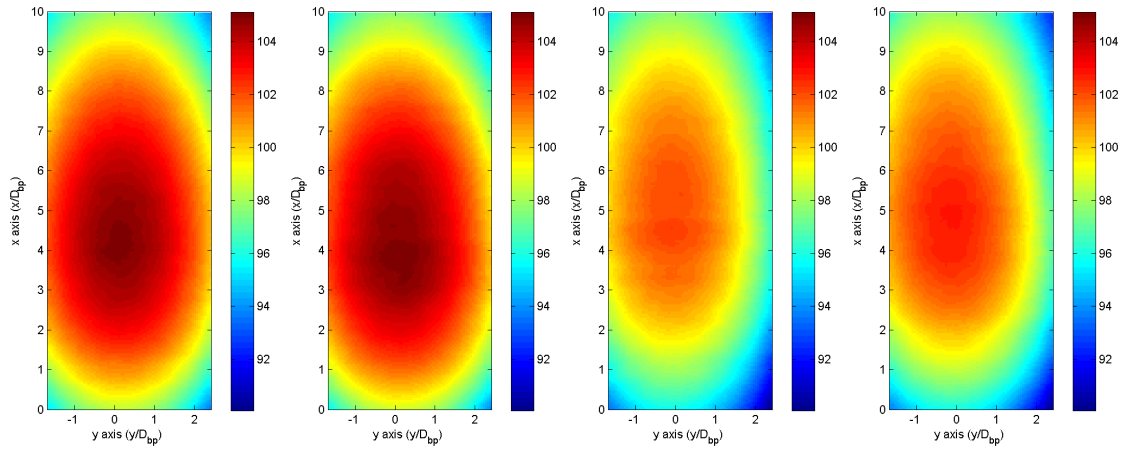

(a) CrCo, BpCo (b) CrCh, BpCo (c) CrCo, BpCh (d) CrCh, BpCh

Figure A.2: 2D sound source maps at 10,240 Hz (colour bar in SPLdB)

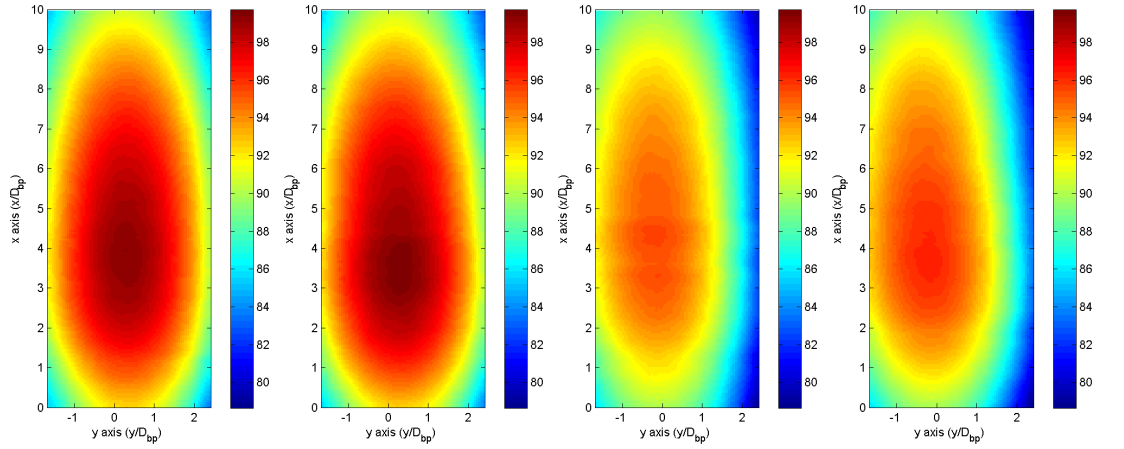

(a) CrCo, BpCo (b) CrCh, BpCo (c) CrCo, BpCh (d) CrCh, BpCh

Figure A.3: 2D sound source maps at 15,104 Hz (colour bar in SPLdB)

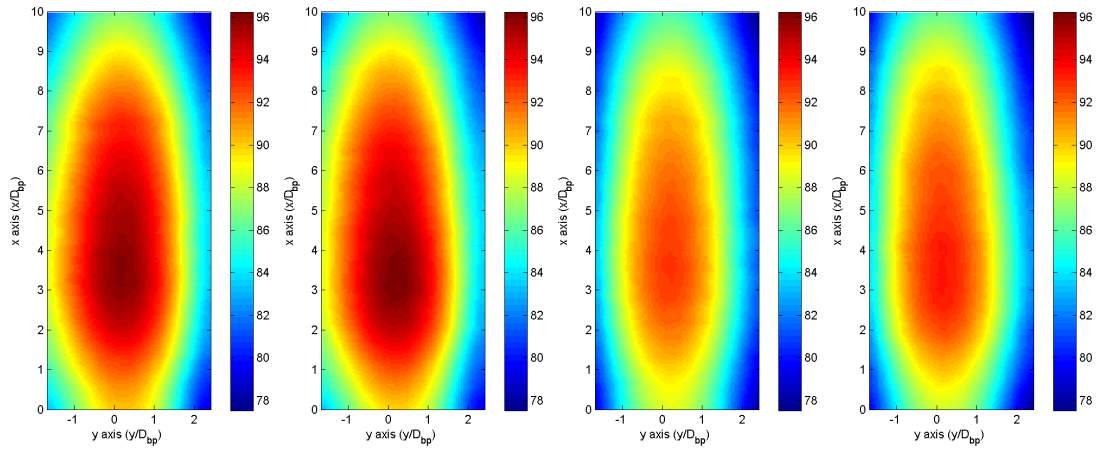

(a) CrCo, BpCo (b) CrCh, BpCo (c) CrCo, BpCh (d) CrCh, BpCh

Figure A.4: 2D sound source maps at 20,224 Hz (colour bar in SPLdB)

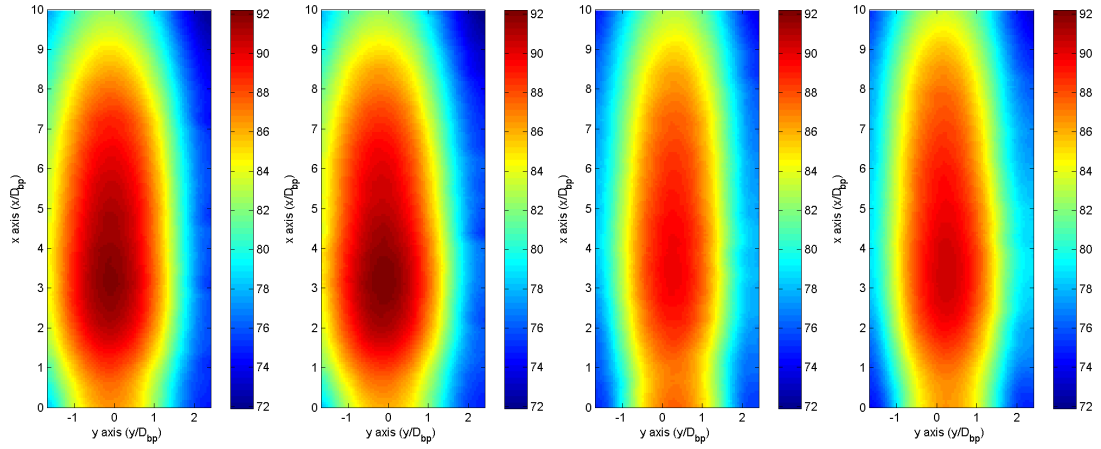

(a) CrCo, BpCo (b) CrCh, BpCo (c) CrCo, BpCh (d) CrCh, BpCh

Figure A.5: 2D sound source maps at 25,088 Hz (colour bar in SPLdB)

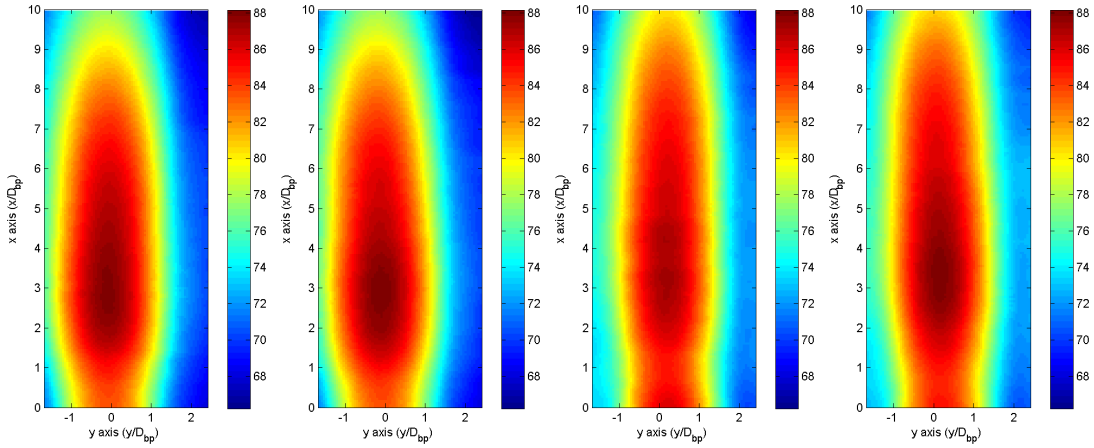

(a) CrCo, BpCo (b) CrCh, BpCo (c) CrCo, BpCh (d) CrCh, BpCh

Figure A.6: 2D sound source maps at 30,208 Hz (colour bar in SPLdB)

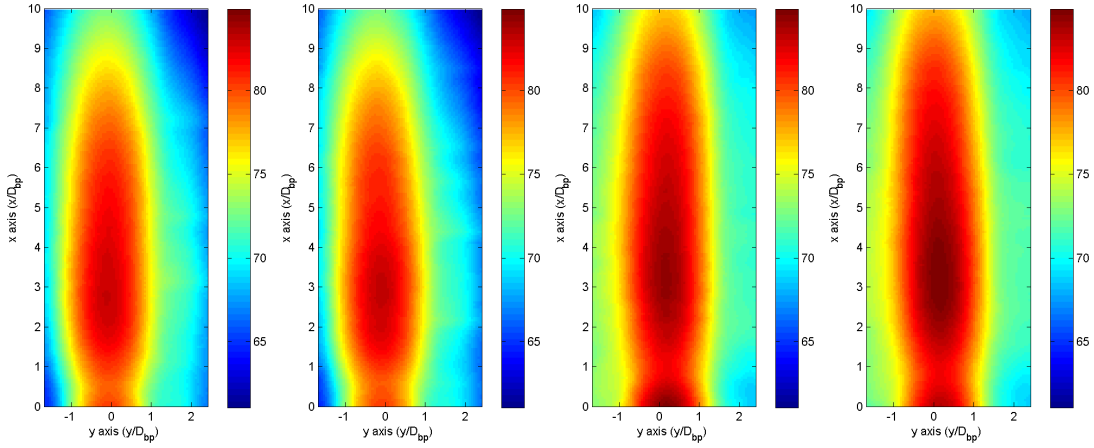

(a) CrCo, BpCo (b) CrCh, BpCo (c) CrCo, BpCh (d) CrCh, BpCh

Figure A.7: 2D sound source maps at 35,072 Hz (colour bar in SPLdB)

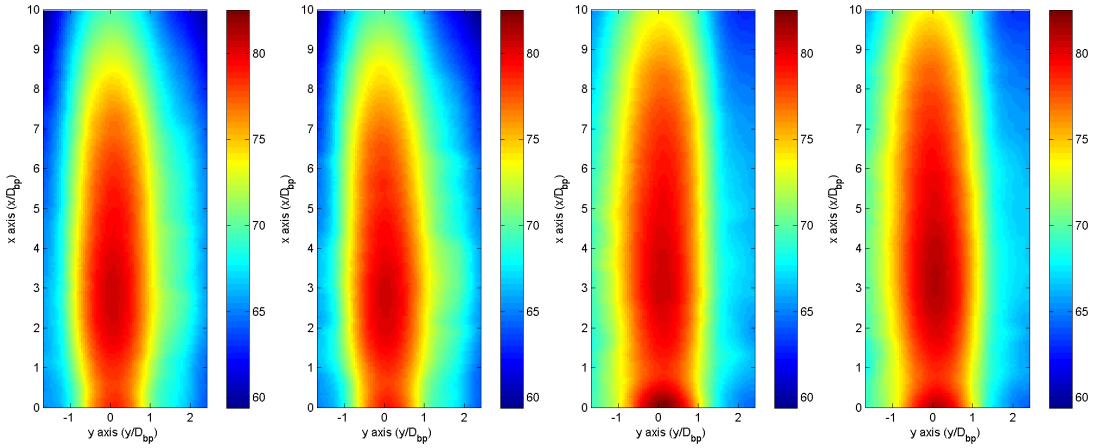

(a) CrCo, BpCo (b) CrCh, BpCo (c) CrCo, BpCh (d) CrCh, BpCh

Figure A.8: 2D sound source maps at 40,192 Hz (colour bar in SPLdB)

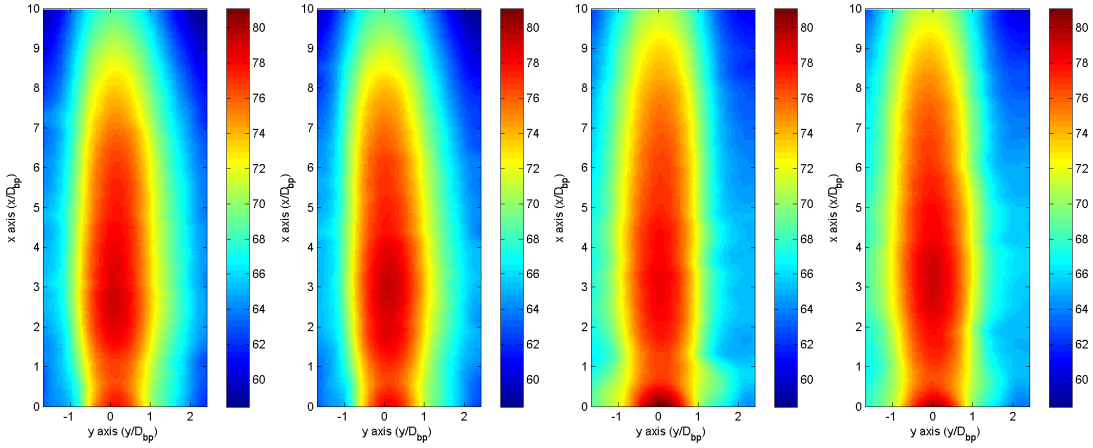

(a) CrCo, BpCo (b) CrCh, BpCo (c) CrCo, BpCh (d) CrCh, BpCh

Figure A.9: 2D sound source maps at 45,056 Hz (colour bar in SPLdB)

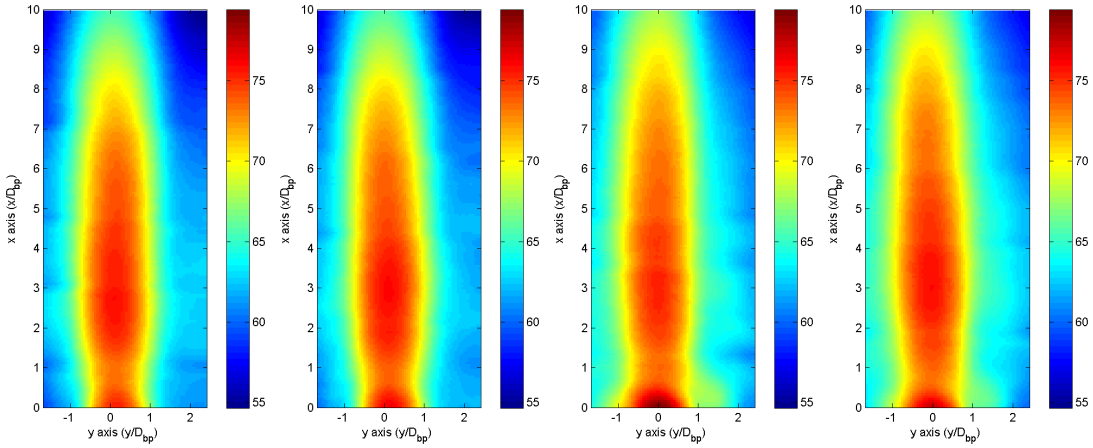

(a) CrCo, BpCo (b) CrCh, BpCo (c) CrCo, BpCh (d) CrCh, BpCh

Figure A.10: 2D sound source maps at 50,176 Hz (colour bar in SPLdB)

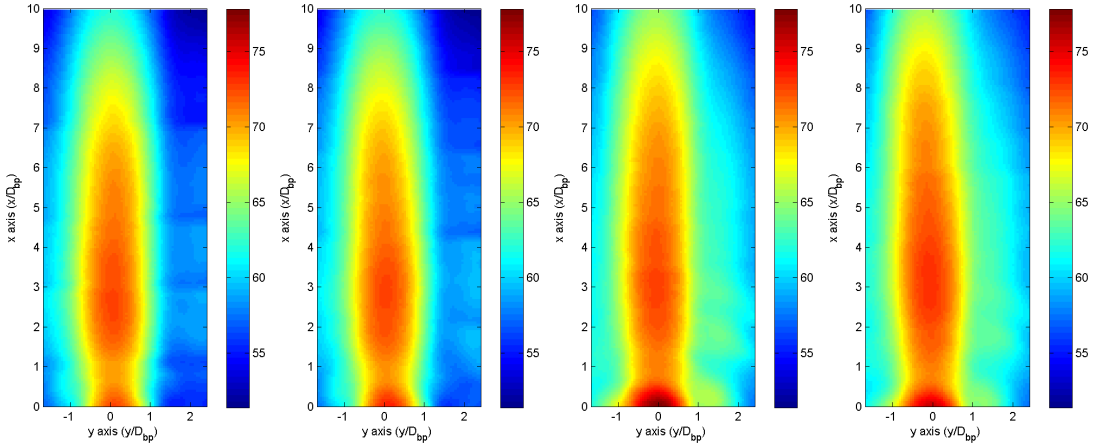

(a) CrCo, BpCo (b) CrCh, BpCo (c) CrCo, BpCh (d) CrCh, BpCh

Figure A.11: 2D sound source maps at 55,040 Hz (colour bar in SPLdB)

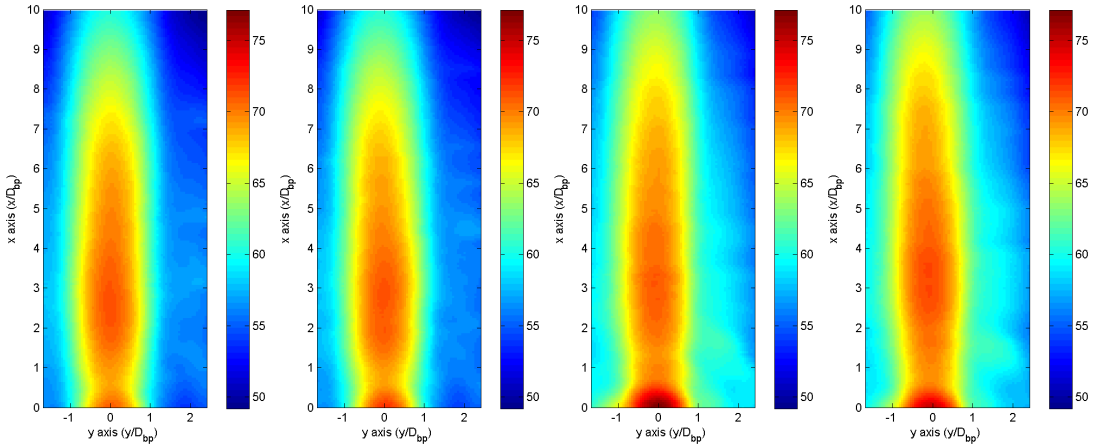

(a) CrCo, BpCo (b) CrCh, BpCo (c) CrCo, BpCh (d) CrCh, BpCh

Figure A.12: 2D sound source maps at 60,160 Hz (colour bar in SPLdB)

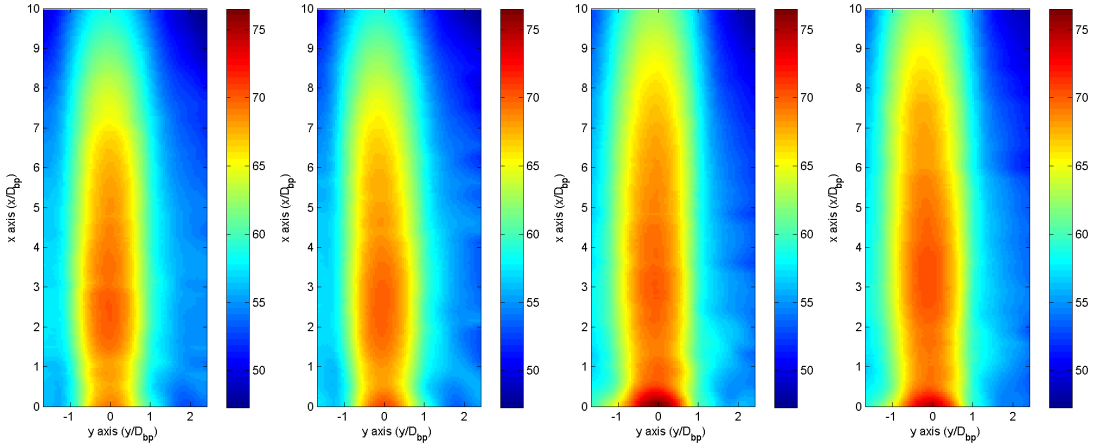

(a) CrCo, BpCo (b) CrCh, BpCo (c) CrCo, BpCh (d) CrCh, BpCh

Figure A.13: 2D sound source maps at 65,024 Hz (colour bar in SPLdB)

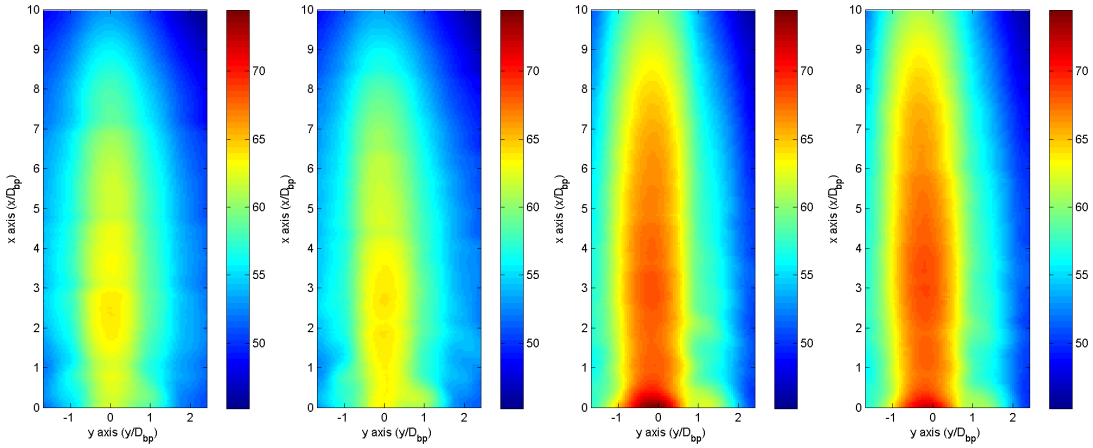

(a) CrCo, BpCo (b) CrCh, BpCo (c) CrCo, BpCh (d) CrCh, BpCh

Figure A.14: 2D sound source maps at 70,144 Hz (colour bar in SPLdB)

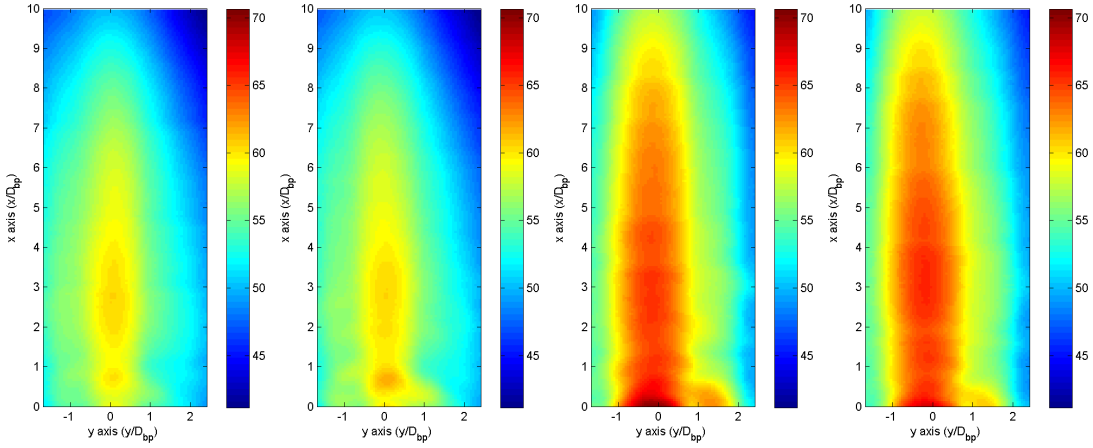

(a) CrCo, BpCo (b) CrCh, BpCo (c) CrCo, BpCh (d) CrCh, BpCh

Figure A.15: 2D sound source maps at 75,008 Hz (colour bar in SPLdB)

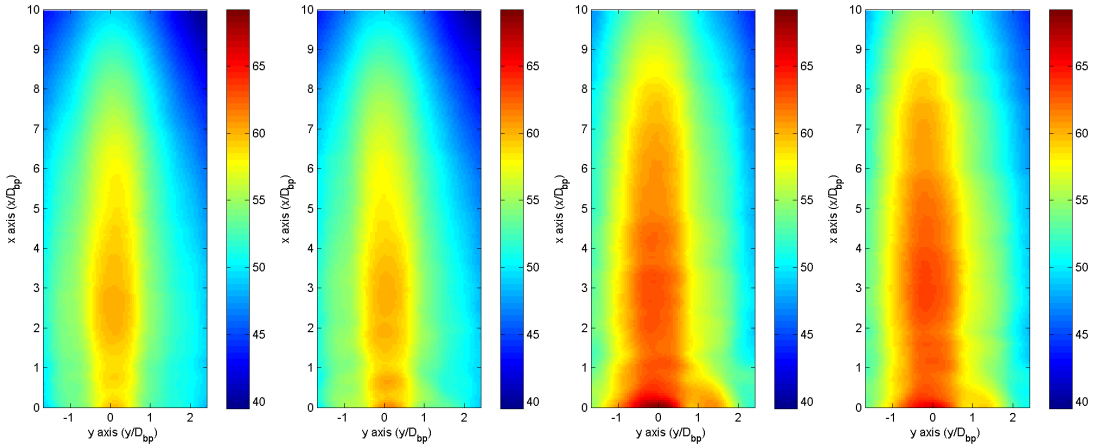

(a) CrCo, BpCo (b) CrCh, BpCo (c) CrCo, BpCh (d) CrCh, BpCh

Figure A.16: 2D sound source maps at 80,128 Hz (colour bar in SPLdB)

A.2 Radial acoustic profile at different positions downstream of the jet

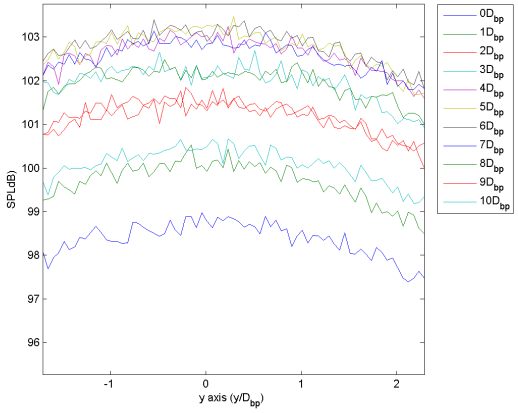

(a) CrCo, BpCo

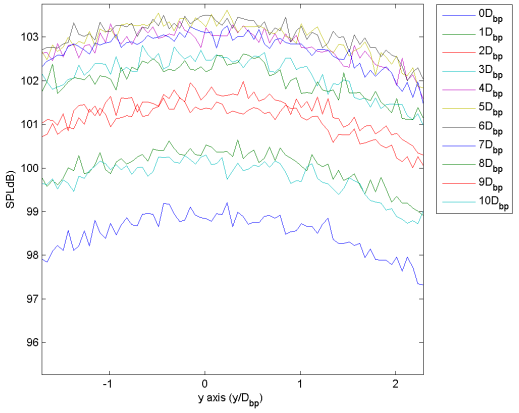

(b) CrCh, BpCo

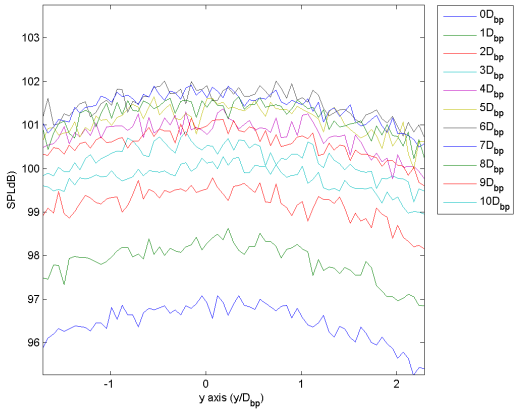

(c) CrCo, BpCh

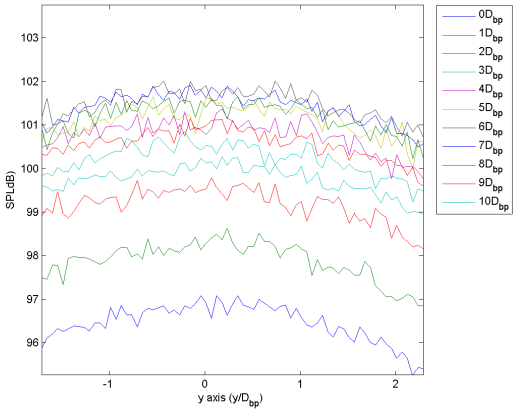

(d) CrCh, BpCh

Figure A.17: Radial profile at 5,120 Hz

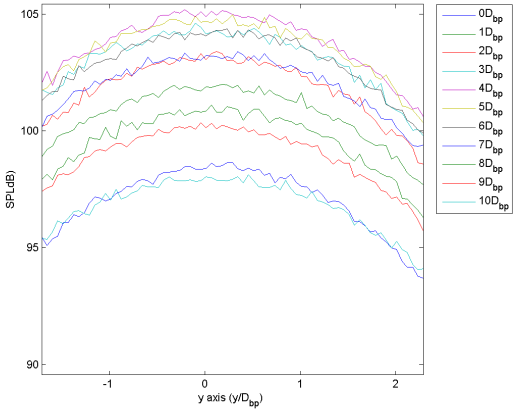

(a) CrCo, BpCo

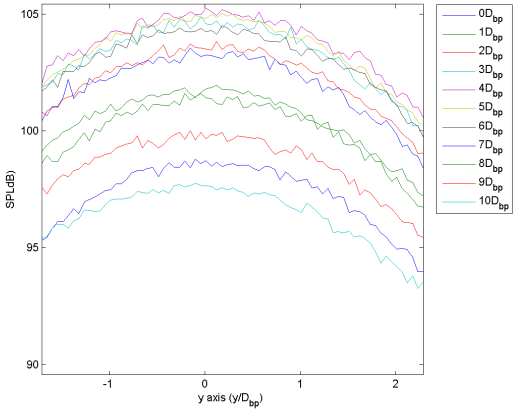

(b) CrCh, BpCo

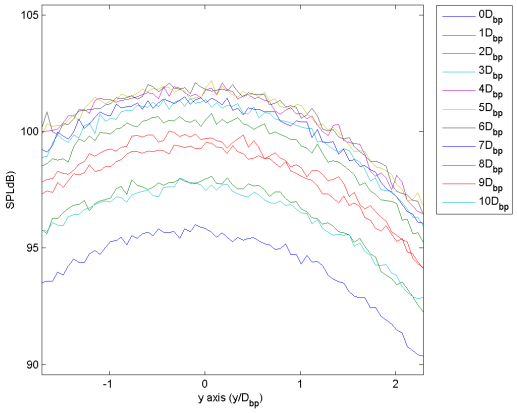

(c) CrCo, BpCh

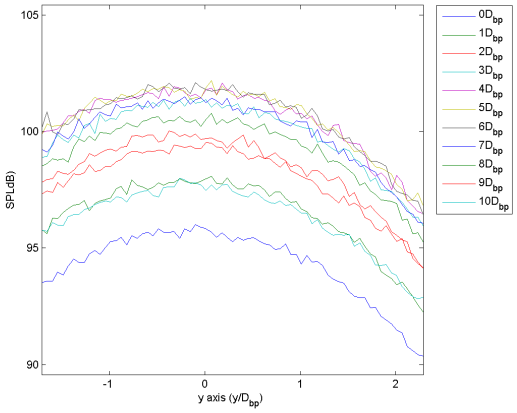

(d) CrCh, BpCh

Figure A.18: Radial profile at 10,240 Hz

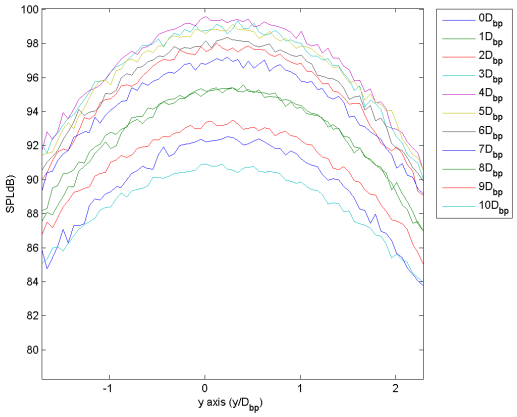

(a) CrCo, BpCo

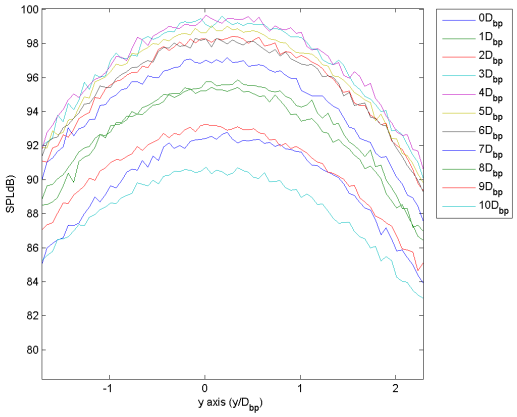

(b) CrCh, BpCo

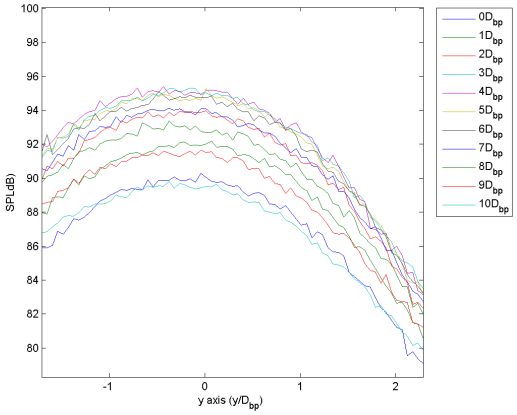

(c) CrCo, BpCh

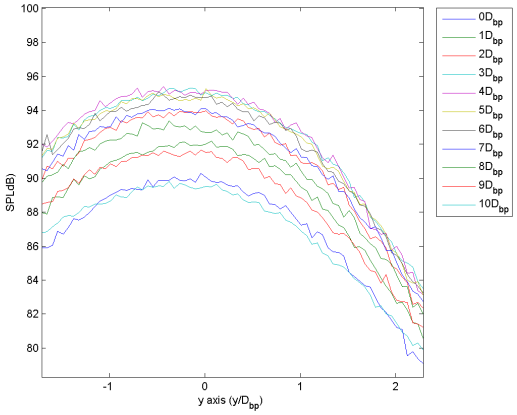

(d) CrCh, BpCh

Figure A.19: Radial profile at 15,104 Hz

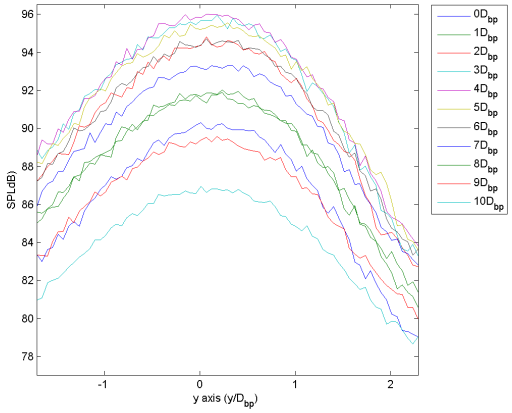

(a) CrCo, BpCo

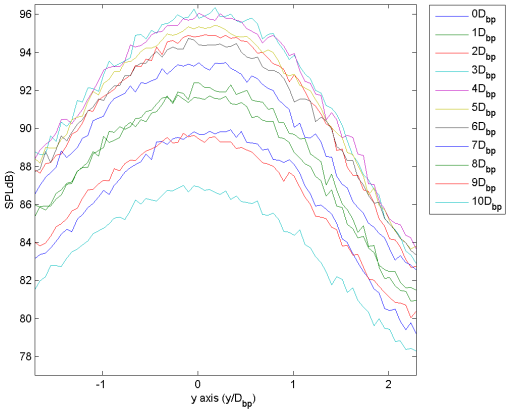

(b) CrCh, BpCo

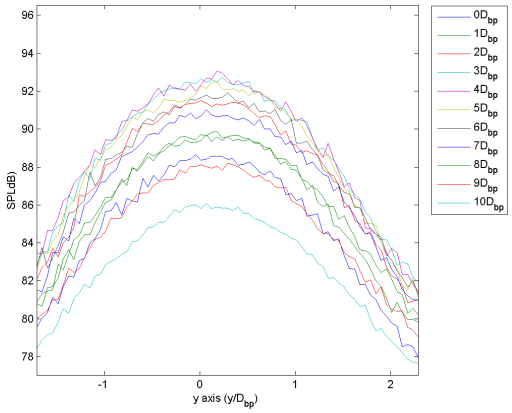

(c) CrCo, BpCh

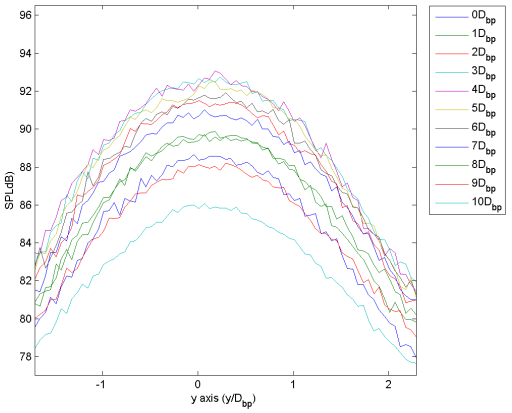

(d) CrCh, BpCh

Figure A.20: Radial profile at 20,224 Hz

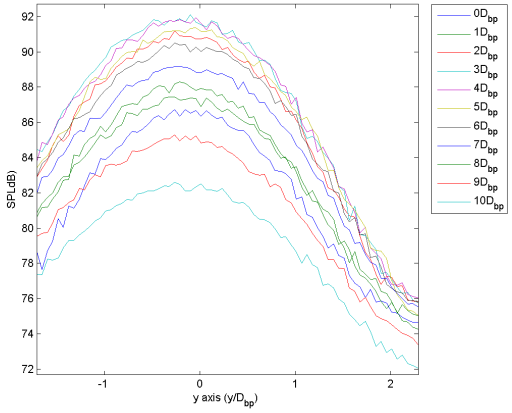

(a) CrCo, BpCo

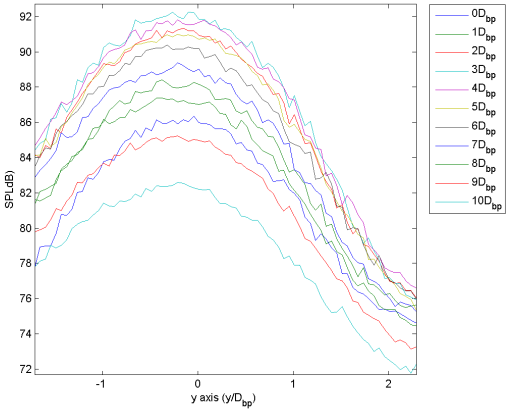

(b) CrCh, BpCo

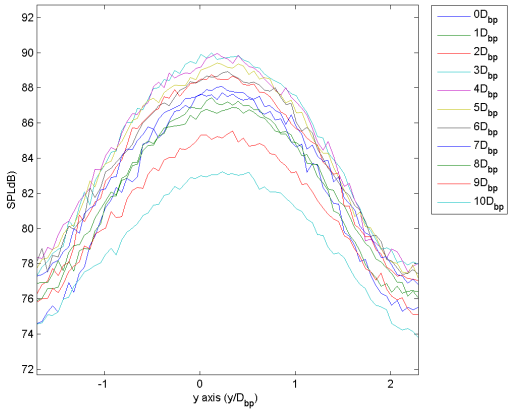

(c) CrCo, BpCh

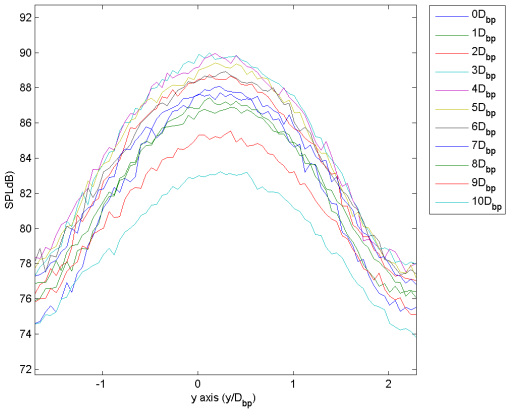

(d) CrCh, BpCh

Figure A.21: Radial profile at 25,088 Hz

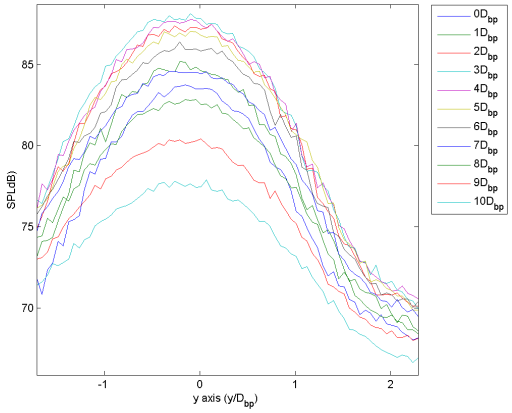

(a) CrCo, BpCo

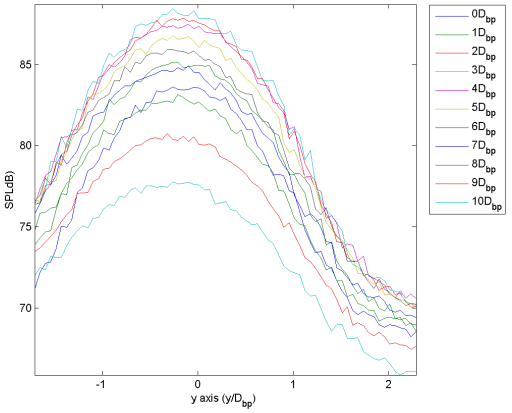

(b) CrCh, BpCo

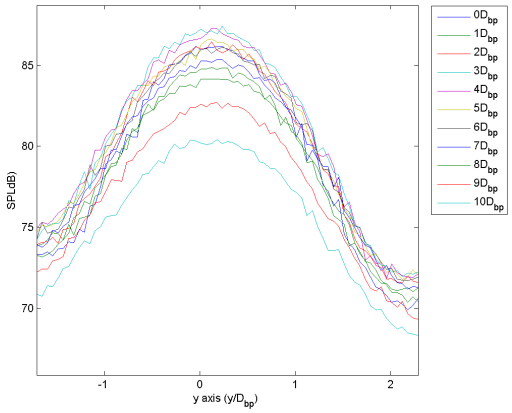

(c) CrCo, BpCh

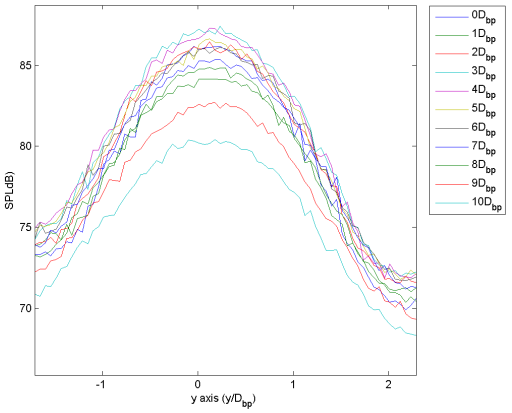

(d) CrCh, BpCh

Figure A.22: Radial profile at 30,208 Hz

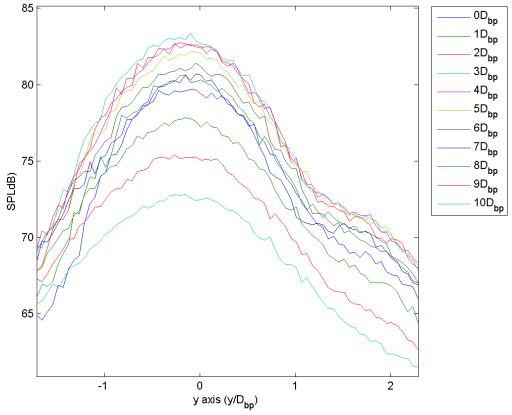

(a) CrCo, BpCo

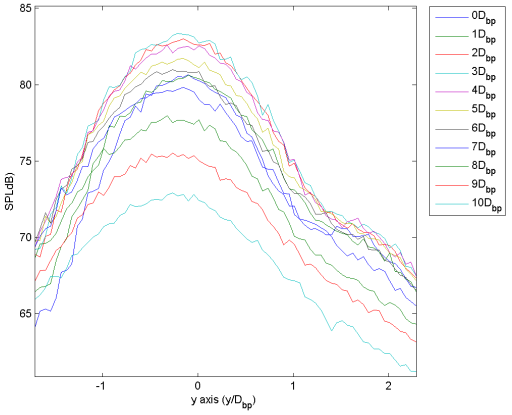

(b) CrCh, BpCo

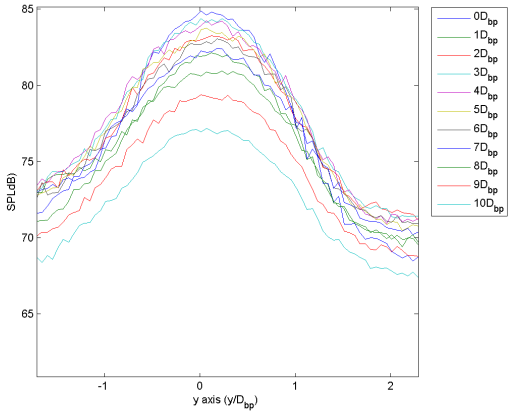

(c) CrCo, BpCh

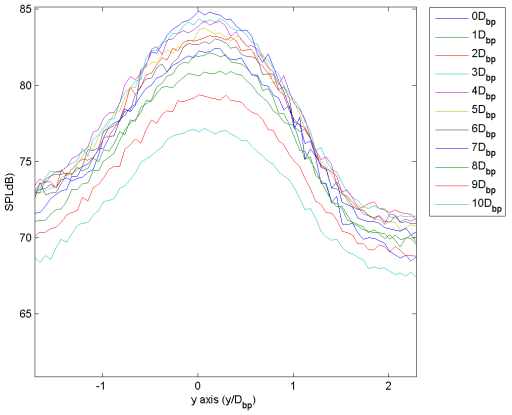

(d) CrCh, BpCh

Figure A.23: Radial profile at 35,072 Hz

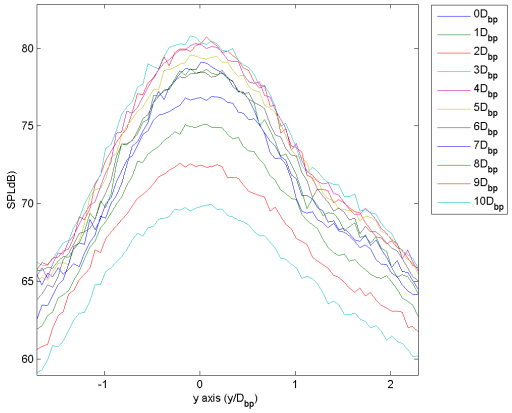

(a) CrCo, BpCo

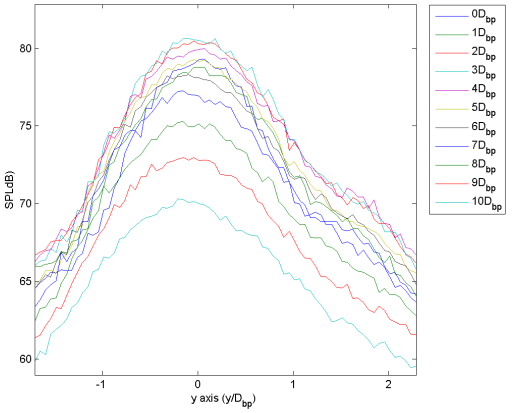

(b) CrCh, BpCo

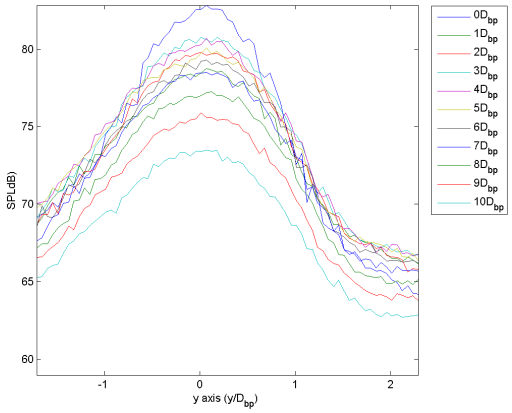

(c) CrCo, BpCh

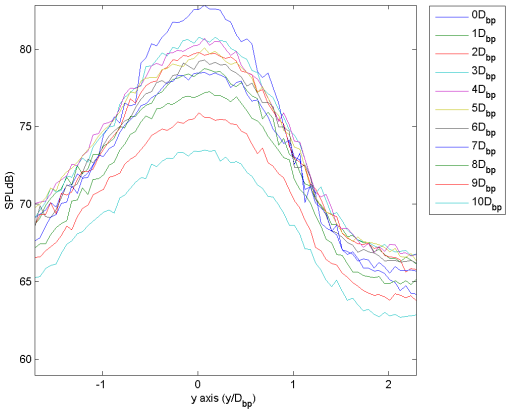

(d) CrCh, BpCh

Figure A.24: Radial profile at 40,192 Hz

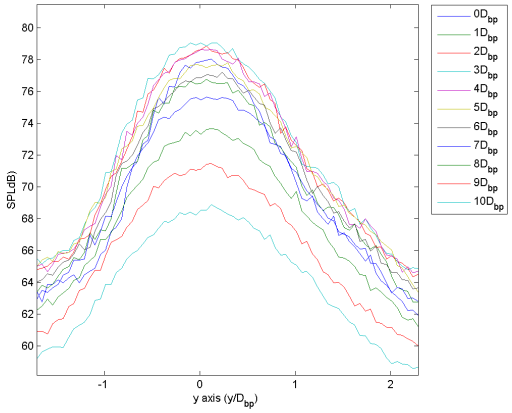

(a) CrCo, BpCo

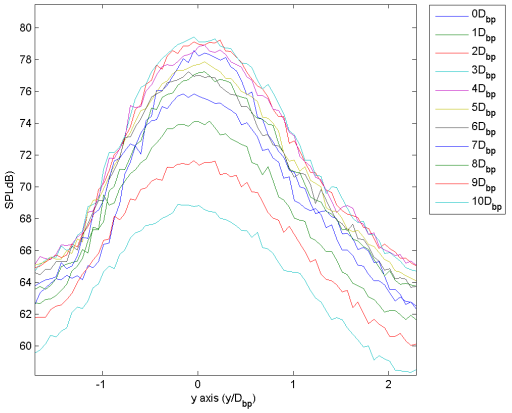

(b) CrCh, BpCo

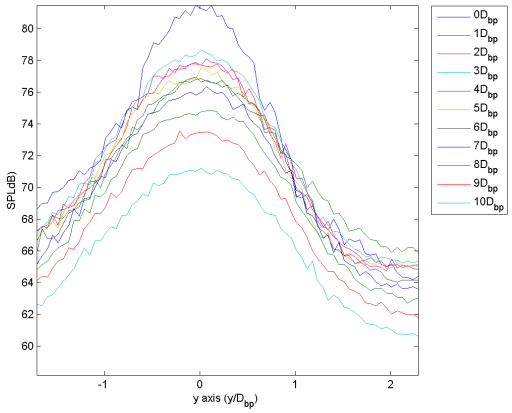

(c) CrCo, BpCh

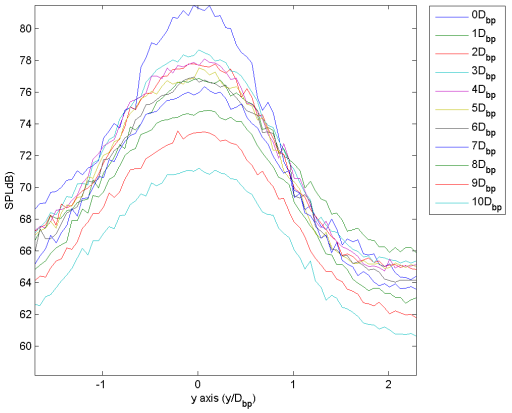

(d) CrCh, BpCh

Figure A.25: Radial profile at 45,056 Hz

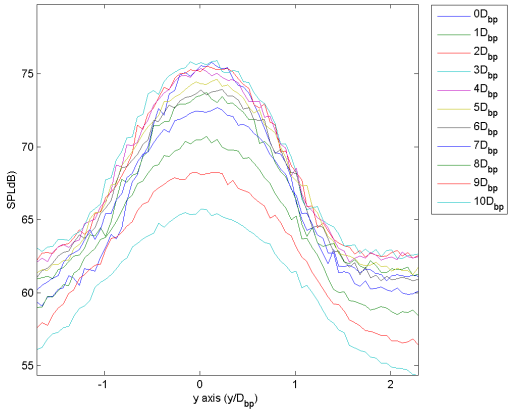

(a) CrCo, BpCo

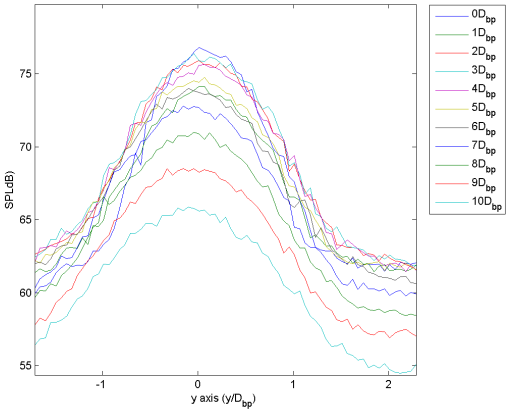

(b) CrCh, BpCo

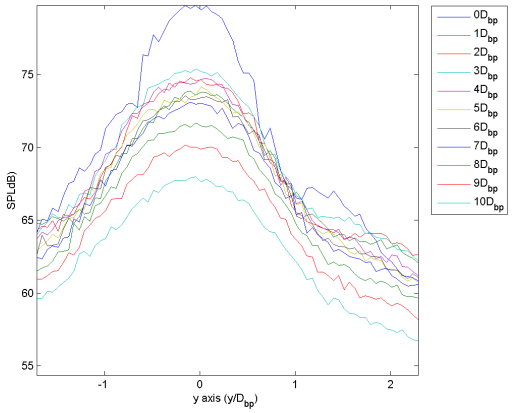

(c) CrCo, BpCh

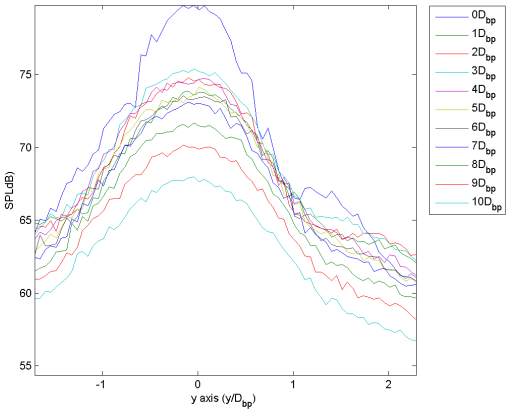

(d) CrCh, BpCh

Figure A.26: Radial profile at 50,176 Hz

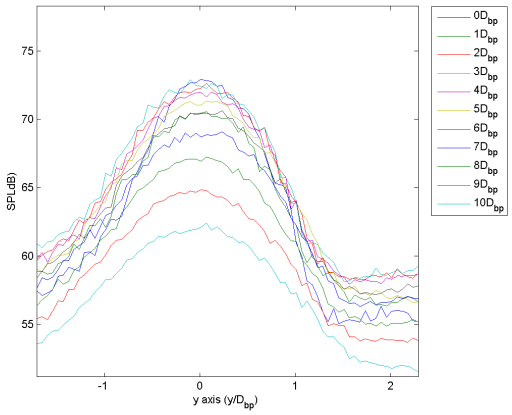

(a) CrCo, BpCo

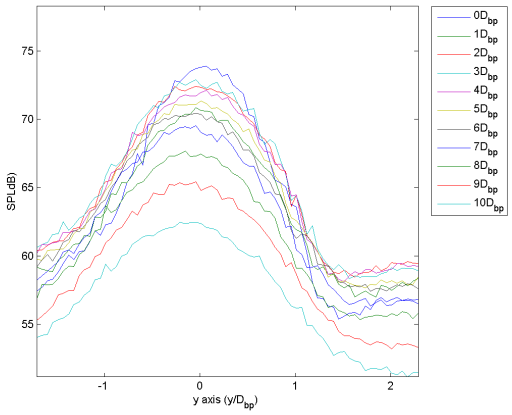

(b) CrCh, BpCo

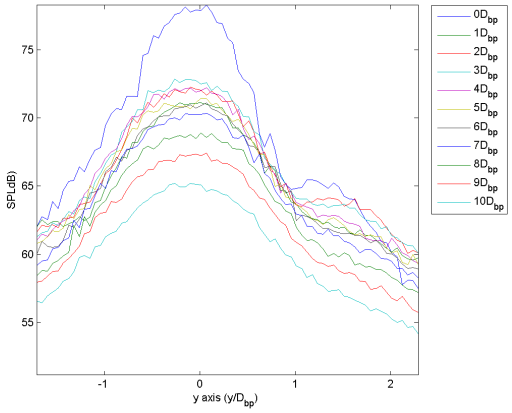

(c) CrCo, BpCh

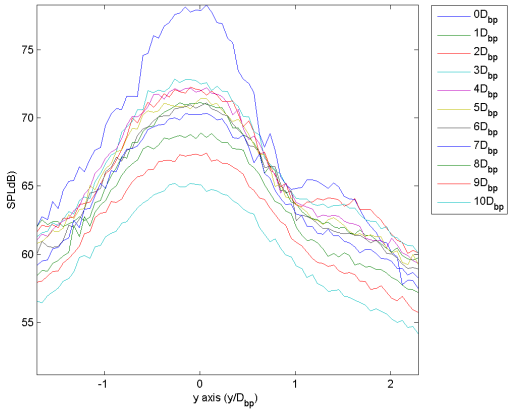

(d) CrCh, BpCh

Figure A.27: Radial profile at 55,040 Hz

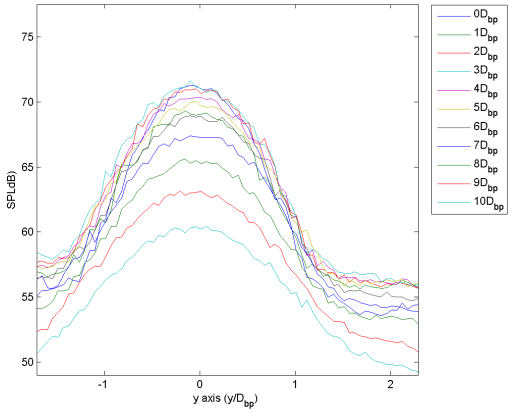

(a) CrCo, BpCo

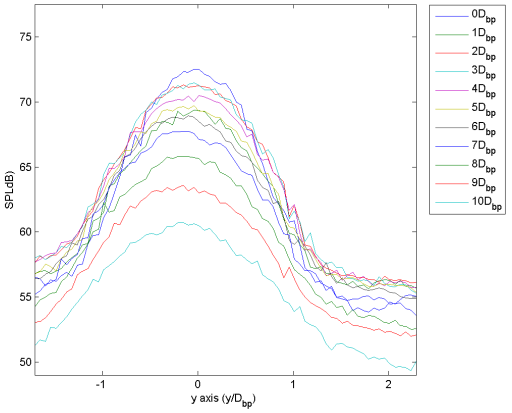

(b) CrCh, BpCo

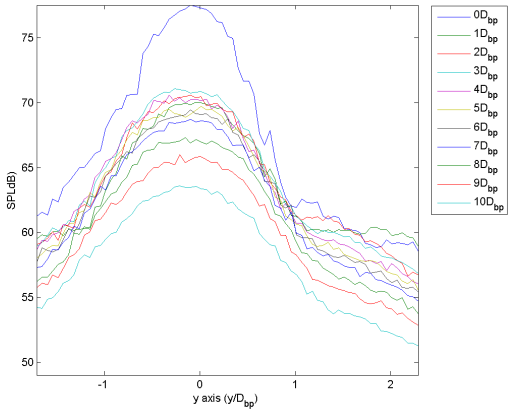

(c) CrCo, BpCh

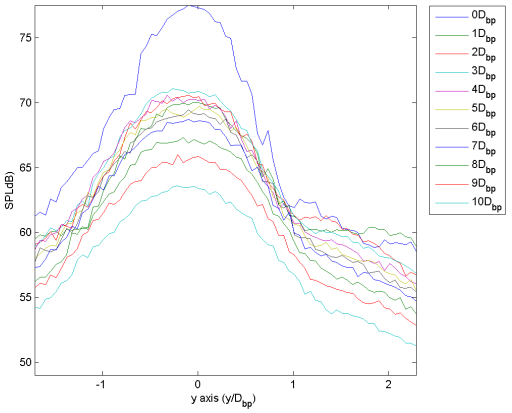

(d) CrCh, BpCh

Figure A.28: Radial profile at 60,160 Hz

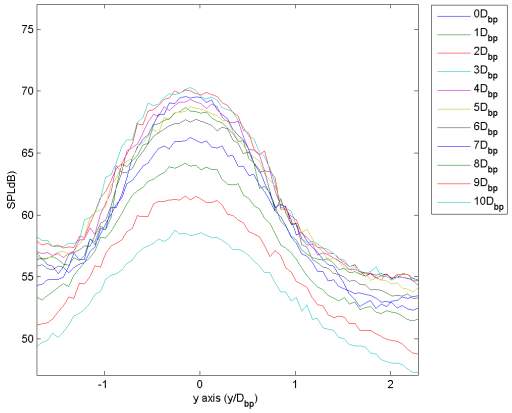

(a) CrCo, BpCo

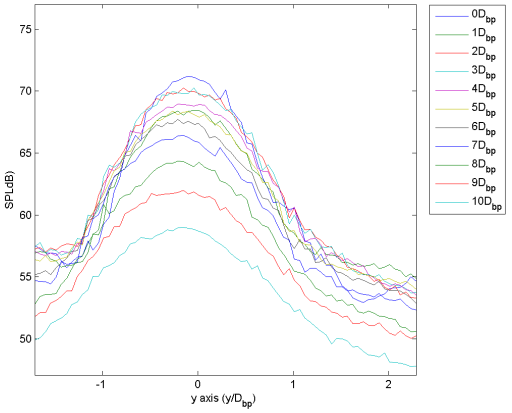

(b) CrCh, BpCo

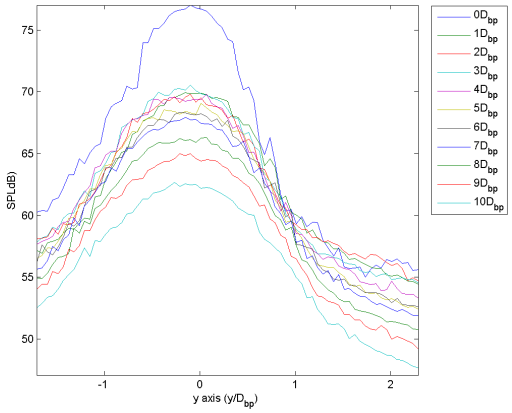

(c) CrCo, BpCh

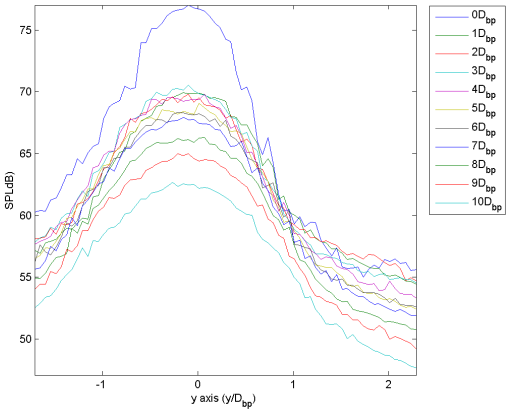

(d) CrCh, BpCh

Figure A.29: Radial profile at 65,024 Hz

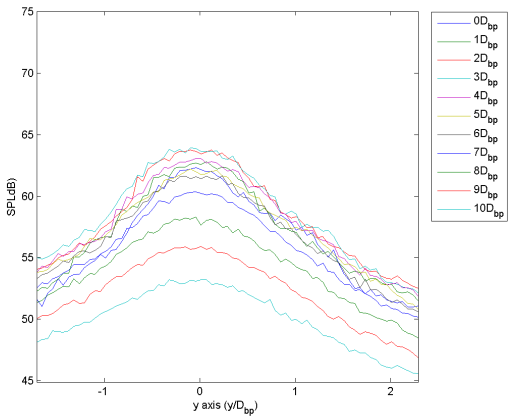

(a) CrCo, BpCo

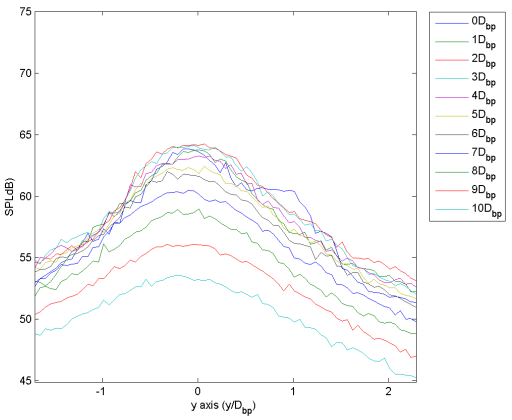

(b) CrCh, BpCo

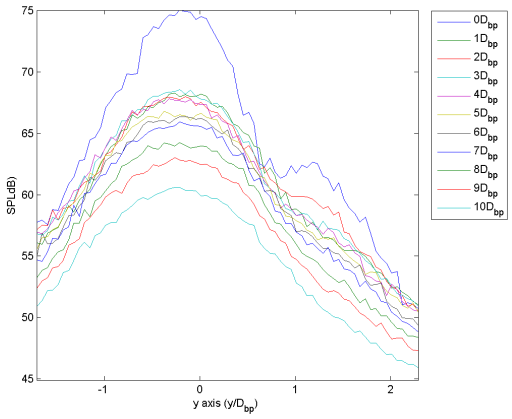

(c) CrCo, BpCh

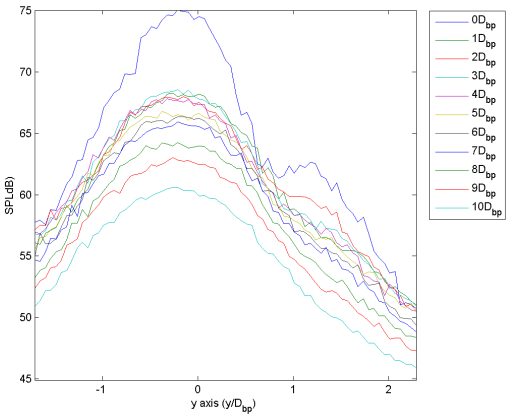

(d) CrCh, BpCh

Figure A.30: Radial profile at 70,144 Hz

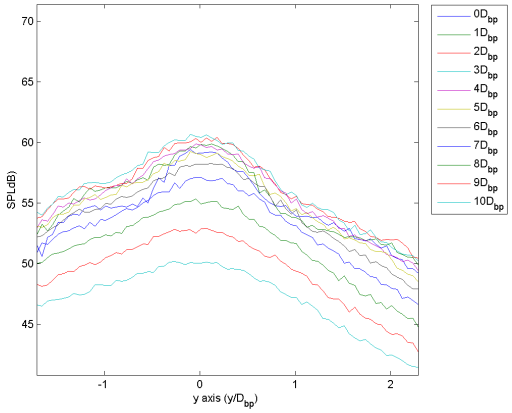

(a) CrCo, BpCo

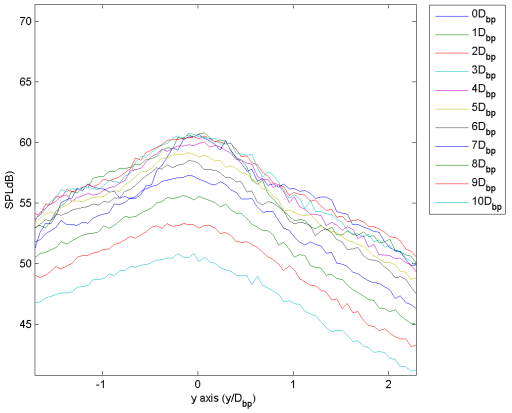

(b) CrCh, BpCo

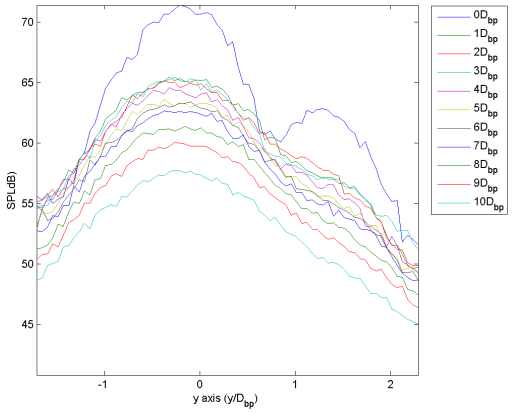

(c) CrCo, BpCh

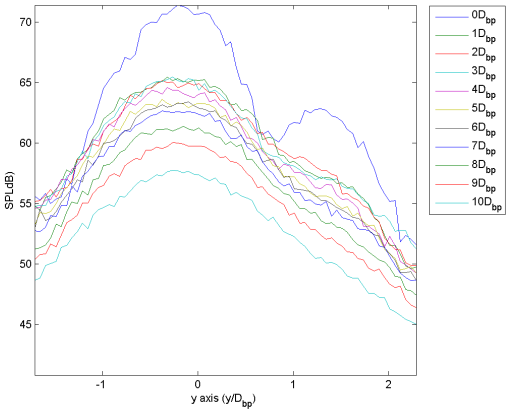

(d) CrCh, BpCh

Figure A.31: Radial profile at 75,008 Hz

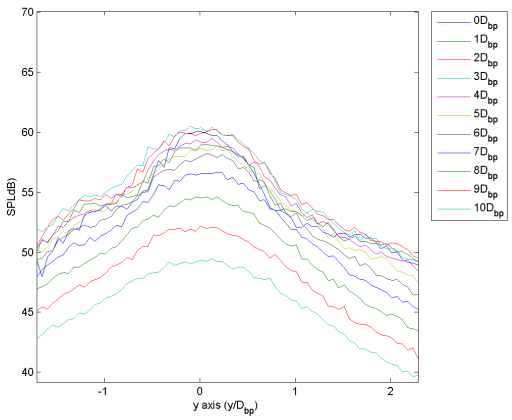

(a) CrCo, BpCo

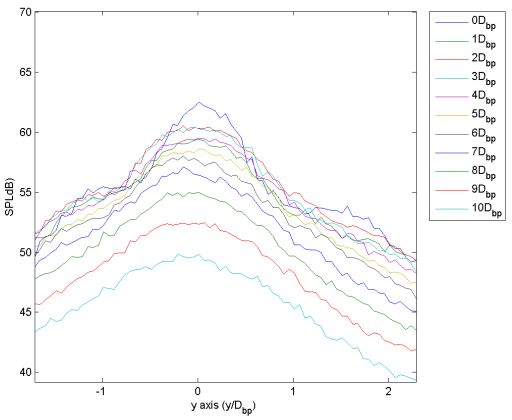

(b) CrCh, BpCo

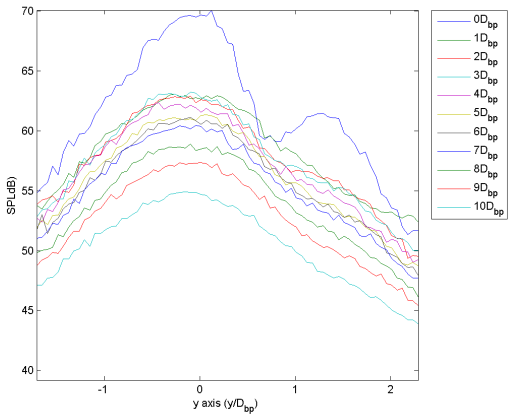

(c) CrCo, BpCh

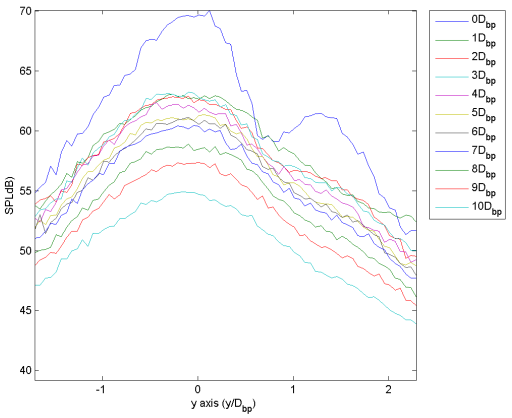

(d) CrCh, BpCh

Figure A.32: Radial profile at 80,128 Hz

A.3 Downstream acoustic profile of the jet at different radial (y-axis) positions

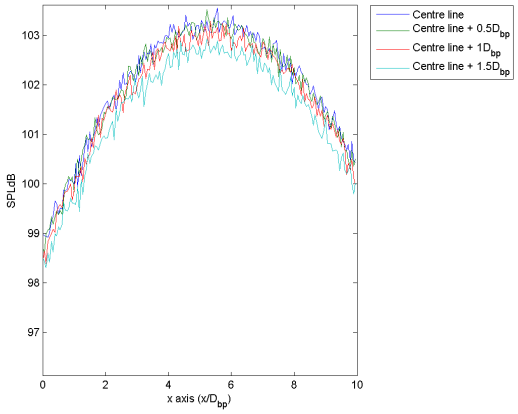

(a) CrCo, BpCo

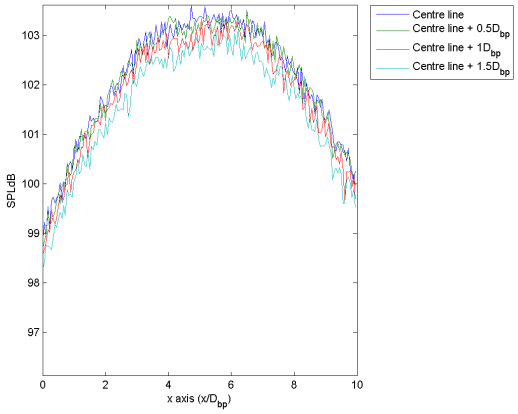

(b) CrCh, BpCo

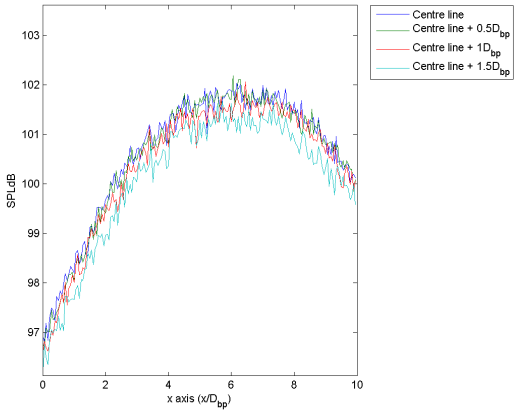

(c) CrCo, BpCh

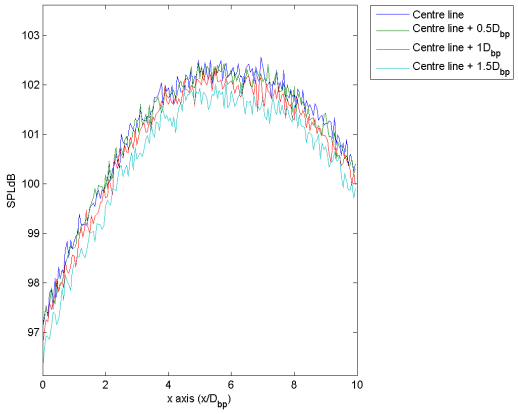

(d) CrCh, BpCh

Figure A.33: Downstream profiles at 5,120 Hz

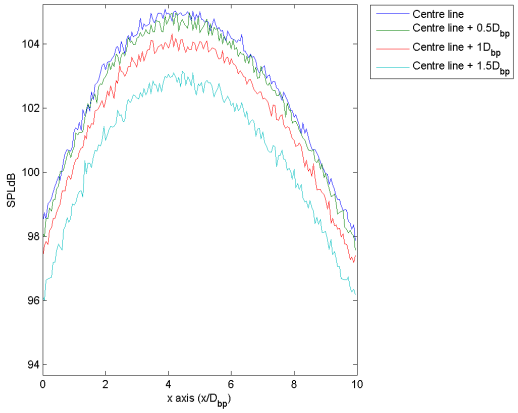

(a) CrCo, BpCo

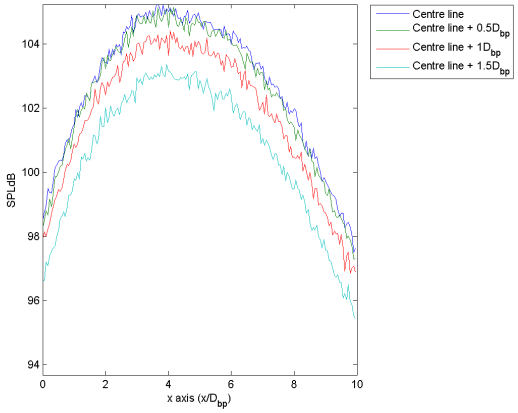

(b) CrCh, BpCo

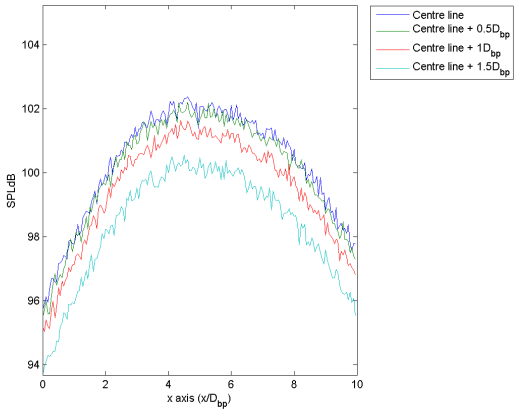

(c) CrCo, BpCh

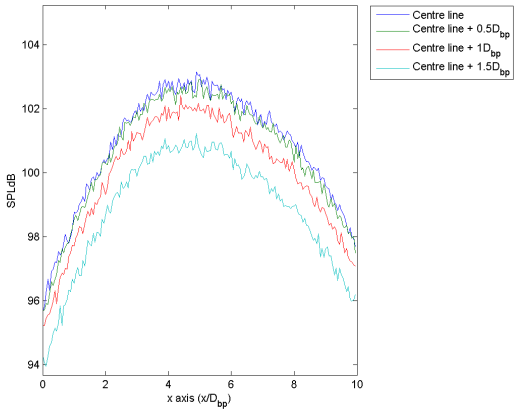

(d) CrCh, BpCh

Figure A.34: Downstream profiles at 10,240 Hz

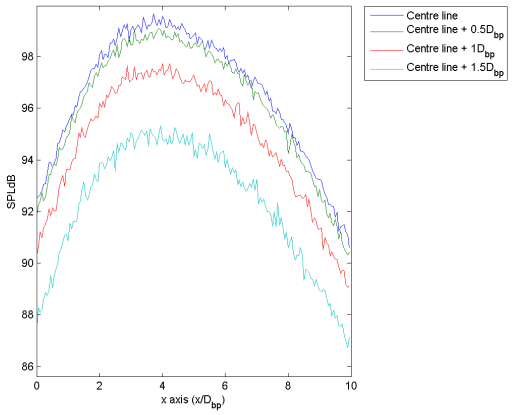

(a) CrCo, BpCo

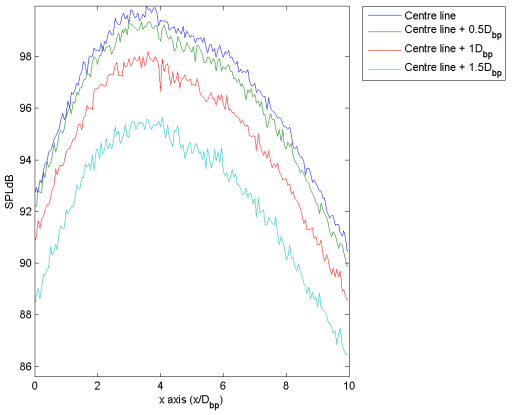

(b) CrCh, BpCo

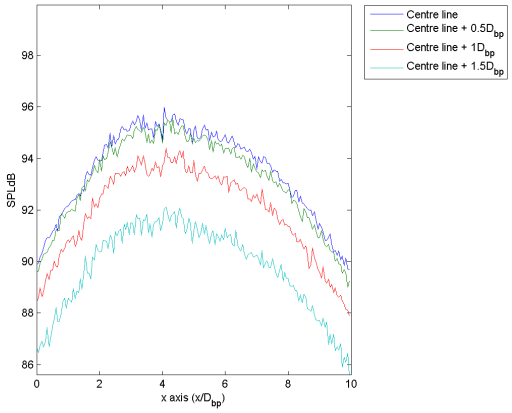

(c) CrCo, BpCh

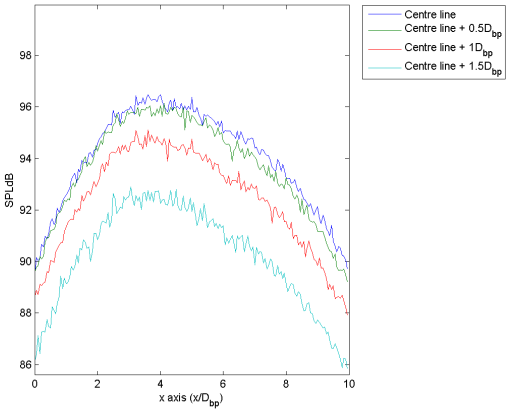

(d) CrCh, BpCh

Figure A.35: Downstream profiles at 15,104 Hz

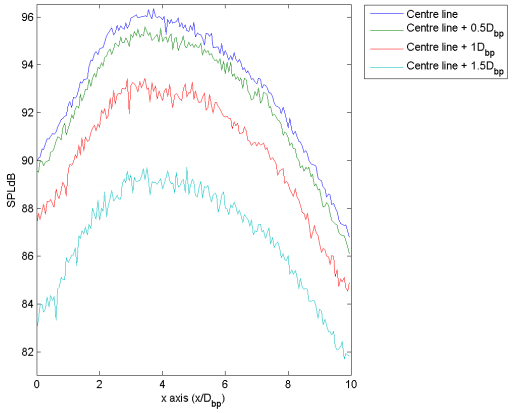

(a) CrCo, BpCo

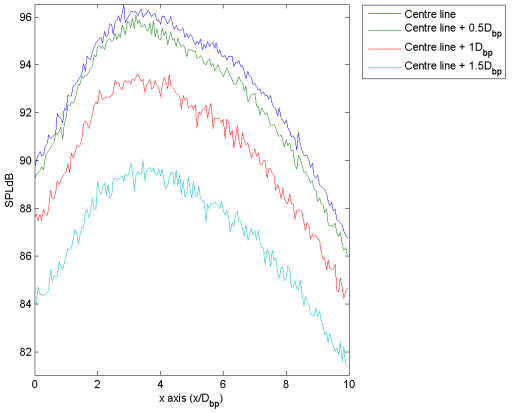

(b) CrCh, BpCo

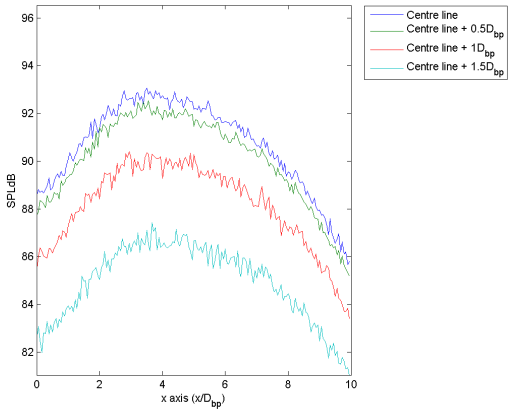

(c) CrCo, BpCh

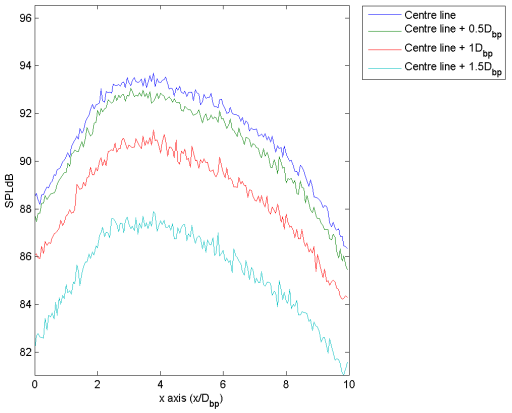

(d) CrCh, BpCh

Figure A.36: Downstream profiles at 20,224 Hz

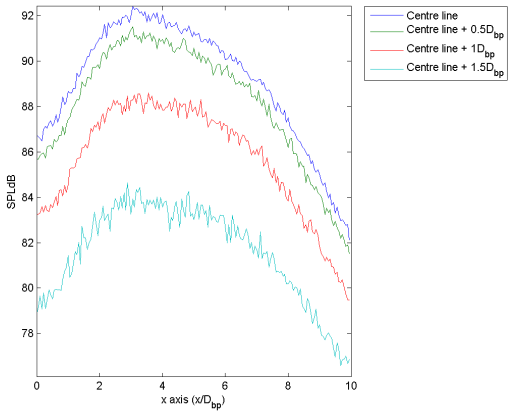

(a) CrCo, BpCo

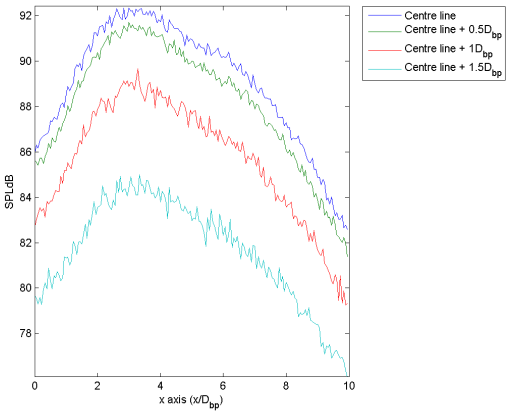

(b) CrCh, BpCo

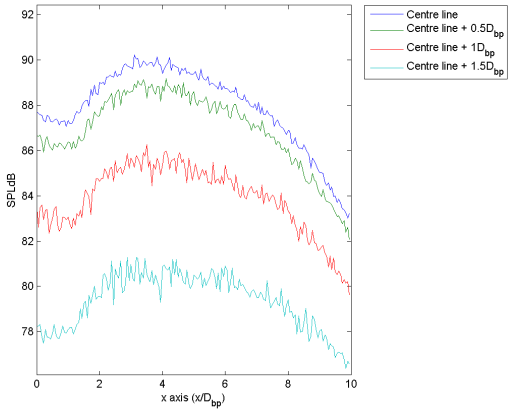

(c) CrCo, BpCh

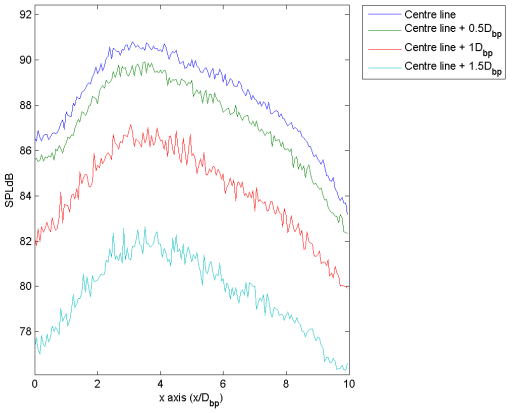

(d) CrCh, BpCh

Figure A.37: Downstream profiles at 25,088 Hz

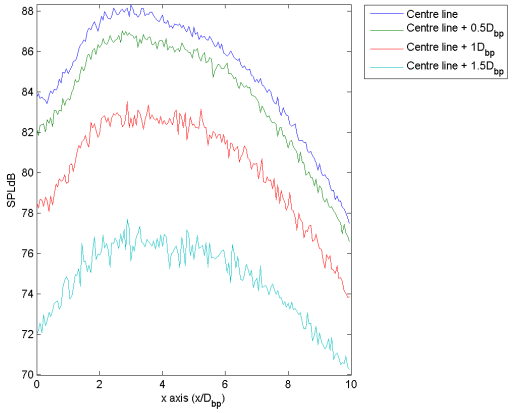

(a) CrCo, BpCo

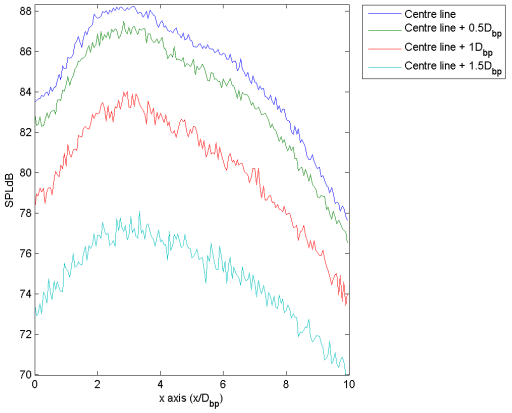

(b) CrCh, BpCo

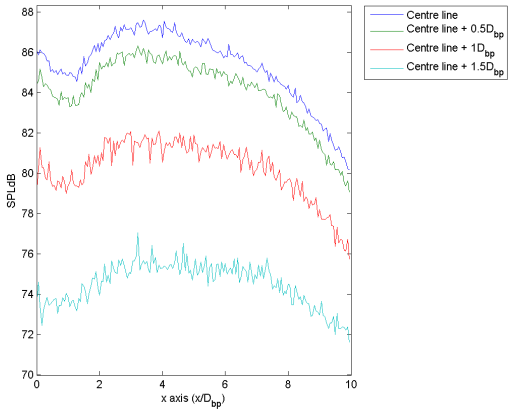

(c) CrCo, BpCh

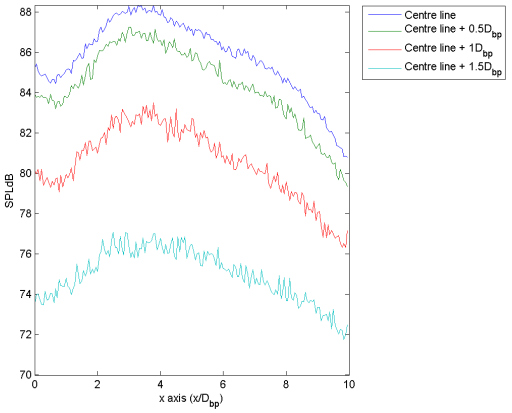

(d) CrCh, BpCh

Figure A.38: Downstream profiles at 30,208 Hz

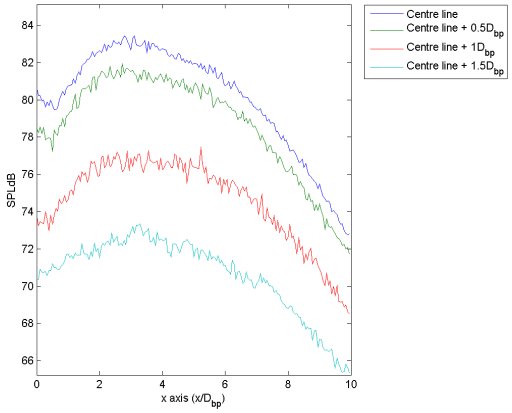

(a) CrCo, BpCo

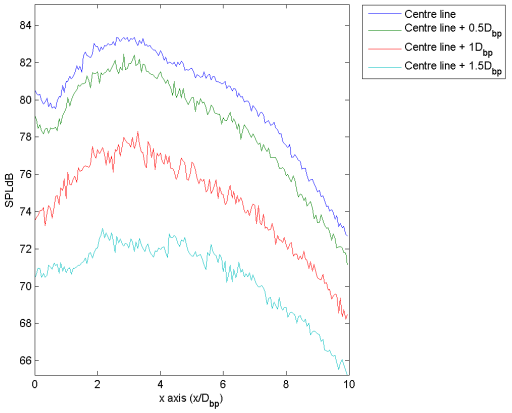

(b) CrCh, BpCo

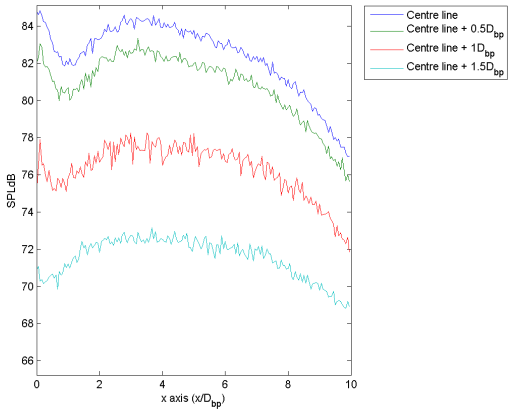

(c) CrCo, BpCh

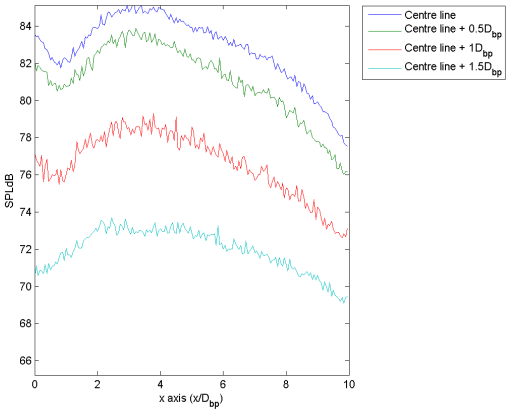

(d) CrCh, BpCh

Figure A.39: Downstream profiles at 35,072 Hz

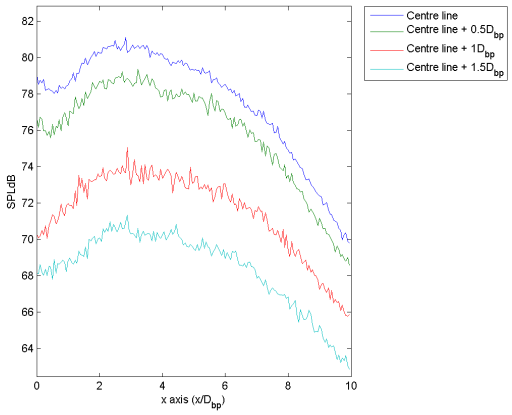

(a) CrCo, BpCo

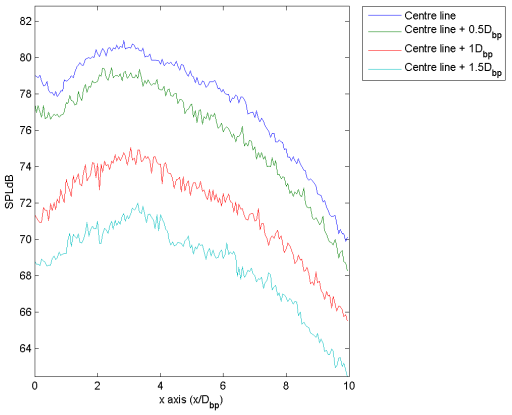

(b) CrCh, BpCo

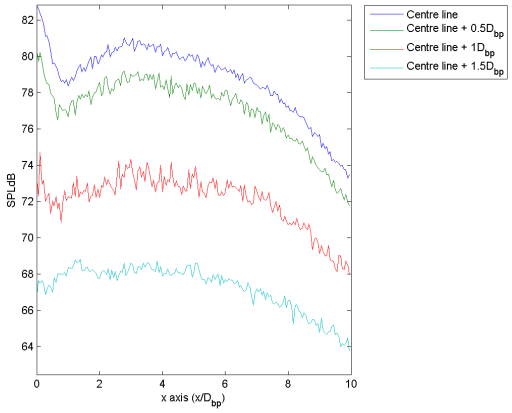

(c) CrCo, BpCh

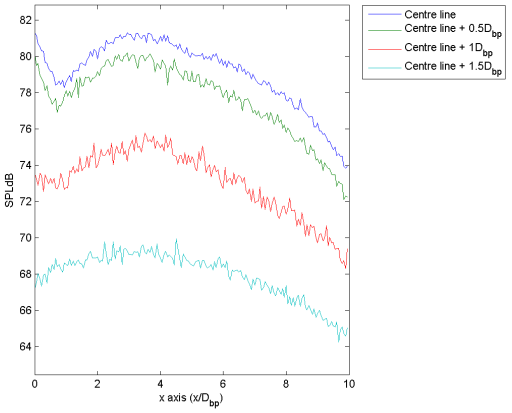

(d) CrCh, BpCh

Figure A.40: Downstream profiles at 40,192 Hz

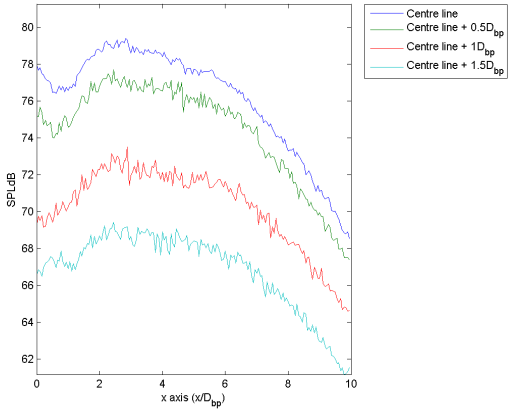

(a) CrCo, BpCo

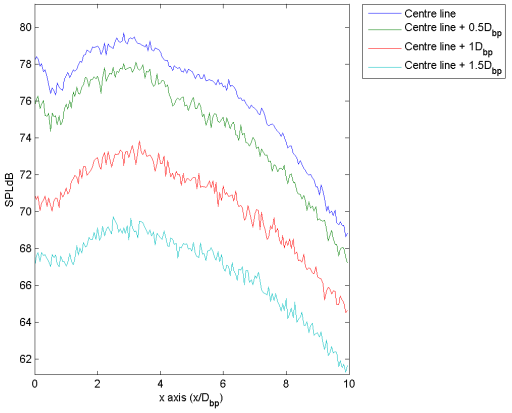

(b) CrCh, BpCo

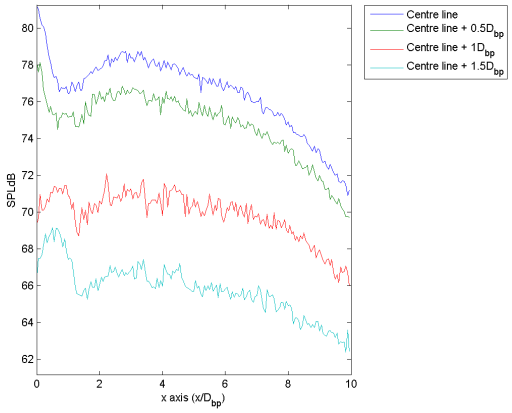

(c) CrCo, BpCh

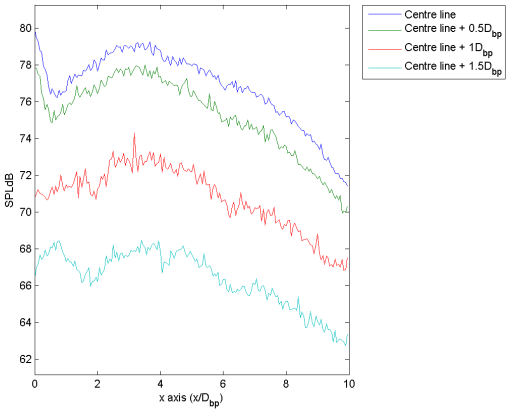

(d) CrCh, BpCh

Figure A.41: Downstream profiles at 45,056 Hz

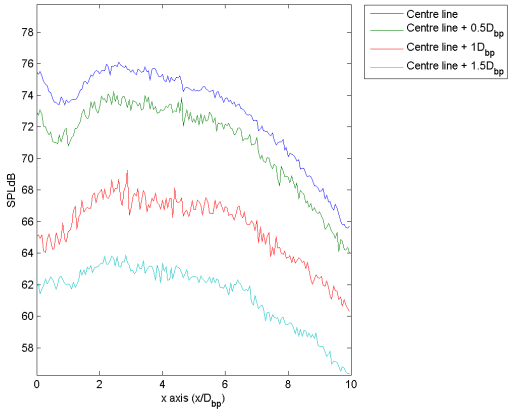

(a) CrCo, BpCo

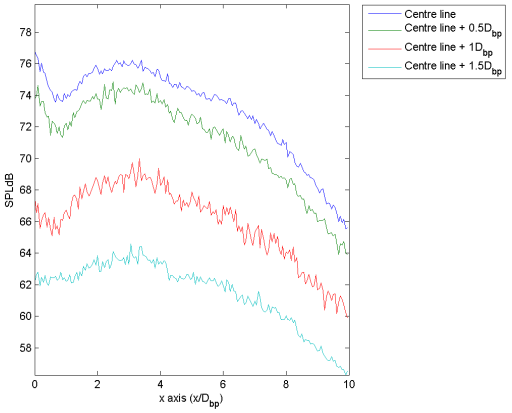

(b) CrCh, BpCo

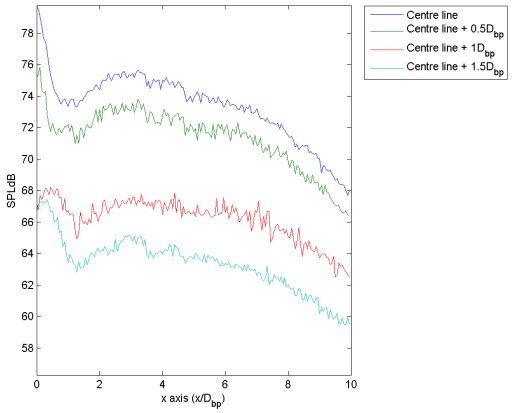

(c) CrCo, BpCh

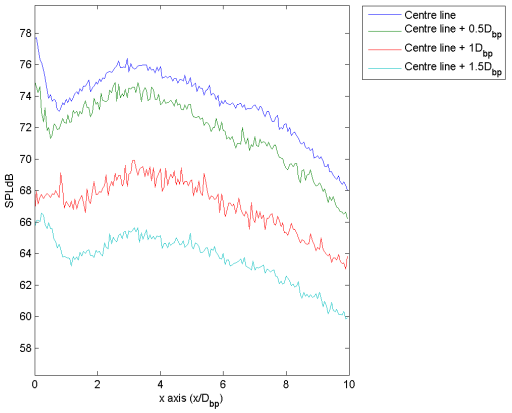

(d) CrCh, BpCh

Figure A.42: Downstream profiles at 50,176 Hz

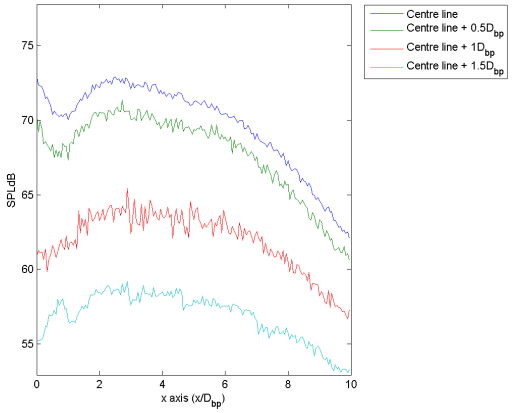

(a) CrCo, BpCo

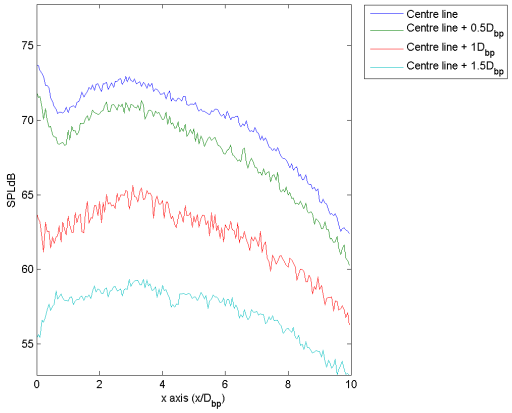

(b) CrCh, BpCo

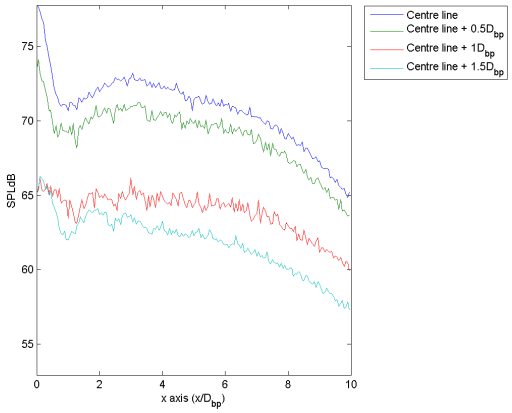

(c) CrCo, BpCh

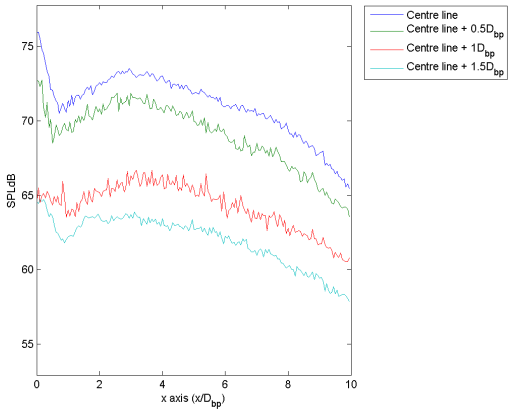

(d) CrCh, BpCh

Figure A.43: Downstream profiles at 55,040 Hz

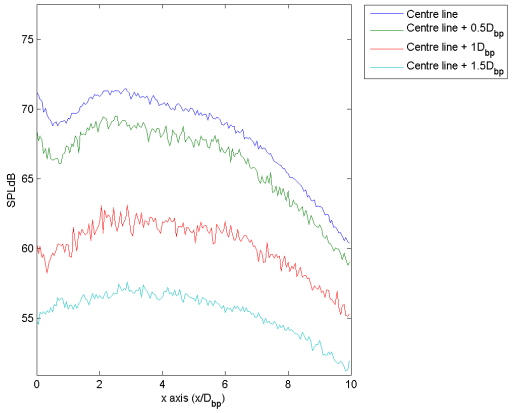

(a) CrCo, BpCo

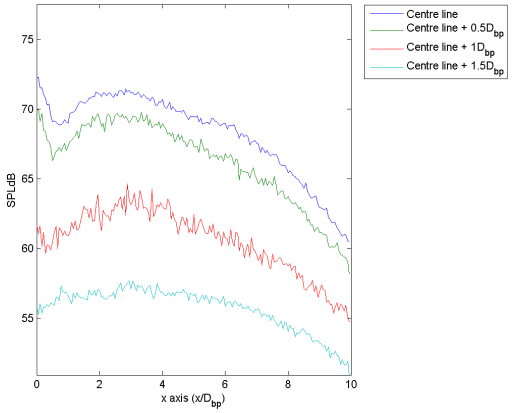

(b) CrCh, BpCo

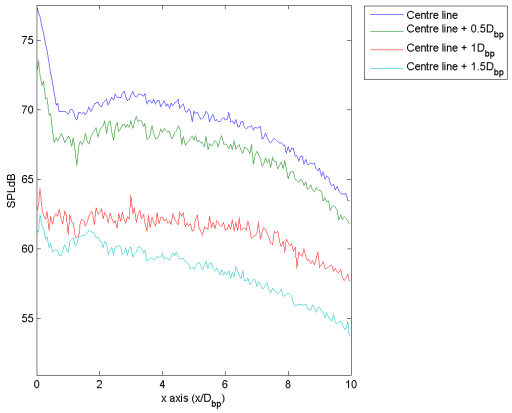

(c) CrCo, BpCh

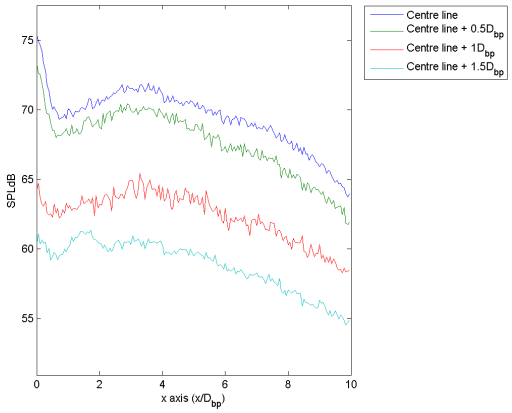

(d) CrCh, BpCh

Figure A.44: Downstream profiles at 60,160 Hz

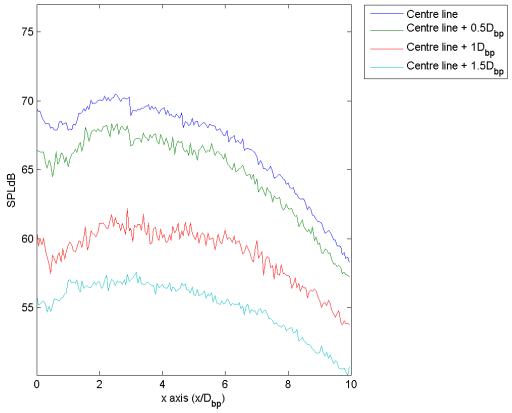

(a) CrCo, BpCo

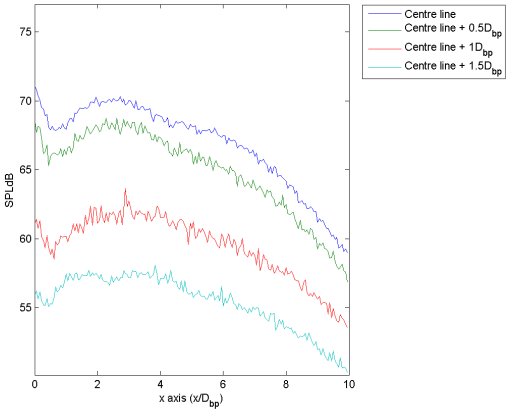

(b) CrCh, BpCo

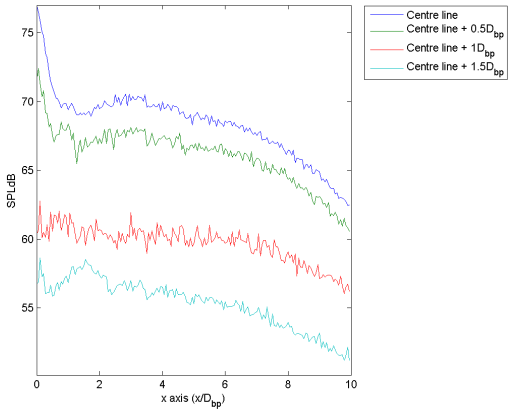

(c) CrCo, BpCh

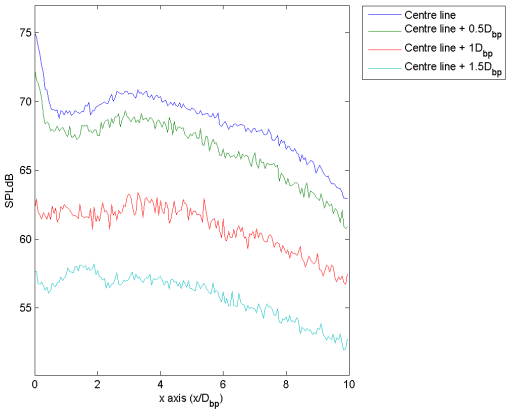

(d) CrCh, BpCh

Figure A.45: Downstream profiles at 65,024 Hz

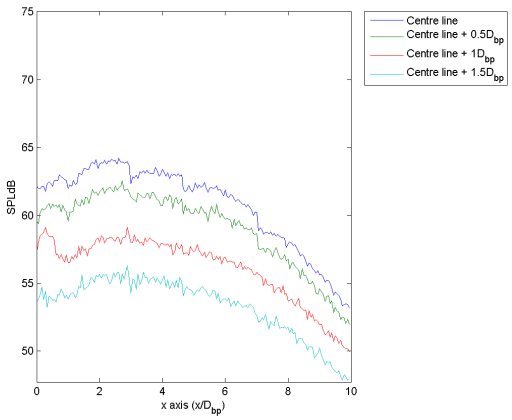

(a) CrCo, BpCo

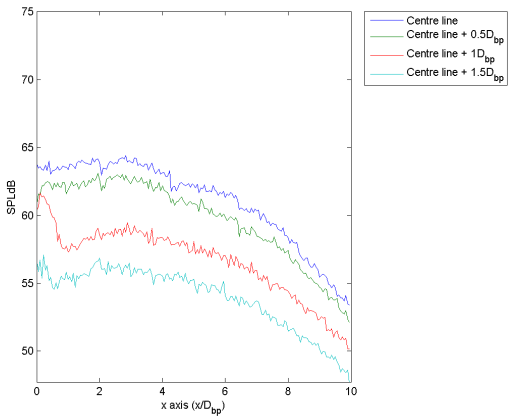

(b) CrCh, BpCo

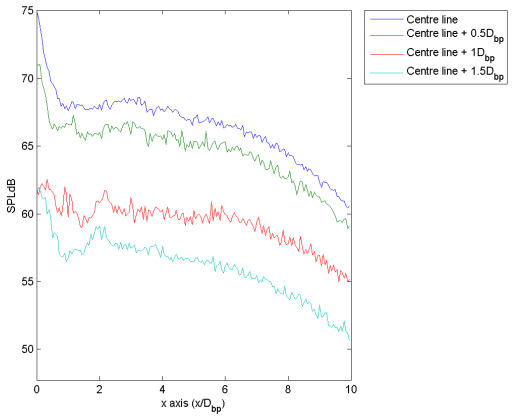

(c) CrCo, BpCh

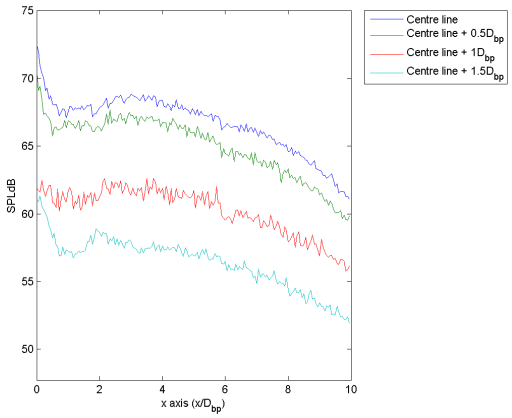

(d) CrCh, BpCh

Figure A.46: Downstream profiles at 70,144 Hz

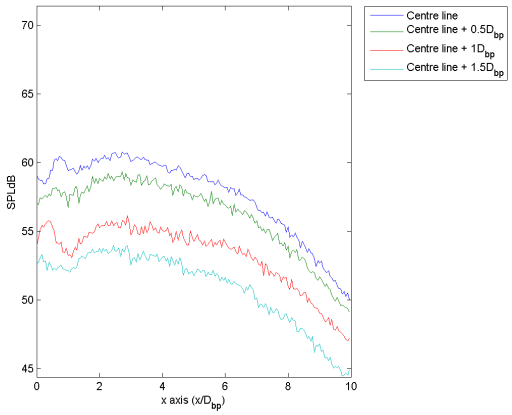

(a) CrCo, BpCo

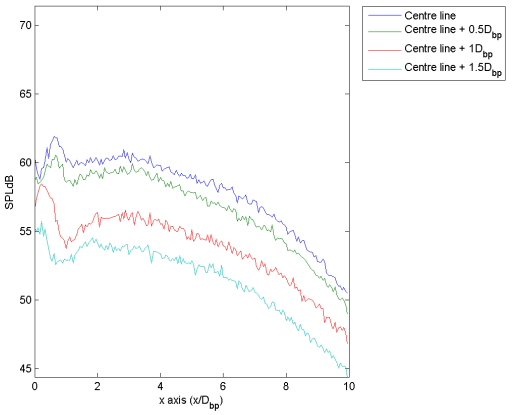

(b) CrCh, BpCo

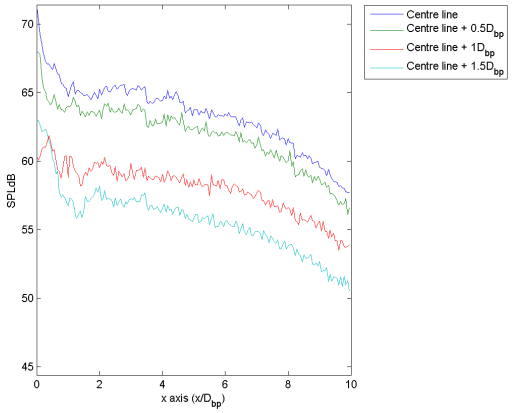

(c) CrCo, BpCh

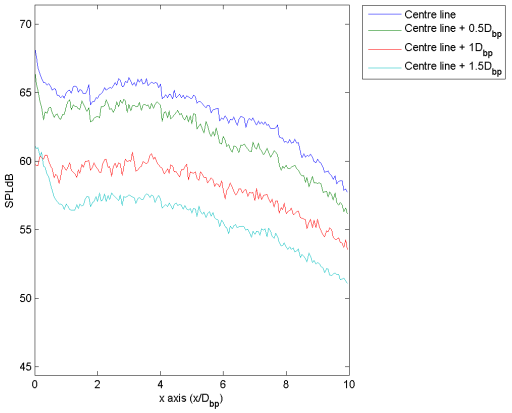

(d) CrCh, BpCh

Figure A.47: Downstream profiles at 75,008 Hz

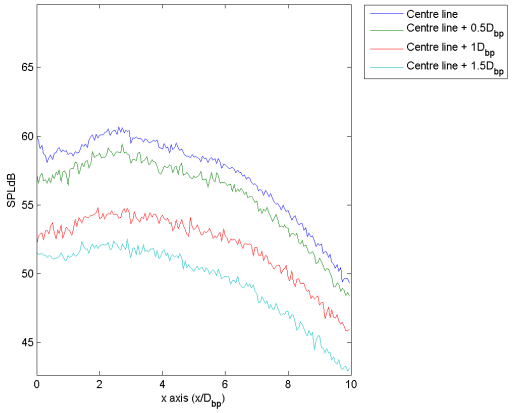

(a) CrCo, BpCo

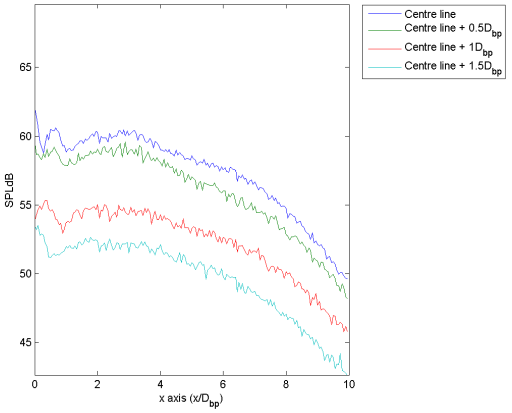

(b) CrCh, BpCo

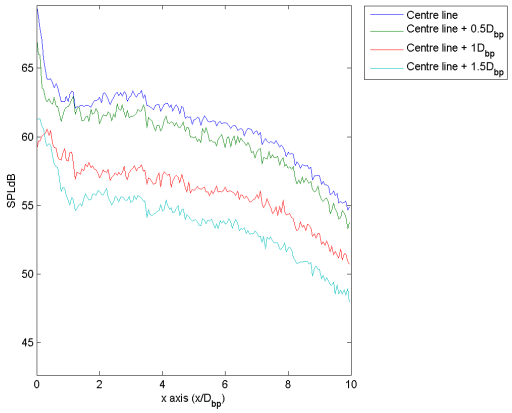

(c) CrCo, BpCh

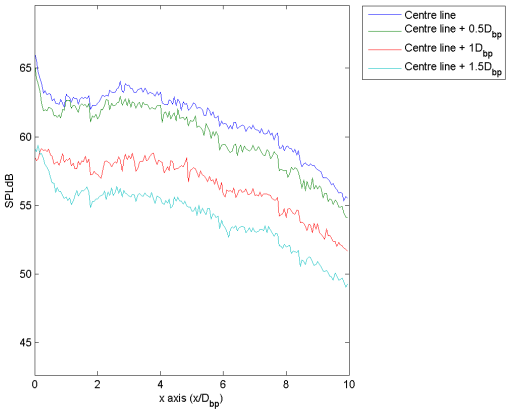

(d) CrCh, BpCh

Figure A.48: Downstream profiles at 80,128 Hz

A.4 Comparison of the downstream acoustic profiles of the jet with different nozzles, at different radial (y-axis) positions

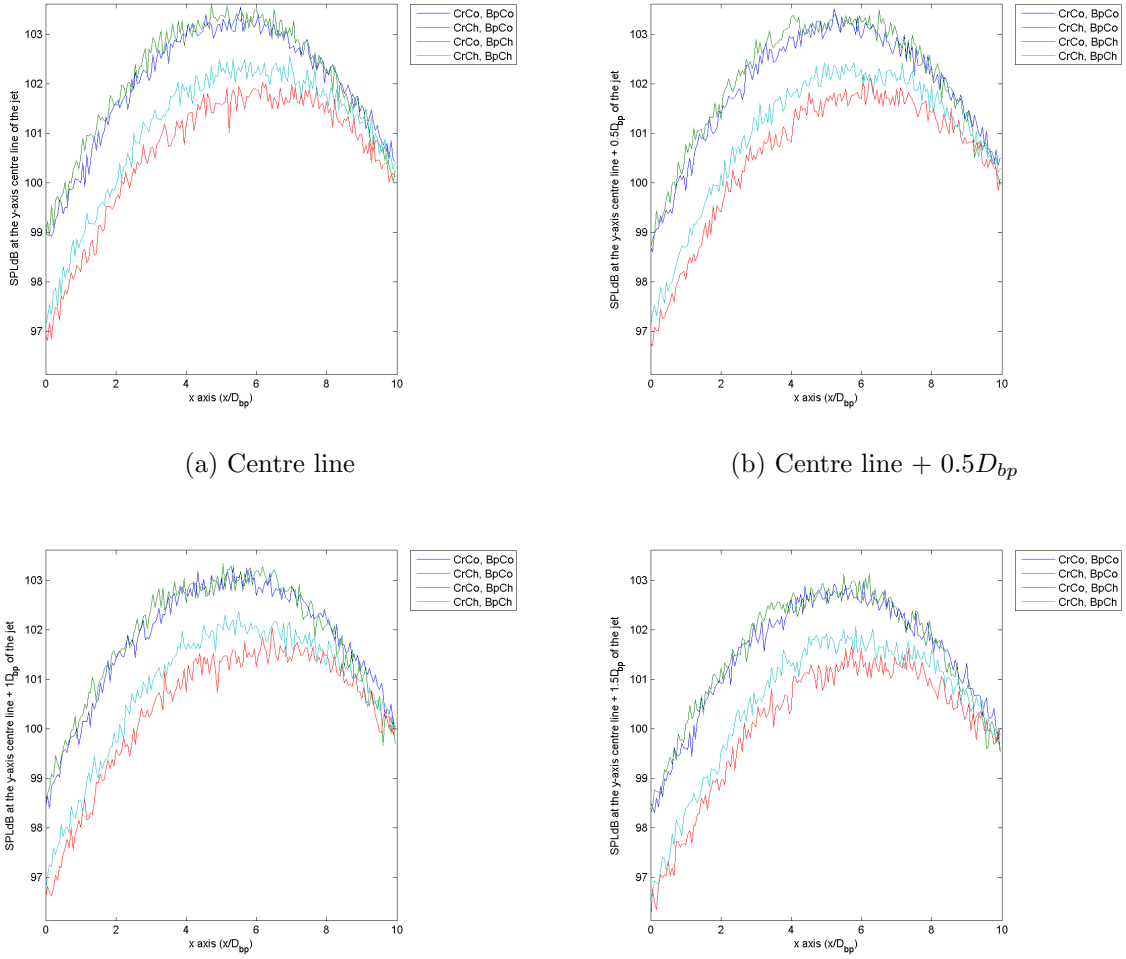

(a) Centre line

(b) Centre line + $0.5D_{bp}$

(c) Centre line + $1D_{bp}$

(d) Centre line + $1.5D_{bp}$

Figure A.49: Downstream acoustic profile of all the nozzles at 5,120 Hz

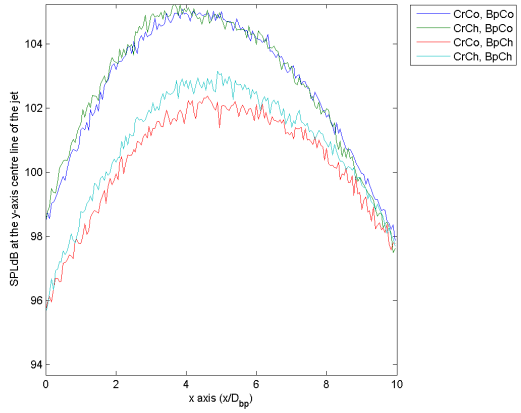

(a) Centre line

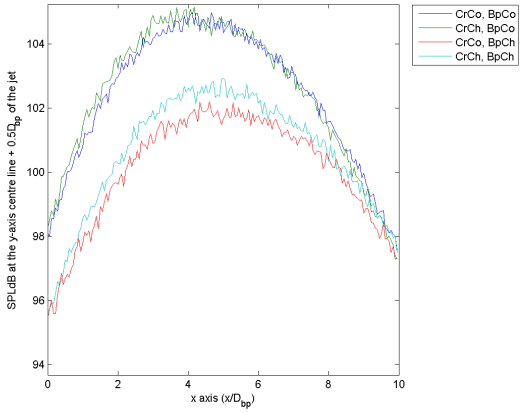

(b) Centre line + $0.5D_{bp}$

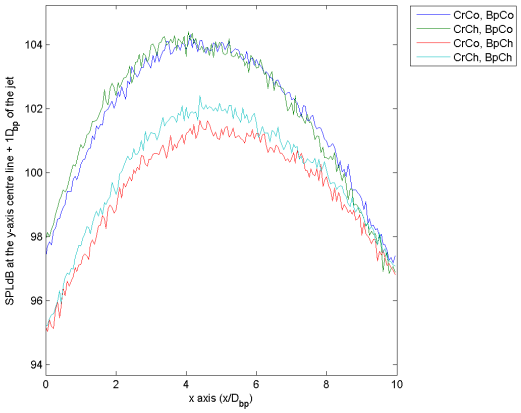

(c) Centre line + $1D_{bp}$

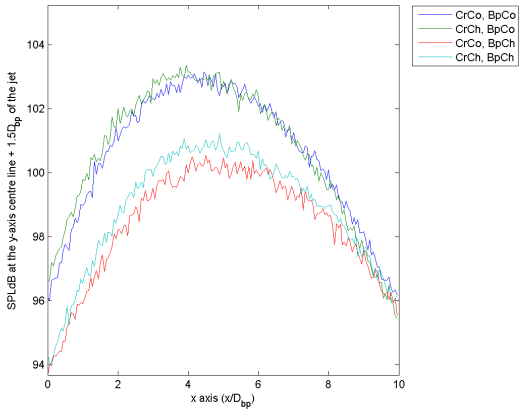

(d) Centre line + $1.5D_{bp}$

Figure A.50: Downstream acoustic profile of all the nozzles at 10,240 Hz

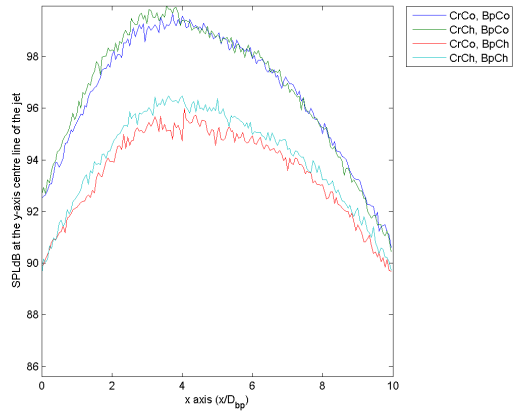

(a) Centre line

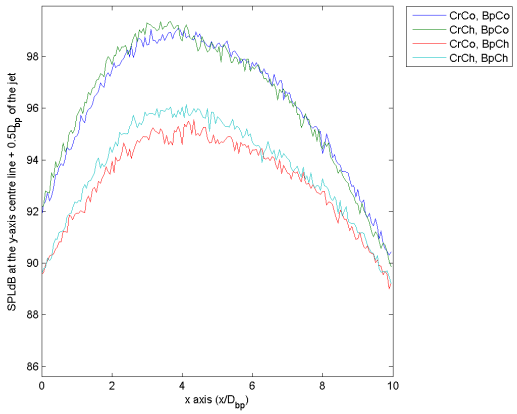

(b) Centre line + $0.5D_{bp}$

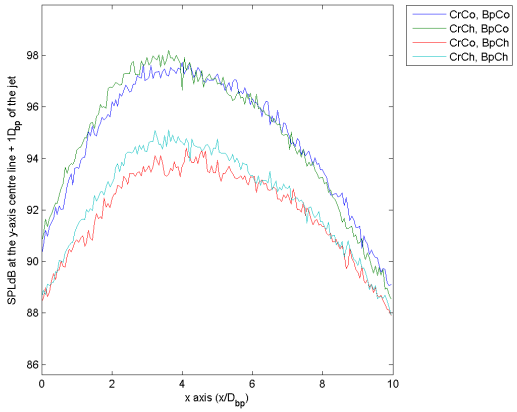

(c) Centre line + $1D_{bp}$

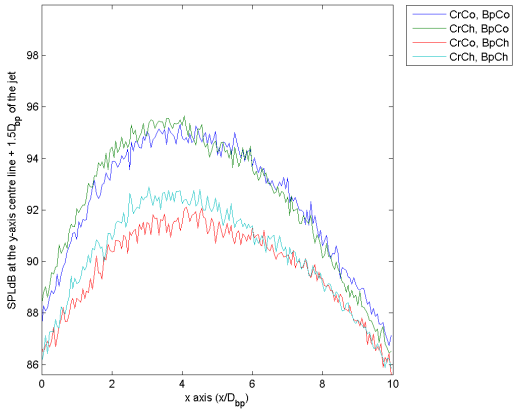

(d) Centre line + $1.5D_{bp}$

Figure A.51: Downstream acoustic profile of all the nozzles at 15,104 Hz

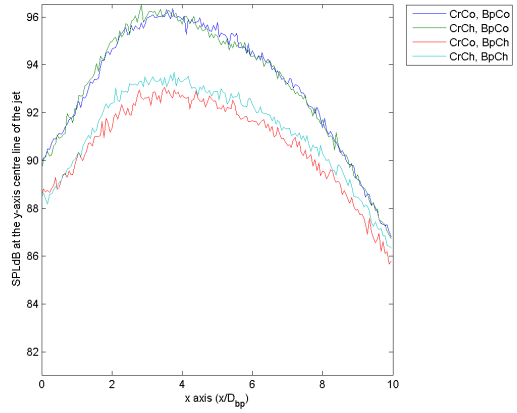

(a) Centre line

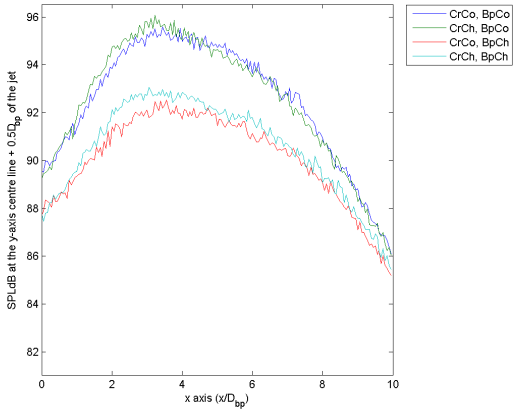

(b) Centre line + $0.5D_{bp}$

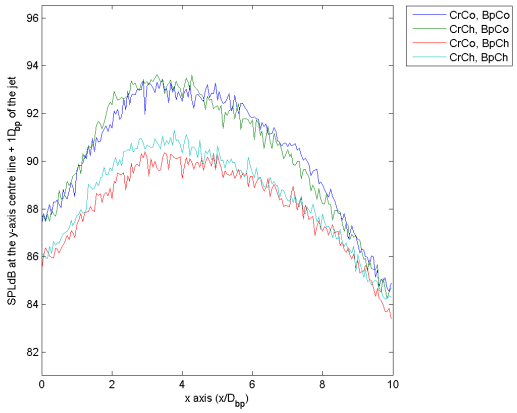

(c) Centre line + $1D_{bp}$

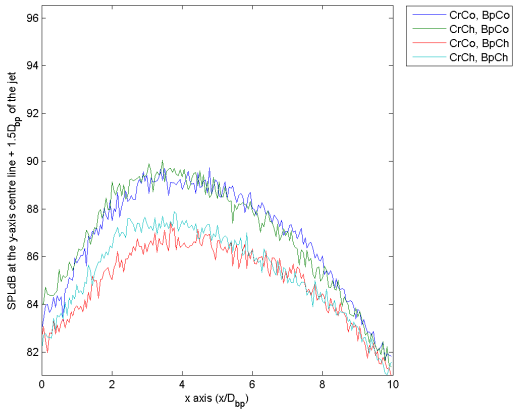

(d) Centre line + $1.5D_{bp}$

Figure A.52: Downstream acoustic profile of all the nozzles at 20,224 Hz

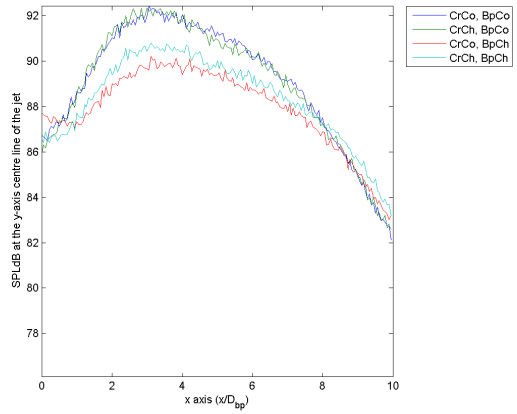

(a) Centre line

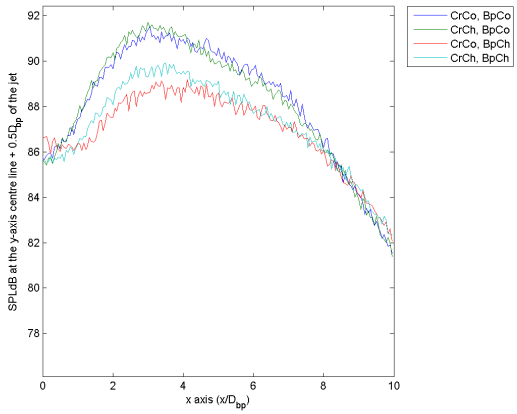

(b) Centre line + $0.5D_{bp}$

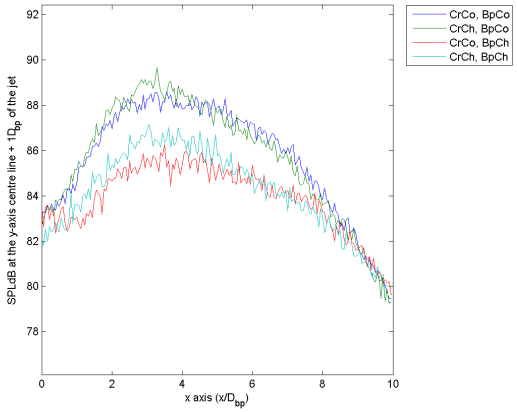

(c) Centre line + $1D_{bp}$

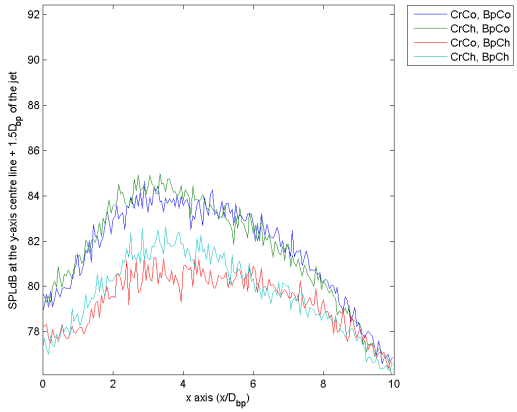

(d) Centre line + $1.5D_{bp}$

Figure A.53: Downstream acoustic profile of all the nozzles at 25,088 Hz

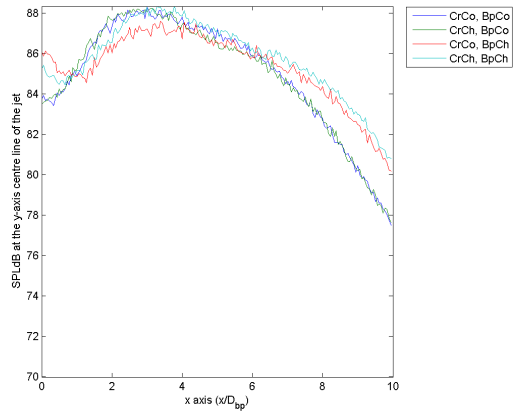

(a) Centre line

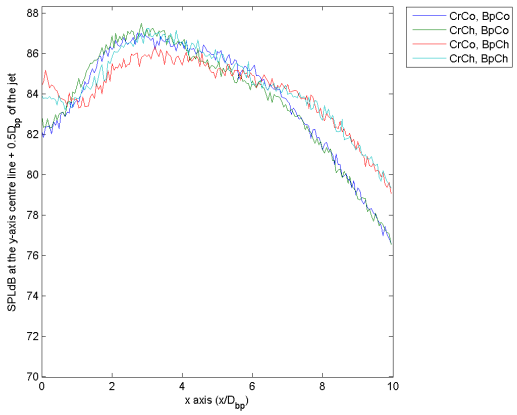

(b) Centre line + $0.5D_{bp}$

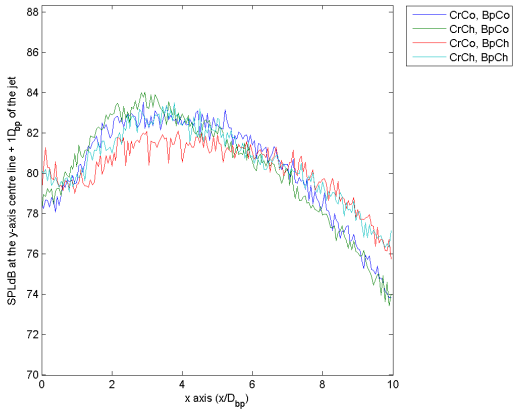

(c) Centre line + $1D_{bp}$

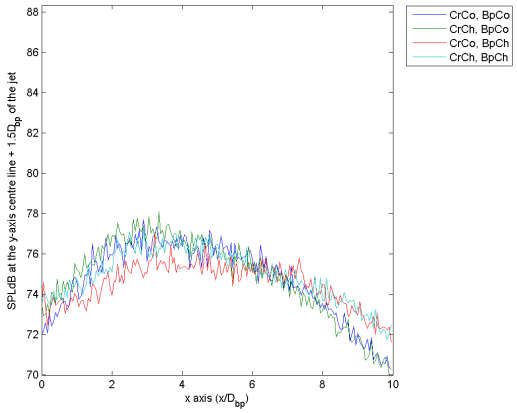

(d) Centre line + $1.5D_{bp}$

Figure A.54: Downstream acoustic profile of all the nozzles at 30,208 Hz

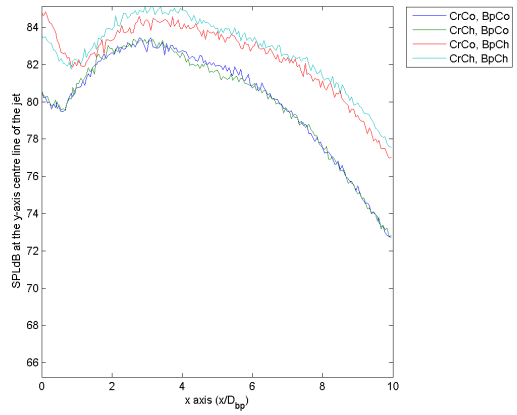

(a) Centre line

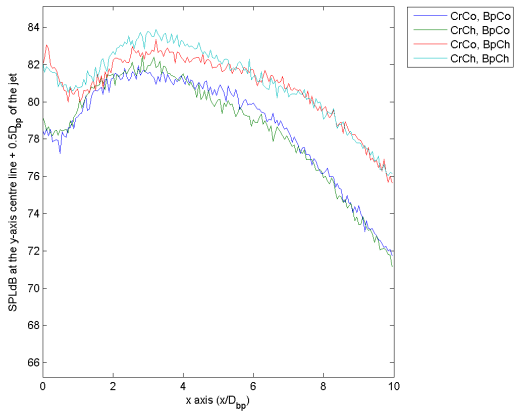

(b) Centre line + $0.5D_{bp}$

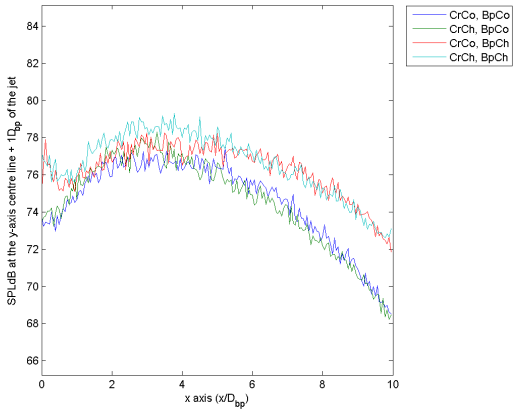

(c) Centre line + $1D_{bp}$

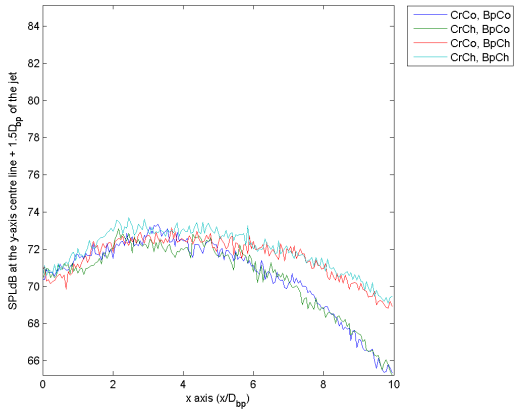

(d) Centre line + $1.5D_{bp}$

Figure A.55: Downstream acoustic profile of all the nozzles at 35,072 Hz

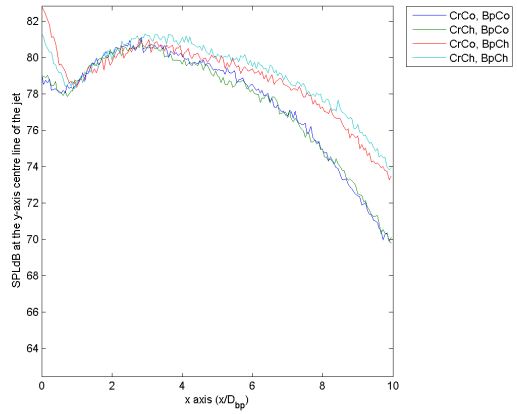

(a) Centre line

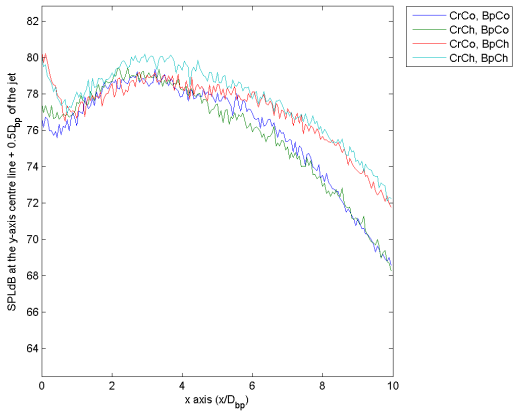

(b) Centre line + $0.5D_{bp}$

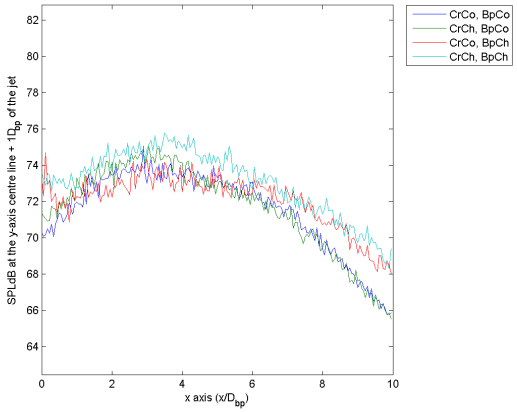

(c) Centre line + $1D_{bp}$

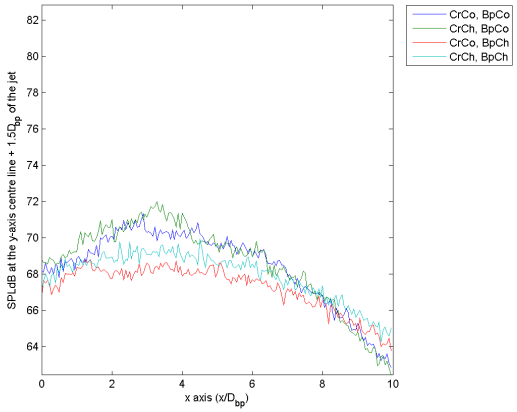

(d) Centre line + $1.5D_{bp}$

Figure A.56: Downstream acoustic profile of all the nozzles at 40,192 Hz

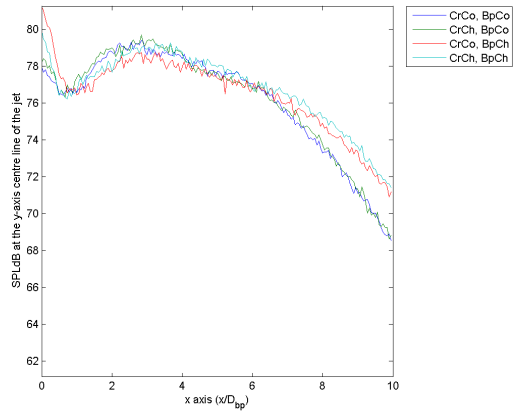

(a) Centre line

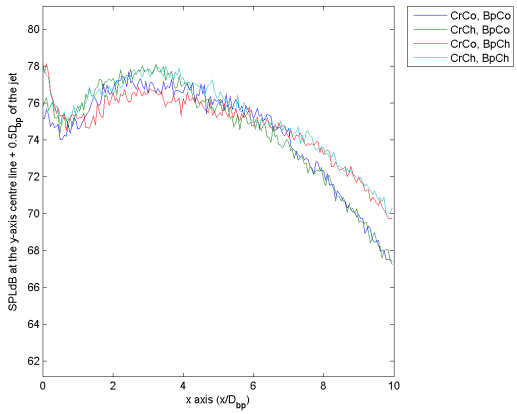

(b) Centre line + $0.5D_{bp}$

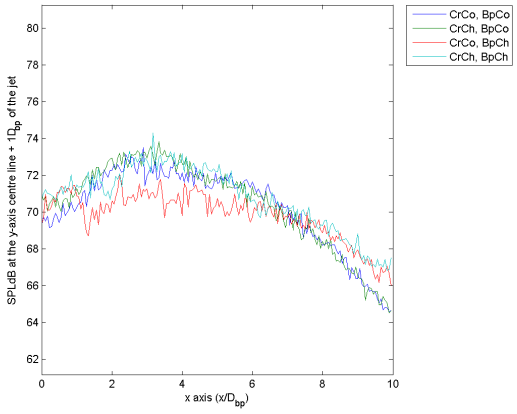

(c) Centre line + $1D_{bp}$

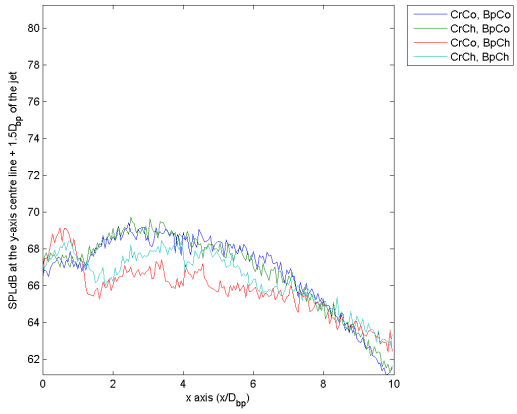

(d) Centre line + $1.5D_{bp}$

Figure A.57: Downstream acoustic profile of all the nozzles at 45,056 Hz

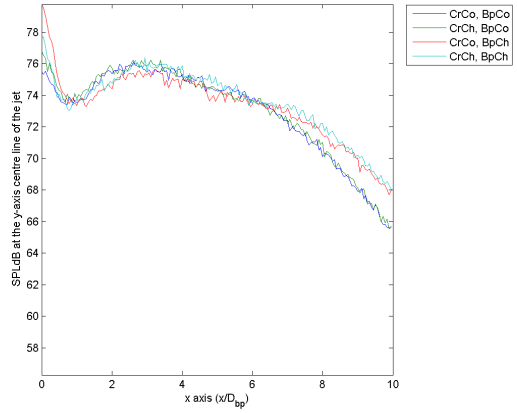

(a) Centre line

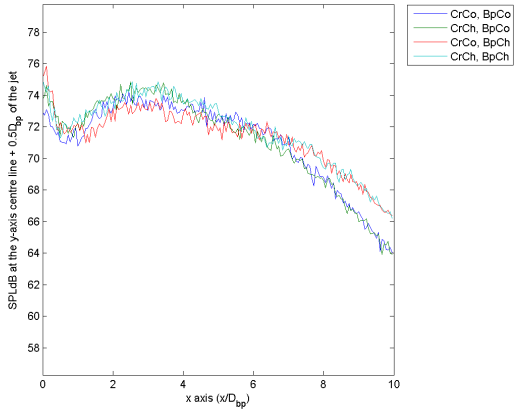

(b) Centre line + $0.5D_{bp}$

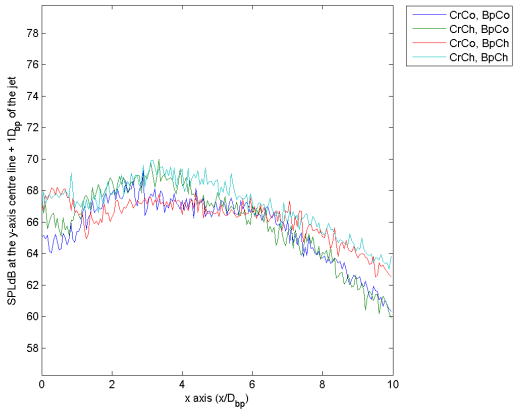

(c) Centre line + $1D_{bp}$

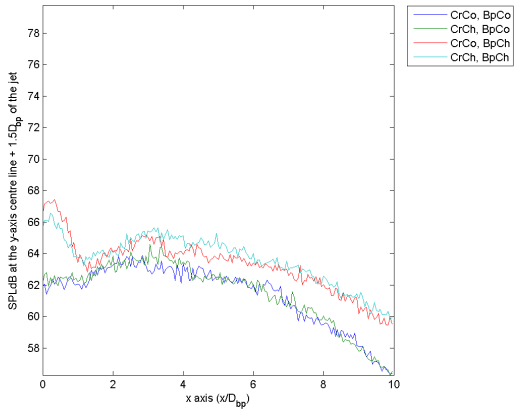

(d) Centre line + $1.5D_{bp}$

Figure A.58: Downstream acoustic profile of all the nozzles at 50,176 Hz

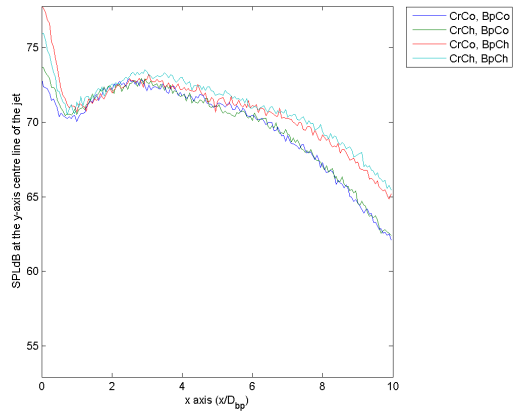

(a) Centre line

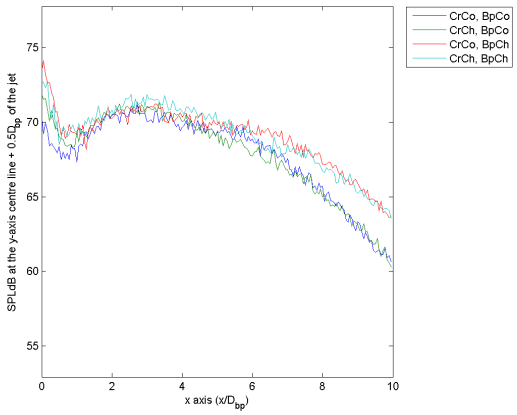

(b) Centre line + $0.5D_{bp}$

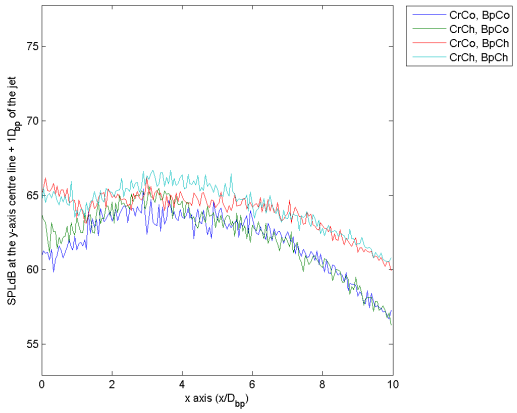

(c) Centre line + $1D_{bp}$

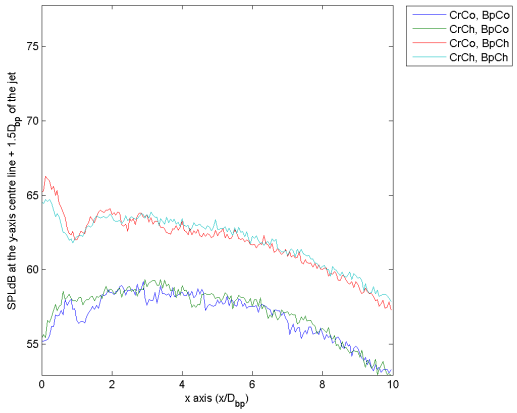

(d) Centre line + $1.5D_{bp}$

Figure A.59: Downstream acoustic profile of all the nozzles at 55,040 Hz

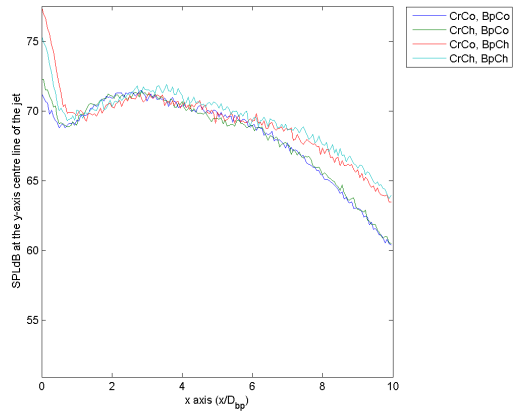

(a) Centre line

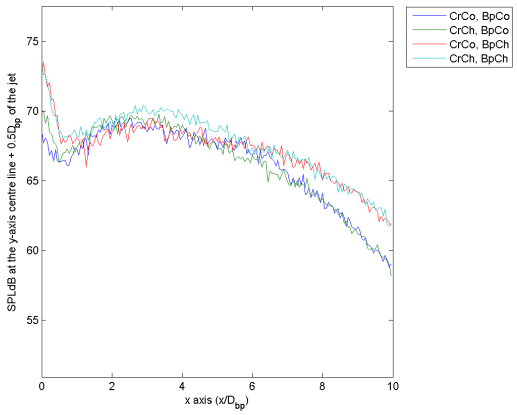

(b) Centre line + $0.5D_{bp}$

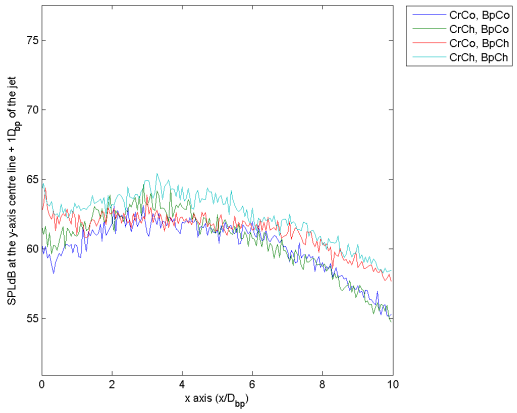

(c) Centre line + $1D_{bp}$

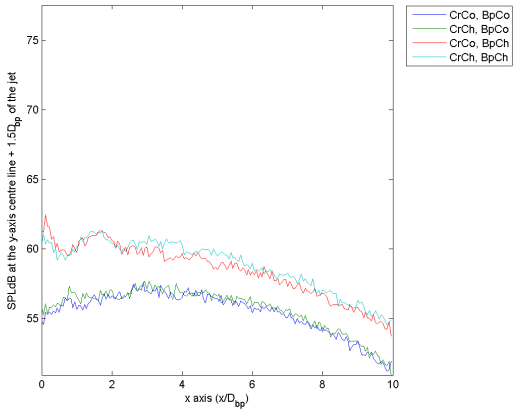

(d) Centre line + $1.5D_{bp}$

Figure A.60: Downstream acoustic profile of all the nozzles at 60,160 Hz

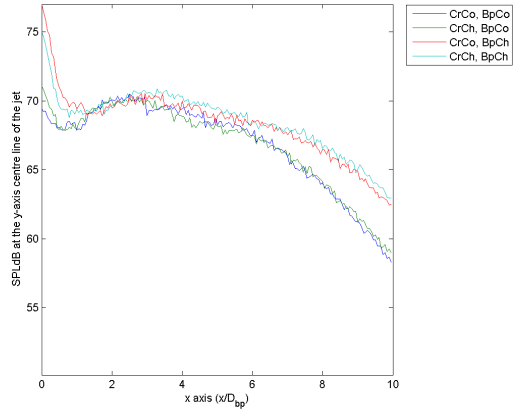

(a) Centre line

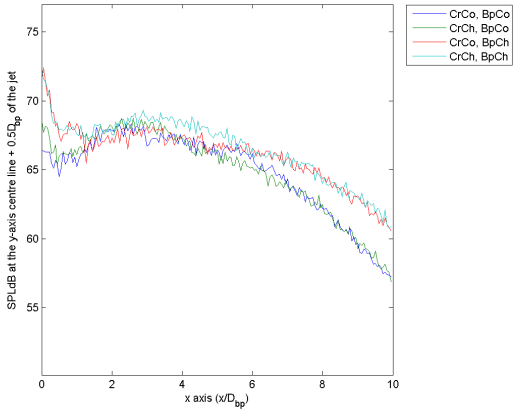

(b) Centre line + $0.5D_{bp}$

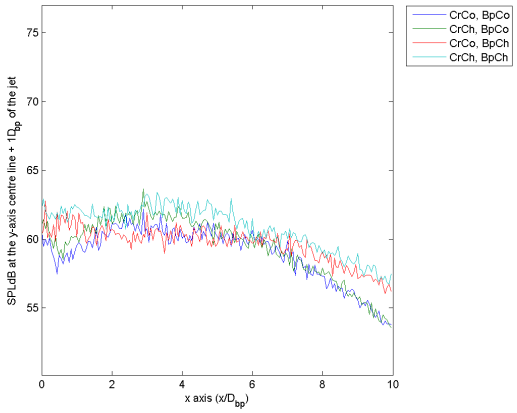

(c) Centre line + $1D_{bp}$

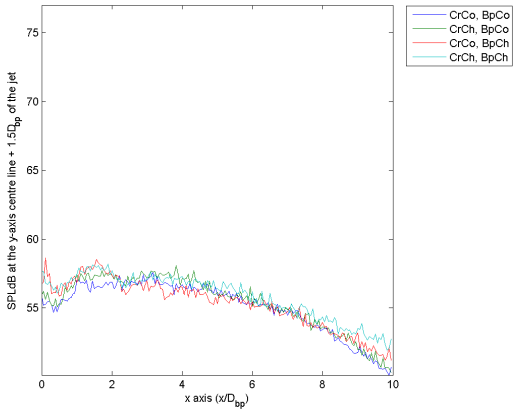

(d) Centre line + $1.5D_{bp}$

Figure A.61: Downstream acoustic profile of all the nozzles at 65,024 Hz

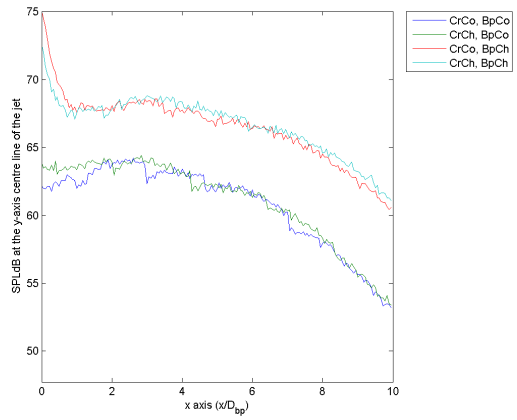

(a) Centre line

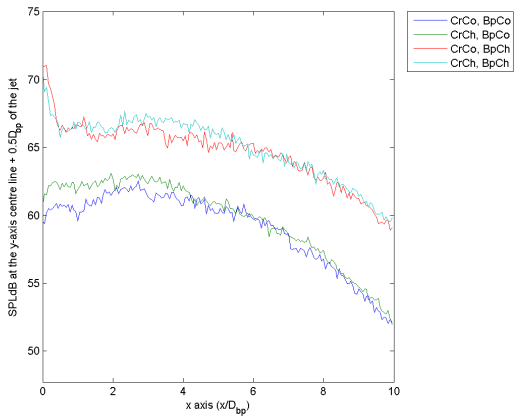

(b) Centre line + $0.5D_{bp}$

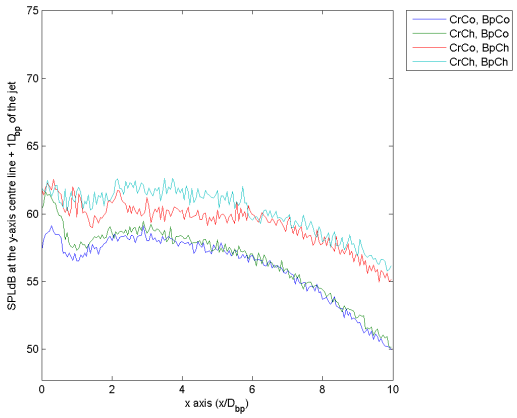

(c) Centre line + $1D_{bp}$

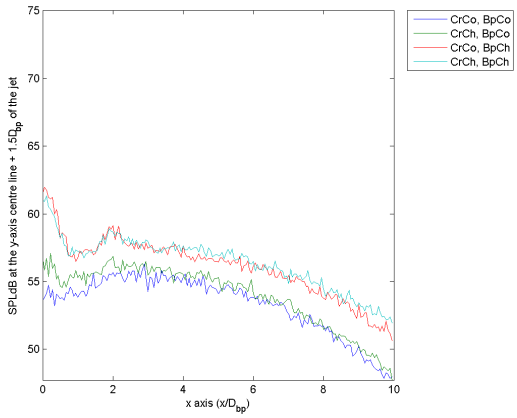

(d) Centre line + $1.5D_{bp}$

Figure A.62: Downstream acoustic profile of all the nozzles at 70,144 Hz

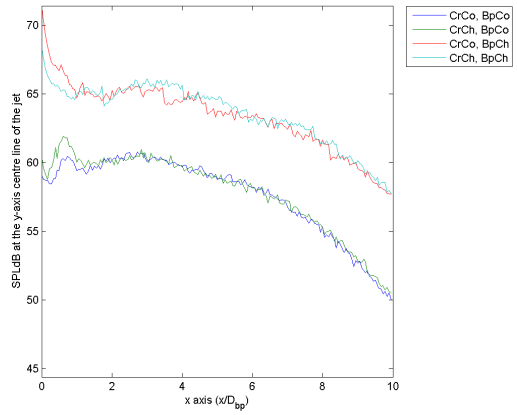

(a) Centre line

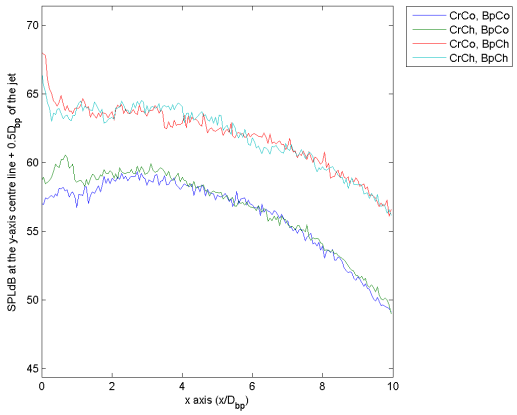

(b) Centre line + $0.5D_{bp}$

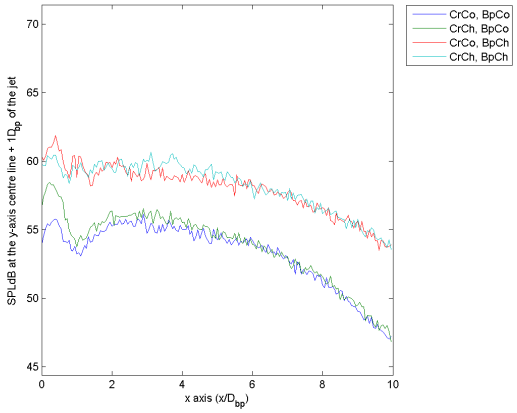

(c) Centre line + $1D_{bp}$

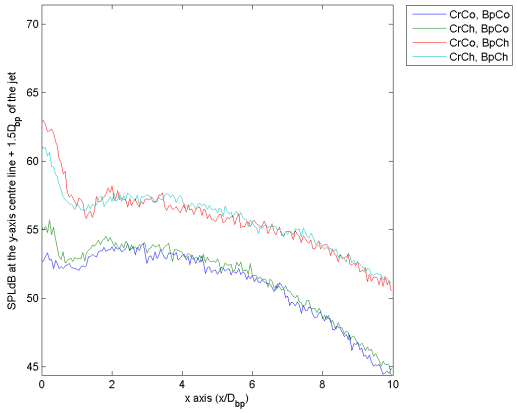

(d) Centre line + $1.5D_{bp}$

Figure A.63: Downstream acoustic profile of all the nozzles at 75,008 Hz

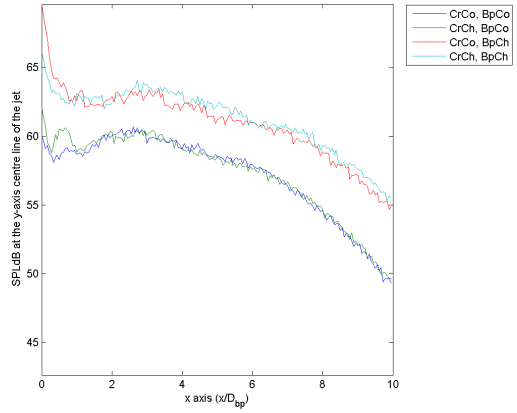

(a) Centre line

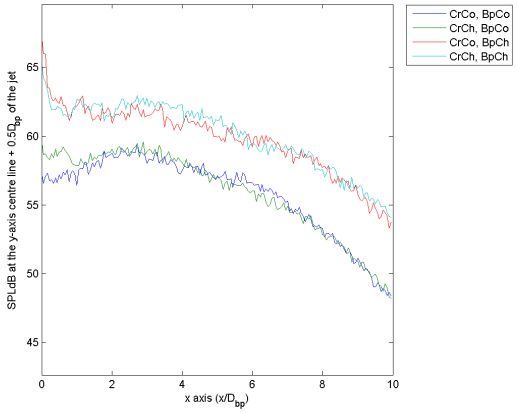

(b) Centre line + $0.5D_{bp}$

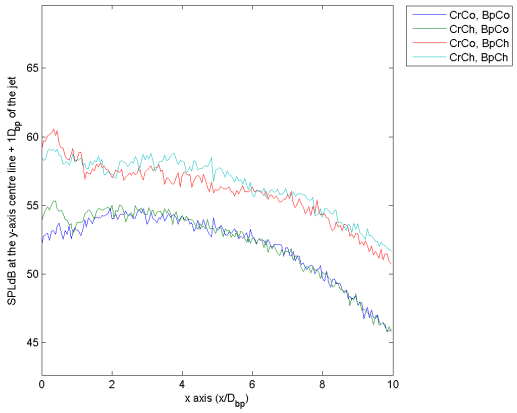

(c) Centre line + $1D_{bp}$

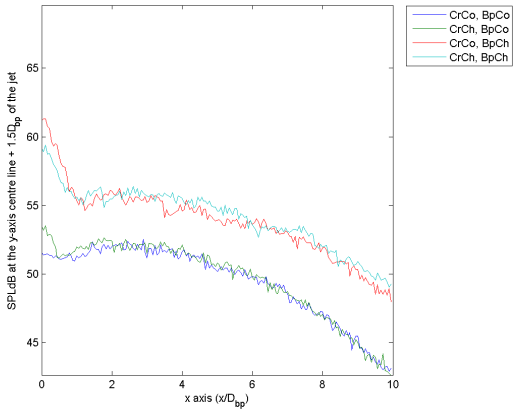

(d) Centre line + $1.5D_{bp}$

Figure A.64: Downstream acoustic profile of all the nozzles at 80,128 Hz

A.5 Sound and frequency distribution at y=0

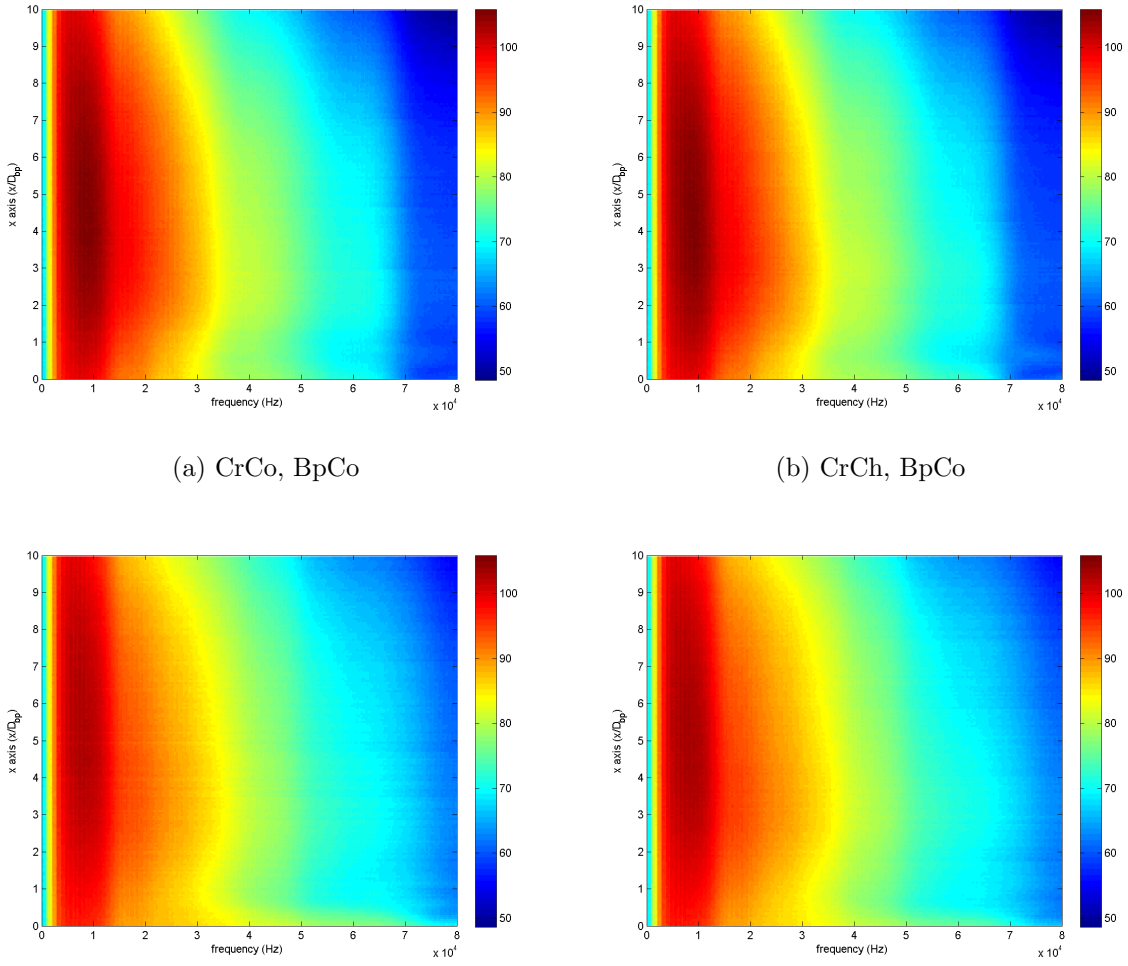

(a) CrCo, BpCo

(b) CrCh, BpCo

(c) CrCo, BpCh

(d) CrCh, BpCh

Figure A.65: Sound and frequency distribution at y=0 (colour bar in SPLdB)

A.6 2D LDA axial and radial component mapping

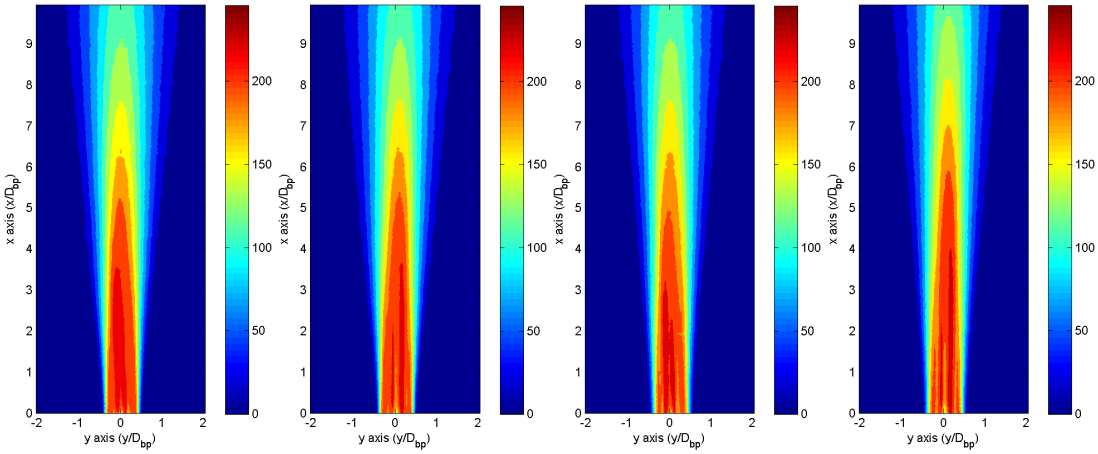

(a) CrCo, BpCo (b) CrCh, BpCo (c) CrCo, BpCh (d) CrCh, BpCh

Figure A.66: Axial velocity (colour bar in ms^{-1}

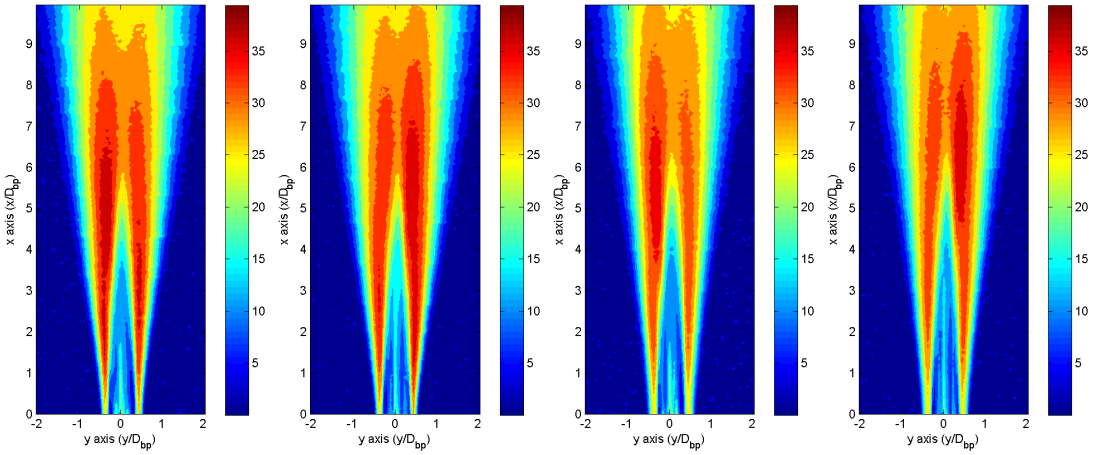

(a) CrCo, BpCo (b) CrCh, BpCo (c) CrCo, BpCh (d) CrCh, BpCh

Figure A.67: Axial rms (colour bar in ms^{-1})

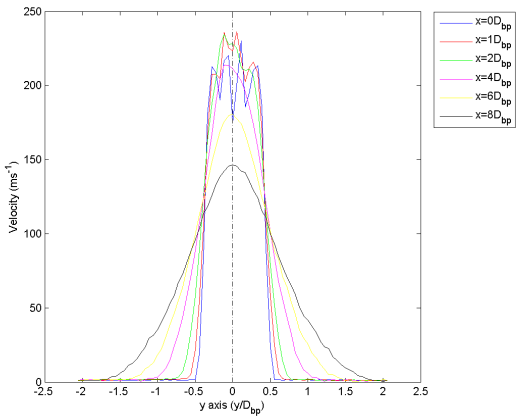

(a) CrCo, BpCo

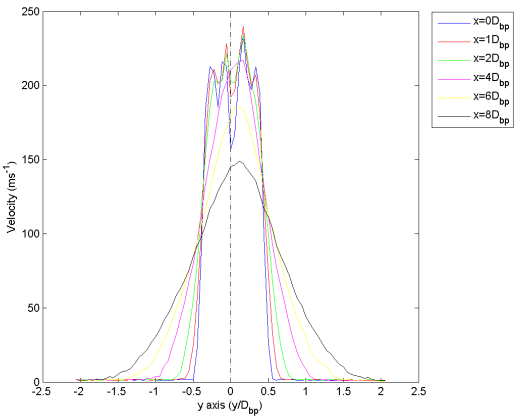

(b) CrCh, BpCo

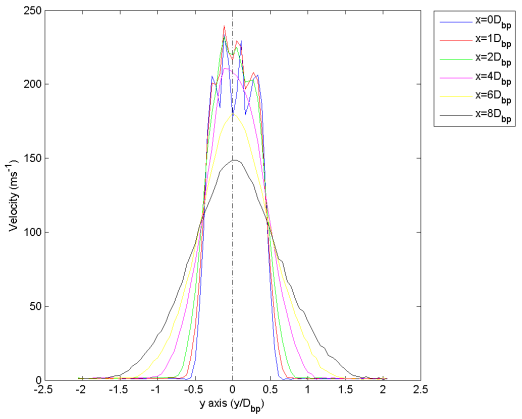

(c) CrCo, BpCh

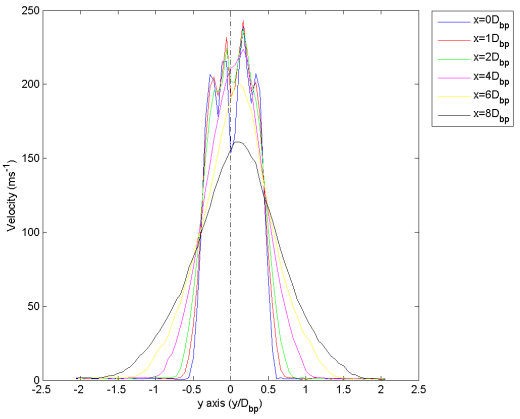

(d) CrCh, BpCh

Figure A.68: Axial velocity profile

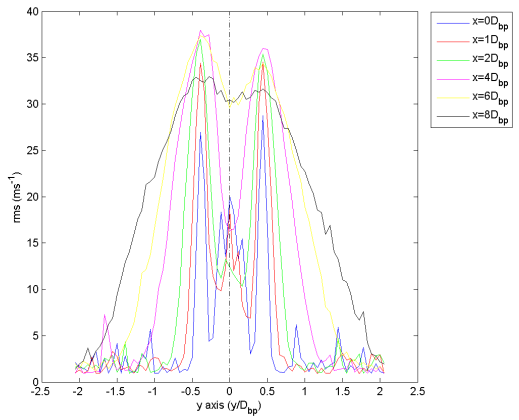

(a) CrCo, BpCo

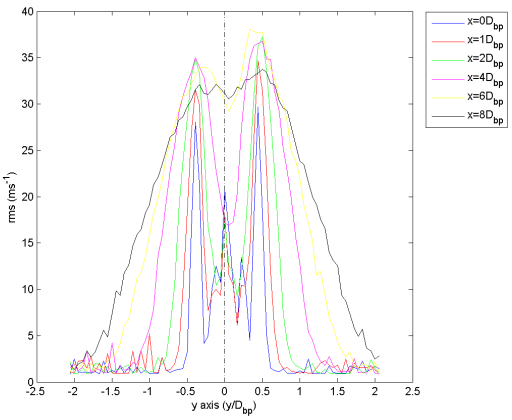

(b) CrCh, BpCo

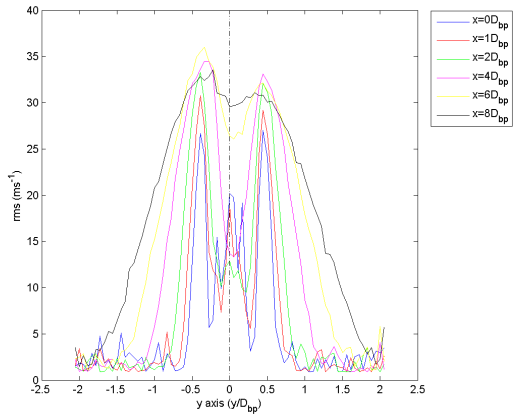

(c) CrCo, BpCh

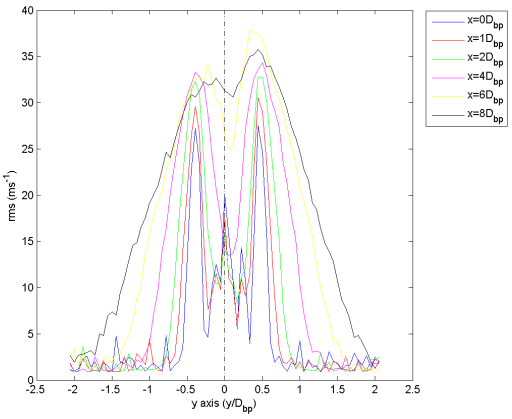

(d) CrCh, BpCh

Figure A.69: Axial rms profile

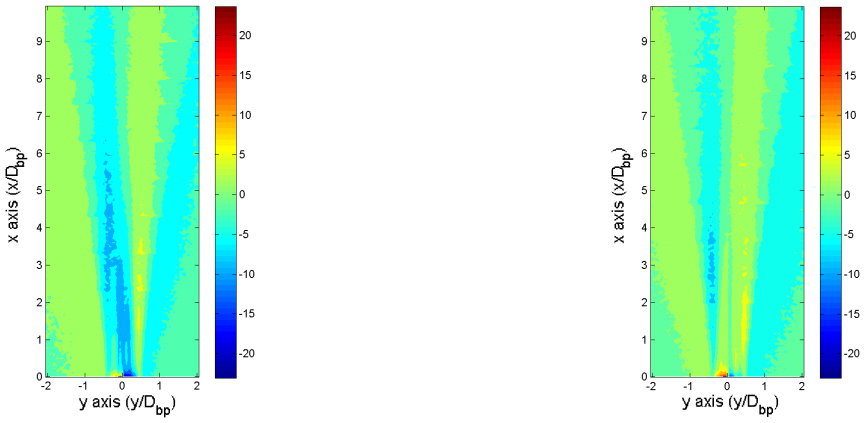

(a) CrCo, BpCo (b) CrCh, BpCo

Figure A.70: Radial velocity (colour bar in ms^{-1})

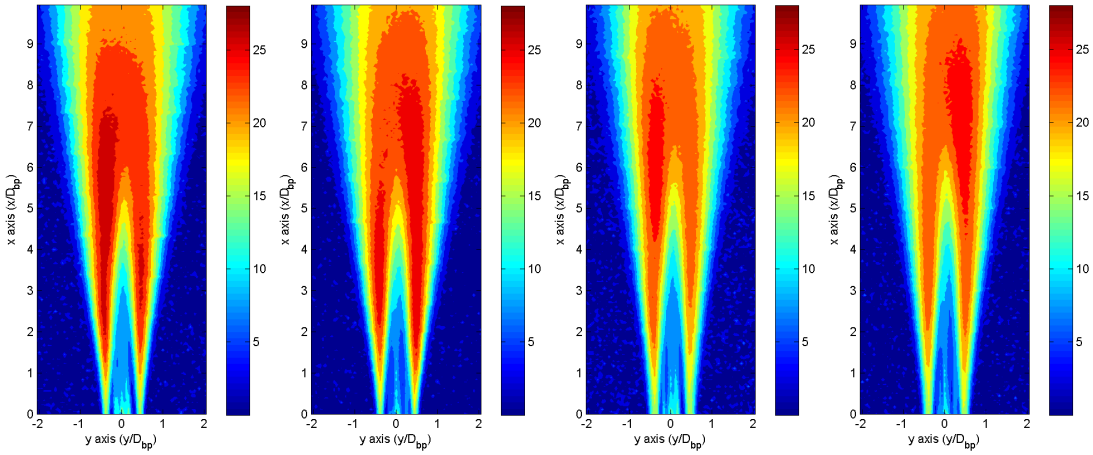

(a) CrCo, BpCo (b) CrCh, BpCo (c) CrCo, BpCh (d) CrCh, BpCh

Figure A.71: Radial rms (colour bar in ms^{-1})

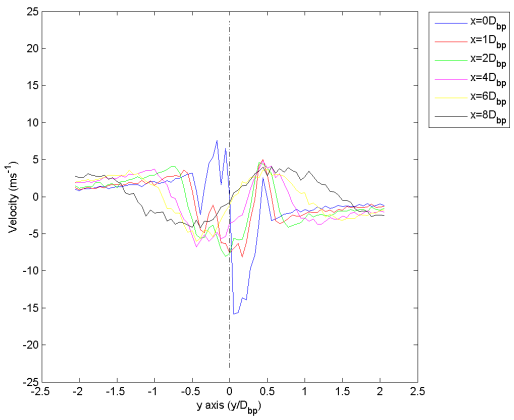

(a) CrCo, BpCo

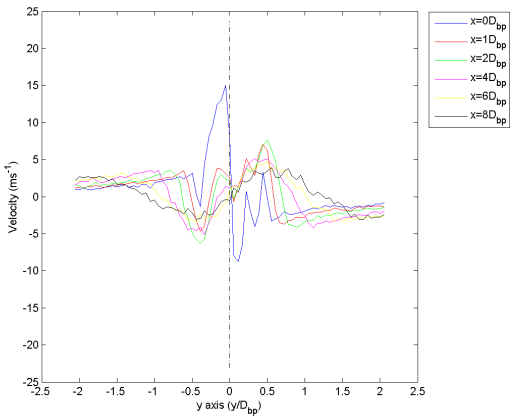

(b) CrCh, BpCo

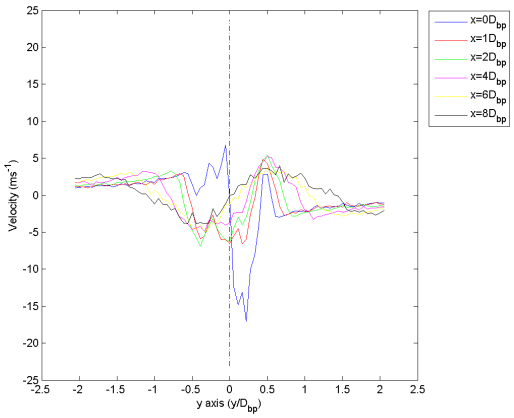

(c) CrCo, BpCh

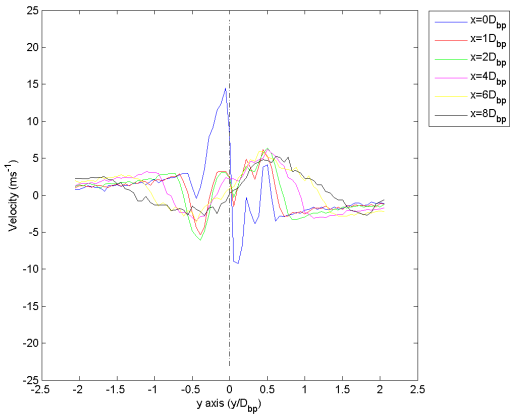

(d) CrCh, BpCh

Figure A.72: Radial velocity profile

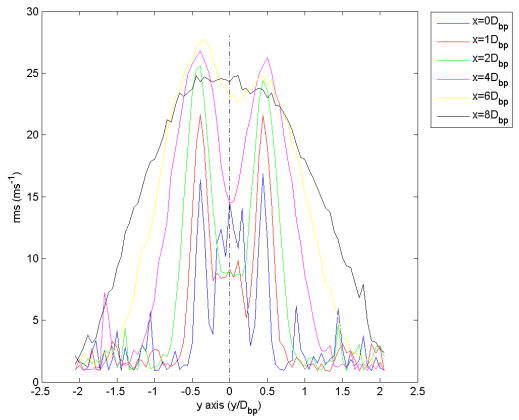

(a) CrCo, BpCo

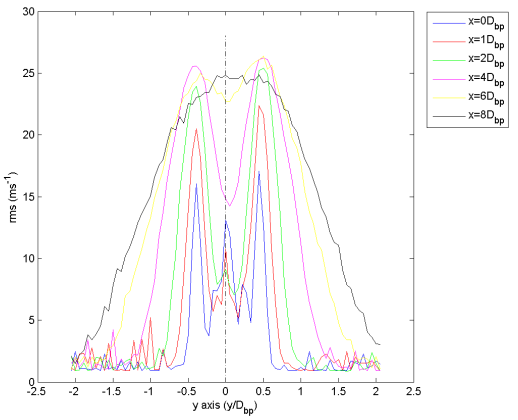

(b) CrCh, BpCo

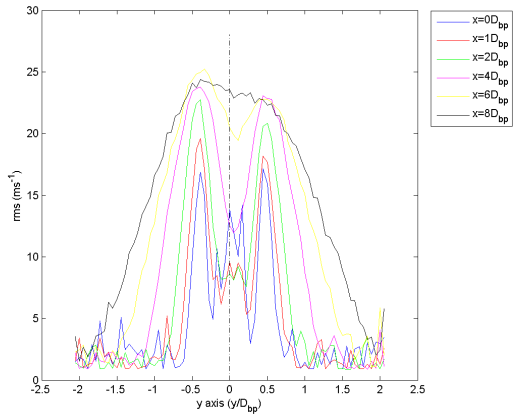

(c) CrCo, BpCh

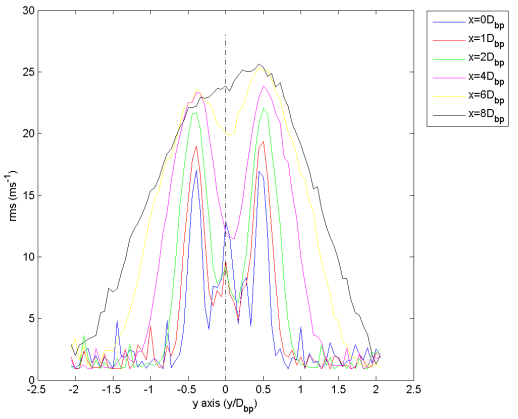

(d) CrCh, BpCh

Figure A.73: Radial rms profile

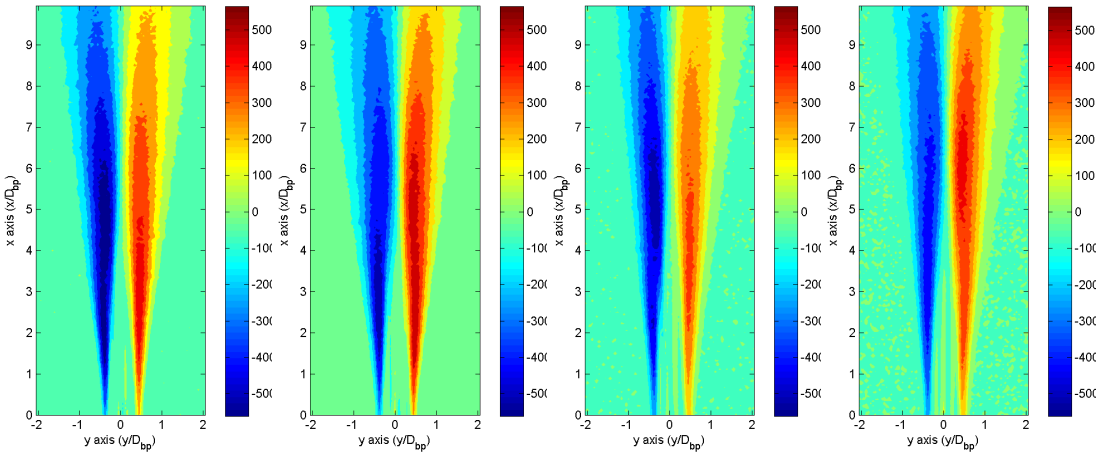

(a) CrCo, BpCo (b) CrCh, BpCo (c) CrCo, BpCh (d) CrCh, BpCh

Figure A.74: Reynolds shear stress UV (colour bar in $m^2 s^{-1}$)

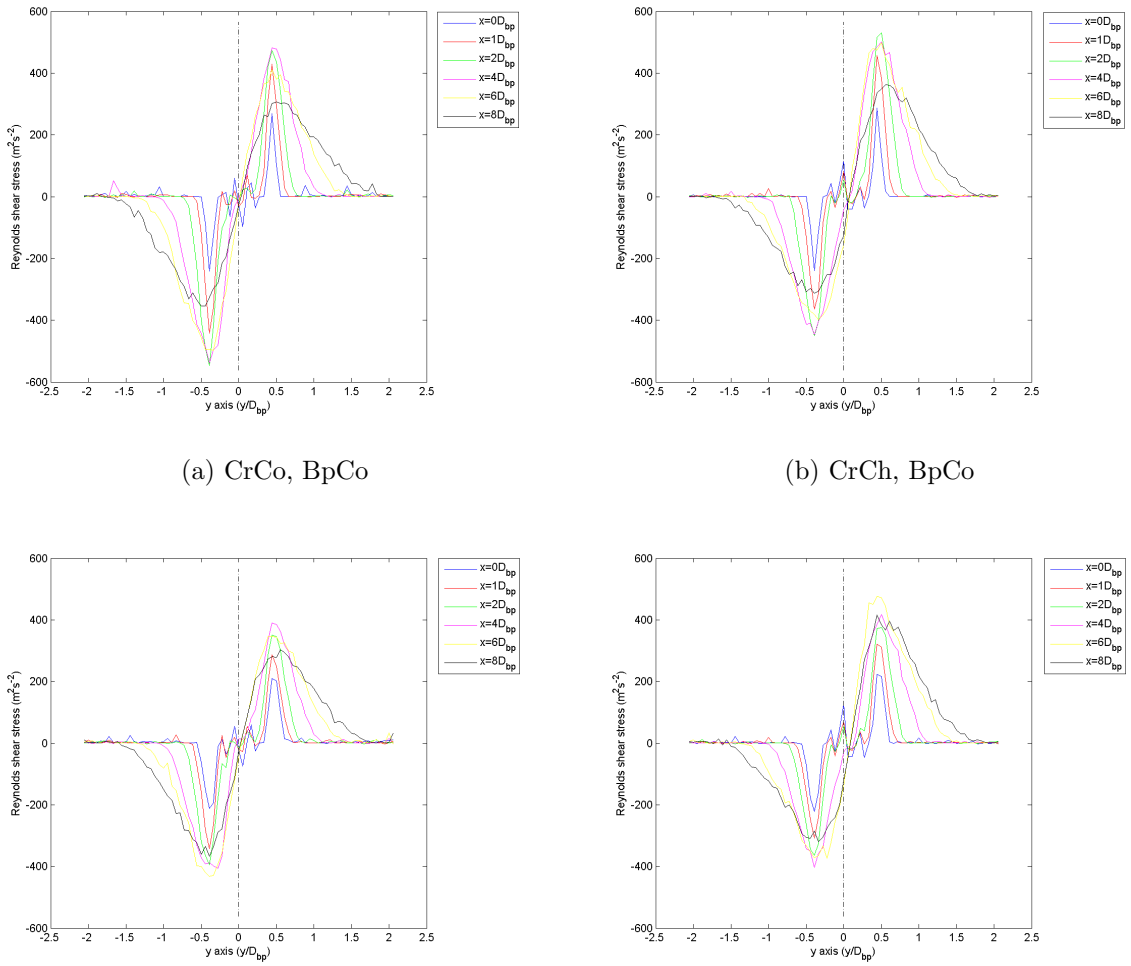

(a) CrCo, BpCo

(b) CrCh, BpCo

(c) CrCo, BpCh

(d) CrCh, BpCh

Figure A.75: Reynolds shear stress UV profile

A.7 Microphone array arrangement and directivity pattern

The directivity of acoustic sources is an important factor to consider when trying to understand and locate noise source mechanisms. The appropriate placement of microphones determines the quality of acoustic measurements. From the array arrangement, the directivity pattern can be determined which effectively calculates the spatial sensitivity of a given array. It indicates the arrays susceptibility to noise contamination in other regions of space.

As an illustration, four B&K 4939 1/4" condenser microphones with preamplifiers were mounted on radial frame (padded with acoustic foam) in the far field. A number of different far field microphone array arrangements were considered with a view to observe the differences in the spatial sensitivity between each arrangement and each microphone within an arrangement.

Three different array arrangements of inline, staged and rhombus were used as shown in Figure A.76. The inline array was a linear array and used microphone spacing of 8 cm. The staged array had each microphone staggered back from the preceding one. The vertical microphone spacing was 8 cm. The rhombus array also had spacing of 8 cm between its vertices where the microphones were placed.

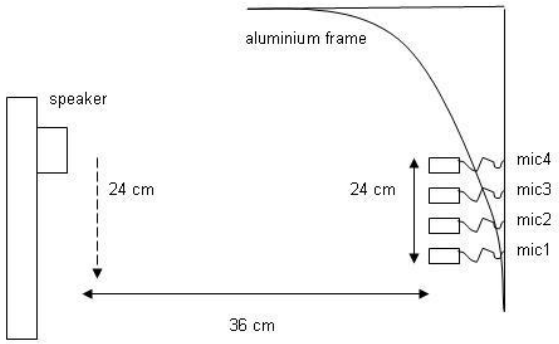

(a) Inline array

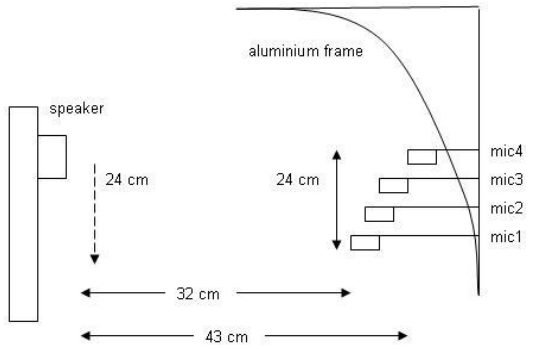

(b) Stage array

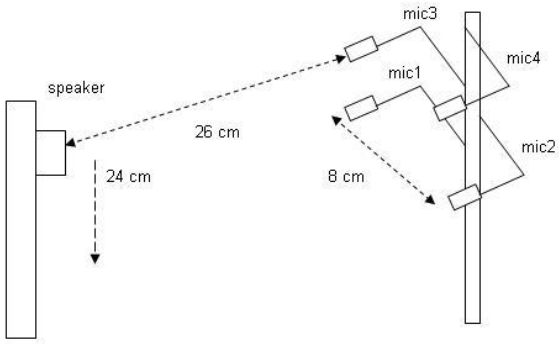

(c) Rhombus array

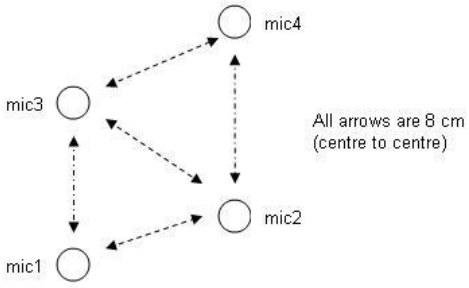

(d) Rhombus array face view

Figure A.76: Microphone arrays

A speaker emitting a 1 kHz tone was placed on a stand facing the microphone array. The speaker then moved vertically downwards in discrete steps of 1 mm. At each position, the microphones measured the sound pressure levels, the results of which can be seen in Figure A.77.

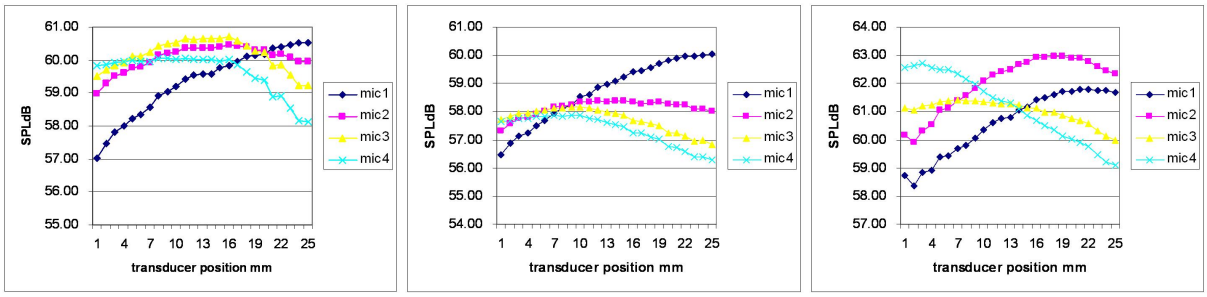

(a) Inline array (b) Stage array (c) Rhombus array

Figure A.77: Directivity patterns for different arrays

The microphone array arrangement highlight the differences in acoustic reception by each microphone within each arrangement, which is especially significant in the case of using beamforming techniques to locate sound source regions. Beamforming is a viable technique that could be used in future co-flow experiments, however it has a microphone spacing requirement of half of the wavelength under consideration. From a practical perspective, this restricts the measurement interest to the audible range, as a 20 kHz frequency has a wavelength of 17 mm, making the required microphone spacing 8.5 mm; higher frequencies have an even smaller microphone spacing requirement.

A.8 Discrete tone and cavity resonance

During the preliminary tests, the jet rig was run on condition and a discrete tone was observed. Steps were taken to find the cause of this tone and remove it providing a clean sound profile of the jet.

A.8.1 Discrete tone

The four B&K 1/4" microphones were calibrated using B&K 4231 Sound Level Calibrator at 1 kHz and positioned in a radial array as shown in Figure A.78. The distances from the microphones to the bullet tip in the jet rig are $r_1 = 100.9$ cm, $r_2 = 104.7$ cm, $r_3 = 107.9$ cm and $r_4 = 110.4$ cm.

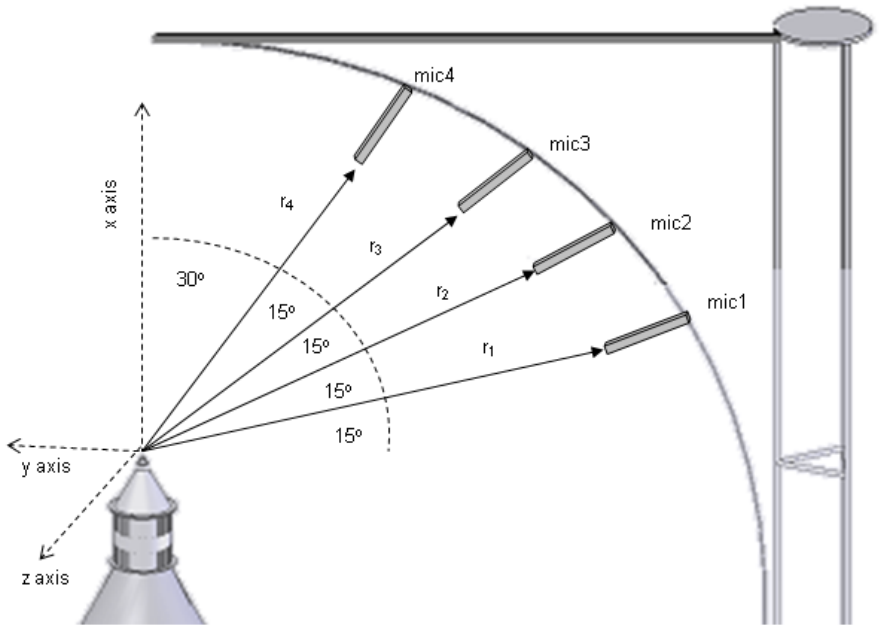

Figure A.78: Microphone arrangement 4

The core flow and the bypass flow were run together on condition and the microphones recorded the far field sound pressure level measurements. A discrete tone of 47 kHz was measured by all four microphones. This was a sharp and distinct peak which was on average 14 dB higher than the sound pressure levels of the neighbouring frequencies either side of the tone at 45 kHz and 49 kHz. Both the 1st harmonic at 47 kHz and 2nd harmonic (observed at ∼95 kHz) can be seen in Figure A.79.

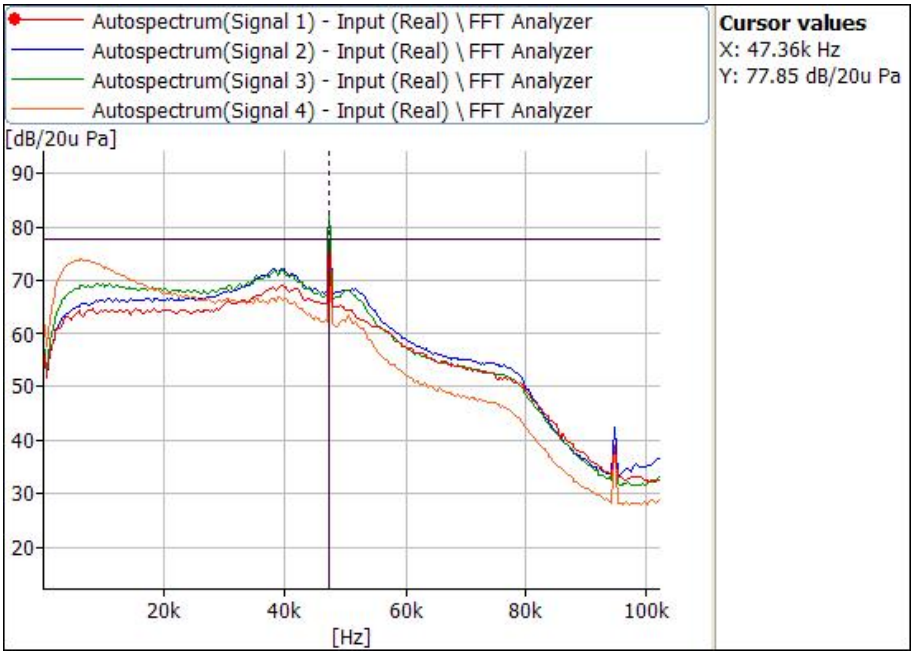

Figure A.79: Far field measurements revealing a discrete tone

The rig was then run with the core flow only and then the bypass only. The discrete tone appeared only when the core flow was running. That is, the tone appeared when either the core flow only was on, or when the core and bypass flow were on (as first observed).

It was first thought that the flow was not being calmed properly by the honeycomb mesh in the top chamber of the rig. Additional honeycomb mesh was inserted to help reduce any turbulence in the flow in this chamber. Unfortunately this had no effect when re-tested with the core flow on condition.

By considering the theory of vortex shedding past a cylinder as described by Kunda & Cohen (2004), shedding frequencies from the temperature and pressure probes for the core flow was then suspected for causing the tone. The probes were removed; the holes they passed through in the top chamber were temporarily sealed with modelling clay and the core flow was run on condition. The

discrete tone was still observed.

Next the vibration of the nozzles were considered. This was investigated to see if the output of the noise could be localized to a particular part of the nozzle.

The PSV-400-M2 Scanning Vibrometer by Polytec was used to measure the vibrations. It was an eye safe Class II He-Ne laser with a power output less than 1 mW. The wavelength was 633 nm with a bandwidth of 1 MHz. It was able to take high frequency non-contact vibration measurements from a distance of 2 m from the nozzles.

The surface of the nozzles was scanned and a measurement grid was mapped onto it providing 317 nodes. Figure A.80 shows this grid and measurements taken at 47.42 kHz (the peak frequency of the discrete tone).

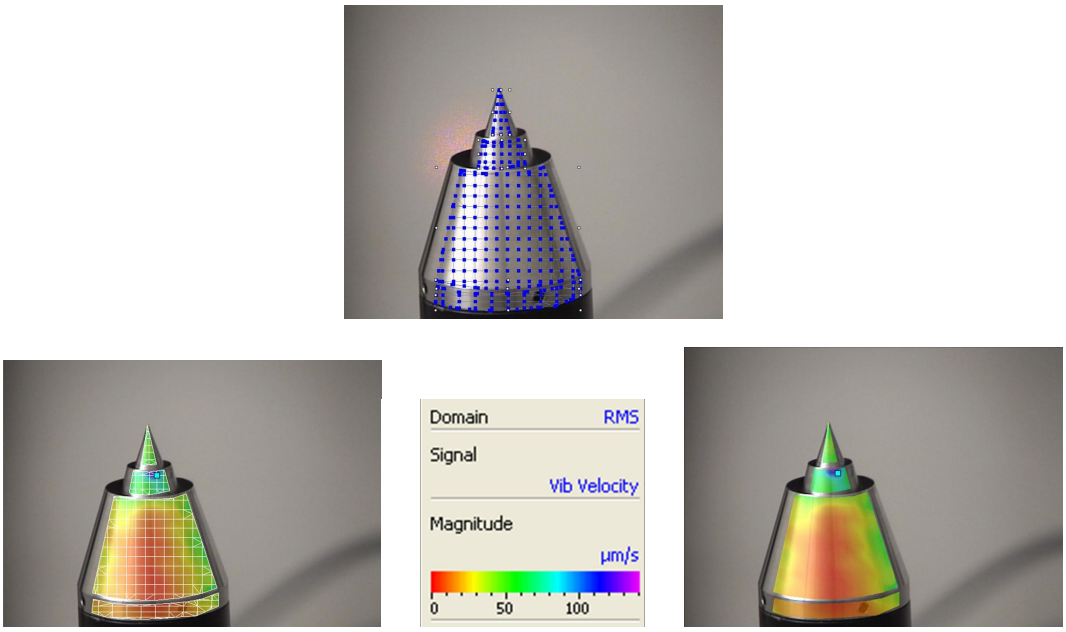

Figure A.80: Grid mapping by the vibrometer

The vibrometer moved to each node on the scanned grid and measured the vibration response. The results can be seen in Figure A.81 for the peak frequency of the discrete tone 47.42 kHz and the neighbouring frequencies of 44.74 kHz and 50.00 kHz. Note, each has its own colour bar scale.

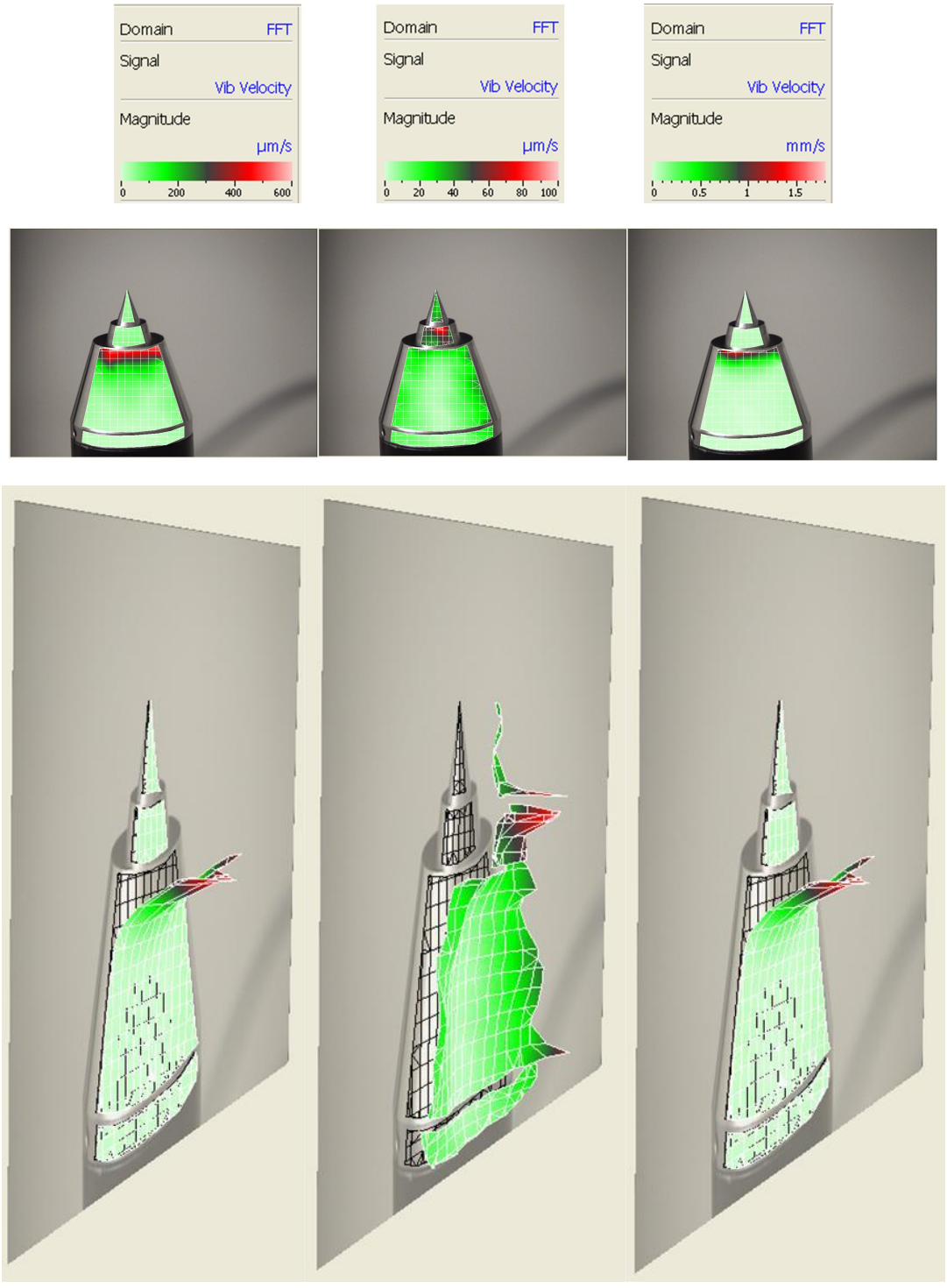

(g) 44.77 kHz (h) 47.42 kHz (i) 50.00 kHz

Figure A.81: Vibrometer results

The neighbouring frequencies have the largest vibrations at the lip of the bypass

nozzle, where as at 47.42 kHz the largest vibrations are at the lip of the core nozzle. However, magnitude of the vibrations at 47.42 kHz is six times smaller than the vibrations at 44.77 kHz and fifteen times smaller than 50.00 kHz. The largest noise disturbance caused by nozzle vibrations in this frequency region does not occur at 47.42 kHz, implying the peak frequency of the discrete tone is not caused by nozzle vibrations.

Another approach to find the source of the discrete tone was taken by reverting back to microphone measurements. Mic1 was placed in the near field of the jet in line with the tip of the bullet and the edge of the bypass nozzle as shown in Figure A.82. Using the bullet tip as a co-ordinate reference point of (0,0,0) for (x,y,z), mic1 was placed at (0,D_{by},0). Measurements were taken by mic1 at this point, followed by (D_{by},D_{by},0), (2D_{by},D_{by},0), (3D_{by},D_{by},0), (4D_{by},D_{by},0) and (5D_{by},D_{by},0).

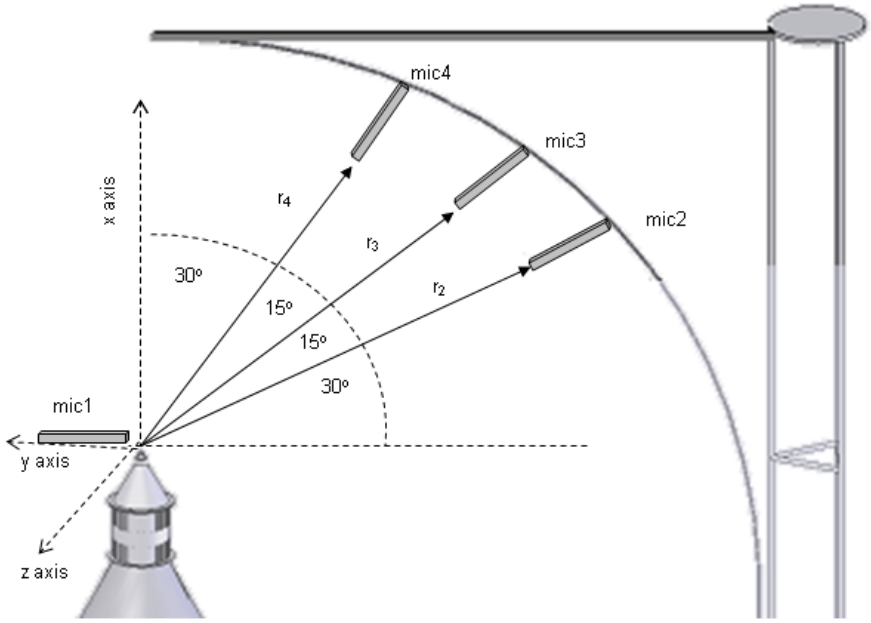

Figure A.82: Microphone arrangement 5

The SPLdB of the discrete tone were higher near the nozzle lip at (0,D_{by},0) and

reduced as mic1 moved up to $5D_{bp}$. This gave rise to the idea that the tip of the bullet may be the cause of the high frequency vortex shedding.

A brass bullet (same dimensions as the original steel bullet) was smoothed over with a coarse grain and then fine grain sanding paper and the core flow was run again. The discrete tone was still present. The bullet tip was further smoothed and as a byproduct was shortened slightly. However, when the jet rig was run on condition, the discrete tone was still present; a change in curvature of the bullet tip made virtually no difference.

The original steel bullet was then replaced and the core flow was turned on with varying levels of velocity. Exit flow speeds of 75, 100, 125, 150, 175, 200 ms^{-1} were measured by the Dantec LDA laser system for each of the varying mic1 positions of (0,D_{by},0), (D_{by},D_{by},0), ($2D_{by}$,D_{by},0), ($3D_{by}$,D_{by},0), ($4D_{by}$,D_{by},0) and ($5D_{by}$,D_{by},0) giving a total of 36 acoustic readings.

A pattern emerged. As the velocity of the core flow increased from 75 ms^{-1} a discrete tone of 38 kHz appeared at 125 ms^{-1}. This remained in place until 200 ms^{-1} when it then 'jumped' to 47 kHz and continued to hold until the core flow was running on condition at 240 ms^{-1}. The velocity of the flow was then decreased from condition with an expectation that the discrete tone of 47 kHz would jump down to 38 kHz when the flow was at 200 ms^{-1}. However this did not happen, the jump occurred at 150 ms^{-1}. The tests were repeated and the same results were observed.

This suggested there was a feedback loop in place which caused the discrete tone jump to occur at different flow velocity values (depending on if the flow was

increasing or decreasing). From past laboratory experiences, this suggested the presence of a cavity. The upper chamber of the jet rig was dismantled and a small gap between the core nozzle and centre chamber rod to which its screwed into was found as shown in Figure A.83.

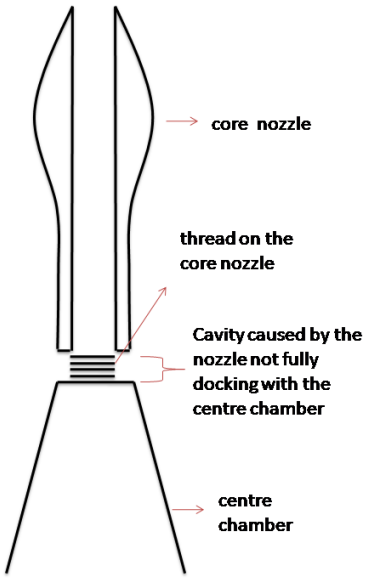

Figure A.83: The location of the cavity

A.8.2 Cavity resonance

As the flow passed over the cavity, the frequency and amplitude of the discrete tone, varied with the velocity of the flow. In fact as the flow velocity was increased, the frequency of the discrete tone 'jumped' to a higher frequency. However when the flow velocity was decreasing, the jumps showed hysteresis; their downward jump occurred at a lower speed than their upward jump. This can be seen in Figure A.84 and Figure A.85. This manner of hysteresis was also observed by Ahuja & Mendoza (1995) in their computational work as described by Howe (1997) and by experimentalists such as Umeda & Ishii (1999) and Raman *et al.* (2002).

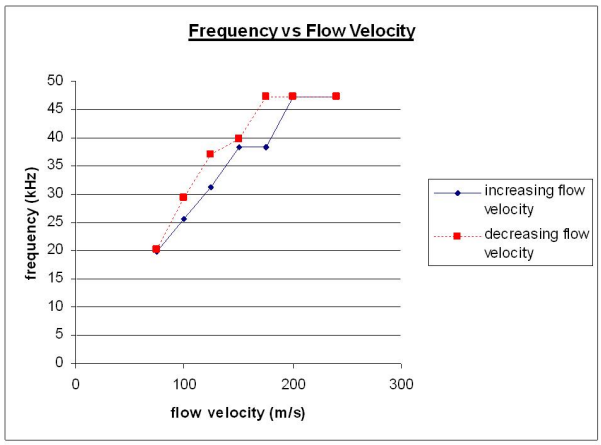

Figure A.84: Discrete tone occurrences 1

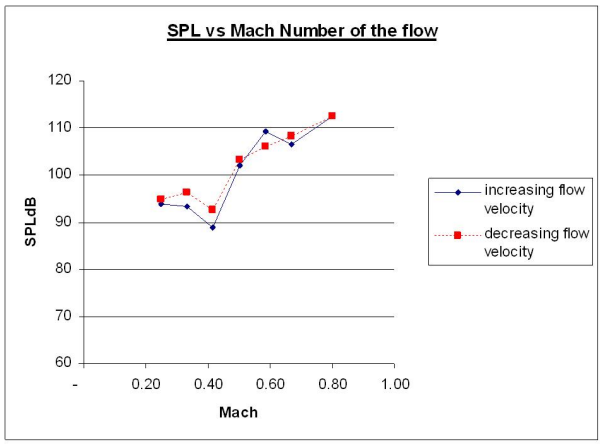

Figure A.85: Discrete tone occurrences 2

Cavity resonance has been studied by many researchers focusing on the Mach number of the flow and the length to depth ratio of the cavity. Plumblee *et al.* (1962) first put forward the notion through his observations that cavity resonances produce discrete tones. As the flow passes over the cavity, a turbulent shear layer forms over the open end region producing a broad band noise source that drives the cavity resonance. The rectangular cavity responds to the excitation of the broadband by amplifying certain narrow band frequencies.

However, this was further explored by Rossiter (1966) and Heller *et al.* (1971) who found in their experiments that if the boundary layer going across the open region of the cavity is laminar, then the tones produced by this flow are louder than the if the boundary layer was turbulent. This was supported by the data from Krishnamurty (1955). Rossiter also found that if the Strouhal numbers (using the flow velocity and length of the cavity) are plotted against Mach numbers (range from 0.4 to 1.2 Ma), the data points produce definitive bands on the graph. He attributed this to acoustic feedback and confirmed this phenomenon with the use of shadow graph images. These revealed that vortices were shed periodically near the upstream lip of the cavity and then travelled downstream along the shear layer (over the open end region of the cavity). This gave rise to Rossiters model for the generation of cavity tones; when the convected vortices in the shear layer reach the downstream end of the cavity, they interact with the wall, creating an acoustic pulse which propagates back upstream in the cavity itself. When they reach the upstream wall of the cavity, they then cause the shear layer by the edge of the cavity wall to separate, resulting in the shedding of new vortices, which then completes the vortices and acoustic disturbance feedback loop. Based on this model and his observations, Rossiter derived a semi-empirical formula for tone frequencies.

$$\frac{fL_{cav}}{U_\infty} = \frac{m - \gamma_f}{Ma + 1/\kappa} \tag{A.1}$$

where f = frequency of tones, L_{cav} = length of cavity, U_∞ = free stream velocity, m = integer, Ma = Mach number, κ = ratio of convection velocity of vortices to free stream velocity, γ_f = a factor to account for the time lag between the passage of a vortex and the emission of a sound pulse at the downstream corner of the cavity.

Rossiter found by experiment that $1/\kappa = 1.75$ and $\gamma_f = 0.25$ provided a good data fit. The prediction of discrete frequencies can be found by re-arranging the above equation.

Significant work has been done on cavity resonance and with notable advances in understanding the mechanisms involved. Cavities albeit small such as the one found in the jet rig can cause disproportionately undesirable results such as a sharp and distinct discrete tone in the acoustic profile of the jet flow. This iterates the importance of precision engineering in experimental arrangements.

The incorrectly manufactured core nozzle was removed and a new core nozzle was commissioned. When the jet rig was reassembled with this nozzle and run on condition, no discrete tone was observed in the acoustic profile of the jet.